THE UNIVERSITY *of* EDINBURGH

Synthesis, Structural and Magnetic Properties of Some Transition Metal Oxides

Kunlang Ji

For the degree of Doctor of Philosophy

The University of Edinburgh

2019

Lay summary

One of the driving forces behind scientific research is to design new materials with novel technological applications. Materials that combine transition metal elements and oxygen are rich in electronic and magnetic properties, which have an important role in the technology landscape. Applications such as rechargeable batteries in portable electronics, solar cells and solid-state data storage devices are well developed and extensively used.

The interesting properties of a particular transition metal oxide material arise from the cation-cation interactions and the atom arrangements. For instance, interactions between cations that have magnetic moments from unpaired electrons can cause a material to have a macroscopic magnetic moment when the atomic moments are aligned through magnetic ordering (ferromagnetism or antiferromagnetism) below a certain temperature. Furthermore, modifications to the arrangements of atoms (the crystal structure), such as by applying high pressures, can also lead to large changes in physical properties. Therefore, understanding the fundamental science such as atomic interactions and arrangements on a microscopic level is very important for the understanding of the related macroscopic properties, so as to discover new materials with useful applications.

The work in this thesis is concerned with the synthesis of novel metal oxide materials which possess interesting structural and magnetic properties. All these new materials belong to the perovskite family or corundum family and contain transition metal cations on which the properties will be focused. Pressure is introduced to some of the materials' syntheses in order to stabilise a crystal structure in which small cations are forced into large cavities. Herein a large Walker type multi-anvil apparatus was used for providing high-pressure (max. 20 GPa) high-temperature (max. 1400 °C) conditions to carry out syntheses such as replacing large La^{3+} ions with smaller Y^{3+} ions in $LaRuO_3$, which cannot be accomplished at ambient pressure.

Moreover, crystallographic studies of $(CuCl)La_{1-x}Sr_xLaNb_2O_7$ investigated how the structural properties vary with chemical substitution. It had been previously reported that $(CuCl)LaNb_2O_7$ underwent two structural phase transitions when heated to critical temperatures. This study of

solid solutions found that structural transitions shifted to lower temperatures upon chemical substitution.

Powder diffraction using X-ray and neutron sources has been used as a powerful experimental technique to analyse metal oxide materials. Neutron beams in particular, generated either by a nuclear reactor or by a particle accelerator, allow the thorough characterisation of both the crystal and magnetic structures of these materials and hence allows the fundamental origins of their physical properties to be understood further.

Abstract

The thesis compiles the synthesis and study of several new materials in the perovskite and corundum families. These transition-metal oxide materials have been structurally characterised and their physical properties have been examined.

The new series of substituted Dion-Jacobson layered perovskites $(CuCl)La_{1-x}Sr_xNb_2O_7$ with x = 0, 0.1 and 0.2 has been prepared via topotactic ion-exchange reactions. Refined powder synchrotron diffraction data confirms that all of these compounds adopt the *Pbam* orthorhombic structure above room temperature and the lattice parameter *a* becomes larger with increasing substitution of Sr^{2+}. The *Pbam* (<500 K) → *Pbmm* (500 ~ 640 K) → *P*4/*mmm* (>640 K) phase transitions found in $(CuCl)LaNb_2O_7$ that have been published in a previous report shift towards room temperature as x increases. The magnetisation data suggests that the transition to the spin dimer ground state, present in $(CuCl)LaNb_2O_7$ at 14.5 K, is fully suppressed upon Sr^{2+} substitution. Low temperature neutron diffraction data indicates that substituted $(CuCl)La_{1-x}Sr_xNb_2O_7$ phases are paramagnetic and retain the *Pbam* structure down to 2 K.

New corundum derivatives Co_2ScSbO_6 and $Ni_{2-x}Co_xScSbO_6$ solid solutions that are of interest as potential multiferroic materials have been synthesised. $Ni_{2-x}Co_xScSbO_6$ (x = 0 – 1.5) was prepared via a conventional solid-state route at ambient pressure while Co_2ScSbO_6 was synthesised under high-pressure condition as the pure phase cannot be prepared at ambient pressure. All of these compounds adopt the polar Ni_3TeO_6-type structure and order ferrimagnetically below the Néel temperature of 60 K. Meta-magnetic transitions are observed for x = 0.5 and 1 revealing complex magnetic behaviour. Ni_2ScSbO_6 is reported to have a helimagnetic spin order with propagation vector k = [0 0.036 0]. A remarkable series of long-period lock-in [0 0 1/3n] helical spin structures with n = 5, 6, 8 and 10 is found in $Ni_{2-x}Co_xScSbO_6$, coexisting with a ferrimagnetic [0 0 0] phase at high Co-contents. The presence of electrical polarisation and spontaneous magnetisation offers possibilities for multiferroic properties.

Ruthenium-containing metal oxides have a diverse range of unusual physical properties as a result of electron-electron correlations within broad 4*d* bands. A new perovskite material $YRuO_3$ with non-magnetic Y^{3+} at the A-site, that is structurally similar to the $LnRuO_3$ perovskites, has been synthesised at 1200 °C and 15 GPa, and adopts a *Pnma* superstructure

with a = 5.835(1), b = 7.528(1) and c = 5.193(1) Å. DC and AC magnetisation data both confirm that magnetic ordering occurs at around 97 K. Apparent changes in spin or domain relaxation processes are observed at 47.2 and 47.4 K in AC magnetisation data as well. Magnetisation steps evidence an unprecedented fractional weak ferromagnetic state at ¾ which reflects extreme single-ion anisotropy resulting from the strong spin-orbit coupling of the d^5 Ru^{3+} ion. Resistivity measurements on a ceramic pellet display a semiconducting behaviour with a relatively small activation energy of 70 meV. A neutron diffraction study of $YRuO_3$ reveals a G-type antiferromagnetic spin structure with an ordered moment of 0.33(3) μ_B at 1.7 K. The refined Ru-site is fully occupied, in comparison to the ~ 10 % Ru-site deficiency found in all the other $LnRuO_3$ compounds, suggesting the existence of the pure unusual Ru^{3+} oxidation state. This study elucidates the electronic and magnetic properties of $YRuO_3$, which appears to be the first Ru^{3+} oxide to exhibit spin ordering phenomena.

Acknowledgement

The research contained in this thesis could not have been achieved without the individuals listed below.

First and foremost, as one of the PhD students from the Attfield Group, I would like to give my chief thanks to my PhD supervisor Prof. J. Paul Attfield for the opportunity to learn and study at Centre for Science at Extreme Conditions (CSEC), as well as funding me to attend conferences, training schools and the research visit to Kyoto University, Japan. His wealth of knowledge, unfaltering assistance, inspiring guidance and patience helped me learn not only the secrets of solid-state science but also allowed me grow up and become mature during the past few years. I would also like to thank to my previous supervisor Dr. Mark de Vries who lead me to the field of solid-state science and provided guidance during my first year. Also my PhD viva examiners, Prof. Duncan Gregory from the University of Glasgow and Dr. Olof Johansson from the University of Edinburgh who would like to share comments and perspectives on the science presented in this work. I must thank to the Tercentenary Scholarship from the School of Chemistry, University of Edinburgh that supported my PhD career and the EPSRC Core-to-Core project for funding my research trip to Japan.

I am grateful and fortunate to learn from other group members who provided me with day-to-day support. Thanks to our former postdoc Dr. Angel M. Arevalo-Lopez who taught me how to use the big Multi-anvil press and guide me on the high-pressure project. He offered me opportunities to measure high quality magnetism data using his advanced PPMS even after he left the group. I would also like to thank Dr. James Cumby for teaching me to use the D8 diffractometer in CSEC, the closed cycle refrigerator (CCR) to measuring the samples resistivity, the GSAS program and for his patience in solving my crystallographic issues. Thanks to Dr. Paula Kayser for sharing her experience on ruthenium based perovskites which gave me a lot ideas on my $YRuO_3$ perovskite presented in Chapter 5. I must give a special thank you to Dr. Elena Solana-Madruga who spent so much time in the press lab helping and giving me advice on my high-pressure projects and sharing with me her secrets of how to analyse neutron data. She made a great contribution to synthesising and analysing the solid solution $Ni_{2-x}Co_xScSbO_6$ in Chapter 4. I must also thank my office neighbour Dr. Elise Pachoud

for her enormous knowledge and patience in answering my Origin questions, refinement questions and life issues, etc. I was extremely lucky to share a desk with you during my PhD career.

In addition, this work would not have been completed without contributions from our kind collaborators. Thanks to our WISH local contact Dr. Pascal Manuel who offered great guidance and assistance during my 'weekend' neutron experiments at ISIS. Thanks to our local contacts Dr. Anatoliy Senyshyn and Dr. Clemens Ritter from FRMII and ILL respectively who offered extra neutron beamtime to help me collect as much data as possible. Also thanks to the whole I11 beamline team at Diamond who provided a comfortable environment and useful guidance during my synchrotron experiment. I would also like to thank Dr. Xiao Wang from CSEC who taught me how to use the SQUID and PPMS and helped me collect magnetism data even during the weekends. In addition, I would like to thank Dr. Gary Nichol for offering the X-ray training courses and maintaining the X-ray diffractometers in the School of Chemistry that provided excellent D2 and D8 diffractometers for preliminary phase analysis in this thesis.

With those individuals I mentioned above, I would also like to thank the PhD students from Attfield group that I have worked with over the past few years: Alex Browne, Giuditta Perversi, Edward Pace, Jacky Hong, Paul Sarte, Hannah Johnston, Padraig Kearins, Patricia Kloihofer and Khalid Alharbi. Special thanks to Alex Browne, Edward Pace and Padraig Kearins who did a lot thesis proofreading and helped correct my grammar. I was also fortunate to meet and work with master students and visitors: Dr. Atsushi Kitada, Dr. Congling Yin, Prof. A. Sundaresan, Simon Engelbert, Jingyi Ran, Yu Sun, Bruno Sousa Araújo and Viliam Hakala. Thanks to everyone for your discussions, assistance and friendships.

On a more personal note, I would like to give a big thank to my non-academic friends who enriched my spare time during my PhD. Thanks to Xiaojiao Liu and Haoxiang Jin with whom I have lunch and chat with every day. Thanks to my brothers and sisters from the Chinese Evangelical Church in Edinburgh (CECE) for your kind support and prayers. Thanks to my neighbourhood friend Xiao Wang and your family for your enormous assistance and helping me have an easy and great life in Edinburgh.

Last but not least, I would like to thank to my parents Tianlong Ji and Huiping Zhao for their unconditionally financial and emotional support. This PhD thesis would not have been completed without your incredible encouragement and love. I would also like to give my biggest thank to my wife Yifang Xu for her encouragement and support over the past few years,

not only in academic but with everything in my daily life. Meanwhile, your cooking is the best in the world.

Content

Chapter 1. Introduction

1.1 Transition-metal oxides

Transition metal oxides (TMOs) are probably the most well studied class of materials in solid-state science, which exhibit many physical and chemical properties. The structural and chemical complexity can be enhanced by increasing the number of constituent elements. The additional cations are not limited to *d*-block elements as there exist numerous examples of materials containing cations from the *s* or *p* block. TMOs have a wide range of applications including uses in solid-oxide fuel cells[1] and magnetic data-storage[2], and these materials play an essential part in electronic and magnetic materials research. A series of representative examples are layered cuprates $La_{2-x}Sr_xCuO_4$[3] which displays high T_C superconductivity; the ferroelectric compound $BaTiO_3$[4]; Sr_2FeMoO_6[5], which has colossal magnetoresistance and the multiferroic materials $BiFeO_3$[6-7] and $TbMnO_3$[8].

The chemical and physical properties of TMOs are significantly determined by their crystal structures, which can adopt a diverse range of configurations such as perovskite-, spinel- and pyrochlore-type. From a macroscopic point of view, by changing external conditions such as temperature and pressure or the inherent conditions, for instance changing the chemical composition, the crystal structures of TMOs can be modified and therefore the intrinsic properties can be altered, e.g. from metallic to insulating or from ferromagnetic to antiferromagnetic and vice versa. On a microscopic scale, the unusual characteristics arise from the unique nature of the valence *d*-electrons. As the *s* and *p* orbitals of neighbouring ions form strongly overlapping bands, the valence electrons are capable of delocalising across the whole structure. In contrast, the localised valence *f*-electrons from rare-earth atoms are pulled towards the atomic core resulting in pure ionic interactions with adjacent atoms. However, the interactions arising from the valence *d*-electrons fall somewhere between the two phenomena. Because of the small orbital overlap between the transition-metal *d* and oxygen *p* orbitals,[9] the width of the valence band *W* is approximately equal to the electrostatic repulsion *U* between two valence electrons on the same atom in many TMOs. Therefore, *d*-elections are on the verge of being fully localised or completely itinerant. This unique phenomenon has been already used

to explain the formation of Cooper pairs in high T_C superconducting cuprates.[10] The preference of either metallic or insulating can be variable,[11] owing to the small band gap between different states in many TMOs and the presence of the small band gap can be used to interpret why this phase transition could be induced by applying outside perturbations such as temperature, pressure, an electric/magnetic field or changing the chemical composition. With physical modifications like temperature or pressure, the crystal structure of one transition metal oxide can also be varied due to the nature of the bonds, and the transition to a different crystal symmetry is normally accomplished with changes in its physical properties.[9] A 3*d* transition metal oxide is a typical strongly correlated electron system as the coulomb interactions between electrons in the 3*d* localised orbitals are relatively strong. In such an anisotropic 3*d* electronic orbital system, the strong couplings between crystal lattice, spin, electric charge and orbital degrees of freedom induce enormous magnetic and electronic phenomena. In some cases with structural distortions, the formation of long range magnetic ordering can break the inversion symmetry and consequently allow a net polarisation.[12] The correlation between the electrical polarisations and magnetisations are introduced as multiferroicism. This topic in the electro-magnetic research area along with other properties are attributed to the subtle interplay of lattice structure, electronic configuration and the magnetic interaction between the unpaired elections from the component ions in TMOs. Investigating the electric charges (electronic state), spins (magnetism) and orbital attributing in TMOs is one of the critical paths to having a better understanding of the structure-to-property relationship and to understand the exceptional characteristics of strongly correlated electronic systems.

In this work, physical chemistry investigations will be carried out and applied to TMOs mainly in the ABO_3 perovskite family and to related derivatives. The thesis will focus on materials that have potentially interesting electric and magnetic properties, for example multiferroism.

1.2 Perovskites

Perovskite is the general term for a large family of compounds that has a crystal structure related to the original calcium titanate ($CaTiO_3$) mineral. The perovskite family name originates from this mineral which was first discovered by Gustav Rose and named after a Russian mineralogist Lev Perovski.[13] The general formula of a perovskite is ABX_3. 'A' usually represents alkaline earth or rare earth elements while the B site ions could be 3*d*, 4*d* or 5*d* transition metal elements. Normally, the negative ions, X, refer to oxygen ions, however large

ions such as Cl^- or Br^- are still possible. In the family of perovskite oxides, cations on the A-site are usually divalent and cations on the B-site are tetravalent. Nevertheless, perovskite compounds with cation combinations of $A^{1+}B^{5+}O_3$ or $A^{3+}B^{3+}O_3$ can be synthesised as well.[14-15] The ideal perovskite, for instance $SrTiO_3$, adopts a cubic crystal structure despite the original $CaTiO_3$ being an orthorhombic-type perovskite. This is described in Fig. 1.1 which shows a cubic perovskite structure formed at room temperature with the space group *Pm*-3*m*, $SrTiO_3$. In this ideal perovskite structure, the corner-sharing $[TiO_6]$ octahedra along with Sr^{2+} ions occupying the 12-coordinate cavities between the octahedra constitute a three-dimensional lattice.[16] Many perovskite structures that have been found are distorted from the ideal cubic structure due to the tilting of $[BX_6]$ octahedra.[17] Specifically, the octahedral tilts normally occur in perovskites when the cations at the A-site are either too small or too large to occupy the 12-fold cavities in the centre of the network. Therefore, the A-O bonds are no longer equivalent, which induces a change of the A-site coordination number, forming a distorted perovskite structure in order to compensate by shrinking (small A-cation) or enlarging (big A-cation) the A-site cavity. This will be described later in more detail.

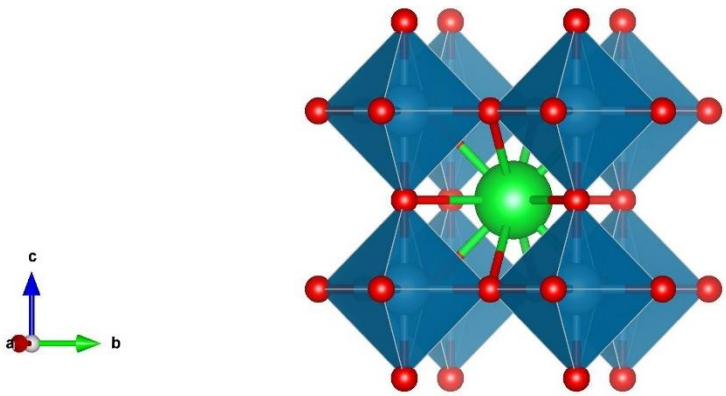

Fig. 1.1 The unit cell of $SrTiO_3$, with an ideal perovskite structure, adopting the cubic *Pm*-3*m* space group. The central Sr cation (green) is surrounded by 8 corner-sharing $[TiO_6]$ octahedra (blue). O atoms are depicted in red. The graphic is generated using VESTA.[18]

1.2.1 Tolerance factor

For an ideal cubic perovskite structure, the cell axis, *a*, is geometrically correlated to the ionic radii of r_A, r_B and r_x as presented in Eq. 1.1:

$$a = \sqrt{2}(r_A + r_X) = 2(r_B + r_X) \quad (1.1)$$

The ratio of the two expressions for the cell length, which is described in Eq. 1.2, was first defined by Goldschmidt[19] in 1926. The dimensionless quantity *t* is called the Goldschmidt tolerance factor which allows scientists to estimate the degree of structural distortion.

$$t = \frac{r_A + r_X}{\sqrt{2}(r_B + r_X)} \quad (1.2)$$

The tolerance factor *t* here is a dimensionless quantity based on ionic radii of the constituent ions. For instance, the ideal cubic perovskite $SrTiO_3$ has Sr^{2+} r_A = 1.44 Å, Ti^{4+} r_B = 0.605 Å and O^{2-} r_O = 1.40 Å, leading to the tolerance factor t = 1.00. Generally the tolerance factor value for a cubic perovskite is in the region of $0.9 < t < 1$. The factor *t* can be used to estimate whether a selected ion could be compatible with the structure or how much the $[BX_6]$ octahedra would have to tilt to compensate for a larger or smaller A-cation. Generally, with larger A- or smaller B-cations, the value of *t* will be greater than 1 yielding a hexagonal structure, for instance $BaNiO_3$.[20] Diverse distorted perovskites with lower symmetry structures, like the orthorhombic perovskite $GdFeO_3$[21], exist when $0.8 < t < 0.9$. Furthermore, the corundum structure (α-Al_2O_3) and its derivatives (ilmenite- and $LiNbO_3$-type) are preferred when *t* is lower than 0.8.[22] The bixbyite-type (e.g. α-Mn_2O_3) structure is exceptionally observed when the A site cation is very small, making *t* in the region of $0.7 < t < 0.75$. It is necessary to note here that complex behaviours such as lone pair effects, Jahn-Teller distortion, metal-metal interactions and the degree of covalency may exist and still need to be considered along with the ionic radii of the component ions. [23]

1.2.2 Distortion of perovskite

1.2.2.1 Glazer notation

The description and classification of octahedral tilting and the relationship between the tilting and the unit-cell geometry were first reported in detail by A. M. Glazer in 1972.[24] An octahedron [MO_6] in the perovskite system can rotate along the Cartesian axes *a*, *b* and *c* in the unit cell resulting in two different types of tilting: in-phase and out-of-phase tilting. An in-phase tilt is described as successive octahedral layers, perpendicular to the rotational axe, rotated in phase (same tilt), written as a positive superscript '+'. An out-of-phase tilt, denoted as a negative superscript '-', indicates octahedral layers along the axis are rotated out of phase (opposite tilt). A superscript of '0' indicates no rotation of the successive octahedra about that axis. For example, an ideal cubic perovskite $Pm\bar{3}m$ with no octahedral tilting will be classified as $a^0a^0a^0$. The three letters *a*, *b* and *c* represent the octahedral tilting along the [100], [010] and [001] axes respectively and equal tilts about axes are denoted by repeating the corresponding letter in sequence. If the [MO_6] successive layers of octahedra about [100] are in-phase tilting in a perovskite and the successive layers of octahedra about [010] and [001] are both out-of-phase tilting with the same tilting angles, then this system could be classified as $a^+b^-b^-$, corresponding to the orthorhombic space group *Pnma*. Generally, all tilting systems can be classed as 3-tilt systems, 2-tilt systems, 1-tilt systems and zero-tilt system; of which the variation can give rise to a total number of 23. The space groups of all the possible 23 tilt systems are summarised in Table 1.1. Selected octahedral tilts from a 3-tilt system are shown in Fig. 1.2.

Table 1.1 A complete list of 23 possible simple tilt systems.[24]

Tilt system number	Symbol	Lattice centring	Space group
Three-tilt systems			
1	$a^+ b^+ c^+$	*I*	*Immm* (No.71)
2	$a^+ b^+ b^+$	*I*	*Immm* (No.71)
3	$a^+ a^+ a^+$	*I*	*Im*-3 (No.204)
4	$a^+ b^+ c^-$	*P*	*Pmmn* (No. 59)
5	$a^+ a^+ c^-$	*P*	*Pmmn* (No. 59)
6	$a^+ b^+ b^-$	*P*	*Pmmn* (No. 59)
7	$a^+ a^+ a^-$	*P*	*Pmmn* (No. 59)
8	$a^+ b^- c^-$	*A*	$A2_1/m11$ (No.11)
9	$a^+ a^- c^-$	*A*	$A2_1/m11$ (No.11)
10	$a^+ b^- b^-$	*A*	*Pmnb* (No. 62)
11	$a^+ a^- a^-$	*A*	*Pmnb* (No. 62)
12	$a^- b^- c^-$	*F*	*F*-1 (No. 2)
13	$a^- b^- b^-$	*F*	*I*2/*a* (No.15)
14	$a^- a^- a^-$	*F*	*R*-3*c* (No.167)
Two-tilt systems			
15	$a^0 b^+ c^+$	*I*	*Immm* (No. 71)
16	$a^0 b^+ b^+$	*I*	*I*4/*mmm* (No. 139)
17	$a^0 b^+ c^-$	*B*	*Bmmb* (No. 63)
18	$a^0 b^+ b^-$	*B*	*Bmmb* (No. 63)
19	$a^0 b^- c^-$	*F*	*F*2/*m*11 (No. 12)
20	$a^0 b^- b^-$	*F*	*Imcm* (No. 74)
One-tilt systems			
21	$a^0 a^0 c^+$	*C*	*C*4/*mmb* (No. 127)
22	$a^0 a^0 c^-$	*F*	*F*4/*mmc* (No. 140)
Zero-tilt system			
23	$a^0 a^0 a^0$	*P*	*Pm*-3*m* (No. 221)

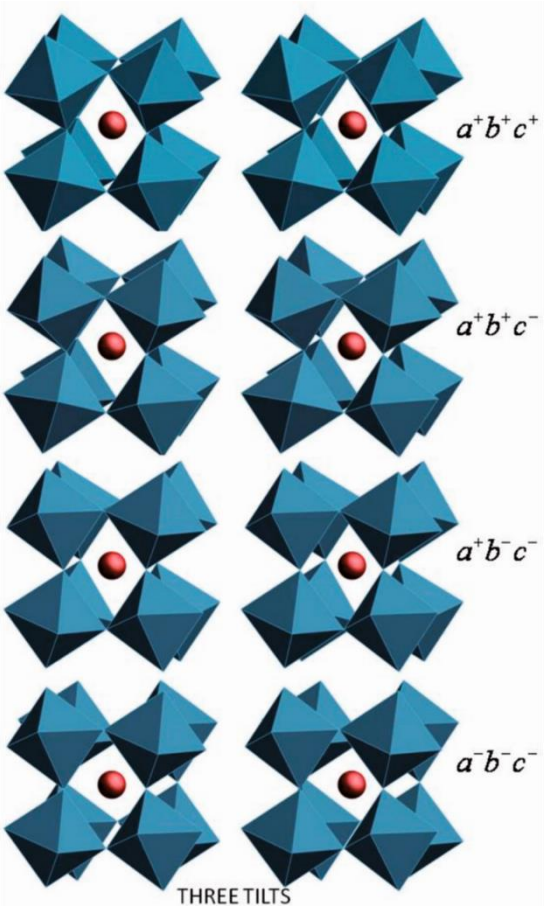

Fig. 1.2 A stereoscopic example of the 3-tilt system with different tilting angles along all the axes. Figure from A. M. Glazer.[25]

1.2.2.2 Jahn-Teller distortion

The Jahn-Teller effect[26] is normally generated when the ground state electronic configuration is unevenly occupied in order to reduce internal energy, accompanied by a lowering of the system symmetry. This geometric distortion is typically observed in octahedral configurations where the two axial bonds can be longer or shorter than the four equatorial bonds. In the ABO_3 transition metal perovskites, 5 *d*-atomic orbitals from the octahedron [BO_6] split into two degenerate sets which are lower energy t_{2g} (d_{xy}, d_{xz}, d_{yz}) and higher energy e_g ($d_{x^2-y^2}$, d_{z^2}) orbitals. The Jahn-Teller effect arises when these degenerate orbitals are partially filled. This effect strongly affects the octahedron especially when the e_g orbitals are unevenly occupied such as a [MO_6] octahedra with $3d^4$ (e.g. Mn^{3+}) or $3d^9$(e.g. Cu^{2+}) cations. Hence, e_g orbitals are split into two single levels while t_{2g} orbitals are split into doubly and singly degenerate sets. The M^{n+}-O bond (conventionally choosing the bond along the *z* direction) of the octahedral complexes will be either elongated or compressed (depicted in Fig. 1.3) as a result of a first

order Jahn-Teller distortion. In a particular system, whether an elongation or a compression is favoured is determined by the electronic configuration of the metal cation.

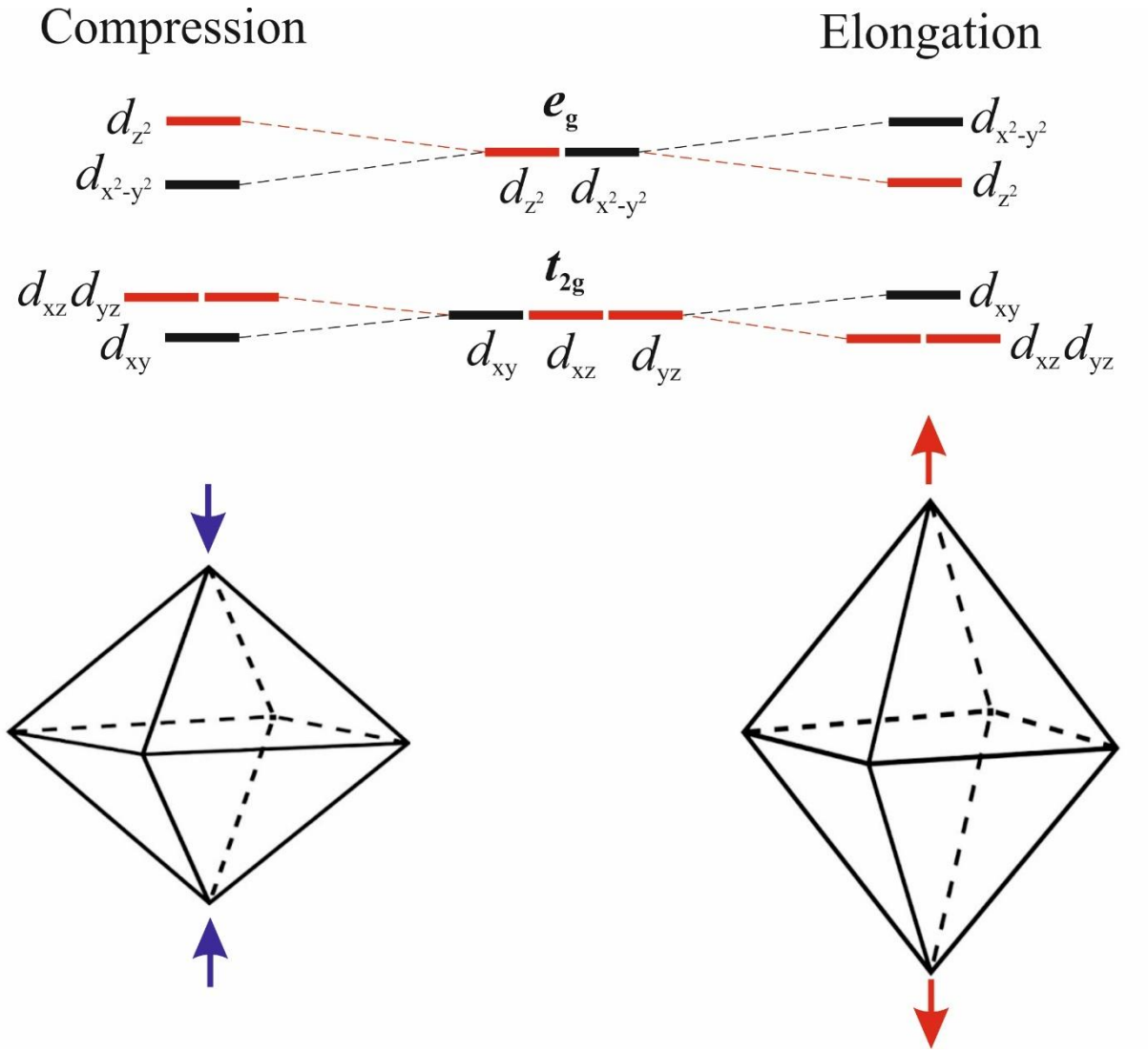

Fig. 1.3 A diagram depicting the breaking of the t_{2g} and e_g orbitals' degeneracy in an octahedral crystal field resulting from the Jahn-Teller distortion as shown by octahedral compression (left) and elongation (right).

1.3 Layered perovskites

Infinite two-dimensional (2D) slabs of the ABO_3 structures described above could constitute a new perovskite-type structure named layered perovskites. In this case, slabs are separated by several motifs giving a general formula $A_{n-1}B_nO_{3n+1}$ of which n refers to the size of the 2D slabs. For example, n = 2 indicates the slab is two [BO_6] octahedra thick. These 2D slabs that are

separated by the motifs are stacked along the [001] direction. The motifs along with the offsetting of the layers from each other are the two main differentiating characteristics for layered perovskites.[27] Scientists expect that layered perovskites could offer great opportunities for further expanding the functionality of perovskites.

As is mentioned above, layered perovskites, which are constituted by thin sheets of intrusive ions, can be classified into three groups: Ruddlesden-Popper (RP)[28], Aurivillius[29] and Dion-Jacobson (DJ) layered perovskites[30]. Recently, solid-state chemists have been strongly attracted by the syntheses of rationally designed novel materials via topotactic approaches. Layered perovskite structures, in this regard, are highly attractive due to their various soft chemistry technical capabilities such as ion-exchange and intercalation.[31] These topotactic approaches provide a feasible route of preparing novel low-temperature and metastable materials which are not accessible by traditional synthetic approaches.

1.3.1 Ruddlesden Popper and Aurivillius phases

RP phases of layered perovskites have been widely studied in the past years. The RP family is a homologous series of compounds with the general formula $A_2[A_{n-1}B_nO_{3n+1}]$ where A typically refers to the large cations, such as alkaline earth or rare earth metal cations (Sr^{2+}, La^{3+}), and B represents smaller transition metal ions, e.g. Nb^{5+}, Ti^{4+}, Co^{2+}.[28] Examples of RP compounds include $Sr_3Ti_2O_7$ and $Sr_4Ti_3O_{10}$.[32] Octahedral [BO_6] tilting phenomena[33] that are mentioned above were observed in the RP phases as well. Woodward et al.[34] recently elucidated a phenomenon in the RP family that two nonpolar lattice distortions as a result of the [BO_6] rotations induced a polar structure, a so-called hybrid-improper ferroelectricity. Precisely because most perovskite-type oxides undergo octahedral rotational distortions, this mechanism provides a great opportunity to design new polar perovskite oxides with compositional flexibility. Many investigations have been devoted to octahedral rotation-induced ferroelectricity[35] in this perovskite-derived system.

In addition to RP family, the Aurivillius series of materials have the chemical formula $Bi_2O_2[A_{n-1}B_nO_{3n+1}]$ which are intercalated with rock-salt Bi_2O_2 layers along the [001] direction.[36] Aurivillius materials are promising candidates for oxide ion-conducting properties, which were firstly discovered in the Aurivillius family by Takahashi et al.[37] in the 1970s. Additionally, chemists have begun to study the Aurivillius phases in other research fields, for example in the field of ferroelectric performance.[38]

1.3.2 Dion-Jacobson layered perovskites

Fig. 1.4 displays the crystal structure of another closely related series of layered perovskites named Dion-Jacobson (DJ) perovskites,[39] defined by a general formula $A'[A_{n-1}B_nO_{3n+1}]$. A′ in the formula typically represents a monovalent alkali metal cation acting as a separating motif of n negatively charged perovskite-like layers $[A_{n-1}B_nO_{3n+1}]^-$, forming the two-dimensional layered structure. This structure was first reported by M. Dion et al.[30] in 1981 and then further characterised by Jacobson et al. in 1985.[40] In contrast to the RP and Aurivillius families, DJ phases have not been comprehensively explored in terms of their chemical / physical properties and numerous controversies concerning the relationship between their crystal structures and physical properties have been starting to emerge ever since. In this thesis, the scientific study of layered perovskites will focus on the DJ layered family.

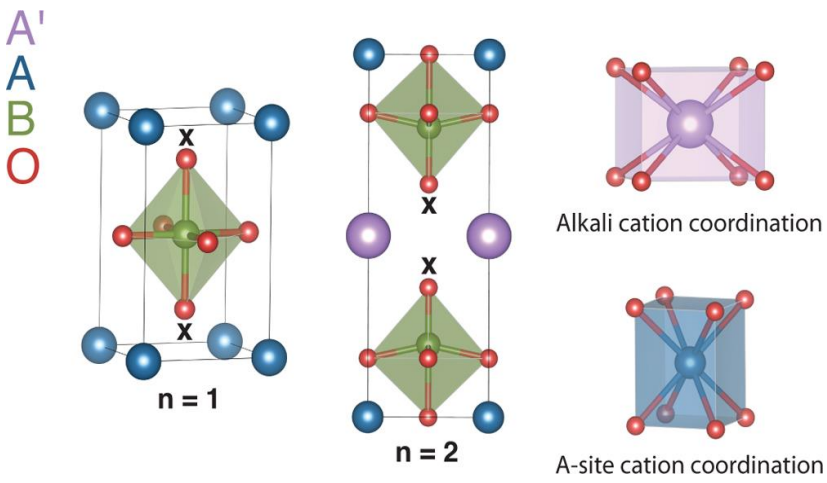

Fig. 1.4 The crystal structure of n = 1 and n = 2 DJ perovskites with space group $P4/mmm$. The figure was taken from N. A. Benedek.[39]

The A′ alkali metal cations, which separate the 2D perovskite-like slabs, are highly chemically reactive due to the weak ionic A′-O bonding, while the remaining perovskite-like slabs $[A_{n-1}B_nO_{3n+1}]$ are strongly bonded and chemical inert.[27] This chemical feature allows topotactic low-temperature reactions such as intercalation[41], deintercalation[42] and ion-exchange reactions to be carried out. In terms of intercalation, the A′ alkali cations are able to be exchanged in acid solution to form protonated perovskite derivatives $H[A_{n-1}B_nO_{3n+1}]$. [43] These protonated materials can readily form intercalation compounds with a rich variety of organic bases. In this work, topotactic ion-exchange approaches for synthesising layered perovskite materials will be

focused on. One advantage of the ion-exchange reaction is that any desired spin lattices can be prepared in principle as long as an appropriate precursor can be found.

In 1999, Prof. J. B. Wiley et al.[44] reported a new type of ion-exchange reaction summarised in Fig. 1.5, by which transition-metal arrays form within the layered perovskite host. Replacing the alkali metal in DJ phases with copper cations and halide anions resulted in a new series of materials with the formula $(CuX)^{+}[A_{n-1}B_nO_{3n+1}]^{-}$. Cu^{2+} ions in this new phase, which bridge between the two apical oxide ions from the $[BO_6]$ octehedra and four halide anions in the layer, are octahedrally coordinated. Additionally, a square lattice network along the *ab* directions has been constituted through the formation of edge-sharing $[CuO_2X_4]$ octahedra. According to Prof. Wiley's crystal model, there are two significant features in terms of magnetic interactions. One is the considerable Cu-X-Cu superexchange interaction arising from the covalent chemical bonds between Cu^{2+} cations and X^{-} anions within the [CuX] layer and the other is that the 2D [CuX] layers are well separated by the nonmagnetic $[AB_2O_7]^{-}$ units along the *c*-axis, e.g. the distance between the interlayers are 12 Å (n = 2) and 16 Å (n = 3), resulting in low dimensional physical properties.[27] Consequently, the structure of $(CuX)A_{n-1}B_nO_{3n+1}$ can be considered as an ideal realisation of the S = ½ 2D square lattice system.

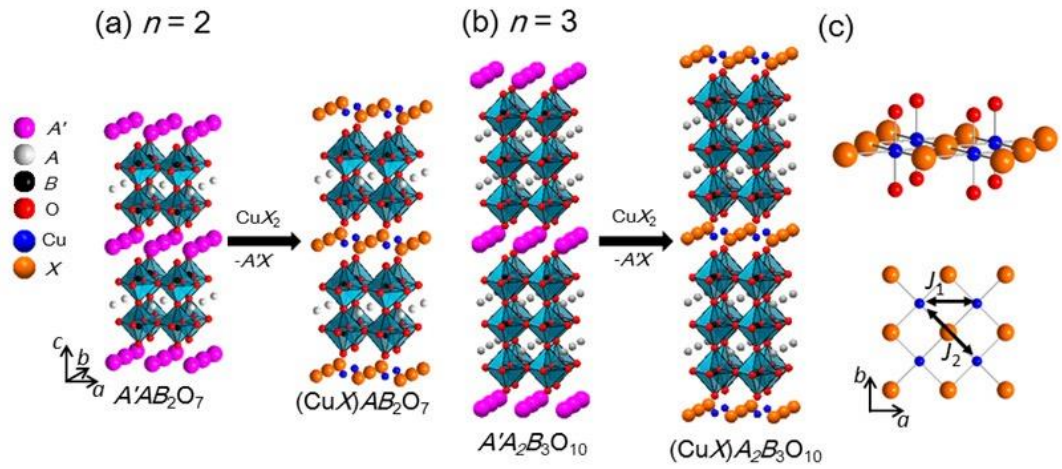

Fig. 1.5 The process of ion-exchanging copper halide into the DJ layered perovskites $(CuX)A_{n-1}B_nO_{3n+1}$ of **(a)** n = 2 and **(b)** n = 3. **(c)** An exhibition of copper coordination environments indicating edge-sharing octahedra $[CuO_2X_4]$. J_1 and J_2 represent the nearest-neighbour and 2nd nearest-neighbour exchange interactions, respectively. Figure was taken from Y. Tsujimoto et al.[27]

1.4 Corundum group

As illustrated in the previous section, ABO_3 compounds usually adopt the corundum-type structure or its derivatives when the tolerance factor t is less than 0.75. The corundum-type M_2O_3 has A and B cations the same, resulting in the tolerance factor $t = \frac{1}{\sqrt{2}} \approx 0.71$ and hence the crossover is near t = 0.75. The corundum structure crystallises with trigonal symmetry in the $R\bar{3}c$ space group and can be described as a slightly distorted hexagonal close packing of oxygen ions with cations (e.g. Al^{3+}) occupying two-thirds of the octahedral sites. In the lattice structure depicted in Fig. 1.6, [MO_6] octahedra share edges with the other three octahedra within the *xy* plane while form face-sharing pairs along the *z*-axis. Cation substitution at A-sites using other trivalent cations that have similar ionic radii with Al^{3+}, such as Cr^{3+} and Fe^{3+}, can retain the corundum structure with octahedral sites randomly occupied.[45] However, manipulating the A site by replacing it with cations that have different valence states or ionic radii can possibly originate long range ordering among the different cations. These derivatives and their properties will be introduced in the next subsections.

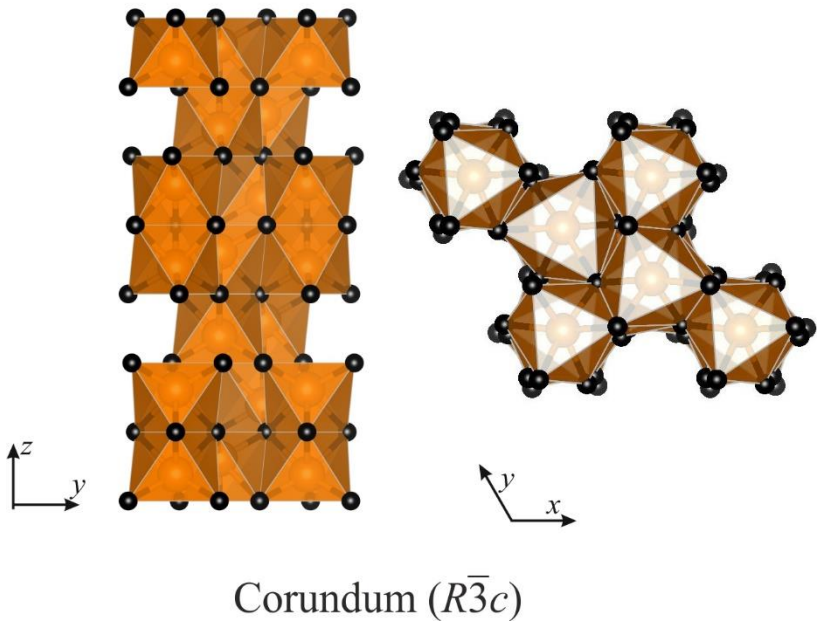

Fig. 1.6 The corundum-related crystal structure with disordered corundum unit cell (e.g. Al_2O_3). Orange octahedra represent [AO_6]. Oxygen atoms here are depicted as black spheres.

1.4.1 Ilmenite and $LiNbO_3$

Ilmenite (ILO)[46] and $LiNbO_3$-type (LNO)[47] by far are the most common structures among the ABO_3 corundum derivatives. Ilmenite, also named as Manaccanite, is the titanium-iron mineral with the idealized formula $FeTiO_3$. This type of structure normally favours combining divalent A-site and tetravalent B-site cations ($A^{2+}B^{4+}O_3$).[23] The ILO structure, shown in Fig. 1.7, crystallises in the space group $R\bar{3}$ and can be denoted based on the general corundum structure where A and B cations lie ordered on alternate *xy* planes perpendicular to the *z*-axis. The dashed black lines in the figure highlight the ordered (00z) layers where [AO_6] / [BO_6] octahedra share edges with the other three [AO_6] / [BO_6] octhedra resepctively, while [AO_6] and [BO_6] form face-sharing octahedral pairs along the *z*-axis. Therefore, the feature of a glide plane along the *z*-axis in the general corundum structure is lost in the ILO-type structure. This can be confirmed by X-ray or neutron powder diffraction pattern where the characteristic (003) and (101) peaks become visible in the ILO-type structure. It is necessary to note here that actually the (00z) planes are undulately set. This phenomenon arises from the cation-cation repulsion which exists in the face sharing octahedral pairs where cations from each octahedron become off-centred and are therefore away from their ideal *z* coordinates. This kind of structural distortion that exists in many corundum derivatives has strong effects on their functional properties. Furthermore, manipulating the ABO_3 structure by introducing another cation at the B site can result in a new type of compound with the formula $A_2BB'O_6$, where layers of [AO_6] and [BO_6] / [$B'O_6$] octahedra are stacked along the [00z] direction. Materials with this formula can retain centrosymmetric ILO-type structures with space group $R\bar{3}$ on the condition that the two different cations on the B sites are totally disordered.

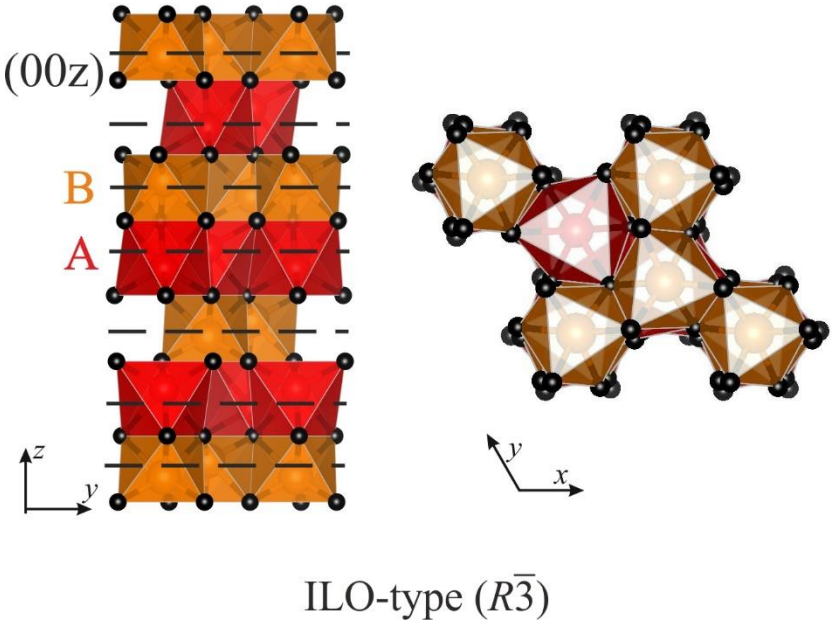

Fig. 1.7 The corundum-related ILO-type structure with alternating layers (dashed black lines) in the *z*-direction (e.g. $FeTiO_3$). Letters refer to the related cationic site. Red and orange octahedra represent [AO_6] and [BO_6] octahedra. Oxygen atoms here are depicted as black spheres.

The LNO-type structure, on the other hand, usually favours monovalent cations on the A site and pentavalent cations on the B site, forming $A^{1+}B^{5+}O_3$.[23] This type of corundum derivative is depicted in Fig. 1.8 where the cyan dashed blue lines highlight the ordered layers. The LNO-type structure crystallises in the space group *R*3*c* where [AO_6] and [BO_6] octahedra are orderly distributed in the layers along the [012] direction. The edge sharing octahedral combination of [AO_6]-[AO_6] or [BO_6]-[BO_6] within the *xy* layers that is observed in ILO is lost as a result of the particular cation arrangement in the LNO-type structure. Hence, pairs of [AO_6] and [BO_6] form both edge sharing and face sharing octahedral pairs. In theory, owing to the driving force from the charge difference between A- and B-sites, the cationic arrangement in the LNO structure (e.g. $LiNbO_3$) reduces the cation-cation repulsion, forming the maximum homogeneity of the electronic distribution. However, a smaller charge difference in the ILO structure (e.g. $FeTiO_3$) allows face sharing of the [FeO_6] and [TiO_6] layers stacked along the [00z] direction, leading to the stronger cation-cation repulsions distributed within the *xy* layers. Compared to the centrosymmetric ILO-type structure, the cationic distribution in the LNO-type structure results in the loss of the inversion centre and the presence of the glide plane along

the *z*-axis, which explains the suppression of the (003) and (101) reflections in the LNO diffraction patterns.

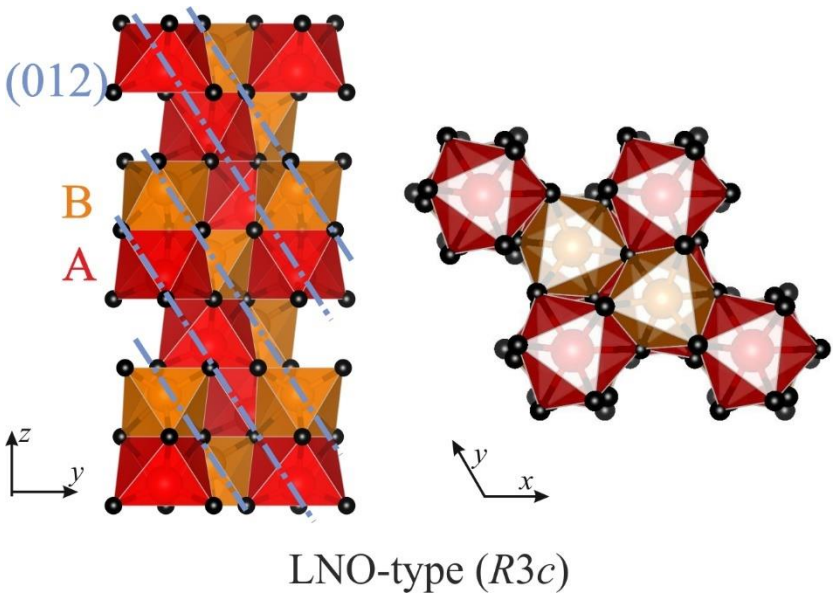

Fig. 1.8 The corundum-related LNO-type material ordered in the diagonal [012] direction (dashed blue line, e.g. $LiNbO_3$). Letters refer to the related cationic site. Red and orange octahedra represent [AO_6] and [BO_6] octahedra. Oxygen atoms here are depicted as black spheres.

1.4.2 Ni_3TeO_6 and its derivatives

Derived from ILO and LNO, another corundum derivative Ni_3TeO_6 (NTO) was first published in 1967.[48] NTO adopts a trigonal structure with space group *R*3 shown in Fig. 1.9. Materials with NTO-type structures have extra degrees of freedom to manipulate their properties owing to the four crystallographically non-equivalent cationic sites denoted as A, A' (red and green), B and B' (orange and violet) along with two different oxygen sites in the crystallographic structure. Pairs of [AO_6] / [BO_6] and [$A'O_6$] / [$B'O_6$] edge sharing octahedra alternatively form layers along the *z*-axis. However octahedra along the *z*-direction are connected by face sharing and are always a combination of [AO_6] / [$B'O_6$] or [$A'O_6$] / [BO_6]. Consequently, for an octahedron with a certain cation from the B site on the centroid (e.g. TeO_6), it will always be face sharing with one and edge sharing with the other from the A site (e.g. NiO_6) and vice versa. The dipole moment across the face sharing octahedra cannot be compensated due to the

different cation displacements from the four independent cation sites, which induces a net polarisation along the *z*-axis.[49] From Fig. 1.9, it shows that the NTO-type structure is a much more order structure on the basis of two individual cations ordered within (00z) layers (ILO-type) or within (012) layers (LNO-type). As illustrated above, the charge mismatch between cations at A and B sites determines the cationic distribution and hence the structure types for corundum derivatives. The NTO-type (e.g. Ni_3TeO_6) structure here has a large charge difference (Ni^{2+} / Te^{6+}) and therefore prefers the LNO-like cationic distribution. In contrast to the LNO-type structure, two different (012) layer formations of Ni^{2+} (A) / Ni^{2+} (A') and Ni^{2+} (B) / Te^{6+} (B') alternate in the unit cell due to the 3:1 ratio of Ni^{2+} and Te^{6+} cations. As a result, Te^{6+} induces the symmetry breaking of [NiO_6] octahedra from the A-site, as A-[NiO_6] and / or A'-[NiO_6] will only be face sharing and / or edge sharing with [TeO_6] octahedra respectively, resulting in different cationic repulsion between Ni^{2+} and Te^{6+} ions. Therefore, four crystallographically non-equivalent sites provide a high degree of freedom to manipulate interesting electric and magnetic properties at low temperatures. For an NTO-type structure formed with magnetic ions, the potential coexistence of polarisation and magnetism open a new path to synthesise and understand new multiferroic candidates.

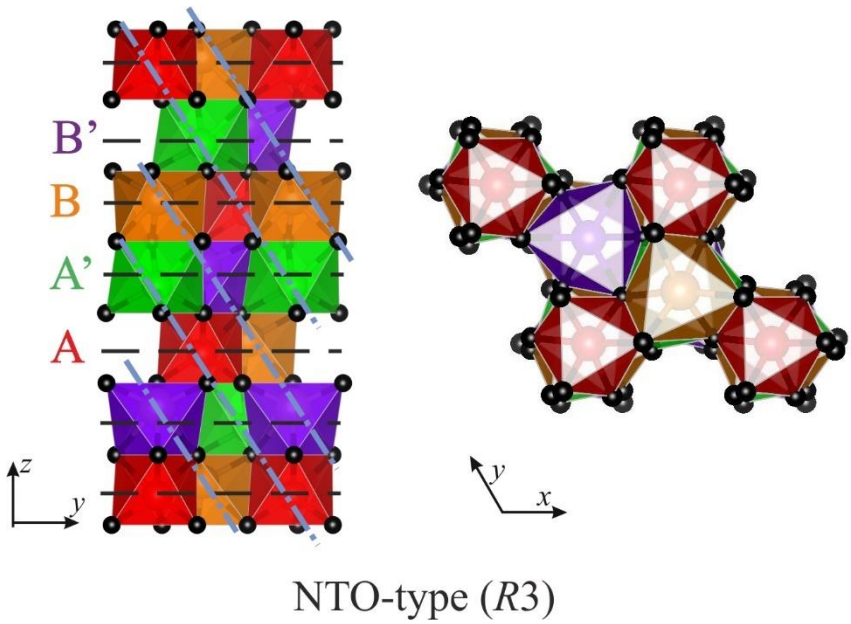

Fig. 1.9 The corundum-related NTO-type structure combining both (00z) and (012) cationic ordered planes (e.g. Ni_3TeO_6). Letters refer to the related cationic site. A / B (red and orange) and A' / B' cations (green and violet) are ordered within alternated (00z) layers. Oxygen atoms here are depicted as black spheres.

1.5 Applications

Perovskites, which have the structural flexibility to accommodate nearly all the elements in periodic table, have various applications such as microwave dielectric resonators, superconductors, high critical temperature (T_c) superconductors and catalysis. A wide range of perovskites such as $MgTiO_3$ and $CaTiO_3$ are suitable materials for microwave dielectrics due to their high dielectric constants, low dielectric loss and low thermal expansion coefficients.[50] Combining the 4*f* ions in the A-site and 3*d* ions in the B-site results in a reasonably conducting phases. Sleight et al.[51] in 1975 reported the $BaPb_{1-x}Bi_xO_3$ perovskite as the highest temperature oxide superconductor. Substituting ions of perovskites has been researched to see if the T_c could be raised. P. Ganguly and C. N R. Rao[52] reported a potential insulating compound, La_2CuO_4, which later became a very popular host for superconducting studies. Many new highly suitable perovskite substrates for high T_c superconductors have then designed and developed.[53] Meanwhile, perovskites have appeared in catalysis applications since the 1980s. Their excellent thermal stability in a wide range of oxygen partial pressures and poison-resistant ability[54] makes several perovskites become substrates or washcoat materials.

Layered perovskites materials, like DJ phases with potentially interesting electrical, magnetic and catalytic properties, provide opportunities to further expand the functionality of general ABO_3 perovskites. A series of new functionalities including photo catalysis[55], ferroelectric behaviour [56], ionic conductivity [57], superconductivity [58], piezoelectric behaviour [59] and photoluminescence[60-61] have been successfully investigated in past years. The possibility of easy ion exchange in layered phases offers great opportunities to design and discover new functional layered perovskites, such as the perovskite solar cell using organic cations to separate the inorganic layers.[62-63]

Corundum derivatives were found to be an ideal platform for combining polar and magnetic properties due to their structural features, where octahedral A- and B-sites can both be occupied by magnetic ions resulting in strong magnetic interactions. In addition, a spontaneous polarisation can be induced if the polar ordered ilmenite (OIL, *R*3), LNO- or NTO-type structure is adopted. LNO-type materials, for example $GaFeO_3$ [64] and NTO-type double corundum derivative Ni_3TeO_6[65], exhibit magnetoelectric couplings. A very recent report on Mn_2MnWO_6 illustrates a promising multiferroic compound with large magnetoelectric coupling and switchable polarisation.[66] These recent promising results encourage scientists to search for more polar magnets in the corundum family. Other physical properties such as

piezoelectric, pyroelectric and second harmonic generation effects have been observed in these corundum derivatives as well.

1.6 Aims and objects

The research in this thesis mainly focuses on synthesising and characterising the magnetic behaviour of transition metal perovskites and corundum derivatives. Specifically, our research will be concentrated on investigating strontium substituted copper halide DJ layered perovskites with the formula $(CuCl)La_{1-x}Sr_xNb_2O_7$, novel NTO-type corundum derivatives $Ni_{2-x}Co_xScSbO_6$ and the new high-pressure perovskite $YRuO_3$ using chemical and physical techniques. The theoretical concepts and practical aspects of experimental measurements will be described in the next chapter. The main results chapters in the thesis are organised as follows.

According to the previous work in the domains of DJ layered perovskites, the precursor $(CuCl)LaNb_2O_7$ was found to undergo structural phase transitions which are *Pbam* (<500 K) →*Pbmm* (500 ~ 640 K) →*P*4/*mmm* (>640 K) in Chapter 3. We anticipate observing shift in phase transition on the basis of partial substituting La^{3+} with Sr^{2+} in the DJ layered perovskite precursor. The investigation into how the magnetic properties are affected under Sr^{2+} chemical substitution as the mother compound $(CuCl)LaNb_2O_7$ is a coupled spin dimers system with predominant antiferromagnetic interactions. These series of compounds will be synthesised via a topotactic ion-exchange reaction. Chemical characterisation of the structural phase transitions using synchrotron X-ray diffraction will be presented and low temperature crystal structure and possible magnetic structure identification will be investigated through neutron diffraction. Considering that the other two layered perovskite family RP and Aurivillius have been extensively studied, it is strongly hoped that the outcomes from this research could trigger more attention to the DJ layered perovskites and provide more understanding of their exotic magnetic behaviour.

Taking into account the multiferroic system recently studied, there remains a challenging area of achieving more Type II multiferroic materials which exhibit strong electric and magnetic correlations. In Chapter 4, considering the high interest on chemical and physical topics from NTO-type materials, the syntheses of a series of new $Ni_{2-x}Co_xScSbO_6$ corundum derivatives are attempted. The new phase Co_2ScSbO_6 with its solid solutions $Ni_{2-x}Co_xScSbO_6$ (x = 0, 0.5, 1 and 1.5) are synthesised through a conventional solid-state approach. High-pressure techniques were used to synthesise Co_2ScSbO_6, as the ambient solid-state synthesis could not

achieve a pure single phase. Physical characterisation and preliminary laboratory X-ray data will be provided before introducing neutron diffraction studies. These compounds have been found to present remarkable lock-in spin structures and ferrimagnetism with a net polarisation. More details of the novel magnetic structures and their corresponding spin phase diagram will be provided.

Chapter 5 will focus on a continuous study of $LnRuO_3$ perovskites with Ln = Y and Ho. The synthesis of these materials requires a high-pressure process to allow the smaller A-site cations to be introduced to the A-site of perovskite structure. The research of the unconventional low spin $4d^5$ Ru^{3+} in these materials will be the main focus. The electric and magnetic measurements will be performed, followed by the neutron diffraction characterisation to explain their structural behaviour on both crystallographic and magnetic domains.

The overall conclusion of the work carried out during the PhD will be summarised and future prospects of the studied materials will be discussed.

References

1. Y. Huang, R. I. Dass, Z. Xing, and J. B. Goodenough, *Science*, 2006, **312**, 254.

2. C. N. R. Rao and A. K. Cheetham, *Science*, 1996, **272**, 369.

3. R. J. Cava, R. B. van Dover, B. Batlogg, and E. A. Rietman, *Phys. Rev. Lett.*, 1987, **58**, 408.

4. H. D. Megaw, *Acta Crystallogr.*,1952, **5**, 739.

5. K. I. Kobayashi, T. Kimura, H Sawada, K. Terakura, and Y. Tokura, *Nature*, 1998, **395**, 677.

6. G. A. Smolenskii and I. Chupis, *Sov. Phys. Usp.*, 1982, **25**, 475.

7. J. Wang, J. B. Neaton, H. Zheng, V. Nagarajan, S. B. Ogale, B. Liu, D. Viehland, V. Vaithyanathan, D. G. Schlom, U. V. Waghmare, N. A. Spaldin, K. M. Rabe, M. Wuttig, and R. Ramesh, *Science*, 2003, **299**, 1719.

8. T. Kimura, T. Goto, H. Shintani, K. Ishizaka, T. Arima and Y. Tokura, *Nature*, 2003, **426**, 55

9. C. N. R. Rao, *Annu. Rev. Phys. Chern.*, 1989. 40, 291.

10. E. Dagotto, *Rev. Mod. Phys.*, 1994, **66**, 763.

11. M. Imada, A. Fujimori and Y. Tokura, *Rev. Mod. Phys.*, 1998, **70**, 1039.

12. M. Fiebig, T. Lottermoser, D. Meier and M. Trassin, *Nat. Rev. Mater*., 2016, **1**, 16046.

13 . M. De Graef and M. E. McHenry, *Structure of materials: an introduction to crystallography, diffraction and symmetry*, Cambridge University Press, 2012

14. S.W. Arulnesan, P. Kayser, B. J. Kennedy and K. S. Knight, *J. Solid State Chem*., 2016, **238**, 109.

15. A. Sinclair, J. A. Rodgers, C. V. Topping, M. Misek, R. D. Stewart, W. Kockelmann, J. G. Bos and J. P. Attfield, *Angew. Chem. Int. Ed*., 2014, **53**, 8343.

16. J. Hutton and R. J. Nelmes, *J. Phys. C Solid State Phys.*, 1981, **14**, 1713.

17. P. M. Woodward, *Acta Crystallogr. Sect. B Struct. Sci.*, 1997, **53**, 32.

18. K. Momma and F. Izumi, *J. Appl. Crystallogr*., 2011, **44**, 1272.

19. V.M. Goldschmidt, *Akad. Oslo I. Mat-Nat.*, 1026, **8**, 112.

20. Y. Takeda, F. Kanamura, M. Shimada and M. Koizumi, *Acta. Cryst*., 1976, **B32**, 2464.

21. S. Geller, *J. Chem. Phys*., 1956, **24**, 1236.

22. W. Travis, E. N. K. Glover, H. Bronstein, D. O. Scanlon and R. G. Palgrave *Chem. Sci*., 2016, **7**, 4548.

23. R. H. Mitchell, *Perovskites: modern and ancient*, Almaz Press Inc., 2002

24. A. M. Glazer, *Acta Crystallogr. Sect. B Struct. Crystallogr. Cryst. Chem.*, 1972, **28**, 3384.

25. A. M. Glazer, *Phase Transitions*, 2011, **84**, 405.

26. H. A. Jahn and E. Teller, *Proc. R. Soc. London, A*, 1937, **161**, 220.

27. Y. Tsujimoto and H. Kageyama, *Ion-Exchange Reactions for Two-Dimensional Quantum Antiferromagnetism*, INTECH Open Access Publisher, 2012.

28. S. N. Ruddlesden and P. Popper, *Acta Cryst.*, 1957, **10**, 528.

29. B. Aurivillius, *Ark. Kemi.*, 1949, **1**, 463.

30. M. Dion, M. Ganne, and M. Tournoux, *Mater. Res. Bull*., 1981, **16**, 1429; A. J. Jacobson, J. W. Johnson, and J. T. Lewandowski, *Inorg. Chem*., 1985, **24**, 3727.

31. M. Sato, J. Abo, T. Jin, and M. Ohta, *Alloys Compd*., 1993, **192**, 81.

32. S. N. Ruddlesden and P. Popper, *Acta Crystallogr.*, 1958, 11, 54-55.

33. S. Šturm, A. Rečnik, C. Scheu and M. Čeh, *J. Mater. Res.*, 2000, **15**, 2131.

34. M. C. Knapp and P. M. Woodward, *J. Solid State Chem.*, 2006, **179**, 1076.

35. N. A. Benedek, A. T. Mulder and C. J. Fennie, *J. Solid State Chem.*, 2012, **195**, 11.

36. P. Boullay, G. Trolliard, D. Mercurio, J. M. Perez-Mato, and L. Elcoro, *J. Solid State Chem.*, 2002, **164**, 252.

37. T. Takahashi, H. Iwahara, and Y. Nagai., *J. Appl. Electrochem*., 1972, **2**, 97.

38. R. L. Withers, J. G. Thompson, and A. D. Rae, *J. Solid State Chem*., 1991, **94**, 404.

39. N. A. Benedek, *Inorg. Chem.*, 2014, **53**, 3769.

40. A. J. Jacobson, J. W. Johnson, J. T. Lewandowski, *Inorg. Chem*., 1985, **24**, 3727.

41. J. Gopalakrishnan and V. Bhat, *Mater. Res. Bull*., 1987, **22**, 413

42. L. Viciu, T.A. Kodenkandath, J.B. Wiley, *J. Solid State Chem*., 2007, **180**, 583.

43. Y. Kobayashi, J. A. Schottenfeld, D. D. Macdonald and T. E. Mallouk, *J. Phys. Chem. C*, 2007, **111**, 3185.

44. T. A. Kodenkandath, J. N. Lalena, W. L. Zhou, E. E. Carpenter, C. Sangregorio, A. U. Falster, W. B. Simmons, C. J. O'Connor, and J. B. Wiley, *J. Am. Chem. Soc*., 1999, **121**, 10743.

45. E. Gaudry, D. Cabaret, P. Sainctavit, C. Brouder, F. Mauri, J. Goulon and A. Rogalev, *J. Phys. Condens. Matter*., 2005, 17, 5467.

46. R. J. Harrison, U. Becker and S. A. T. Redfern, *Am. Mineral.*, 2000, **85**, 1694

47. Y. Shiozaki, T. Mitsui, *J. Phys. Chem. Solids*, 1963, **24**, 1057.

48. R.E. Newnham, E.P. Meagher, *Mater. Res. Bull.*, 1967, **2,** 549.

49. N. A. Spaldin, *J. Solid State Chem*., 2012, **195**, 2.

50. A. S. Bhalla, R. Guo and R. Roy, *Mat. Res. Innovat*., 2000, **4**, 3.

51. A. W. Sleight, J. L. Gilson and P. E. Bierstedt, Sol State Commun., 1975, **17**, 27.

52. P. Ganguly and C. N. R. Rao, *J. Solid State Chem.*, 1984, 53,19.

53. A. S. Bhalla and R. Guo, *Acta Phys. Pol. A*, 1997, **92**, 7.

54. L. A. Isupova, V. A. Sadykov, V. P. Ivanov, A. A. Rar, S. V. Tsybulya, M. P. Andrianova, V. N. Kolomilchuk, A. N. Petrov, and O. F. Kononchuk, *React Kinet. Catal. Lett.*, 1994, **53**, 223.

55. K. Domen, J. Yoshimura, T. Sekine, A. Tanaka and T. Onishi, *Catal. Lett*., 1990, **4**, 339.

56. C. Chen, H. Ning, S. Lepadatu, M. Cain, H. Yan and M.J. Reece, *J. Mater. Chem. C*., 2015, **3**, 19.

57. K. Toda, J. Watanabe, M. Sato, *Solid State Ionics*, 1996, **90**, 15.

58. I. Nagai, Y. Abe, M. Kato, Y. Koike, and M. Kakihana, *Solid State Ionics*, 2002, **151**, 265.

59. G. Gou, and J. Shi, *EuroPhys. Lett*., 2014, **108**, 67006.

60. A. Kudo and E. Kaneko, *J. Mater. Sci. Lett*., 1997, **16**, 224.

61. S. Ida, C. Ogata, M. Eguchi, W. J. Youngblood, T. E. Mallouk, and Y. Matsumoto, *J. Am. Chem. Soc*., 2008, **130**, 7052.

62. C. C. Stoumpos, D. H. Cao, D. J. Clark, J. Young, J. M. Rondinelli, J. I. Jang, J. T. Hupp and M. G. Kanatzidis, *Chem. Mater*., 2016, **28**, 2852.

63. D. H. Cao, C. C. Stoumpos, O. K. Farha, J. T. Hupp and M. G. Kanatzidis, *J. Am. Chem. Soc*., 2015, **137**, 7843.

64. H. Niu, M. J. Pitcher, A. J. Corkett, S. Ling, P. Mandal, M. Zanella, K. Dawson, P. Stamenov, D. Batuk, A. M. Abakumov, C. L. Bull, R. I. Smith, C. A. Murray, S. J. Day, B. Slater, F. Cora, J. B. Claridge and M. J. Rosseinsky, *J. Am. Chem. Soc*., 2017, **139**, 1520.

65. Y. S. Oh, S. Artyukhin, J. J. Yang, V. Zapf, J. W. Kim, D. Vanderbilt, & S. W. Cheong., 2014, *Nat. Commun.*, **5**, 3201.

66. M. Li, E. E. McCabe, P. W. Stephens, M. Croft, L. Collins, S. V. Kalinin, Z. Deng, M. Retuerto, A. S. Gupta, H. Padmanabhan, V. Gopalan, C. P. Grams, J. Hemberger, F. Orlandi, P. Manuel, W. Li, C. Jin, D. Walker and M. Greenblatt, *Nat. Commun*., 2017, **8**, 2037.

Chapter 2. Theoretical concepts and experimental techniques

2.1 Synthesis methods

2.1.1 Conventional ceramic synthesis

Transition metal based compounds are commonly prepared by a conventional solid state ceramic synthesis. The stoichiometric starting chemicals, which are normally in forms of high-quality oxides or carbonates, are thoroughly ground and mixed using an agate pestle and mortar in order to reduce the particle size. Additional treatment of the mixture by the sol-gel process further decreases the particle size by ~2 orders of magnitude, resulting in larger specific surface area of solid grains and shorter diffusion distance between grain boundaries. Once finished, the homogeneous mixture is then transferred to the pellet die, and pressed with a hydronic designed pellet press for improving particle contacts and reducing diffusion distances. Next, the pellets are placed into an inert alumina crucible and sintered in a high temperature muffle furnace (Fig. 2.1), with a typical temperature range between 800 °C and 1600 °C. Heating enhances the kinetic energy of ion diffusion across the particle boundaries, according to the Arrhenius rate law. Tube furnaces (Fig. 2.1(b)) are also used for sintering under different gas atmospheres such as Ar, O_2 and H_2. Ar gas remains inert and protects elements that are easily oxidised. An O_2 atmosphere provides an oxidising environment, while a flow of H_2 (often 5%~10% diluted by Ar or N_2) is used as a reducing agent. For air or moisture-sensitive regents, the grinding process is carried out in a dry Ar filled glove box (Fig. 2.1(c)) and the resulting mixture is loaded in a quartz tube, and sealed under a vacuum condition using the Schlenk line, as shown in Fig. 2.1(d). The sintering process is then conducted within a certain period of time, manipulated by the heating program which is installed in the furnace. Afterwards the pellets are either quenched or annealed from the high sintering temperature for the purpose of obtaining a homogeneous phase.[1] The materials are investigated with a laboratory X-ray powder diffractometer after each firing process. For some compounds, intermediate grindings,

repelleting and reheating are necessary to optimise the completion of the reaction and sample purification.

In this thesis, solid-state ceramic approaches have been employed to synthesise DJ perovskite $(CuCl)La_{1-x}Sr_xNb_2O_7$ and corundum derivatives $Ni_{2-x}Co_xScSbO_6$ (x=0, 0.5, 1 and 1.5), as well as preparing precursors of high-pressure material Co_2ScSbO_6 and $YRuO_3$.

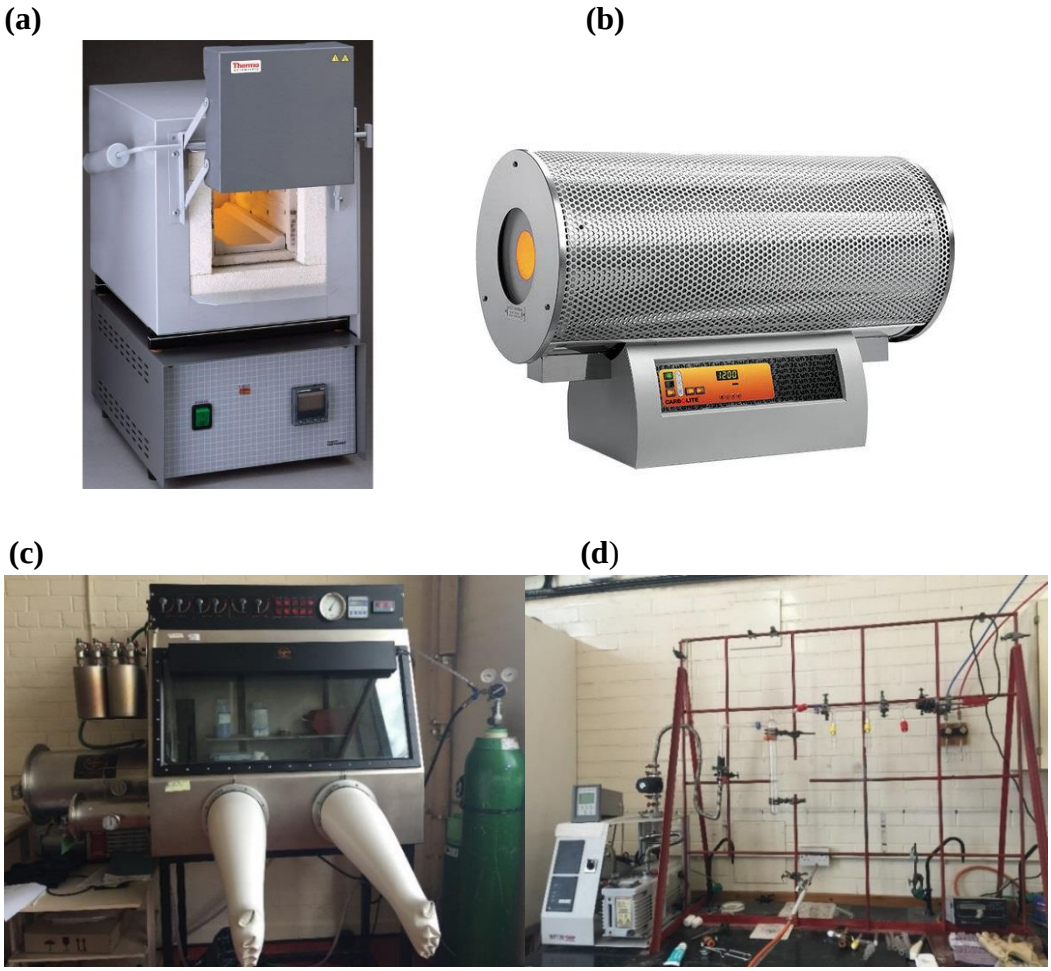

Fig. 2.1 (a) The common bench-top furnaces and **(b)** a tube furnace used in the laboratory. The tube furnace can be connected with the gasline to allow gases such as oxygen or hydrogen to flow through the tube during the sintering process. **(c)** An argon atmosphere based glove box. **(d)** The Schlenk line with turbo pump for creating a vacuumed environment.

2.1.2 High pressure high temperature (HPHT) solid-state synthesis

Solid-state ceramic synthesis can also be carried out under high pressure. According to the tolerance factor *t* mentioned in Chapter 1, the stability of a desired ABO_3 oxide can be estimated.

Perovskite structures with *t* values in-between 0.8 and 1 are usually structurally stable.[2] In order to achieve perovskite structures with lower *t* values (poor structural stability), high pressure (> 1 GPa) high temperature (~1000 °C) techniques are introduced.[3] Moreover, high-pressure treatment enables an increase in ionic diffusion between reactants, resulting in a higher solid-state reaction rate and a lower sintering temperature. This advantage avoids generating possible by-products with similar formation temperature, and negates the thermal decomposition of reactants and products.[4] Recently high pressure syntheses have been widely used for inducing phase transformations, and synthesising metastable phases such as the well-known phase transition between pyrochlores ($A_2B_2O_{7-x}$) and perovskites (ABO_3) which will be discussed in detail in Chapter 5.

2.1.3 Walker-type multi-anvil press

Generally speaking, to achieve the same pressure, a greater force is required to compress sample with a larger size than smaller volume samples. This relationship of pressure, force and contact area can be explained in Eq. 2.1 as below:

$$P = F/A \tag{2.1}$$

The same high pressure (HP) devices have been widely used at the frontier high-pressure science for many years, similar to Bridgeman's original multi-anvil press.[5] The laboratory press is composed of three main components: i. the hydraulic press generating the target pressure, ii. the anvils (HP module) acting as a pressure transmitting part between the press and the sample and iii. the octahedron press cell which contains the sample capsule. The piston-cylinder press, which is the most common high-pressure device in a laboratory, can only generate pressure no higher than 5 GPa. To satisfy the increasing demand of a higher pressure, several new HP devices have been designed. According to the different setups of the anvils, the HP devices can be classified into two categories: the single-stage or two-stage press. A single-stage press such as a Belt-type press can provide a pressure up to 10 GPa and higher pressure (>10 GPa) requires a two stage press, for instance the Walker-type multi-anvil press.[6] In this thesis, all high-pressure samples are prepared through the Walker-type multi-anvil press. The details of the multi-anvil press equipment and the assembly process of the press cell will be introduced later.

The two-stage Walker-type multi-anvil press,[7-8] which is manufactured by Max Voggenreiter GmbH, is located in the School of Chemistry, University of Edinburgh (Fig. 2.2). This multi-anvil press is utilised to provide a high-pressure environment during solid-state synthesis.

Fig 2.2 The 1000 t Walker-type multi-anvil press in Edinburgh.

The initial precursor was created by thoroughly mixing and grinding the stoichiometric reactants. Then the mixed precursor is well packed into a platinum capsule, to ensure uniform heating and pressure, which is then placed in a hexagonal-boron nitride (BN) cylindrical container with a stopper on top. A platinum capsule is suitable for a heating temperature, T > 1373 K while a gold capsule is adopted when T is lower than 1373 K. Outside the BN container, two concentric graphite sleeves (one small and one large) are utilised as a furnace; this special construction minimises the thermal gradient of the cylinder-size sample during heating. BN, as an insulator, blocks the direct contact of the platinum and graphite heaters. Graphite as a heater can bring the temperature up to 1773 K. If the required temperature is even higher, then Re or $LaCrO_3$ can be used as heating materials to bring the temperature over 2273 K. It should be noted that graphite will transform to amorphous diamond, losing the ability to heat resistively under pressures of P > 20 GPa, whereas Re and $LaCrO_3$ are still usable. Additional thermal insulator MgO disks are installed to fill up the interior space of the graphite sleeve, in order to

reinforce the whole cylindrical structure. A ZrO_2 cylindrical sleeve acting as a thermal shield is then placed outside the graphite layer. Two Mo disks with surrounding MgO rings are separately laid on top and bottom of the ZrO_2 sleeve, which allows the electric current to pass through the whole capsule and generate heat from the resistance heaters (graphite sleeves). Fig. 2.3 below shows the sizes of all components built for the press cell.

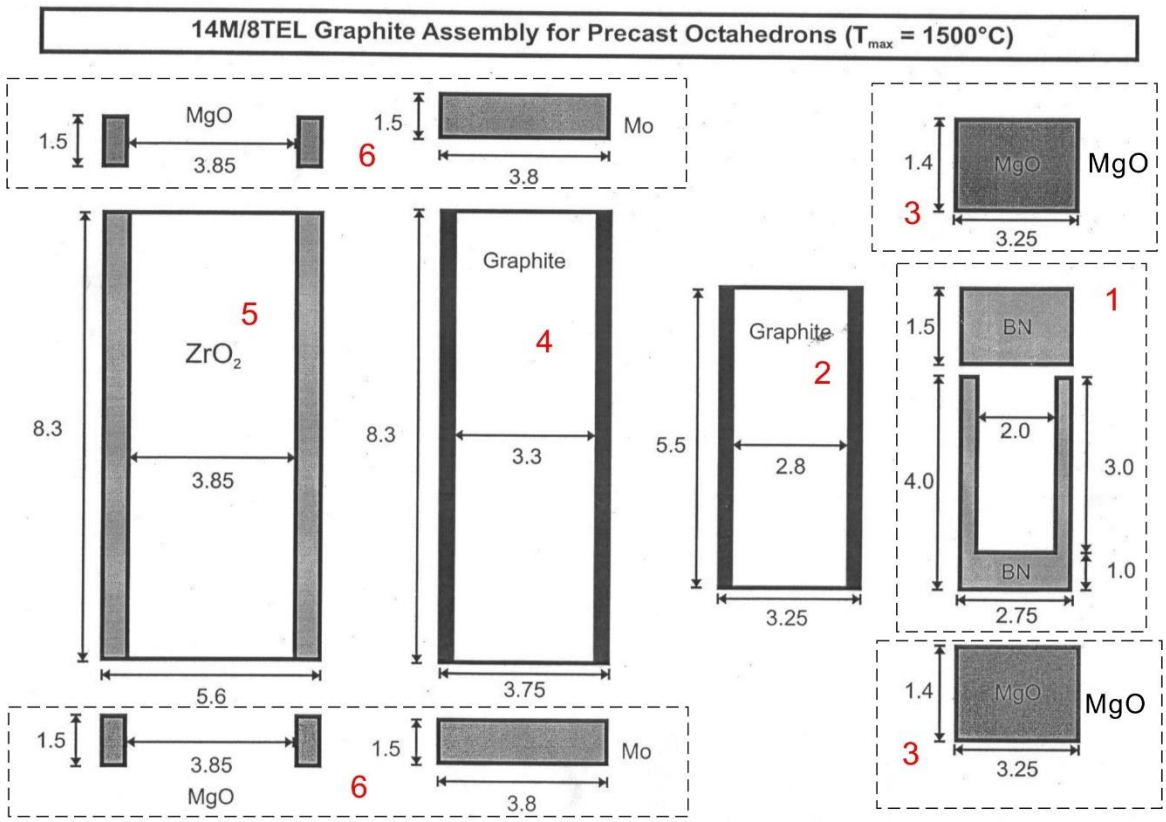

Fig. 2.3 The diagram of all the components constituted of a press cell. Parts are grouped and labelled with red numbers. Assembly sequence: load part 1 into part 2, then loaded into part 4 together with part 3; and then put all of them into part 5 with part 6 on top and bottom. All the dimensions are in 'mm'.

The assembled cylindrical suite is loaded into a drilled pressure transmitting chrome magnesia octahedron (95% MgO and 5% Cr_2O_3) which is then surrounded by eight tungsten carbide (WC) cubes with corner truncations (Fig. 2.4). This set of eight cubic anvils is known as the second-stage anvil. Assembling these cubic anvils through face-sharing (Fig. 2.4(b)) leaves an octahedral cavity in the centre of the eight cubes which precisely fits the octahedron press cell. The octahedral edge length (OEL) of the chrome magnesia octahedron used during this study is 14 mm and the matched truncation edge length (TEL) of the WC cubes is 8 mm. This '14/8 set' could reach a pressure up to 16 GPa with a resultant sample volume of approximately 10

mm^3. There are different sets of OEL/ TEL length ratios such as 25/17, 19/12, 18/11, 14/8, 10/5, 10/4 and 7/3 for different pressure requirements.[9] The 7/3 set for a Walker type multi-anvil press enables pressures as high as 26 GPa with a sample size of ~ $1mm^3$. The WC cubes are electronically insulated from one to another with PTFE tape over three orthogonal faces on each of the 4 cubes. Pyrophyllite gaskets are attached to the truncations of the other 4 cubes with super-glue. The gaskets will flow under high pressure to seal the sample cavity. Paper is glued to the cubic faces with glued gaskets to limit the gasket flow. Gaskets here also prolong cubes lifetime by reducing the stress arising from the contact between neighbouring cubes. Finally, the large cubic assembly constructed of 8 WC cubes is constructed and reinforced by gluing fibreglass pads on the outer surface of the model. Two copper strips are placed on the two cubes in contact with the Mo disks allowing the current to pass from the heating rack to the graphite furnace (Fig. 2.4(c)).

(a)

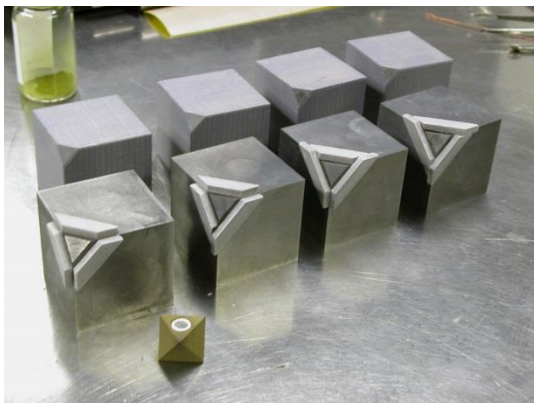

(b

(c)

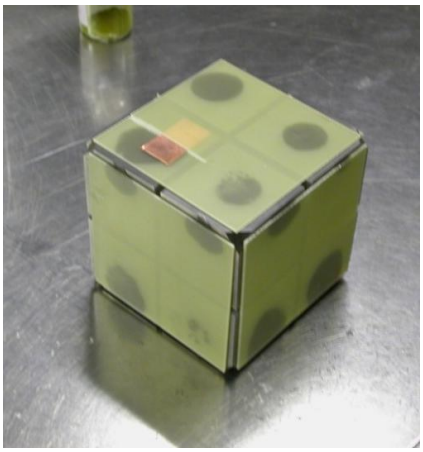

Fig. 2.4 (a) The prepared octahedron press cell with 8 second-stage WC cubes. Gaskets are attached to the truncations of 4 out of 8 cubes and PTFE tapes cover the truncations of the other 4 cubes. **(b)** Cubes assembled around the press cell with a visible Mo disk. **(c)** Assembly of the 8 joined cubes with one Cu strip on the top. The fibreglass pads are attached by superglue.

The assembled set which 8 WC cubes with the octahedron in the core is then placed into the containment ring with the surrounded six steel anvils known as the first-stage anvils (Fig. 2.5). Plastic sheets act as insulating components, are employed to cover the contact surface of the six steel anvils and the inner wall of the containment ring in order to avoid an electric short circuit during heating. After closing the heavy steel lid, force is generated by a hydraulic press applied uniaxially to the top of the steel lid increasing to the desired load over a given period of time.

(a) **(b)**

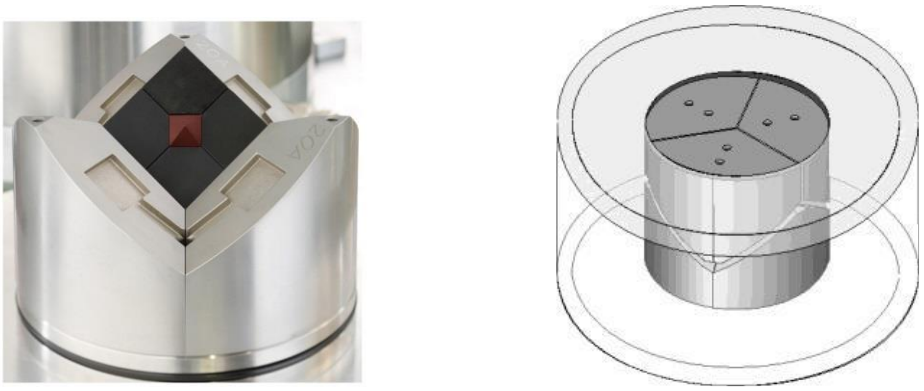

Fig. 2.5 (a) Three of the six steel anvils with a model cube placed in position. **(b)** A perspective drawing of a cylinder of six steel anvils inside the steel ring.

Once the target pressure is reached and stabilised, the sample loaded in the press cell is quickly heated to the requested temperature, as introduced in the schematic of the high temperature high pressure (HPHT) process (Fig. 2.6). The energy required for sample heating is achieved by applying an electric power generated from a specially designed heating rack. High-pressure conditions are well known to shorten the solid-state reaction time, therefore the duration of the heating process at high pressure is normally under 30 minutes. After the heating process is finished, the entire system is quenched to room temperature within 5 seconds through a cooling jacket, followed by releasing pressure gently. Through this heating process, the metastable phase of the material can be protected.[9]

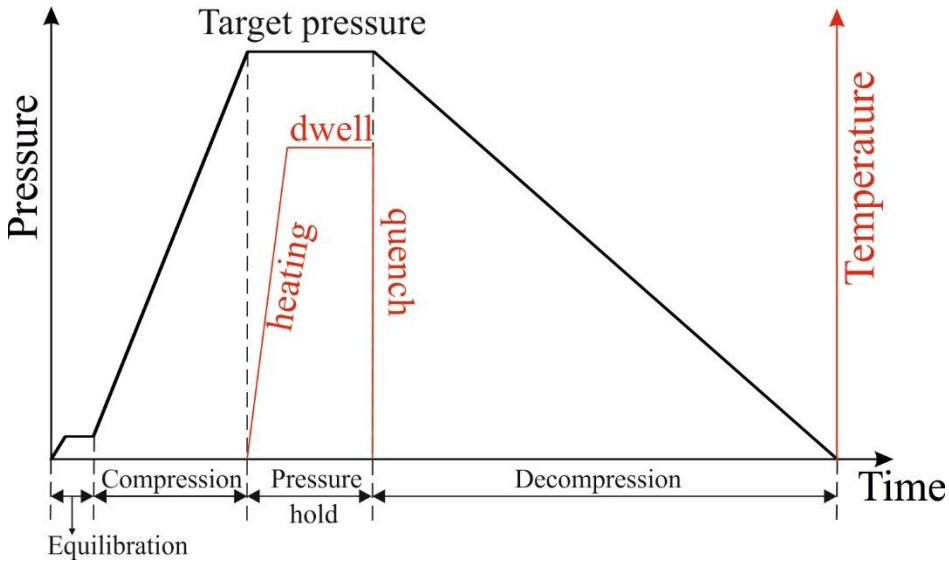

Fig. 2.6 A schematic of a typical HPHT process showing the relationship between pressure, heating and time.

The accurate pressure and temperature conditions for each HPHT experiment are acquired from calibrations that must be repeated every few months. Pressure calibration is designed by measuring the resistivity of Bi sample against the applied forces generated from the hydraulic ram at ambient temperature. Fig. 2.7(a) shows the pressure calibration of the 14/8 assembly as an example. The reported pressure-induced phase transitions of Bi were at 2.55, 3.15 and 7.70 GPa respectively, elucidated by the discontinuities of resistivity.[10] Thus the relationship between the applied load generated from the press and the pressure of a certain sample volume can be established through these well-known transition points of bismuth. On the other hand, temperature calibration under different pressures (Fig. 2.7(b)) is programed by applying different power supplies to the graphite heater through the heating circuit, whilst monitoring the corresponding temperature values using a Pt-Rh thermocouple in direct contact with the press cell set up. Through this calibration, the required pressure and temperature values of HPHT experiments can be translated into a function of the applied force and electric power, respectively. The pressure and temperature calibration measurements of 14/8 assembly were performed by Dr. Angel M. Arevalo-Lopez.

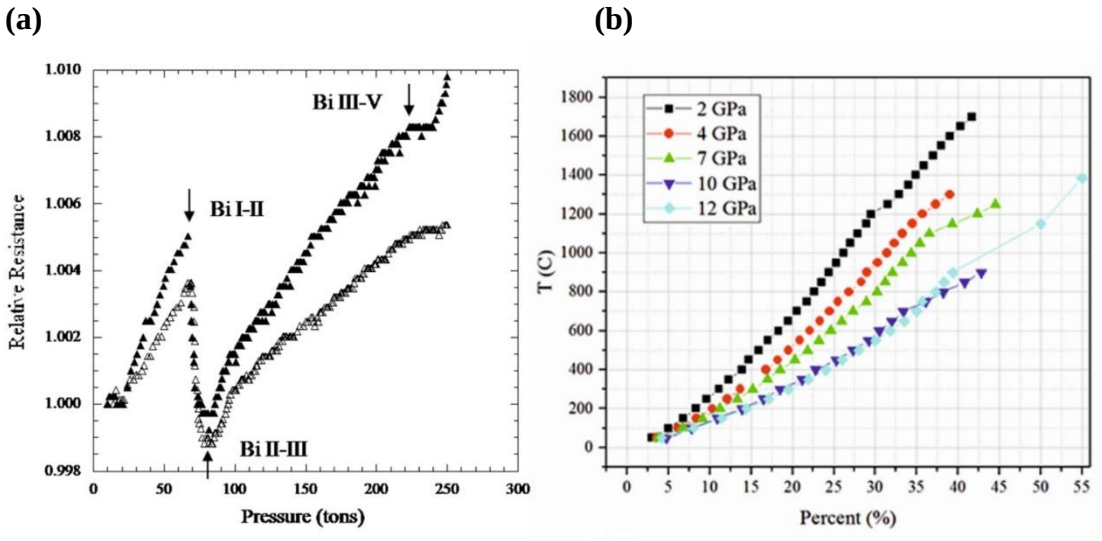

Fig. 2.7 (a) Bi resistance as a function of the applied load (tons) generated from the press. Three Bi phase transitions are labelled. **(b)** Measured temperature (°C) as a function of the input electric power (%) at selected pressures.

The description of the optimised HPHT synthesis conditions for each particular compound studied in this thesis is described in Chapters 3, 4, and 5.

2.2 Crystallographic basics and methods

2.2.1 Bragg's law

Diffraction, a special case of scattering, occurs when waves pass through a narrow obstacle or aperture with the width similar to the radiation wavelength. The diffracted radiation can be described as an interference pattern that consists of regions with maximum and minimum intensities.

So far diffraction has been widely used and developed for many remarkable techniques that can be used to determine and non-destructively characterise the crystal structures. A crystal is a material where a three-dimensional array of atoms is arranged periodically. This arrangement can be considered as the duplication of the unit cell in three dimensions. The unit cell, which is the smallest building block in the crystal material, can be expressed by a set of lattice parameters, with three edge lengths *a*, *b*, *c* and their corresponding angles *α*, *β*, *γ*. As shown in Fig. 2.8, when the wavelength of the incident light source has a similar order of magnitude to the interatomic distances (*d*) in a crystal (orders of Å), atoms will act as a diffraction grating, diffracting the incident radiation and generating an interference pattern. Diffraction patterns can provide characteristic information of the crystal such as the size, symmetry and the content of its unit cell.

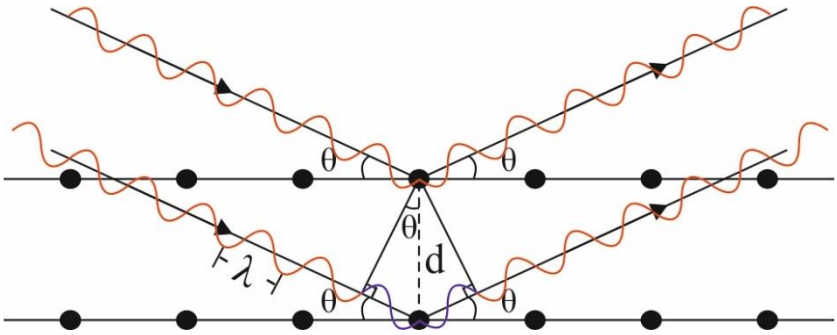

Fig.2.8 The schematic of a typical Bragg scattering showing the relationships between the lattice plane distance *d*, wavelength *λ* and the incidence angle *θ*. The path difference was highlighted in blue.

The parallel planes of atoms are denoted by the Miller indices (*hkl*), which determines the position of an internal plane of a crystal. The distance between a set of (*hkl*) lattice planes is

equal and labelled by d_{hkl}, and the incident waves remain parallel after being reflected by atoms, but a path difference incurred from the interaction with adjacent lattice planes – this has a value of $2dsin\theta$. W.H. Bragg and his son W.L. Bragg discovered that[11] when the phase difference of the travel-paths of two waves is equal to an integer multiple of the wavelength, $n\lambda$, the interference of diffracted waves will be constructive and a net intensity in the diffraction pattern will be given (the Bragg peak), as described by the Bragg's Law,

$$n\lambda = 2d_{hkl} \sin\theta \tag{2.2}$$

where d_{hkl} is the distance of the selected lattice plane (hkl) and θ is the angle between the incident wave and the lattice plane. There will be no scattering intensity due to the destructive interference between the reflected waves when the path difference does not equal $n\lambda$. For an orthorhombic system with unit cell parameters $a \neq b \neq c$ and $\alpha = \beta = \gamma = 90°$, the relationship between the distance d_{hkl} of neighbouring (hkl) planes and unit cell parameters can be denoted as,

$$\frac{1}{d_{hkl}^2} = \frac{h^2}{a^2} + \frac{k^2}{b^2} + \frac{l^2}{c^2} \tag{2.3}$$

Therefore in combination with Bragg' Law, the unit cell parameters can be calculated from the 2θ positions of the Bragg peaks observed in the diffraction pattern. However the unit cell content such as the atom arrangement revealed by the observed relative peak intensities cannot simply be explained by the Bragg's Law. To establish the accurate relationship between a crystal structure and a diffraction pattern, the information provided by the peak intensities must also be understood.

2.2.2 Diffraction of X-rays and neutrons

X-ray and neutron sources which have a range of wavelengths between 0.1 - 100 Å are applicable for diffraction experiments for the purpose of crystal structure characterisation.

2.2.2.1 X-rays

Diffraction has two main character. One is that diffraction is an elastic scattering process which means the radiation is treated as a classic wave without a change of energy during the diffraction process. The other is that diffraction is also coherent, indicating that waves diffracted from different atoms can interfere constructively to give high intensities.

X-rays are electromagnetic radiation, scattered from the electron density of an atom. As X-ray diffraction is elastic and coherent, only the radiation direction changes during the diffraction process, and it can be defined by the scattering vector $\boldsymbol{Q}$,

$$\boldsymbol{Q} = \boldsymbol{k}_i - \boldsymbol{k}_f \tag{2.4}$$

where $\boldsymbol{k}_i$ and $\boldsymbol{k}_f$ represent the incident and diffracted wavevectors respectively. Conventionally, diffraction patterns are displayed as intensity against the scattering angle (θ); however intensity against Q or d-spacing are used for time-of-fight experiments with variable wavelengths, as θ is wavelength dependent. When combined with Bragg's Law, the relationship between $\boldsymbol{Q}$, d and θ can be mathematically defined as:

$$|\boldsymbol{Q}| = Q = \frac{4\pi \sin\theta}{\lambda} = \frac{2\pi}{d} \tag{2.5}$$

This relationship also helps to compare diffraction data collected from different diffractometers using different wavelengths.

The peak position can be well defined using the equations listed above. In addition, the intensity of a Bragg reflection (I_{hkl}) containing the information of the unit cell content, is proportional to the square of the absolute value of the structure factor, shown as:

$$I \propto |F_{hkl}|^2 \tag{2.6}$$

F_{hkl} is summation of all the waves diffracted with atoms in the (hkl) plane and mathematical expression of F_{hkl} for X-ray diffraction can be written as:

$$F_{hkl} = \sum_j f_j \, e^{2\pi i(hx_j + ky_j + lz_j)} \cdot e^{\frac{-B_j \sin^2\theta}{\lambda^2}} \quad (2.7)$$

where f_j is the X-ray form factor describing the degree of interaction between the X-ray waves and electrons of a given atom. The f_j varies with atomic number Z, as the X-rays are scattered by the electron density of an atom; therefore X-rays cannot provide accurate information regarding light atoms such as hydrogen or oxygen, especially when compounds also contain heavier elements. Neighbouring elements or isotopes in the periodic table cannot be distinguished by X-rays due to their similar or same electron densities. In addition, X-rays interact with electron clouds, of which the size has a similar magnitude to the X-ray wavelength and therefore the Fourier transform of a large scattering object (electron cloud around an atom) results in f_j decreasing at higher scattering angle(Fig. 2.9(a)). h, k and l are the Miller indices for a certain lattice plane and x_j, y_j and z_j represent the atomic coordinates of atom j in the unit cell. B_j refers to the thermal factor which can be transformed to the mean square thermal displacement U by:

$$B = 8\pi^2 U \quad (2.8)$$

where U is proportional to the temperature and illustrates the thermal motion of a specific atom.

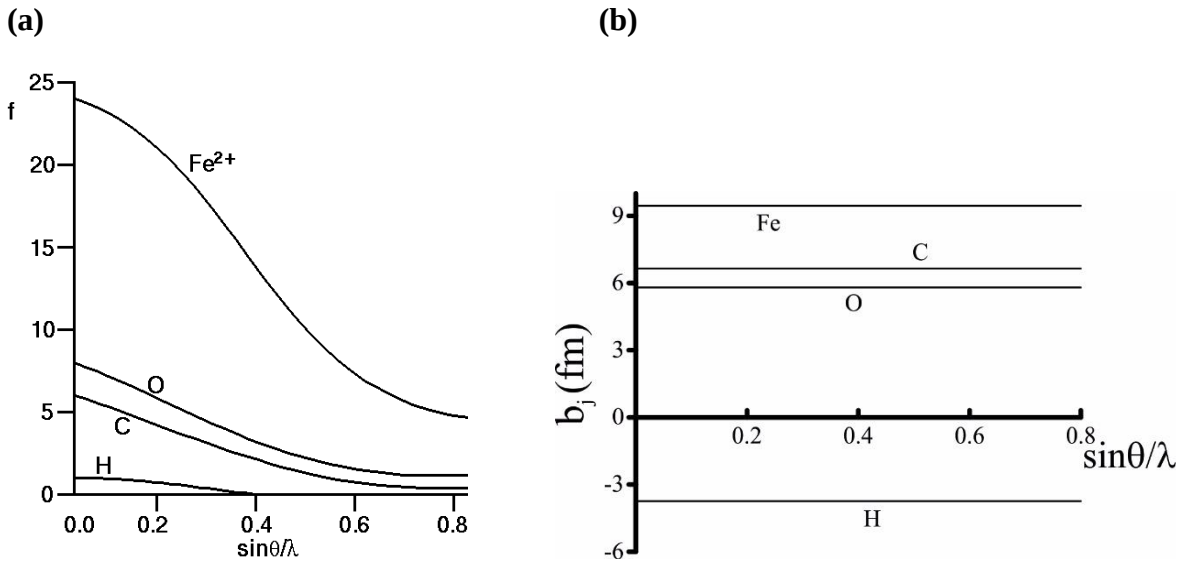

Fig. 2.9 (a) The atomic X-ray form factors of several elements as a function of scattering angle.[12] **(b)** The angular independent neutron form factor (the coherent neutron scattering length) of the same elements selected in Fig. 2.9 (a).

2.2.2.2 Neutrons

According to the wave-particle duality, each particle has its own wavelength which can be mathematically described by the de Broglie equation,

$$\lambda = \frac{h}{mv} \tag{2.9}$$

where h is Plank constant (6.626×10^{-34} J·s), m is the particle mass and v is the particle velocity. Particle (e.g. neutron) wavelengths can therefore be altered to a similar magnitude as the atomic spacing by tuning their speed.[13] In contrast to X-rays which are diffracted by 'electron clouds' surrounding the nucleus, neutrons interact with the atomic nucleus itself. The strength of this interaction is expressed by b_j, the neutron scattering form factor. As the nucleus is several orders of magnitude smaller than the value of neutron wavelength, it can be treated as a point scatter resulting in an angular independent b_j from the Fourier transform, as shown in Fig. 2.9(b). In general, neutron diffraction can distinguish between neighbouring elements and isotopes. In this thesis neutron diffraction was particular useful for accurately determining the oxygen positions in the crystal structures of transition metal oxides, since oxygen has a relatively large b_j. In addition, another unique benefit that neutron diffraction could offer is the

determination of the spin structure of a magnetic material owing to the neutron's intrinsic non-zero magnetic moment. Since the magnetic moment of a neutron can interact with unpaired electrons of the atoms, the magnetic contribution reflections from a magnetic material can be observed in a neutron diffraction pattern, and magnetic information such as the magnetic unit cell and the value of the ordered magnetic moment of a magnetic cation can be determined. Therefore, for a neutron diffraction pattern of a material with long range magnetic ordering, the structure factor is expressed as a combination of the nuclear and magnetic components:

$$|F_{hkl}|^2 = |F_{nuc}|^2 + \left|\boldsymbol{F}_{mag}\right|^2 \tag{2.10}$$

Each contribution can be respectively described as,

$$F_{nuc} = \sum_j b_j \, e^{2\pi i\left(hx_j+ky_j+lz_j\right)} \cdot e^{\frac{-B_j \sin^2\theta}{\lambda^2}} \tag{2.11}$$

$$\boldsymbol{F}_{mag} = \sum_j p f_j \boldsymbol{q}_j \, e^{2\pi i\left(hx_j+ky_j+lz_j\right)} \cdot e^{\frac{-B_j \sin^2\theta}{\lambda^2}} \tag{2.12}$$

where b_j and f_j are neutron and magnetic form factors respectively. The magnetic form factor is angular dependent, the same as X-ray form factor, so magnetic reflections are usually observed at lower scattering angles. The symbol p is the magnetic cross section, x, y, z refer to the coordinates of atom j in the unit cell and $\boldsymbol{q}_j$ represents the magnetic interaction vector.

Despite neutron diffraction having many advantages over X-ray diffraction, neutron sources are still limited to a few large-scale facilities around the world. This is due to the inherent difficulties of neutron generation, therefore the cost of neutron diffraction experiments is enormously high. In addition, the neutron flux still needs to be improved compared to the very bright synchrotron X-ray sources. These sources will be introduced in the later subsections.

2.2.3 Powder diffraction

Diffraction techniques can be applied on single crystal or polycrystalline specimens; however it is very hard to grow a single crystal large enough for neutron diffraction experiments.

Polycrystalline materials, composed of many randomly oriented crystallites, are on the other hand, easy to prepare in the laboratory. In contrast to a single crystal diffraction pattern where the observed diffraction spots contain additional crystal orientation information, powder diffraction patterns exhibit a series of Debye Scherrer cones (a set of concentric rings) which superimpose many diffraction spots derived from the different (*hkl*) planes of all crystallites with different orientations in the powder sample. Hence the orientation of the powder material is unknown. A comparison of single crystal and polycrystalline diffraction patterns is shown in Fig 2.10. One of the issues for powder samples is that different Bragg reflections can overlap with each other due to the loss of crystal orientation, resulting in the loss of correlated structural information, for instance symmetry and unit cell content information. This peak overlap issue has been solved by refining the crystal structure using Rietveld Method, as described in section 2.2.6.

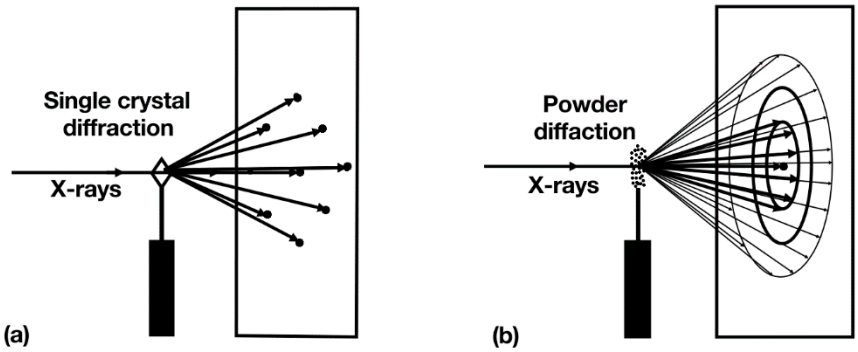

Fig 2.10 Schematics of **(a)** a single crystal diffraction pattern and **(b)** a polycrystalline diffraction pattern where a series of Debye Scherrer cones formed.[14]

2.2.4 Laboratory X-ray sources

The X-ray source of a laboratory diffractometer, which is generated by a sealed X-ray tube, is utilised for initial sample characterisation in the laboratory. A beam of electrons in the sealed tube is accelerated via a potential difference which then bombards onto a water-cooled metal anode target, inducing X-ray radiation that is emitted through beryllium windows. Generally, there are two types of X-ray radiation, distinguished by their different generation mechanisms. Bremsstrahlung radiation, also known as 'breaking radiation', arises from electrons rapidly decelerating when they collide with the metal target. These X-rays have a broad range of

energies but are relatively weak. Characteristic radiation, on the other hand, is generated from outer-shell (higher energy state) electrons filling vacancies of the inner shell (lower energy state) of the target metal atom after excitation. These X-rays are quite intense and have discrete wavelengths as photons are quantized corresponding to the energy differences between two states upon relaxation. Elements have their own set of energy levels and therefore the wavelength of X-rays resulting from electron transitions between different energy levels is characteristic of the target metal in the X-ray tube.

Inside powder diffractometers, two different geometries named as Bragg-Brentano and Debye-Scherrer geometries can be set up. In the Bragg-Brentano geometry set up, the X-ray beam is reflected off the polycrystalline sample loaded on a flat glass or silica plate.[15] The advantage of this flat plate mode is that large sample volumes can be held upon it, and the resulting diffraction pattern has high intensity. Debye-Scherrer mode, which utilises capillaries as the sample holder, is desirable for air-sensitive samples and significantly reduces the effect from preferred orientation of small crystallites in power samples. However, under such geometry a longer counting time may needed due to the increasing absorption and small allowable sample volume in a capillary.

Preliminary structural characterisation and phase identification of the materials studied in this thesis was achieved from powder X-ray diffraction patterns collected on a Bruker D2 Phaser powder diffractometer, as shown in Fig. 2.11. The D2 diffractometer was set up with the Bragg-Brentano geometry, where ~20 mg polycrystalline specimen was spread uniformly on a flat glass plate using methanol or ethanol. The X-ray beam of D2 was generated using copper as the target anode in the sealed X-ray tube where $K_{\alpha1}$, $K_{\alpha2}$ and K_{β} with wavelengths of 1.54056, 1.54439 and 1.39225 Å respectively were emitted. Nickel foil was used in the D2 to remove the K_{β} source. Other target metal such as Mo with λ = 0.7107 Å can be used as well under specific conditions. All the laboratory X-ray diffraction patterns presented in this thesis were collected within a $10° < 2\theta < 70°$ angular range, with a 0.03° step size and a counting time of 0.45 s per step, using a Cu $K_{\alpha1}$ radiation source at ambient temperature.

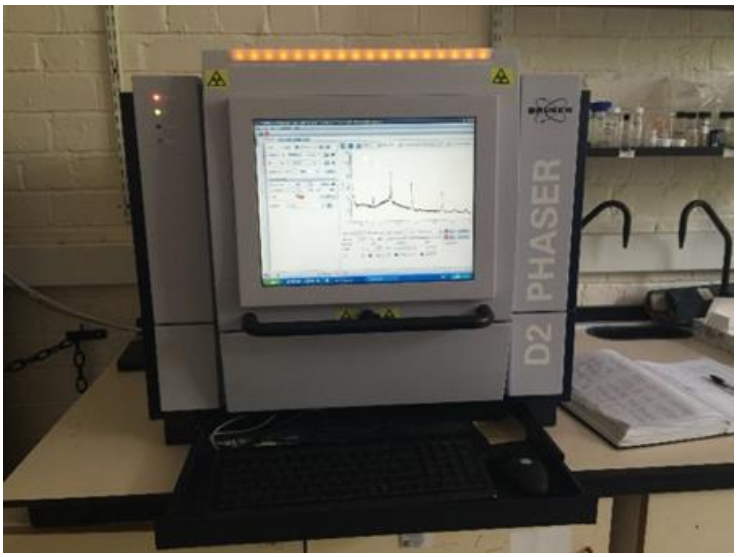

Fig. 2.11 Bruker D2 laboratory X-ray diffractometer using Cu K_α/K_β radiation source.

Preliminary structural characterisation for a rough approximation of the phase purity and/or a confirmation of the target phase formation can be performed using laboratory X-ray sources with a relatively fast collection time and at low cost. However due to the limited resolution and low radiation flux, chemical compounds with complex crystal structures cannot be accurately determined. Synchrotron X-ray sources, mostly based in national facilities with super high resolution and flux, are therefore required.

2.2.5 National sources of X-rays and neutrons

2.2.5.1 I11 at Diamond Light Source

As mentioned above, a laboratory X-ray source is easily accessible but the energy is limited by heat generation in the metal target. The number of useable metal anodes with desired wavelengths are limited as well. Synchrotron X-ray source however, overcomes these limitations by using an advanced method for generating X-ray radiations.

A synchrotron X-ray source is generated by accelerating electrons to near relativistic speeds in a large storage ring. These charged particles emit photons corresponding to a change in their momentum. The Diamond Light Source, which is a national scientific facility largely funded by the UK Government, provides a third-generation synchrotron source. Fig. 2.12 below shows a schematic diagram of the essential components assembled in a typical synchrotron facility. Electrons originating from the electron gun are fired into a linear accelerator (LINAC) and are

accelerated inside here to 100 MeV. Then electrons are shot to the second particle accelerator - the booster ring. Here electrons will be further accelerated until reaching an energy of 3 GeV, before being transferred into the storage ring. The storage ring at the Diamond Light Source, which is 562 m in circumference, consists of 24 straight sections and 48 bending magnets. Electrons are curved in between two adjacent straight sections by bending magnets, so that they can circulate inside the ring and generate synchrotron radiation, tangential to the curved path. The whole storage ring operates under extreme vacuum conditions to avoid electrons being scattered by air molecules. Finally, the emitted synchrotron radiation with not only high brilliance but also a broad spectral range will be delivered to each experimental hutch for various purposes.

In contrast to the laboratory X-ray sources, synchrotron X-ray sources are magnitudes brighter than in-house sources, with incredibly high intensity and flux. High flux in synchrotron sources can provide rapid data collection along with high counting rates, enabling a better signal-to-noise ratio. In addition, synchrotron radiation is also highly collimated with a high resolution, such that a sophisticated crystal structure can be precisely determined. The wide spectral range of the emitted synchrotron radiation also allows a desired wavelength to be used for experiments with different purposes.

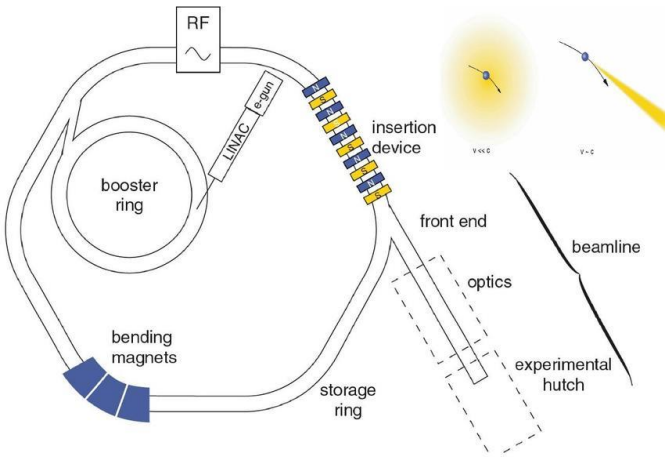

Fig. 2.12 A schematic diagram of the generation process in a sychrotron source. The main components are labeled. Figure was generated from P. Willmott[16].

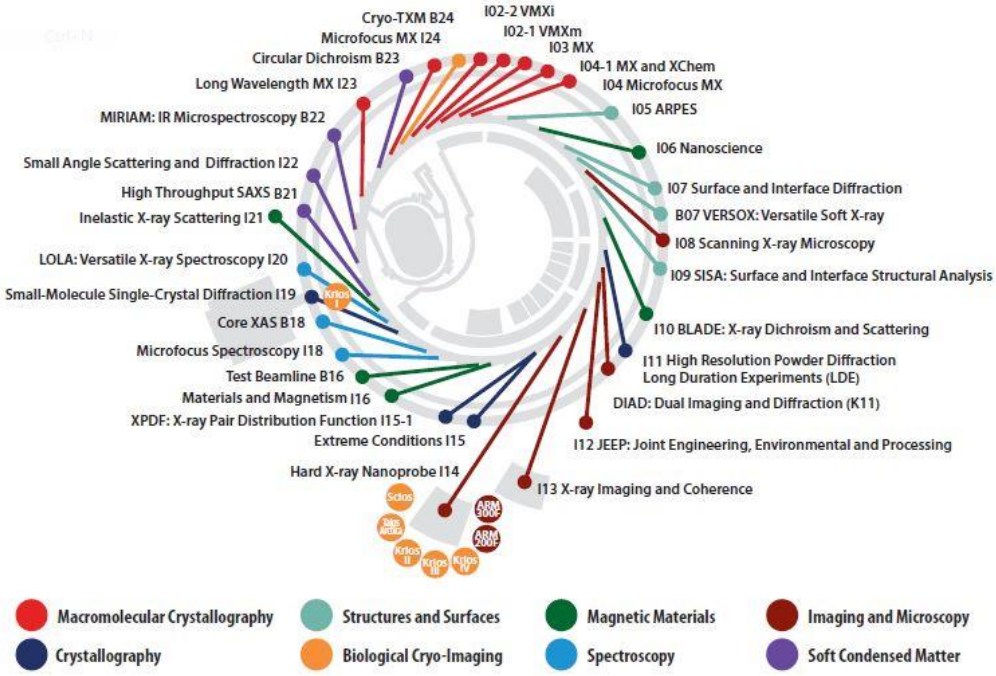

Fig. 2.13 The current beamline layout at the Diamond Light Source. The figure was taken from Diamond annual review 2018.[17]

As shown in the beamline plan above (Fig. 2.13), the Diamond Light Source has a total of 31 operating beamlines, of which I11 is designed for high resolution powder diffraction. Beamline I11 consist of three hutches: the optics hutch, where the light source is filtered and focused by a double-crystal-monochromater using Si (111) crystals, resulting in a selection of energy ranges from 5 – 25 keV (wavelength of 0.4 – 2.1 Å); Experimental Hutch 1, for general powder diffraction requirements, and Experimental Hutch 2, for a particular Long Duration Experiment (LDE). One special design at I11 is the five identical multi-analysing crystal (MAC)-arms, each carrying 9 Si (111) analyser crystals and 9 photomultiplier based detectors mounted at intervals of 30° on the 2θ cycle, as shown in Fig. 2.14. The total 45 analysing crystals are mounted on an α rotary table while 45 detectors are on the 2α rotary table, allowing the Bragg condition to be met for the Si (1 1 1) reflections from each analyser crystal. For a fixed incident X-ray beam energy (constant wavelength), each arm of the diffractometer only needs to rotate a little bit more than 30° to obtain the whole scanning pattern (e.g. 5° - 145°), which significantly shortens the data collection time. Furthermore, as the sample is scanned, 45 powder patterns are simultaneously measured by detectors before being converted into a single pattern to improve the data statistics.[18] This special design at I11 means the measured diffraction pattern not only has accurate diffraction peak positions, from a very short collection time but also maintains high angular resolution where the full width at half maximum (*FWHM*)

is only approximately 0.00149(2)° under a radiation energy of E = 15 keV. I11 provides different experimental environments. Powder specimens prepared either in a capillary or on a flat plate holder can be mounted onto the diffractometer. The sample carousel can hold as many as 200 capillary samples at the same time and a robotic arm controlled by a program can automatically change and align the capillary specimens, even with the radiation beam on. A Helium Cryostat (down to 4 K) or a hot air blower (up to 1273 K) can be installed to provide variable temperature conditions.

All the synchrotron data present in this thesis is collected from I11 Experiment Hutch 1 using a spinning quartz capillary with a diameter of 0.3 mm and a beam energy of 15 keV. The diffraction patterns were collected in the angular range of $5° < 2\theta < 145°$ and in the temperature region of 300 K < T < 700 K using a hot air blower, with a counting time of 30 minutes for each diffraction pattern.

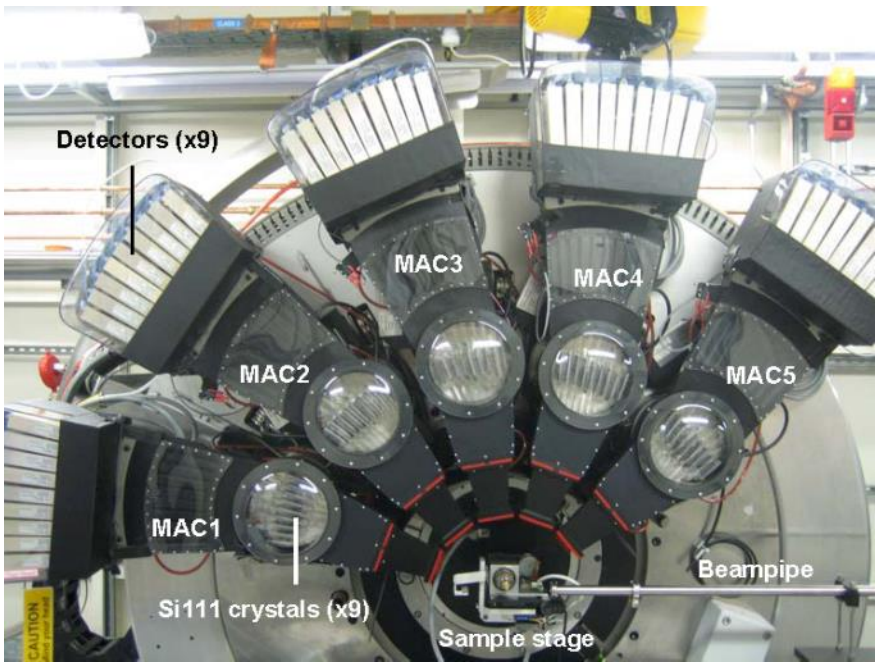

Fig. 2.14 A schematic of the I11 diffractometer showing the 5 multi-analysing crystal (MAC) arms on the 2θ cycle with each having 9 Si (111) analysing crystals and 9 detectors mounted on α and 2α rotary tables， respectively. All the important components are labelled.[18]

2.2.5.2 Constant wavelength powder neutron diffraction using a reactor source

Neutrons are generated for scientific research purposes by two different processes: using nuclear fission at a reactor or through spallation. In the first method, 'fast' (high energy, MeV) neutrons are produced through the fission of unstable uranium, ^{235}U. However, the energies of these 'fast' neutrons are far too high to be utilised in the study of the crystal structures through diffraction. To tune the value of the neutron wavelength to a similar magnitude of the lattice spacing (~2 Å) in a crystal, 'fast' neutron themselves need to pass through a moderator that contains massive of low mass nuclei at a certain temperature, in order to 'slow down'. For a diffraction experiment, the moderated neutrons still have a broad range of energies (as a polychromatic beam) and hence crystal monochromators, such as germanium monochromators, were employed to select a single wavelength of the neutron beam for a diffractometer, although monochromation significantly reduces the neutron flux before arriving at the diffractometer.

In the thesis, several powder neutron diffraction experiments were carried out at SPODI (FRM II) and D20 (ILL), both of which produce neutrons through nuclear fission at a nuclear reactor. The details of the facilities and instruments are listed below.

2.2.5.2.1 SPODI at Forschungs-Neutronenquelle Heinz Maier-Leibnitz

The Forschungs-Neutronenquelle Heinz Maier-Leibnitz (FRM II), located at Garching, Germany, is a research reactor that came into service in 2005. The core of FRM II is a single fuel element producing a thermal power of 20 MW with more than 10^{14} free neutrons generated per second per square centimetre. FRM II offers a broad range of the neutron spectrum including hot neutrons, cold neutrons and ultra-cold neutrons with corresponding neutron energies from MeV to neV. As shown in Fig. 2.15, representing the beamline layout of FRM II, there are currently 26 instruments in service for neutron science such as elastic or inelastic neutron scattering experiments.[19] In this thesis, some of the neutron diffraction patterns were collected on instrument SPODI at FRM II.

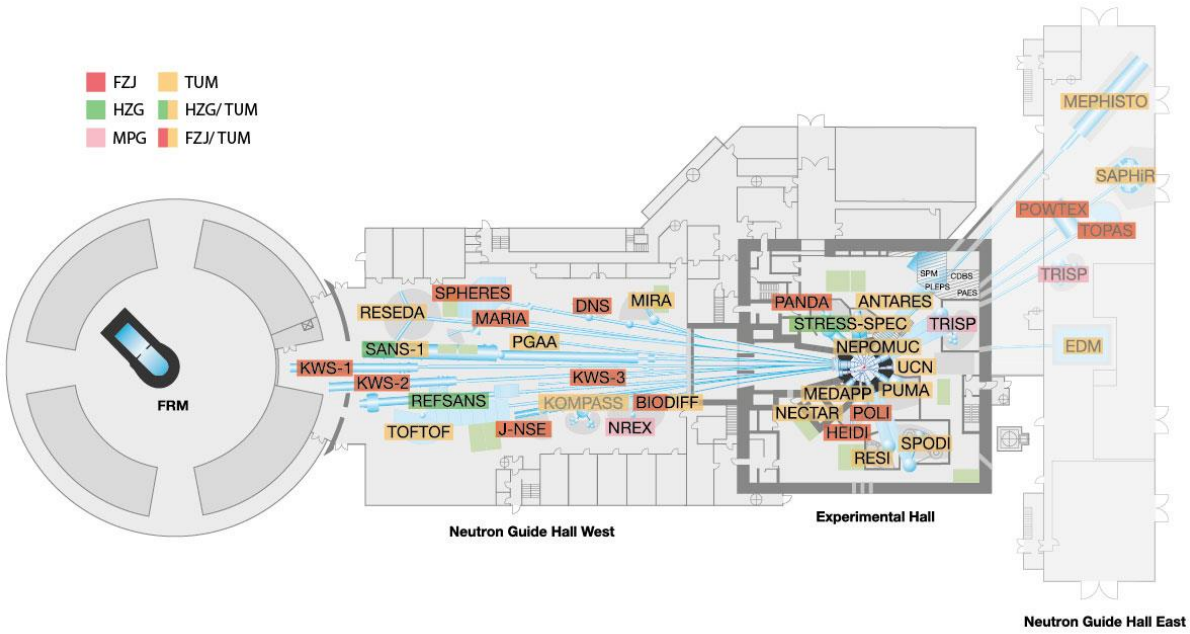

Fig. 2.15 The beamline layout at FRM II with all the instruments (in service or under construction) labelled. Figure was taken from I. Lommatzsch.[19]

The 'Structure Powder Diffractometer' (SPODI), is a high-resolution powder diffractometer designed for complex structural analysis of polycrystalline specimens. As shown in Fig. 2.16, a germanium monochromator with a high take-off angle of 155° (135°, 112.5° and 90° configurations are also available) and a long monochromator-to-sample distance were used at SPODI to provide a high-resolution, with a wide range of scattering angles. The Ge(551), Ge(331) and Ge(771) monochromators, for example, can provide particular neutron wavelengths of 1.548 Å, 2.536 Å and 1.111 Å, respectively. The rotatable detector array utilised at SPODI is constitutive of 80 ^{3}He position sensitive detector tubes of which each tube covers an angular range of 2°, resulting in a total scattering range of 160°. The diffraction pattern is collected through the stepwise positioning of the detector array of which the profile is conventionally set as $\Delta(2\theta)$ = 0.05° per step, for a total of 40 steps (~ 2°) to finish a full diffraction pattern collection.[20] Polycrystalline samples are loaded in vanadium cans with variable sizes at SPODI, as the vanadium has a very low neutron scattering length (–0.3824 fm). As SPODI is dedicated for investigating polycrystalline materials with complex structures, multiple conditions are available during diffraction by installing specially designed equipment. Temperature can be varied by installing a closed-cycle refrigerator (4 - 300 K) or vacuum high-temperature furnace (300 – 2100 K), while a maximum magnetic field of 7.5 T or a maximum

pressure of 10 GPa can be applied via a closed-cycle cryomagnet, or the Paris-Edinburgh cell, respectively. In this thesis, data were collected at SPODI using a wavelength of λ = 1.548 Å and 2.536 Å at temperatures of 4 K, 30 K, 50, 70 K and 100 K. λ = 2.536 Å was selected to obtain better peak resolution of the magnetic satellites. The experimental details will be described in Chapter 4.

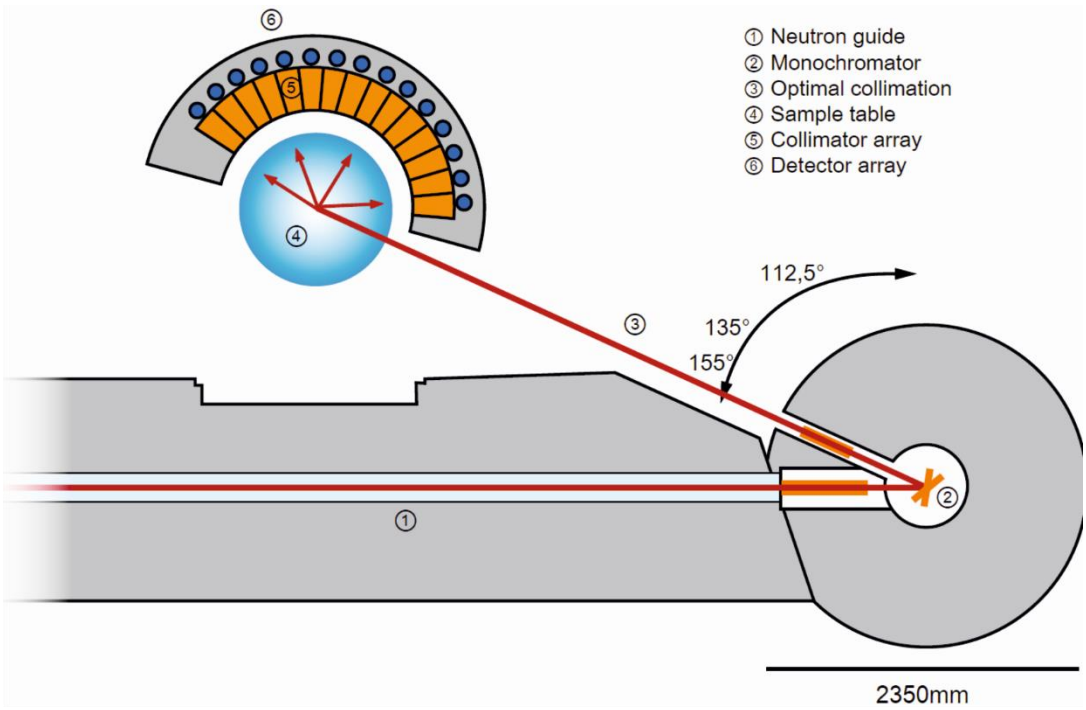

Fig. 2.16 A schematic of the high-resolution SPODI diffractometer with labelled components.[20]

2.2.5.2.2 D20 at Institute Laue-Langevin

The Institute Laue-Langevin (ILL) in Grenoble, France, is another European reactor for generating neutrons with a thermal nuclear power of approximately 58.3 MW, and a raw neutron flux of 1.5×10^{15} $s^{-1}cm^{-2}$, offering one of the most intense neutron sources in the world, allowing 49 state-of-art instruments to be operated for scientific research every year.[21,22] One of these instruments that was utilised for measuring materials studied in this thesis is D20, which is a high flux (up to 10^8 $s^{-1}cm^{-2}$) two-axis powder diffractometer, allowing analysis of small quantity, precious samples such as those synthesised from high-pressure techniques.[23] As shown by the D20 diffractometer schematic in Fig. 2.17, the neutron beam from the reactor is first monochromated before leaving from one of the five take-off ports with its corresponding

instrument resolution. The beam is diffracted when it arrives at the sample and the diffracted beam can be simultaneously recorded by a large number of microstrip detectors which cover a scattering range up to 153.6°. The sample environment can be modified by installing a cryostat or a furnace to the diffractometer, to provide a wide temperature range of 1.7 K < T < 1373 K.[23] Like the sample preparation at FRMII, vanadium is used as container and the powder sample must be well ground in advance. For data collected at D20, a newly built monochromator was used, to select a beam with a longer wavelength of λ = 3.6 Å, and a high take-off angle of 65°, in order to obtain a high resolution pattern for solving complex magnetic structure. The detailed structural characterisation will be introduced in Chapter 4. This diffractometer with its extremely high neutron flux especially favours high-pressure samples (of limited quantity) with low temperature magnetic structures.

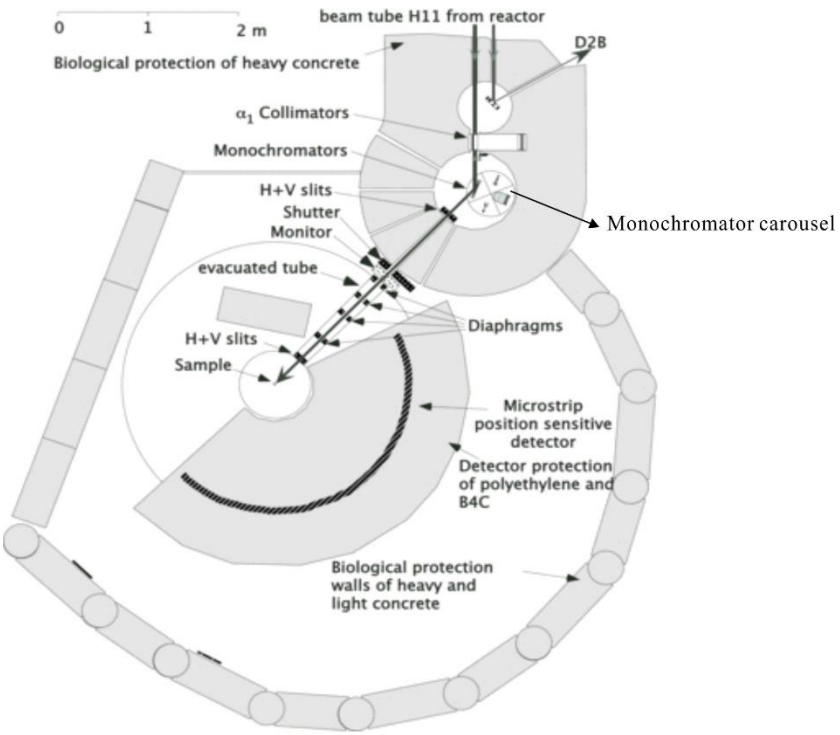

Fig 2.17 A schematic of the D20 diffractometer at ILL showing that the incident wavelength can be easily selected by mounting the monochromators on the carousel. The components of the diffractometer set up are labelled. Figure is generated from T.C. Hansen et al.[23]

The neutron source produced from a nuclear reactor has a wide range of neutron wavelengths which can be used in many applications. However, the maximum reactor-based neutron flux is limited by the heat generation inside the reactor during nuclear fission, so the flux reaching the sample is relatively low as a suitable wavelength (rational energy) needs to be selected through monochromation for a given experiment. To overcome these disadvantages, and perhaps to lower the risk of nuclear pollution, another process of generating neutrons called 'spallation sources' was invented.

2.2.5.3 T.O.F powder neutron diffraction using a spallation source (ISIS facility)

The word 'spallation' describes a process where neutrons are 'peeled off' from a heavy-metal target when it is bombarded by a beam of high-energy protons. This technology has been used for producing neutrons since the 1960s.[22] The ISIS Neutron and Muon Source at the Rutherford Appleton Laboratory (UK), of which the layout is depicted in Fig. 2.18, is a modern spallation source facility producing neutrons for more than 30 instruments to carry out scientific research.

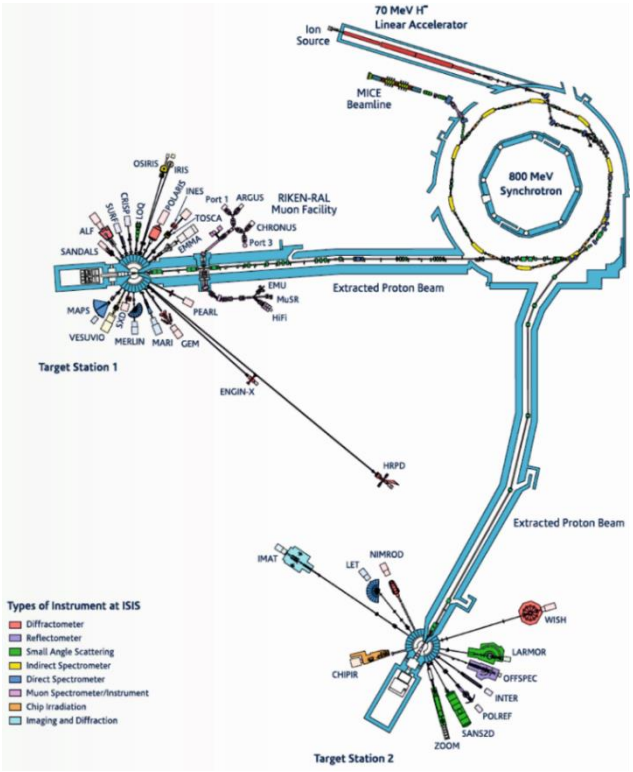

Fig. 2.18 A layout of ISIS Neutron and Muon Facility. All the instruments in Target Station 1(TS1) and Target Station 2 (TS2) that currently in operation are labelled and the WISH diffractometer that was utilised in this thesis in shown at the right bottom. The figure was taken from the ISIS Neutron and Muon Source Annual Review 2018.[24]

'Bunches' of protons are successively accelerated by a 40 m long LINAC and a synchrotron ring (26 m in radius, as discussed in the last section) until they reach an energy of 800 MeV (equal to 84% of the speed of light). The high-energy protons are then delivered to the target stations (TS1 & TS2) where they strike the heavy-metal (tantalum-clad-tungsten) target, resulting in ejection of epithermal neutrons with extremely high energies. Similar to the reactor-produced-neutron process, moderators such as water or liquid methane are utilised to 'slow down' these 'fast' polychromatic neutrons, which can have wavelengths of similar magnitude to the lattice spacing of crystals. However, monochromators are not necessary for spallation neutron sources, as the reflection intensity is not measured as a function of 2θ, but as a function of energy or time-of-flight (T.O.F). The neutron pulses are therefore polychromatic and their different wavelengths can be determined by the modified de Broglie equation,

$$\lambda = \frac{ht}{mL} \tag{2.13}$$

where *h* is Planck's constant; *m* is the neutron mass; *L* is the path between the source and fixed detector and *t* is the time of a neutron traveling a distance *L*.[22] When combined with the Bragg law, the *d*-spacing can be determined as:

$$d = \frac{ht}{2mL \sin\theta} \tag{2.14}$$

One of the advantages of a spallation source is that it can be used to measure samples with very low *d*-spacing, as the polychromatic neutron source has a wider energy spectrum than that of reactor-based neutron sources, allowing more energetic neutrons to be selected for diffraction experiments. The peak resolution of a diffraction pattern obtained from the diffractometer with fixed banks of detectors at a certain 2θ can be expressed as:

$$\frac{\Delta d}{d} = \left[\left(\frac{\Delta t}{t}\right)^2 + (\Delta \cos\theta)^2 + \left(\frac{\Delta L}{L}\right)^2\right]^{1/2} \tag{2.15}$$

Hence a better resolution can be obtained by elongating the flight path L and increasing the 2θ scattering angle of the detector (close to 180°) – known as a backscattering position.

2.2.5.3.1 WISH at the ISIS neutron facility

The 'wide angle in a single histogram' diffractometer, shortened to WISH, is located at Target Station 2 at the ISIS Neutron and Muon facility. The WISH diffractometer, exhibited in Fig. 2.19, is specially designed for magnetic studies on powders or single crystals. By utilizing a dedicated solid-methane moderator (maintained at 40 K) and low frequency (10 Hz) neutron source, WISH delivers high-quality neutron diffraction patterns with a broad *d*-spacing range (0.7 – 50 Å).[25]

Fig. 2.19 The layout of the WISH diffractometer without its sealed top, clearly shows the ten banks of detectors. Figure is taken from the ISIS twitter.[26]

As shown in the WISH schematic (Fig. 2.20), the delivered neutron beam is modified by 5 sets of piezoelectric slits before arriving at the sample in order to have an appropriate trade-off between the resolution and the flux. Ten banks of 1520 ^{3}He tubes (exhibited in Fig. 2.19) form the detector array mounted on a cylindrical locus in an angular range of $10° \leq 2\theta \leq 170°$ and $-170° \leq 2\theta \leq -10°$ with no gap between adjacent detector tubes; each bank therefore covers an scattering angle of 32°. With a relatively high neutron flux, high quality data from samples of less than 100 mg can be obtained within an hour. This, plus the ten banks of detectors allows

precious high-pressure samples with complex magnetic structures (possible large *d*-spacing magnetic reflections) to be studied. Just like the other diffractometers introduced above, a closed-cycle refrigerator or a furnace can be supplied by WISH to provide a broad range of temperature conditions during experiments. In addition, pressure cells and re-condensing superconducting magnets can be installed on WISH, allowing diffraction patterns to be collected under pressure or magnetic fields, respectively.

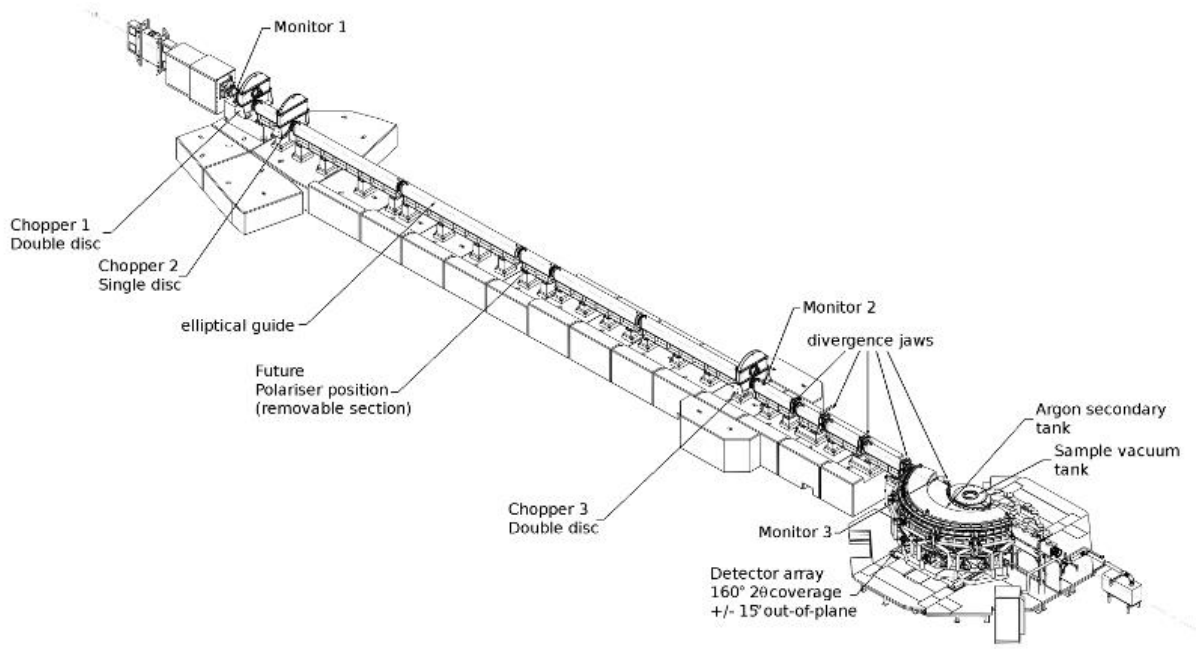

Fig. 2.20 A schematic of the WISH diffractometer at TS2 showing the neutron source controlled by 5 sets of slits. Figure was taken from L. Chapon et al.[25]

Some of the neutron diffraction data in this thesis were collected at the WISH diffractometer using a vanadium-can at variable temperatures between 1.7 K and 120 K. Neutron data and refinements are presented in detail in Chapter 3 and Chapter 4.

2.2.6 Rietveld refinement & magnetic symmetry analysis

2.2.6.1 Rietveld refinement

The X-ray and neutron diffraction patterns of polycrystalline specimens are characterised by reflections at certain positions, as the width, height and positions of these diffracted peaks

elucidate the structural information of the sample. Back to the 1960s, the identification of the integrated intensity of individual diffraction peaks was difficult as many Bragg reflections of a powder sample strongly overlap with each other. In 1969, the Rietveld method, named after a Dutch crystallographer Hugo Rietveld, was published to enable powder diffraction patterns to be clearly characterised using a least-squares approach.[27] Instead of characterising each *hkl* reflection, the Rietveld method executes a curve fitting procedure by simultaneously defining the individual intensity y_i to be the sum of the contributed Bragg peaks' intensities $y_{i,hkl}$ near the position i, presented in equally spaced steps divided across the entire 2θ range, plus the background intensity $y_{i,b}$:

$$y_i = y_{i,b} + \sum_{hkl}^{i} y_{i,hkl} \tag{2.16}$$

It is necessary to mention that the Rietveld method is a structural refinement approach, not a structural solution technique, because the instrument profile, space group, lattice parameters and approximate atom coordinates must be known in advance to successfully carry out the refinement. The mathematical purpose of Rietveld refinement of powder diffraction patterns is to minimise the difference, S_y, between the observed intensity $y_{i,obs}$ and the calculated intensity $y_{i,calc}$ through a least-square approach for all equally divided 2θ steps, as expressed below:

$$S_y = \sum_i \frac{(y_{i,obs} - y_{i,calc})^2}{y_{i,obs}} = \sum_i w_i \, (y_{i,obs} - y_{i,calc})^2 \tag{2.17}$$

where the statistical weighting factor w_i is equal to $1/y_{i,obs}$, and $y_{i,calc}$ is the intensity calculated by the Rietveld method at each step i, which can be described as:

$$y_{i,calc} = s \sum_{hkl} L_{hkl} \, |F_{hkl}|^2 \emptyset(2\theta_i - 2\theta_{hkl}) P_{hkl} A + y_{i,b} \tag{2.18}$$

where s is the scale factor quantitatively expressing the percentage weight fraction of each phase in sample; *hkl* are the miller indices; L_{hkl} consists of Lorentz, polarisation and multiplicity

factors; F_{hkl} is the structure factor varied with the refinement of unit cell parameters (a, b, c; α, β, γ) and atom information (typically x, y, z; thermal parameters and site occupancy). These values are initially set using a starting model downloaded from the online database (e.g. ICSD). If the atom information cannot be found, the Le Bail method[28] can be initially employed, as it only requires the unit cell parameters. F_{hkl} will also contain a magnetic component when refining the magnetic reflections from low temperature neutron diffraction. φ refers to the reflection profile function and P_{hkl} represents the preferred orientation factor, which are only refined when crystallites in polycrystalline samples are not packed randomly, but in specified (preferred) orientations. The absorption factor A is different with different phases and $y_{i,b}$ is the background intensity at the step i of the 2θ region. All the terms and their parameters in the equation can be altered during the Rietveld refinement process in order to better match the calculated pattern with the observed one, and hence minimise the S_y.

The profile function, φ, is one of the most important aspects in Rietveld refinement as it calculates the peak shape of a reflection which is qualified by the Full Width at Half Maximum (*FWHM*) expression. Each radiation source will have its characteristic and angular dependent peak shape profile; however the measured powder sample itself also affects the peak shape resulting in varied peak shape parameters, from the values given in the instrument parameter files. In addition, a reduction of the periodicity of a crystal structure, induced by the stress or strain, may vary the peak shape parameters as well. The peak shape parameters describing the *FWHM* is given by H_G, H_L,

$$H_G = \mathrm{U}tan^2\theta + Vtan\theta + W \tag{2.19}$$

$$H_L = Xtan\theta + \frac{Y}{cos\theta} \tag{2.20}$$

H_G is Gaussian component of the peak shape profile often known as the Caglioti Equation[29] and H_L is the Lorentzian component. U, V and W are refinable parameters, and X, Y are normally refined for diffraction patterns collected from high resolution diffractometers, where Bragg peaks become adequately sharp & narrow and the contribution from powder sample defects to the peak shape become significant.

The peak shape profile of T.O.F neutron diffraction is complex, as the moderation of neutron pulses contributes an asymmetric component to the peak shape. As shown is Fig. 2.21, an unusual T.O.F peak shape can be well described by the Ikeda-Carpenter function, which is a convolution of a sharp leading edge Gaussian shape contributed from the instrument, and a long trailing edge. The sharp leading edge arises from the initial rapid neutron flux and the trailing edge originates from the slow moderation process for neutrons.

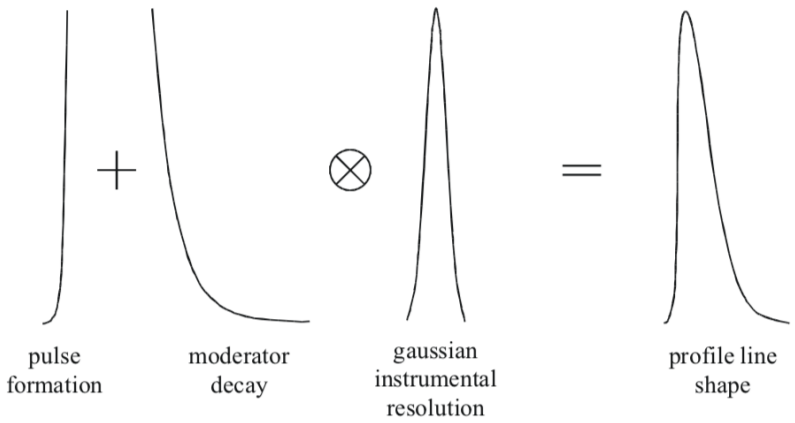

Fig. 2.21 The schematic of a typical Ikeda-Carpenter peak shape usually observed in T.O.F neutron diffraction pattern exhibiting a combination of sharp leading Gaussian shape and a long trailing edge. Figure is taken from ISIS Neutron Training Handbook.[13]

With the refinement of several structural parameters including scale factors, peak shape, background function, lattice parameter, atomic positions, thermal factors and site occupancies, the calculation converges when the refinement progress is successful, and the resulting parameters along with the output crystal model in theory represent the real crystal structure. Herein the quality of fitting the experimental pattern with the calculated model can be examined by three factors, the profile R-factor R_p, the weighted profile R-factor R_{wp} and 'goodness of fit' (GOF) parameter χ^2,

$$R_p = \frac{\sum_i |y_{i,obs} - y_{i,calc}|}{\sum_i y_{i,obs}} \tag{2.21}$$

$$R_{wp} = \left(\frac{\sum_i w_i (y_{i,obs} - y_{i,calc})^2}{\sum_i w_i (y_{i,obs})^2} \right)^{1/2} = \left(\frac{S_y}{\sum_i w_i (y_{i,obs})^2} \right)^{1/2} \quad (2.22)$$

$$\chi^2 = \frac{\sum_i w_i (y_{i,obs} - y_{i,calc})^2}{N - P + C} = \frac{S_y}{N - P + C} \quad (2.23)$$

where N is the number of the observations, P is the number of refined parameters and C is the number of applied constraints. The R_{wp} and χ^2 factors are commonly regarded since they both contain S_y of which the values will be minimised through the least square refinements. As the refinement cycles, the values of R_p and R_{wp} will tend to 0 while the value of χ^2 will close to the ideal value of 1.

In this thesis, all the powder diffraction patterns collected either from X-ray powder diffractometers or neutron powder diffractometers were refined using the Rietveld method to solve the crystal and/or magnetic structures. The Rietveld method was carried out using the General Structure Analysis System (GSAS)[30] written by A. C. Larson and R. B. Von Dreele as well as the Fullprof Suite[31] developed by J. Rodríguez-Carvajal.

2.2.6.2 Magnetic symmetry analysis

Analysis of the magnetic structure of an inorganic compound is of great importance in solid-state chemistry, as it furthers understanding of the intrinsic electronic and magnetic interactions existing in the material. For a polycrystalline magnetic material, the determination of the magnetic structure from its unique magnetic intensities, observed in neutron diffraction patterns can only be carried out if the space group (structural symmetry) of its crystal structure has been already solved.

For a crystal structure, the space group explains the possible atomic arrangements in a unit cell and the atom positions are represented through polar vectors. While as axial vectors, magnetic moments are represented differently via symmetry operators. The mirror plane symmetry operation shown in Fig. 2.22, induces exactly the opposite effect on polar and axial vectors; the magnetic moment here can be considered as arising from electric current loops for clarity. This is due to the change of current direction in the loop when the axial vector is parallel to the mirror plane, although the position of the loop is still transformed in the same way as that of the polar axis. In order to keep the axial vectors (e.g. magnetic moment) invariant, a new symmetry operation is defined, called time reversal that inverts only axial vectors. All of the

possible combinations of symmetry operations in the 230 space groups and the time reversal operation, which are named as anti-symmetry operations or primed operations, generate a total of 1651 magnetic or Shubnikov groups that correctly describe the magnetic structure.[32-33] To solve the correct magnetic structure of a material, one needs to consider all the possible magnetic space groups that can be derived from its crystal space group. For finding the symmetry properties of a magnetic structure, representation theory is a useful tool that reduces the number of possible magnetic solutions. Theoretically, a representation is formed by a set of linear operators Γ, which is mathematically described by a matrix, and is associated with the symmetry elements of a space group in a certain way. Applying appropriate rotations to these matrices reduces the representation into a number of low-dimensional representations, so called irreducible representations (IrReps). Possible magnetic symmetries of a material can be selected by IrReps under the symmetry operations from its crystallographic space group and thus the possible alignments of the moments can be determined. An IrRep consist of several basis vectors and the relative ratios between basis vectors (Ψ) are the focused parameters which will be refined during the process of fitting magnetic intensities in a diffraction pattern. In most cases the symmetry in a magnetic structure is determined by a single IrRep (e.g. $YRuO_3$ in Chapter 5), however a set of IrReps are required to describe a magnetic material with multiple ordered magnetic cation-sites or with multiple coexisting magnetic phases (e.g. $Ni_{2-x}Co_xScSbO_6$ in Chapter 4). In this thesis, magnetic symmetry analysis is carried out using the program BasIreps[34] installed in the FullProf Suite.[31] The detailed magnetic symmetry results containing IrReps and their corresponding basis vectors will be presented in each result chapter.

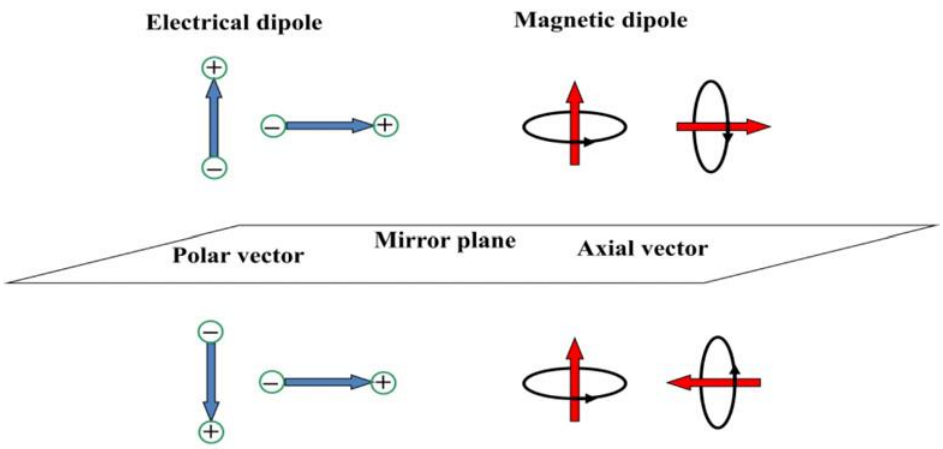

Fig. 2.22 The spatial arrangements of a polar vector (left) and an axial vector (right) that carried out by a symmetry operation 'mirror plane'. Figure was taken from J. Rodríguez-Carvajal and F. Bourée.[35]

2.2.7 Bond valence sums

In a metal oxide, the valence state of a metal ion can be estimated from its coordination number and M-O bond lengths, determined from the Rietveld refinement. The method of mathematically calculating the metal ion's valence state is called bond valence sum (BVS) analysis, which is based on Pauling's second rule[36-37], confirming the correctness of a structural refinement. The mathematical relationship between the valence state of a selected metal ion V_n, which is the sum of the individual bond valences v_n in the coordination environment of the cation, and the refined bond distances can be described as:

$$V_n = \sum_i v_n = \sum_i exp\left(\frac{d_n - d_i}{B}\right) \tag{2.24}$$

where d_i is the refined distance between the cation and its coordinating anions; d_n is the bond valence parameter of the metal at the assumed oxidation state n, and B is the global constant which is empirically determined as 0.37 Å.[38-39] A table of bond valence parameters d_n for metal cations at multiple oxidation states can be found online for BVS calculation.[40]

2.3 Magnetism in transition metal compounds

2.3.1 Magnetism

The magnetic moment μ of an electron originates from the orbital angular momentum l and the spin angular momentum s. l is the angular momentum of an orbiting electron, revolving around its axis – the orbit that the electron occupies determines the value of l. Spin angular momentum is intrinsic to a particle itself thus the values of s for all electrons have the same magnitude. An atom with an electron configuration of unpaired electrons will have a magnetic moment determined by the total angular momentum J, which is a combination of orbital and spin angular momentum through spin-orbit coupling. The formula of the total magnetic moment μ of an atom with unpaired electrons can be described as:

$$\mu_{eff} = g_J\sqrt{J(J+1)}\mu_B \tag{2.25}$$

where g_J is the Landé *g*-factor, μ_B is the Bohr magneton and g_J can be defined as:

$$g_J \approx \frac{3}{2} + \frac{S(S+1)-L(L+1)}{2J(J+1)} \tag{2.26}$$

In the case of 3*d* transition metal oxides where 3*d* metals exist in coordination complexes with a strong ligand field, the *d* orbitals are no longer all degenerate and orbital angular momentum is thus 'quenched' ($L = 0$). The equations of the effective moment for the first row transition metal cations can be simplified to a spin only model:

$$\mu_{eff} = 2\sqrt{S(S+1)}\mu_B \tag{2.27}$$

To understand the magnetic behaviour of a chemical compound, the magnitude of the atomic moment and how they interact with each other must be characterised. Paramagnetic compounds that have cations with unpaired electrons can be magnetised by applying an external magnetic field *H*. The average magnetic moment per mole is defined as the magnetisation *M* which has a linear relation with the magnitude of *H*, as expressed below,

$$M = \chi \mathrm{H} \tag{2.28}$$

where χ is the magnetic susceptibility describing the change of magnetisation in regard to the magnitude of *H* with a unit emu·mol^{-1}. The measurement of DC magnetisation against temperature for example allows χ to be determined under a fixed magnetic field and the variation of χ against temperature reveals different magnetic behaviours.

Diamagnets are materials generating an induced magnetic field that is opposite to the applied magnetic field. Diamagnetism actually occurs in all materials. However it is only observed in samples without unpaired electrons, as the value of diamagnetic susceptibility is orders of magnitude smaller than the susceptibility originating from unpaired electrons. A compound containing one or more unpaired electrons exhibits paramagnetism, of which the magnitude is expressed as the μ_{eff} discussed above. The moments of different atoms from the paramagnet

will align in the same direction with the applied magnetic field, leading to a positive susceptibility that has an inverse relation to temperature *T*, known as Curie Law:

$$\chi = \frac{C}{T} \tag{2.29}$$

where *C* is the Curie constant with units of emu·K·mol^{-1}. For a perfect paramagnet without interacting spins, the χ^{-1} as a function of *T* should be linear and the x-intercept of χ^{-1} should be zero. However, when interactions between adjacent magnetic moments in a compound exist, the intercept of χ^{-1} will no longer be zero. The interaction can be ferromagnetic when the adjacent moments align parallel or antiferromagnetic when moments align antiparallel. The Curie law can be modified as:

$$\chi = \frac{C}{T-\theta} \tag{2.30}$$

This equation is known as the Curie-Weiss Law. Θ is the Weiss constant with the unit K and it is the temperature where the inversely fitted susceptibility intersects the *x*-axis. θ is negative when the coupling between adjacent moments is antiferromagnetic and is positive with ferromagnetic coupling. The Curie constant *C* is specific to a material, which is determined by the material's effective moment μ_{eff},

$$C = N\frac{N_A \mu_B^2 \mu_{eff}^2}{3k_B} \tag{2.31}$$

where *N* is the number of the magnetic atoms per formula unit, N_A and k_B refer to Avogadro's constant and Boltzmann's constant respectively. There are other types of paramagnets of which the susceptibility may deviate from the Curie-Weiss behaviour. For example Pauli paramagnetism, which shown by metallic materials, has delocalised electrons aligned with the applied magnetic field resulting in paramagnetism.

Materials normally exhibit paramagnetic behaviour, especially at high temperatures where thermal motion randomizes the magnetic moments. However, some materials can undergo a

magnetic transition from a paramagnetic state to a long-range ferromagnetic or antiferromagnetic ordered state below a critical temperature. This critical temperature is defined as the Curie temperature for ferromagnetic ordering and as the Néel temperature for antiferromagnetic ordering. During the DC magnetic susceptibility measurement, the critical temperature can be confirmed at the point where the gradient sharply changes. In the case of ferromagnetic materials, the magnetic moments align parallel and give rise to spontaneous magnetisation below T_C, and therefore the susceptibility value will reach saturation at very low temperatures when the magnetic moments in all different domains align with H. On the other hand, there is no net magnetisation in antiferromagnetic materials due to the antiparallel alignments of adjacent moments, so the magnetic susceptibility will decrease below T_N and theoretically reach 0 when the T = 0 K.

2.3.2 Magnetometry

Magnetisation measurements can be carried out on a very sensitive device known as Direct Current Superconducting Quantum Interference Device (DC-SQUID)[41] installed in a Quantum Design Magnetic Property Measurement System (QD-MPMS). By using this instrument, the magnetisation of a material can be measured between a temperature range of 2 K $\leq T \leq$ 400 K and a field range of –7 T $\leq H \leq$ 7 T. A SQUID is one of the most sensitive magnetometers that is capable of detecting the magnetic moment of a material with a magnitude of 10^{-18} G or in a field as low as 5 x 10^{-18} T. This is attributed to the crucial component of a SQUID, the Josephson junction. The Josephson junction consists of two superconducting closed loops coupled with a very thin 'non-superconducting barrier', which is able to detect a subtle magnetic field.[41] The 'barrier' acts as a gap bisecting the superconducting loops, and is made from an insulating material or a non-superconducting metal. A voltage will develop across the junctions when the critical current is exceeded; this voltage is strongly correlated to the total magnetic flux penetrating the area of SQUID. In this thesis, all the chemical compounds measured by SQUID were polycrystalline.

The sample preparation for SQUID measurement is described as follows: 5 - 60 mg powder polycrystalline samples (pellets are also appropriate) are loaded into a gelatin capsule, which is then fixed inside a plastic straw. The straw is mounted onto the sample rod and then inserted into the magnetometer chamber through the air lock to ensure no air enters. The sample in the capsule is directly positioned within the superconducting pickup coils and a uniform magnetic

field H is used to magnetise the sample. The magnetic sample is moved through the pickup coils, which are connected to a second set of coils, inducing an electric current. The current arising from the movement of the sample will generate a magnetic field at the second set of coils and hence alter the voltage across the Josephson Junctions. The change of voltage is measurable and is proportional to the sample magnetisation.

The measurements of magnetisation (M) against temperature (T) under a fixed magnetic field (H) carried out on the SQUID magnetometer can be classified as zero field cooling (ZFC) and field cooling (FC). A sample cooled down from $T > T_C$ to base temperature with $H = 0$ is subjected to ZFC while with $H \neq 0$ is subjected to FC. In the case of ZFC, a certain value of H is applied to the sample when the base temperature is reached. M is then collected as the sample warms up for both ZFC and FC measurements. Magnetisation measurements here are used to determine the type of magnetic interactions presented in the materials. Ferromagnetic interactions are suggested when the value of FC susceptibility (χ_{FC}) is larger than that of ZFC susceptibility (χ_{ZFC}). Although the magnetic moments in a single domain are parallel, moments from different domains are not aligned upon zero field cooling therefore reducing the total net magnetisation in χ_{ZFC}. However all the moments will align with the applied field H in χ_{FC} upon cooling which results in suppressing the formation of small magnetic domains, while the net magnetisation could reach to a saturation value at very low temperature as illustrated above. In addition, there is no splitting between FC and ZFC curves for an antiferromagnet. It is necessary to mention that in highly frustrated systems such as the short-range magnetic ordered spin glass, the divergence in ZFC and FC susceptibility is similar to that in ferromagnets. In this case, powder neutron diffraction is required to distinguish their different magnetically ordered states.

In this thesis, the DC magnetisation measurements of some compounds were also carried out on a Quantum Design Physical Property Measurement System (QD-PPMS). The magnetisation is measured similarly by using the Vibrating Sample Magnetometer (VSM) to move the sample through pick up coils. The accuracy and sensitivity of the PPMS is not as high as that of the SQUID, as the induced voltage is measured by a conventional method rather than using the superconducting loops interrupted by two Josephson junctions.

2.4 Electrical resistivity

Electric resistance (R), measured in units of ohms (Ω), describes how the material opposes the electric current (I) that flows through it. The resistance can be defined as:

$$R = \frac{U}{I} \tag{2.32}$$

where U is the voltage across the material, measured in units of volts (V) and I is the electric current through the material with units of amperes (A).

For an ideal material with uniform cross-section, flow of electric charge and physical composition, its intrinsic property, the resistivity ρ (Ωm), can be expressed as:

$$\rho = \frac{RA}{L} \tag{2.33}$$

where R represents the specimen resistance, A is the cross-section area in m^2 and L is the length of the specimen in m.

Resistivity measurements elucidate whether a specimen is a metal, semiconductor or an insulator. In this thesis, resistivity measurements were carried out on the QD-PPMS in the temperature region of 2 K < T < 400 K using a four-probe method (Fig. 2.23).

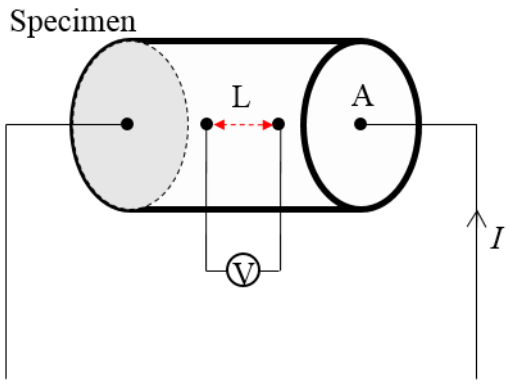

Fig. 2.23 A schematic of a resistivity measurement using a typical four-probe configuration.

The pellet samples for measuring resistivity in the QD-PPMS were prepared via high-pressure synthesis (as described in '2.1.2 High pressure high temperature solid-state synthesis'). As shown in Fig. 2.23, with the help of a conducting silver paint, two sets of copper wires with micrometre-diameters were connected to the surface of the sintered pellet. The first set of wires on either edge of the specimen are connected to the power supply to drive a current through the specimen while the second set in the middle is connected to a voltmeter to measure the voltage across the specimen. The parameters for calculating the resistivity can be expressed as *L*, the distance between the middle two wires (the second set) and *A*, the cross-section of the specimen. In contrast to the 2-probe method where one set of wires is used to measure both the voltage and current, the 4-probe method minimises errors such as the resistance contribution from the wires. The specimen with copper wires was soldered to a 'puck' before being transferred into the PPMS chamber. The temperature-dependent voltage and current measurements were then carried out in the PPMS where the temperature can be cooled to 2 K using liquid ^{4}He or 500 mK using ^{3}He.

Compared to a metal specimen where the resistivity slowly decreases upon cooling, the resistivity of an insulator or a semiconductor increases with decreasing temperature. The activation energy of a semiconductor can be determined by fitting the data of the logarithmic resistivity verse the inverse of temperature (1/*T*) using an Arrhenius expression, as defined below:

$$\rho(T) = Ae^{\frac{-E_a}{k_B T}} \tag{2.34}$$

$$\log(\rho) = \log(A) + \frac{-E_a}{k_B}\left(\frac{1}{T}\right) \tag{2.35}$$

where *A* represents the pre-exponential factor; E_a refers to the activation energy related to the bandgap of a semiconductor and k_B is the Boltzmann constant (8.617×10^{-5} eV·K^{-1}).

References

1. C. N. R. Rao and J. Gopalakrishnan, *New directions in solid state chemistry*, Cambridge University Press, 2nd ed., 1997.

2. W. Travis, E. N. K. Glover, H. Bronstein, D. O. Scanlon and R. G. Palgrave *Chem. Sci.*, 2016, **7**, 4548.

3. J. A. Rodgers, A. J. Williams and J. P. Attfield, *Z. Naturforsch*., 2006, **61b**, 1515.

4. G. Demazeau, *High Pressure Res.*, 2008, **28**, 483.

5. P.W. Bridgman, *Phys. Rev*., 1935, **48**, 825.

6. J. Loveday, *High-pressure physics*, Chapman and Hall/CRC, 2012.

7. D. Walker, M. A. Carpenter, and C. M. Hitch, Am. Mineral., 1990, **75**, 1020.

8. H. Huppertz, *Z. Kristall.*, 2004, **219**, 330.

9. W. Grochala, R. Hoffmann, J. Feng and N. W. Ashcroft, *Angew. Chem. Int. Ed*., 2007, **46**, 3620.

10. W. Klement, A. Jayaraman, and G. C. Kennedy, *Phys.l Rev.*, 1963, **131**, 632.

11. W.H. Bragg and W. L. Bragg, *Proc. R. Soc. Lond. A.*, 1913, **88**, 428.

12. Scattering of X-rays by a Collection of Electrons as in an Atom, accessed on March 14th, 2019, *http://pd.chem.ucl.ac.uk/pdnn/diff1/scaten.htm.*

13. G. E. Bacon, *Neutron diffraction*, Clarendon Press, Oxford, 3rd ed., 1975

14. Powder X-ray Diffraction Identification of an Unknown Crystalline Compound, accessed on March 14th, 2019, *https://www.monash.edu/rlo/assignment-samples/engineering/sample-engineering-lab-report.*

15. C. Hammond, *The basics of crystallography and diffraction*, International Union of Crystallography/Oxford University Press, Oxford, 2nd ed., 2001.

16. P. Willmott, *An Introduction to Synchrotron Radiation: Techniques and Applications*, Wiley-VCH, 2011.

17. Annual Review 2018/19-Diamond Light Source, accessed on March 16th, 2019, *https://www.diamond.ac.uk/Home/Corporate-Literature/Annual-Review/Review2018.html.*

18. S. P. Thompson, J. E. Parker, J. Potter, T. P. Hill, A. Birt, T. M. Cobb, F. Yuan, and C. C. Tang, Rev. Sci. Instrum., 2009, **80**, 075107.

19. I. Lommatzsch, *Experimental Facilities: Heinz Maier-Leibnitz Zentrum (MLZ)*, Technische Universität München, Forschungs-Neutronenquelle Heinz Maier-Leibnitz (FRM II), 2015.

20. M. Hoelzel, A. Senyshyn, N. Juenke, H. Boysen, W. Schmahl and H. Fuess, *Nucl. Instr. A*, 2012, **667**, 32.

21. The Institut Laue-Langevin, The Yellow Book: *Guide to neutron research facilities at the ILL*, Grenoble, 2008.

22. S. M. Bennington, A. C. Hannon and S. E. Rogers, *The ISIS Neutron and Muon Facility Neutron Training Course*, Didcot, 2006.

23. T. C. Hansen, P. F. Henry, H. E. Fischer, J. Torregrossa and P. Convert, *Meas. Sci. Technol.*, 2008, **19**, 034001.

24. The ISIS Neutron and Muon Source, *Annual Review 2018*, Didcot, 2018.

25. L. Chapon, P. Manuel, P.G. Radaelli, C. Benson, L. Perrott, S. Ansell, N.J. Rhodes, D. Raspino, D. Duxbury, E. Spill, J. Norris, *Neutron News*, 2011, **22**, 22.

26 . WISH 2014, ISIS Neutron and Muon Source accessed on March 27th, 2019, *https://twitter.com/isisneutronmuon/status/1072446281711280129.*

27. H. M. Rietveld, *J. Appl. Crystallogr.*, 1969, **2**, 65.

28. A. Le Bail, *Powder Diffr.*, 2005, **20**, 316.

29. G. Caglioti, A. Paoletti and F. P. Ricci, *Nucl. Instrum.*, 1958, **3**, 223.

30. A. C. Larson, R. B. Von Dreele. Los. Alamos National Laboratory Report LAUR, 2000, 86.

31. J. Rodriguez-Carvajal. *Physica B.*, 1993, **192**, 55.

32. J. Rodríguez-Carvajal and F. Bourée, *EPJ Web Conf.*, 2012, **22**, 00010.

33 . D. B. Litvin, Magnetic space groups, IUCr-ebook, accessed on April 4th, 2019, *https://www.iucr.org/publ/978-0-9553602-2-0.*

34 J. Rodriguez-Carvajal 2007 BASIREPS: a program for calculating irreducible representations of space groups and basis functions for axial and polar vector properties; C. Ritter, *Solid State Phenom.*, 2011, **170**, 263.

35. J. Rodriguez-Carvajal and F. Bourée, *EPJ Web of Conferences*, 2012, **22**, 00010.

36. L. Pauling, *J. Am. Chem. Soc.*, 1929, **51**, 1010.

37. L. Pauling, *J. Am. Chem. Soc.*, 1947, **69**, 542.

38. I. D. Brown and D. Altermatt, *Acta Crystallogr. B.* 1985, **41**, 244.

39. J. P. Attfield, *Solid State Sci.*, 2006, **8**, 861.

40 . I. D. Brown, *The Chemical Bond in Inorganic Chemistry. IUCr Monographs in Crystallography*, Oxford University Press. ISBN 0-19-850870-0, 2012.

41. W. G. Jenks, S. S. H. Sadeghi and J. P. Wikswo, *J. Phys. D. Appl. Phys.*, 1997, **30**, 293.

Chapter 3. Synthesis and characterisation of Dion-Jacobson $(CuCl)La_{1-x}Sr_xNb_2O_7$ perovskite solid solutions.

3.1 Introduction

In recent years, many researchers have expressed great interest in the discovery of new solid-state materials with unique structural and physical properties. Perovskite-type transition metal oxides are popular due to their magnetic, electric and transport properties arising from the spin, charge and orbital degrees of freedom.[1] One area of particular interest for perovskites is in synthesising possible layered perovskite materials consisting of $[NbO_6]$ or $[TaO_6]$ octahedral blocks with interlayers of alkali metal ions. These layers of alkali metal ions exhibit various chemical properties such as allowing ion-exchange reactions to be carried out to synthesise potential metastable phases. The family of ion exchangeable layered structures provides benefits for investigating two-dimensional (2D) physical properties for example luminescence or ionic conduction, which can be controlled by the ordered cations at the interlayer site. In this thesis, we will focus on one of the popular Dion-Jacobson (DJ) layered perovskites – $(CuCl)LaNb_2O_7$. The first crystallographic study of the layered perovskite $(CuCl)LaNb_2O_7$ was carried out by John B. Wiley's group identifying a tetragonal layered perovskite structure with the space group *P4/mmm*, which belongs to the DJ perovskite family.[2] Later in 2010, with the help of high-resolution synchrotron powder X-ray diffraction, Alexander A. Tsirlin et al.[3] reported the existence of structural phase transitions in $(CuCl)LaNb_2O_7$ and the correct room temperature crystal structure can be described as an orthorhombic superstructure with the space group *Pbam*. For this project, we examine the effect of chemical substitution of La^{3+} with Sr^{2+} on structural phase transitions and magnetic properties. This work has revealed a shift of the structural phase transition to the lower temperature region and a suppression of the magnetic transition at around 15 K.

In this chapter, (CuCl)$La_{1-x}Sr_xNb_2O_7$ solid solutions (x = 0, 0.1, and 0.2) were prepared through ion-exchange reactions with the intermediate compound $RbLa_{1-x}Sr_xNb_2O_{7-1/2x}$ which was synthesised via conventional solid-state methods. A crystallographic study of (CuCl)$La_{1-x}Sr_xNb_2O_7$ was carried out using high resolution powder X-ray diffraction at Diamond while possible magnetic structure detection was performed at the WISH neutron diffractometer at ISIS.

3.2 Background

3.2.1 Previous studies of Dion-Jacobson perovskite (CuCl)$LaNb_2O_7$

Much attention has been given to (CuCl)$LaNb_2O_7$ since it was first synthesised by John. B. Wiley et al.[2] This Cu-containing material provides numerous unusual magnetic properties because of its low spin, $S = ½$, magnetic moment of Cu^{2+} ions and its two-dimensional layered structure which results in unique quantum behaviours at low temperatures.[4] (CuCl)$LaNb_2O_7$ is a typical compound for the family of layered materials, derived from Dion-Jacobson perovskites where [NbO_6] octahedral blocks alternate with magnetic (CuCl) layers. The room temperature crystal structure of (CuCl)$LaNb_2O_7$, shown in Fig. 3.1, was previously reported to be tetragonal adopting space group *P4/mmm* with lattice parameters a = 3.8792(1) Å and c = 11.7282(3) Å.[2] Both Cu and Cl atoms in the layer site were refined to be on the 4-fold axis, forming a square lattice of Cu-Cl. Subsequently, data collected from the high-resolution powder synchrotron X-ray diffractometer (SXRD) exhibited extra superstructure reflections indicating a break of the square lattice in the CuCl layers which is attributed to the cooperative tilts of octahedra and Cu and Cl atomic displacements. The crystal structure was found to adopt a *Pbam* symmetry with an orthorhombic unit cell a = 7.76290(8) Å, b = 7.76197(7) Å and c = 11.73390(6) Å, as presented in Fig. 3.1.[3] Another two high temperature polymorphs are observed which adopt *Pbmm* symmetry in the temperature range of 500 K < T < 640 K and then the *P4/mmm* space group when the temperature is above 640 K. The *P4/mmm* phase can be described as the random displacement of Cu^{2+} and Cl^- ions from special positions (½, ½, ½) and (0, 0, ½) along the {100} directions. The displacement of Cl^- ions in the layer site was reported to be frozen upon cooling below 640 K (*Pbmm*) and the disorder of Cu^{2+} ions was further suppressed below 500 K (*Pbam*) as a result of [NbO_6] octahedral tilting.

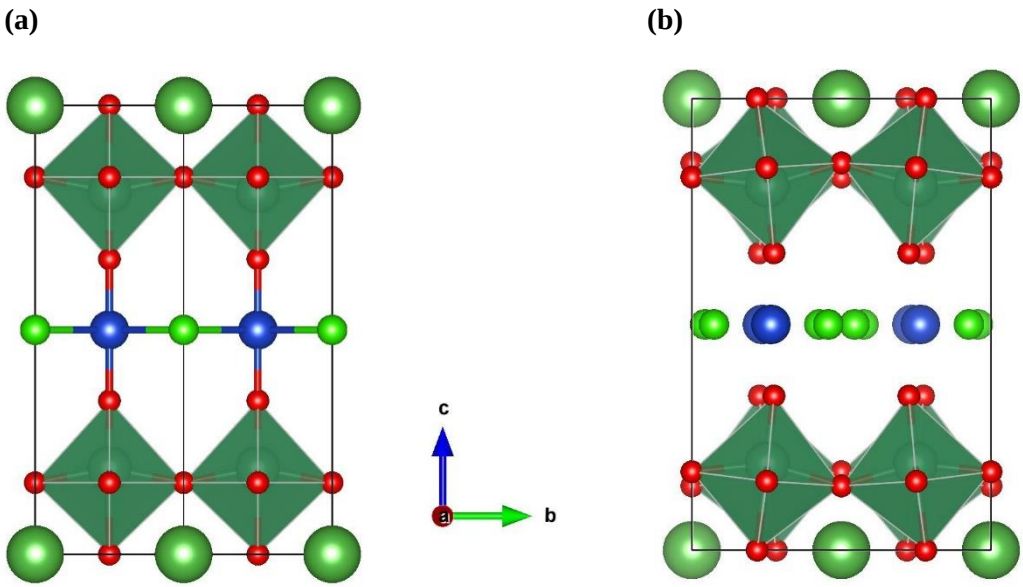

Fig 3.1. (a) High temperature tetragonal *P4/mmm* and **(b)** room temperature orthorhombic *Pbam* (right) structures of (CuCl)$LaNb_2O_7$. Blue, light green, green and red circles represent Cu ions, Cl ions, La ions and O ions, respectively. Dark green Octahedra represent [NbO_6] octahedra. Images are generated from VESTA.[5]

H. Kageyama et al. in 2005 first observed the absence of long-range magnetic order down to low temperatures in (CuCl)$LaNb_2O_7$.[6] As shown from Fig 3.2, the high temperature susceptibility displays a Curie-Weiss (CW) behaviour with a broad peak at around 16.5 K, which may be characteristic of a short-range antiferromagnetic (AFM) behaviour. The Weiss temperature θ is estimated to be –9.6 K according to CW fits of the high temperature susceptibility region. Recently A. A. Tsirlin et al. reported this magnetic behaviour as spin dimers between the Cu-Cl-Cl-Cu fourth neighbours in the interlayers.[7] The dimerization also naturally explained the observed spin-gap behaviour of (CuCl)$LaNb_2O_7$.

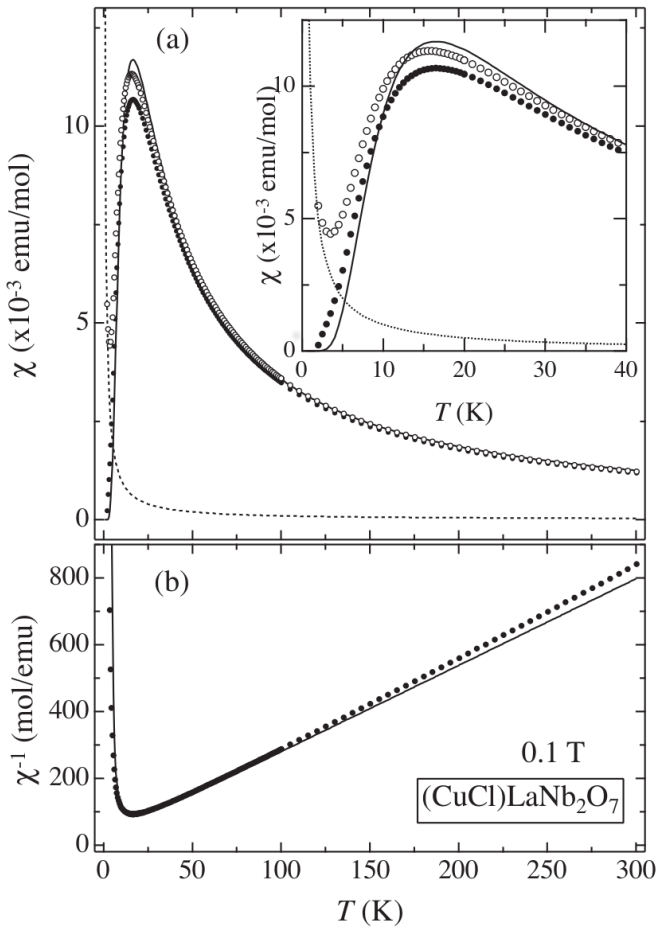

Fig. 3.2 (a) The ZFC magnetic susceptibility recorded in the temperature of 2 K < *T* < 300 K with a field of 0.1 T and **(b)** the reciprocal susceptibility of $(CuCl)LaNb_2O_7$. The open circles represent the raw susceptibility while closed cycles refers to the spin susceptibility after subtracting the impurity signal shown by Curie tail. The solid line represents the raw susceptibility data fit using S = 1/2 isolated AFM dimer model[6] and the dotted line represents the Curie term. The Inset shows the susceptibility with the selected region between 2 K and 40 K.

$(CuCl)LaNb_2O_7$ and its derivatives $(CuBr)LaNb_2O_7$ or $(CuCl)LaTa_2O_7$ have been well studied in past years. However, solid solutions of layered perovskites are less reported. In this project, the chemical substitution of La^{3+} with Sr^{2+} can be carried out due to their similar ionic radius. Nevertheless, the presence of Sr^{2+} ions in the solid solutions $(CuCl)La_{1-x}Sr_xNb_2O_7$ allows us to understand how Sr-substitution changes the superstructure and affects the structural phase transition temperatures.

3.3 Experimental

3.3.1 Synthesis of (CuCl)$La_{1-x}Sr_xNb_2O_7$

Solid solutions (CuCl)$La_{1-x}Sr_xNb_2O_7$ (x = 0, 0.1, 0.2) were synthesised using a two-step solid-state approach.[2] The first step is to prepare the intermediate compound $RbLa_{1-x}Sr_xNb_2O_{7-1/2x}$. The stoichiometric proportions of oxide reactants La_2O_3 (Alfa Aesar, 99.99%), $SrCO_3$ (Alfa Aesar, 99.99%) and Nb_2O_5 (Alfa Aesar, 99.99%) with a 20% molar excess of Rb_2CO_3 (Sigma-Aldrich, 99.8%) were ground together in an agate mortar with acetone and were then pressed into pellets using the pelletizer under 5 tons. The chemical reaction can be elucidated as below:

$$Rb_2CO_3 + La_2O_3 + SrCO_3 + Nb_2O_5 \rightarrow RbLa_{1-x}Sr_xNb_2O_7 + CO_2 \quad (3.1)$$

La_2O_3 was initially heated at 1173 K for 12 hours before weighing to allow water removal and formation of the stoichiometric oxide, as the rare earth oxides readily absorb moisture from air. The prepared pellet was then placed in an alumina crucible and preheated (the calcination process) at 1173 K for 4 hours in a box furnace in order to decompose the rubidium carbonate and strontium carbonate. Once cooled, the pellet was reground and re-pelleted and then sintered in a Lenton tube furnace for 12 h at 1373 K. The sintering process was repeated twice with intermediate grindings with the purpose of making a high purity sample. The excess of Rb_2CO_3 was added to compensate for any losses during sintering due to its volatilisation above 1173 K.

In the following step is called ion exchange reaction, the Rb^+ is exchanged with the copper halide. The synthesised intermediate compound $RbLa_{1-x}Sr_xNb_2O_7$ (x = 0, 0.1 and 0.2) was ground with a 3-fold molar excess of anhydrous reactant $CuCl_2$ (Alfa Aesar, 99.995%) and then the mixture was pressed into a pellet with a hand press and loaded into a Pyrex tube. Adding an excess of $CuCl_2$ during the synthesis is to guarantee the ion-exchange reaction can be accomplished. This whole procedure was carried out in an argon-filled glove box in order to minimise air exposure. The next step is to evacuate the Pyrex tube using the Schlenk line. Finally, the tube was sealed using a propane flame and was sintered in a box furnace at 673 K for 5 days. The annealed product, a light green pellet, was ground into fine powder and washed with distilled water to eliminate any excess copper chloride and the by-product rubidium

chloride, followed by drying overnight at 393 K. The ion-exchange chemical reaction can be elucidated as below:

$$RbLa_{1-x}Sr_xNb_2O_7 + CuCl_2 \rightarrow (CuCl)La_{1-x}Sr_xNb_2O_7 + RbCl \quad (3.2)$$

3.3.2 X-ray powder diffraction

3.3.2.1 In house X-ray diffraction

Initial laboratory X-ray patterns of $RbLa_{1-x}Sr_xNb_2O_{7-}$ and $(CuCl)La_{1-x}Sr_xNb_2O_7$ (x = 0, 0.1, 0.2) solid solutions were collected using a Bruker D2 Phaser diffractometer, with a Cu K_α/K_β radiation source of wavelength λ_{K_α} = 1.54050 Å. The profile for the measurement was set to a 15 minutes scan with an angle range of $5^\circ \leq 2\theta \leq 70^\circ$ and a step size of 0.1° and a counting time of 2s per step. The preliminary X-ray data were checked by using the EVA software and the ICSD database to identify the presence of the target phase along with any possible impurities.[8-9] Rietveld refinement for the sample characterisation was then carried out using GSAS[10] software with EXPGUI[11] and then Visualisation for Electronic and Structural Analysis (VESTA)[5] software was employed for visualising the crystallographic structures obtained from the Rietveld refinements. X-ray diffraction was performed on compounds after each cycle of heating to ensure the intermediate phase purity.

3.3.2.2 Synchrotron X-ray diffraction

High resolution synchrotron powder X-ray diffraction patterns were collected for all $(CuCl)La_{1-x}Sr_xNb_2O_7$ (x = 0, 0.1 and 0.2) compounds to characterise the crystallographic structures using the I11 beamline at the Diamond Light Source (Oxfordshire, UK). Each sample was loaded into a quartz capillary with a diameter of 0.3 mm and then the measurements were made on warming from 298.15 K to 703.15 K, using a hot air blower. Data were collected using 5 arms of multi-analysing crystal-detectors (MACs) for 45 minutes for each pattern in the angle region of $3^\circ < 2\theta < 150^\circ$ at several intermediate temperature points (Table 3.1). A position sensitive detector (PSD) for fast data collection (1s per pattern) was also used over a range of temperature 298.15 K < T < 703.15 K with intervals of 5 K. The radiation energy of

the different detectors was set to 15 keV (λ = 0.82660 Å). Rietveld fits of these patterns were carried out with the FullProf software package.[12]

Table 3.1 A list of temperature points selected for collecting SXRD data for (CuCl)$La_{1-x}Sr_xNb_2O_7$. The multi-analysing crystal-detectors (MACs) was used.

x	0	0.1	0.2
Temperature points (K)	298.15, 373.15, 443.15, 458.15, 468.15, 483.15, 523.15, 548.15, 573.15, 593.15, 603.15, 618.15, 633.15, 703.15	298.15, 373.15, 443.15, 458.15, 468.15, 483.15, 523.15, 548.15, 573.15, 593.15, 603.15, 618.15, 633.15, 703.15	298.15, 323.15, 373.15, 423.15, 458.15, 498.15, 523.15, 548.15, 573.15, 593.15, 703.15

3.3.3 Neutron powder diffraction

Neutron powder diffraction data were collected for x = 0, 0.15 and 0.2 and using the time of flight (T.O.F.) WISH beamline at the ISIS Neutron Facility (Oxfordshire, UK). Approximately 0.6 g of each composition was loaded into a sealed cylindrical vanadium can and then transferred into a helium cryostat. Data were collected as follows: for x = 0 at 1.5 K (150 mins), 20 K (120 mins) 50 K (30 mins) and 100 K (20 mins), for x = 0.15 at 1.5 K (360 mins) and 10 K (360 mins) and for x = 0.2 at 1.5 (120 mins) and the 30 mins scans from 3 K to 10 K with intervals of 1 K. Rietveld analysis of all the neutron diffraction patterns was carried out using the FullProf Suite.[12]

3.3.4 Magnetic studies

Magnetic susceptibility measurements were carried out using a Quantum Design Physical Property Measurement System (QD-PPMS) for (CuCl)$La_{1-x}Sr_xNb_2O_7$ (x = 0, 0.1 and 0.2). Around 50 mg of each (CuCl)$La_{1-x}Sr_xNb_2O_7$ compound was placed in a gelatine capsule which was then inserted into a straw and loaded into the chamber. The zero-field cooling (ZFC) and field cooling (FC) DC magnetisation measurements were recorded on warming over the temperature region of 2 K < T < 300 K under a magnetic field of 0.3 Tesla. The data were analysed and plotted through Origin software.[13]

3.4 Experimental results

Based on the successfully prepared intermediate compounds $RbLa_{1-x}Sr_xNb_2O_7$ (x = 0.1 and 0.2), two samples of $(CuCl)La_{0.9}Sr_{0.1}Nb_2O_7$ and $(CuCl)La_{0.8}Sr_{0.2}Nb_2O_7$ were synthesised via the additional ion-exchange approach as mentioned above. The precursor Rb-based DJ layered perovskite was found to be white in colour whereas the two Cu oxychloride layered perovskites were observed to be light green, as shown in Fig. 3.3.

Fig. 3.3 Powder samples of white $RbLa_{1-x}Sr_xNb_2O_7$ (x=0.1) and green $(CuCl)La_{1-x}Sr_xNb_2O_7$ (x = 0.1).

3.4.1 In house X-ray diffraction analysis

3.4.1.1 Intermediate compound $RbLa_{1-x}Sr_xNb_2O_7$

The preliminary room temperature XRD structure of $RbLa_{1-x}Sr_xNb_2O_7$ (x = 0, 0.1 and 0.2) polycrystalline samples were refined using the Rietveld Method.[14] Rietveld powder data fitting analysis was conducted over a 2θ range between 7˚ and 60˚ using the GSAS software.[10] The following parameters were refined and converged: lattice parameters for each phase, background fitted using equidistant experimental points and modelled by interpolation, scale factors, atom coordinates, phase fractions, and the peak shape parameters *U*, *V*, *W*, *Y* using a pseudo-Voigt function. The thermal parameters B of the cations and anions in $RbLa_{1-x}Sr_xNb_2O_7$ were constrained to have identical values. This is because data collected with the D2 lab X-ray diffractometer cannot provide very accurate atomic positions, especially for light atoms like oxygen.

The refinement patterns of $RbLa_{1-x}Sr_xNb_2O_7$ are shown in Fig. 3.4. No secondary phases were observed and this indicates Sr was successfully introduced into the structure. As shown in Fig. 3.5, $RbLa_{1-x}Sr_xNb_2O_7$ (x = 0, 0.1 and 0.2) all adopt an orthorhombic *Imma* structure with layers of $[RbO_8]$ hexahedra. $[NbO_6]$ and $[LaO_{10}]$ form block units which makes this layered structure a good candidate for an ion-exchange reaction. Rb^+ cations in the layer can be stoichiometrically ion-exchanged with many units, such as $[CuCl]^+$ here, to form new DJ perovskites. The refined value of the Sr-site occupancy was 0.062(1) (x = 0.1) and 0.173(2) (x = 0.2). The refined value of the Rb occupancy was close to 1. A small oxygen deficiency could help to balance the charge difference between Sr^{2+} and La^{3+}. However, determining oxygen occupancy by structural refinement is very challenging with laboratory X-ray data. Further advanced methods, especially neutron diffraction, would be useful to accurately determine such an oxygen deficiency. Crystallographic data and selected bond distances are listed in Table 3.2 and Table 3.3. The smaller calculated valences of the La and Nb ions may due to the inaccurate oxygen positions from the laboratory XRD results. Further neutron diffraction is needed to confirm the accurate oxygen positions and cation valences. The detailed information such as atomic positions, B_{iso} and occupancy can be found in Appendix A.

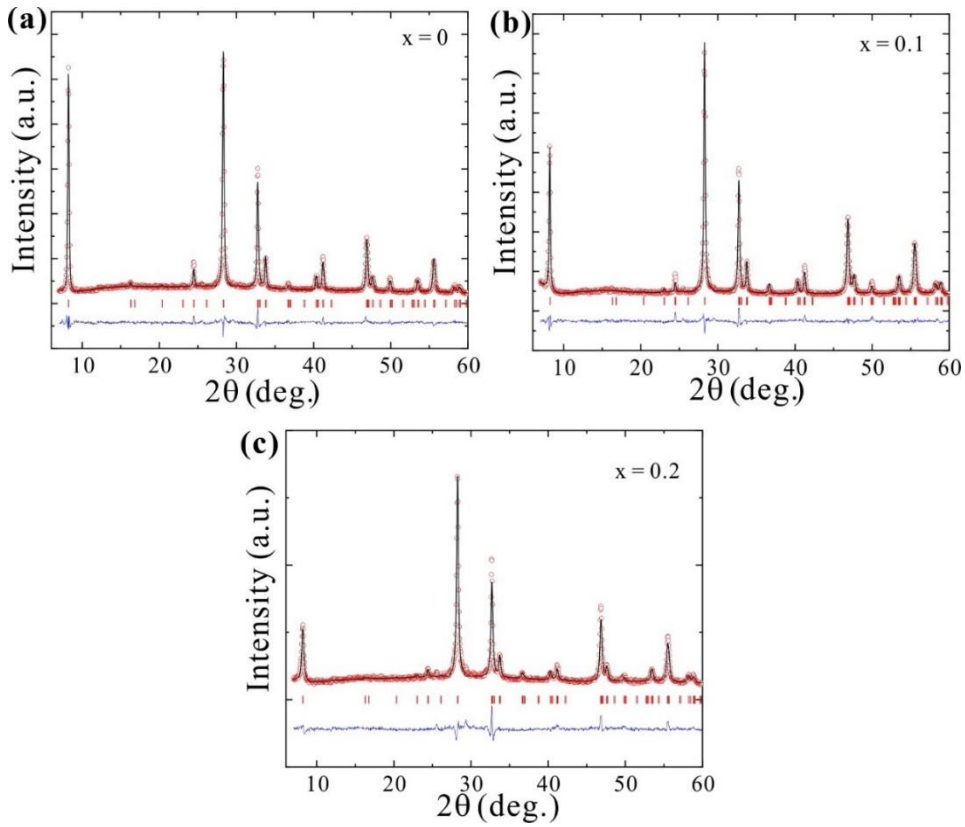

Fig. 3.4 (a), **(b)**, **(c)** The observed (red circle) calculated (black line) Rietveld fits of the room temperature XRD patterns of $RbLa_{1-x}Sr_xNb_2O_7$ (x = 0, 0.1, 0.2, respectively) compounds.

(a) **(b)**

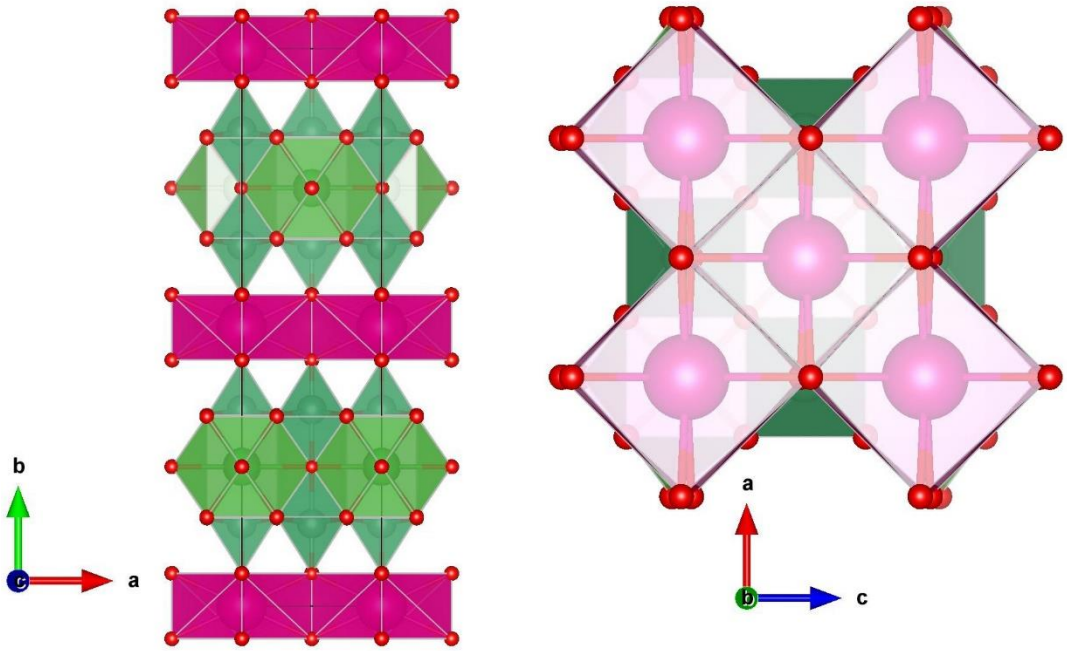

Fig. 3.5 Polyhedral representation of the $RbLa_{0.9}Sr_{0.1}Nb_2O_{7-\delta}$ along **(a)** *b*-axis and **(b)** *a*-axis. It adopted orthorhombic *Imma* crystal structure with layers of [RbO_8] hexahedra. Rb, La/Sr, Nb and O atoms are shown in pink, green, dark green and red.

Table 3.2 Crystallographic data and refined parameters for $RbLa_{1-x}Sr_xNb_2O_7$

x	Space group	N. of formula unit	Unit cell (Å)	Density(g/cm^3)	Cell Vol. (Å^3)	χ^2 / R_{wp}(%)
0	*Imma*	4	*a* = 5.4983(2) *b* = 21.994(3) *c* = 5.4976(2)	5.217(3)	664.8(1)	4.9 / 7.5
0.1	*Imma*	4	*a* = 5.5071(2) *b* = 21.983(2) *c* = 5.5062(2)	5.156(2)	666.6(1)	3.6 / 5.4
0.2	*Imma*	4	*a* = 5.5020(1) *b* = 21.989(1) *c* = 5.5071(3)	2.294(2)	666.3(1)	3.9 / 7.1

Table 3.3 Selected metal-anion bond distances for $RbLa_{1-x}Sr_xNb_2O_7$.

	x =0	x = 0.1	x = 0.2
Rb-O2 x2 (Å)	3.44(6)	3.14(4)	3.10(2)
Rb-O2 x2 (Å)	2.72(2)	2.93(3)	2.91(2)
Rb-O2 x4 (Å)	3.09(1)	3.04(2)	3.04(2)
BVS Rb	1.09(6)	1.01(3)	1.04(2)
La-O1 x1 (Å)	2.43(8)	2.50(7)	2.47(7)
La-O1 x2 (Å)	2.75(1)	2.78(1)	2.78(1)
La-O3 x4 (Å)	2.69(6)	2.81(1)	2.87(8)
La-O4 x4 (Å)	2.69(6)	2.67(2)	2.61(7)
BVS La	2.78(6)	2.69(6)	2.61(7)
Nb-O1 x1 (Å)	2.20(1)	2.27(1)	2.31(1)
Nb-O2 x1 (Å)	2.00(3)	1.96(3)	1.94(4)
Nb-O3 x2 (Å)	1.94(2)	1.99(4)	1.98(4)
Nb-O4 x2 (Å)	2.00(3)	1.93(4)	1.99(4)
BVS Nb	4.66(3)	4.77(4)	4.53(4)

3.4.1.2 DJ perovskite $(CuCl)La_{1-x}Sr_xNb_2O_7$

The preliminary room temperature XRD structure of $(CuCl)La_{1-x}Sr_xNb_2O_7$ (x = 0, 0.1 and 0.2) polycrystalline samples calcined at 673 K were refined using the Rietveld Method. The tetragonal space group *P4/mmm* of $(CuCl)LaNb_2O_7$ was used as the starting refinement model.[2] As shown in Fig. 3.6 of the refinement results, the calculated tetragonal model fits well with the experimental data. During the refinement, the (0 0 l) preferred orientation correction was employed to improve the Rietveld fit, probably resulting from the formation of the relatively large plate-like grains. The refined parameters including χ^2 and R_w factors are presented in Table 3.4. These preliminary in house X-ray diffraction results indicate the solid solutions of the Dion-Jacobson layered perovskites $(CuCl)La_{1-x}Sr_xNb_2O_7$ were successfully synthesised, however high resolution synchrotron and neutron techniques are required to fully understand the accurate crystal structure, especially the oxygen positions and the potential cation displacements.

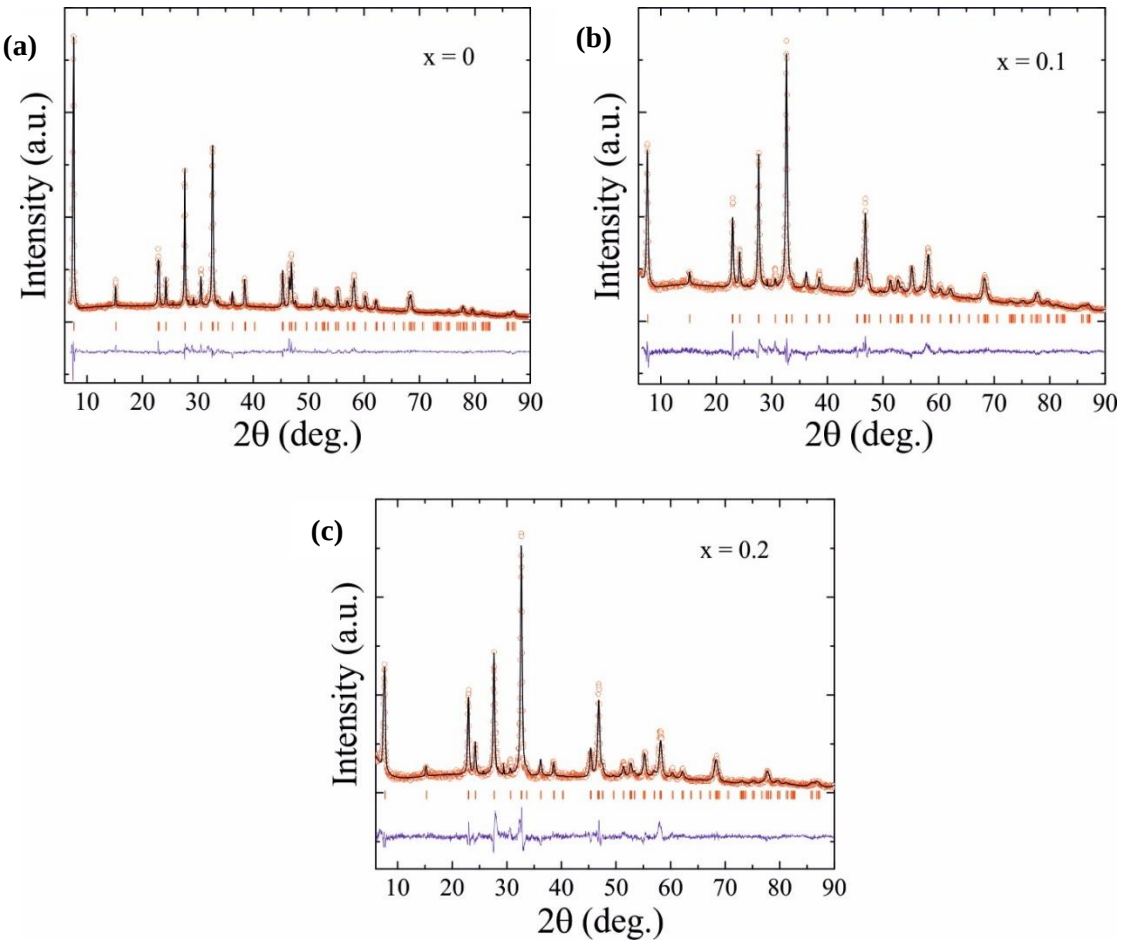

Fig. 3.6 (a), **(b)**, **(c)** The observed (red circle) and calculated (black line) Rietveld fits of the room temperature XRD patterns of the DJ $(CuCl)La_{1-x}Sr_xNb_2O_7$ (x = 0, 0.1 , 0.2, respectively) compounds. Data was collected from 7˚.

Table 3.4 Crystallographic data and refined parameters for $(CuCl)La_{1-x}Sr_xNb_2O_7$

$(CuCl)La_{1-x}Sr_xNb_2O_7$	Space group	Unit cell (Å)	Cell Vol. (Å^3)	χ^2 / R_{wp}(%)
x = 0	*P4/mmm*	*a* = 3.8808(1) *c* = 11.732(1)	176.68(2)	4.8 / 6.9
x = 0.1	*P4/mmm*	*a* = 3.8848(2) *c* = 11.704(2)	176.63(4)	3.0 / 6.1
x = 0.2	*P4/mmm*	*a* = 3.8873(4) *c* = 11.705(3)	176.88(6)	2.6 / 11.7

3.4.2 Synchrotron X-ray diffraction & neutron diffraction study

As mentioned above, by using high resolution synchrotron X-ray diffraction in 2010, Tsirlin et al. reported that there are 3 polymorphs of $(CuCl)LaNb_2O_7$ and the room temperature structure does not adopt *P4/mmm* symmetry but forms a superstructure in space group *Pbam*.[3] The very

weak superstructure reflections were not observed in our preliminary in house XRD and this is possibly due to the power limitation of the benchtop diffractometer.

The experimental, calculated and difference SXRD patterns for $(CuCl)La_{1-x}Sr_xNb_2O_7$ (x = 0, 0.1 and 0.2) collected at room temperature are presented in Fig. 3.7. Rietveld powder data fitting analysis was conducted over a 2θ range between 5˚ and 50˚ using the FullProf software package.[15] A secondary phase, CuCl (6%), was observed in the x = 0.2 compound. The following parameters were refined and converged: lattice parameters for each phase, background fitted using equidistant experimental points and modelled by interpolation, scale factors, atom coordinates, phase fractions, and the peak shape parameters *U*, *V*, *W*, *Y* using a Thompson-Cox-Hastings pseudo-Voigt function (Npr 7). The thermal parameters B of all cations and anions of $(CuCl)La_{1-x}Sr_xNb_2O_7$ were constrained to have an identical value. This was done because the refinement could not be converged when attempted with different thermal parameters for the cations and anions. The refined Sr-site occupancy was 0.122(1) (x = 0.1) and 0.190(2) (x = 0.2), which improved the goodness-of-fit, while the all the other site occupancies were fixed to 1 as no significant vacancy concentration was found. Individual oxygen occupancy refinement was unsuccessfully attempted as the x-rays are very hard to distinguish very small oxygen deficiency. Therefore all the oxygen sites were fixed to 1 as well. The refinement and crystallographic data including atomic coordinates are given in Table 3.5 and Table 3.6, while the representative interatomic distances and BVS calculations are listed in Table 3.7. The high symmetry *P4/mmm* structure used for the laboratory X-ray diffraction analysis was chosen as the starting model. However, the additional small reflections which appeared at 2θ = 9.5°, 13.6° and 14.2° could not be fitted, resulting in very large R factors and therefore the room temperature *Pbam* superstructure reported by A. A. Tsirlin was used for carrying out the Rietveld refinement and the additional reflections were successfully fitted[3] and it confirmed that the $(CuCl)La_{1-x}Sr_xNb_2O_7$ layered perovskites adopt the orthorhombic *Pbam* superstructure.

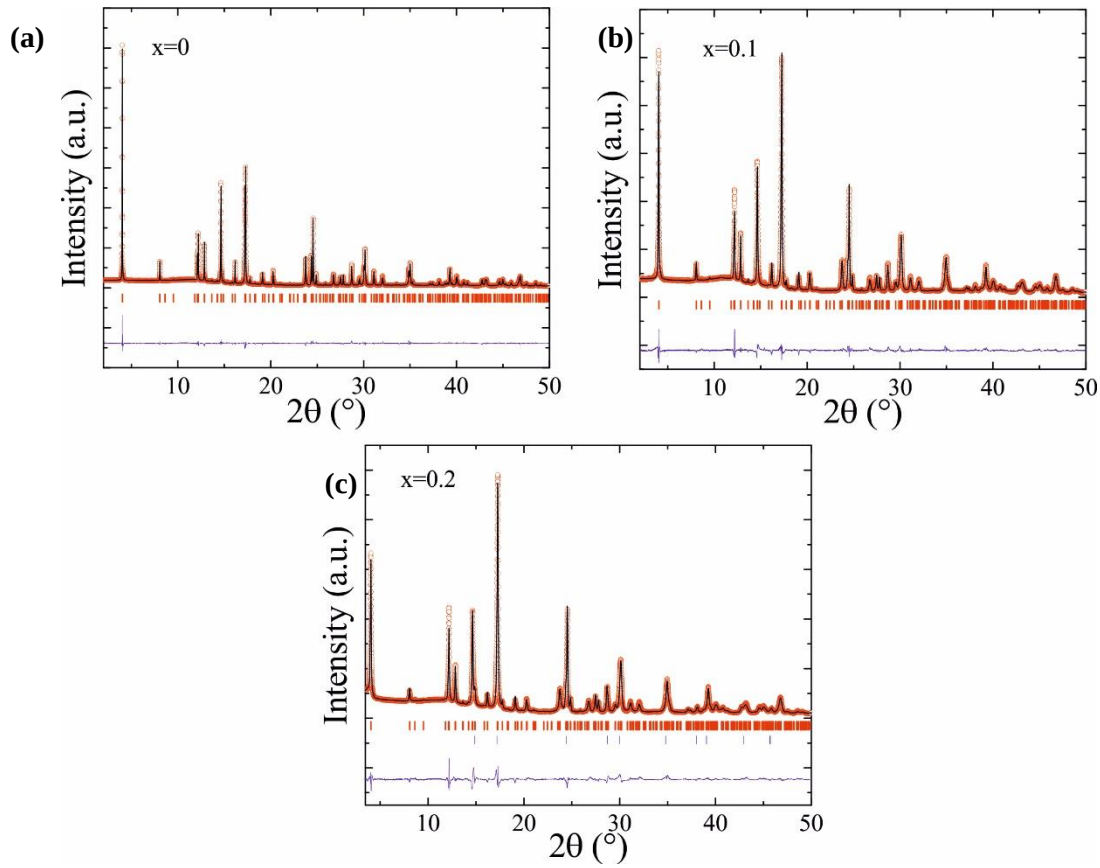

Fig. 3.7 (a), **(b)**, **(c)** Room temperature SXRD patterns for (CuCl)$La_{1-x}Sr_xNb_2O_7$ (x = 0, 0.1, 0.2 respectively). All of them adopted *Pbam* orthorhombic structure. The blue tick marks in the x = 0.2 pattern refer to the secondary phase $CuCl_2$.

Table 3.5 Refinement data for (CuCl)$La_{1-x}Sr_xNb_2O_7$ (x = 0, 0.1, 0.2) from the SXRD Rietveld fit at 300 K. All compounds adopt in orthorhombic *Pbam* space group.

x	Lattice parameters (Å)	Cell volume (Å^3)	N. of formula unit	Density (g / mol)	*R*-factors (%)	χ^2
0	*a* = 7.7723(1) *b* = 7.7717(1) *c* = 11.7501(1)	709.75(1)	4	5.014(1)	R_p=3.36 R_{wp}=4.39 R_B=4.88 R_F=4.84	5.88
0.1	*a* = 7.7807(2) *b* = 7.7826(2) *c* = 11.7385(2)	710.82(3)	4	4.947(2)	R_p=4.03 R_{wp}=5.43 R_B=4.19 R_F=5.50	9.16
0.2	*a* = 7.7889(2) *b* = 7.7756(1) *c* = 11.7359(3)	710.77(3)	4	4.915(2)	R_p=4.60 R_{wp}=6.15 R_B=4.32 R_F=3.99	11.7

Table 3.6 Crystallographic details for $(CuCl)La_{1-x}Sr_xNb_2O_7$ (x = 0, 0.1, 0.2) from the SXRD Rietveld fit at 300 K.

	Atom	Wyckoff	x	y	z	Occupancy	B_{iso}/Å^2
x = 0	Cu	4*h*	0.73115(3)	0.51451(5)	0.5	1.0	0.02(1)
	Cl	4*h*	0.5677(4)	0.236(1)	0.5	1.0	0.02(1)
	La	4*g*	0.0007(4)	0.2535(3)	0	1.0	0.02(1)
	Nb	8*i*	0.7505(2)	0.4986(2)	0.80861(4)	1.0	0.02(1)
	O1	4*f*	0	0.5	0.827(1)	1.0	0.02(1)
	O2	8*i*	0.265(3)	0.770(3)	0.870(1)	1.0	0.02(1)
	O3	8*i*	0.262(1)	0.004(2)	0.6603(3)	1.0	0.02(1)
	O4	4*g*	0.766(1)	0.5011(5)	0	1.0	0.02(1)
	O5	4*e*	0	0	0.844(1)	1.0	0.02(1)
x = 0.1	Cu	4*h*	0.7706(2)	0.5041(8)	0.5	1.0	0.02(1)
	Cl	4*h*	0.5645(5)	0.243(3)	0.5	1.0	0.02(1)
	La/Sr	4*g*	0.0009(3)	0.2490(5)	0	0.878(1)/0.122(1)	0.02(1)
	Nb	8*i*	0.7510(3)	0.5	0.80964(6)	1.0	0.02(1)
	O1	4*f*	0	0.5	0.802(1)	1.0	0.02(1)
	O2	8*i*	0.263(2)	0.759(2)	0.861(1)	1.0	0.02(1)
	O3	8*i*	0.246(2)	0.0023(4)	0.6564(4)	1.0	0.02(1)
	O4	4*g*	0.747(1)	0.505(3)	0	1.0	0.02(1)
	O5	4*e*	0	0	0.838(2)	1.0	0.02(1)
x = 0.2	Cu	4*h*	0.7347(7)	0.491(1)	0.5	1.0	0.024(3)
	Cl	4*h*	0.5631(8)	0.225(2)	0.5	1.0	0.024(3)
	La/Sr	4*g*	-0.0005(6)	0.2512(6)	0	0.810(2)/0.190(2)	0.024(3)
	Nb	8*i*	0.7502(5)	0.5	0.8116(1)	1.0	0.024(3)
	O1	4*f*	0	0.5	0.769(1)	1.0	0.024(3)
	O2	8*i*	0.265(2)	0.7513(5)	0.869(1)	1.0	0.024(3)
	O3	8*i*	0.246(3)	-0.0016(5)	0.6545(5)	1.0	0.024(3)
	O4	4*g*	0.7450(5)	0.4963(1)	0	1.0	0.024(3)
	O5	4*e*	0	0	0.837(2)	1.0	0.024(3)

Table 3.7 The Metal-anion bond distances, nearest metal-metal distance and BVS calculation. Cu^{2+} ions bond with two O^{2-} and two Cl^- ions forming $[CuCl_2O_2]$ plaquettes.

Pbam 300K	x =0	x = 0.1	x = 0.2
Cu-O3 x2 (Å)	1.904(4)	1.847(5)	1.817(6)
Cu-Cl (Å)	2.512(7)	2.590(2)	2.41(1)
Cu-Cl (Å)	2.324(7)	2.260(3)	2.26(1)
Cu-BVS	1.76(1)	1.97(1)	2.01(1)
La-O2 x2 (Å)	2.37(2)	2.45(1)	2.40(2)
La-O2 x2 (Å)	2.58(3)	2.62(1)	2.58(2)
La-O4 x1 (Å)	2.66(1)	2.74(3)	2.73(1)
La-O4 x1 (Å)	2.85(1)	2.75(3)	2.75(1)
La-O4 x1 (Å)	2.64(1)	2.71(3)	2.75(1)
La-O4 x1 (Å)	2.86(1)	2.80(3)	2.80(1)
La-O5 x2 (Å)	2.70(1)	2.71(2)	2.72(2)
La-BVS	3.03(2)	2.99(3)	3.11(2)
Nb-O1 x1 (Å)	1.951(3)	1.939(3)	2.01(1)
Nb-O2 x1 (Å)	1.94(3)	1.97(2)	2.02(1)
Nb-O2 x1 (Å)	2.21(3)	2.11(1)	2.06(1)
Nb-O3 x1 (Å)	1.745(4)	1.79(1)	1.81(1)
Nb-O4 x1 (Å)	2.252(1)	2.235(1)	2.211(1)
Nb-O5 x1 (Å)	1.989(3)	1.981(5)	1.972(6)
Nb-BVS	5.04(2)	4.97(2)	4.82(1)
Cu-Cu (Å)	3.602(1)	3.776(3)	3.659(1)
Nb-Nb (Å)	3.885(1)	3.875(3)	3.887(1)
La-La (Å)	3.886(1)	3.904(3)	3.895(1)

As shown in Fig. 3.8 for the crystal structure of $(CuCl)La_{1-x}Sr_xNb_2O_7$ (x = 0.1 as an example), the intermediate layer is not constructed by the Cu-Cl square lattice but the Cu-Cl zig-zag chains, resulting from the displacements of Cu^{2+} and Cl^- ions from (½, ½, ½) and (0, 0, ½) to (x, y, ½). The four coordinated Cu^{2+} cations, bridging the apical oxygen anions from the $[NbO_6]$ octahedra and connecting with 2 Cl^- ions in the (CuCl) plane, forms corner shared $[CuCl_2O_2]$ plaquettes. On the other hand, Nb^{5+} ions are octahedrally coordinated, forming corner-sharing $[NbO_6]$ slabs which act as nonmagnetic perovskite blocks sandwiching the magnetic (CuCl) layer and therefore result in a potential formation of a 2D magnetic structure. $[NbO_6]$ octahedra are tilted around the *b* axis in the structure while $[CuCl_2O_2]$ plaquettes align along the *b* axis as well, resulting in the Glazer tilt notation of the crystal structure to be $a^0b^-c^0$. The Sr^{2+} ions are localised well in the La^{3+} atomic position and the refined occupancy can be found in Table 3.6.

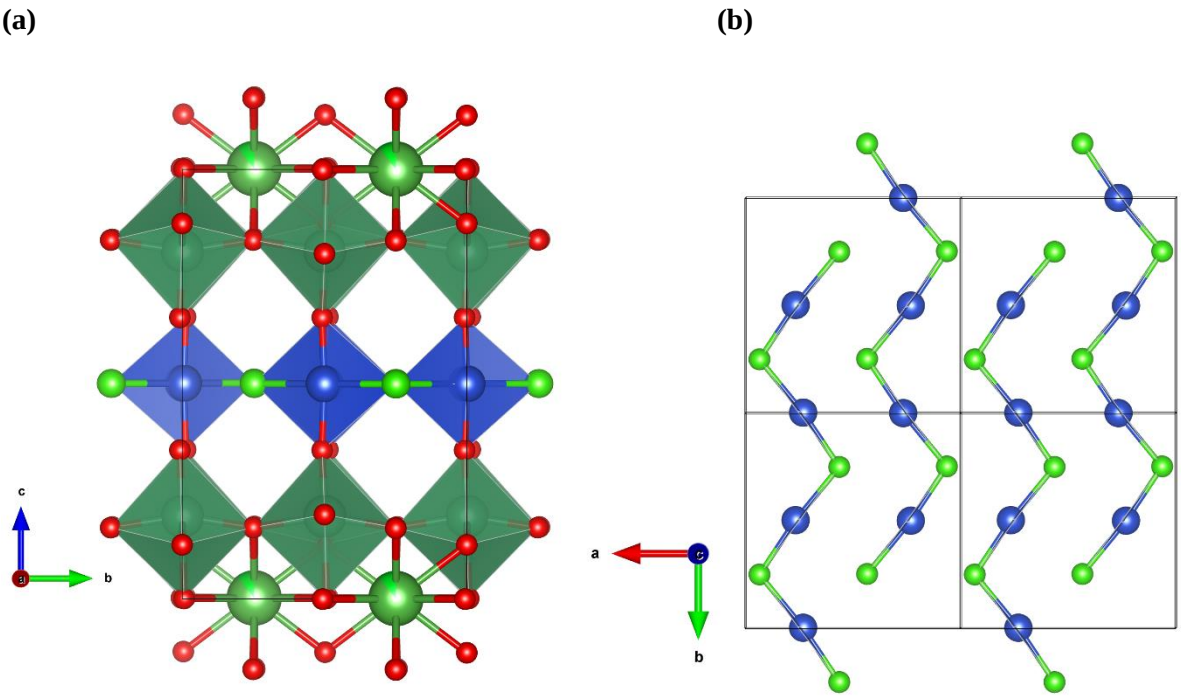

Fig. 3.8 (a) Polyhedral representation of the (CuCl)$La_{0.9}Sr_{0.1}Nb_2O_7$ orthorhombic *Pbam* crystal structure with [NbO_6] octahedra and [$CuCl_2O_2$] plaquette. **(b)** Four unit cells of zig-zag (CuCl) array within the interlayer. Cu, Cl, La/Sr, Nb and O atoms are shown in blue, light green, green, dark green and red. Image generated using VESTA.[5]

The evolution of the superstructure of (CuCl)$La_{1-x}Sr_xNb_2O_7$ was investigated by thermal SXRD above room temperature. Using the patterns at several selected temperatures, the high temperature polymorphs that adopt the *Pbmm* and *P4/mmm* structures are obtained for all the solid solutions, as shown in Appendix A. The high temperature tetragonal phase (> 598 K, x = 0.1), with no additional superstructure reflections, can be simply written as $a_{sub} \times a_{sub} \times c_{sub}$. The superstructure reflections that appeared between 448 K and 598 K can be identified with the propagation vector [0 ½ 0], leading to the unit cell expression $a_{sub} \times 2a_{sub} \times c_{sub}$ for the *Pbmm* structure. The other orthorhombic polymorph *Pbam* exhibits extra reflections below 448 K, which can be identified using the [½ 0 0] propagation vector, resulting in the unit cell expression $2a_{sub} \times 2a_{sub} \times c_{sub}$. Plots of the refined lattice parameters and unit cell volumes from the PSD synchrotron data as a function of temperature are shown in Fig. 3.9, Fig. 3.10 and Fig. 3.11. Heat maps (Fig.3.12 and Fig.3.13) of (CuCl)$La_{1-x}Sr_xNb_2O_7$ show that the superstructure peaks for *Pbam* → *Pbmm* and → *P4/mmm* are vanished near the corresponding transition temperature regions.

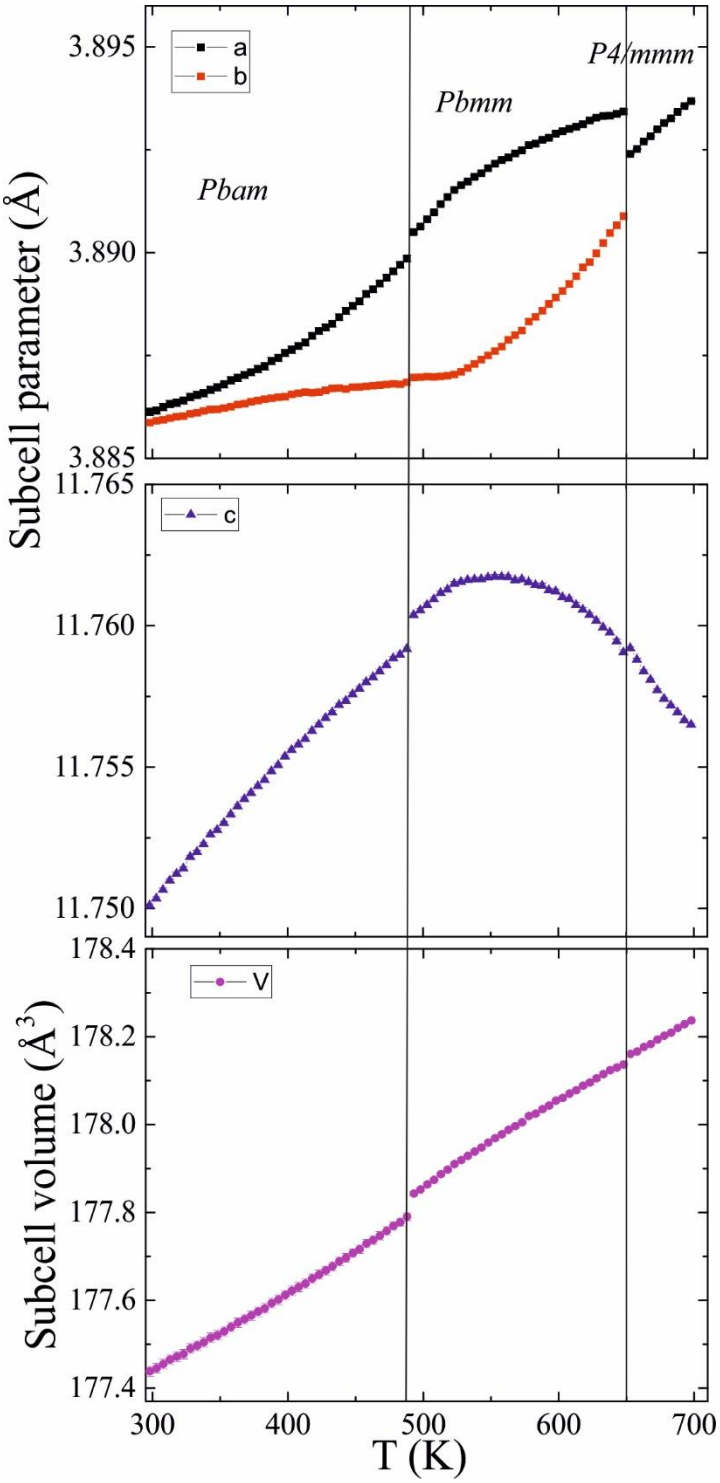

Fig. 3.9 The subcell lattice parameters and the corresponding cell volume of the reference sample (CuCl)$LaNb_2O_7$ as a function of temperature. The error bars are smaller than the marker size.

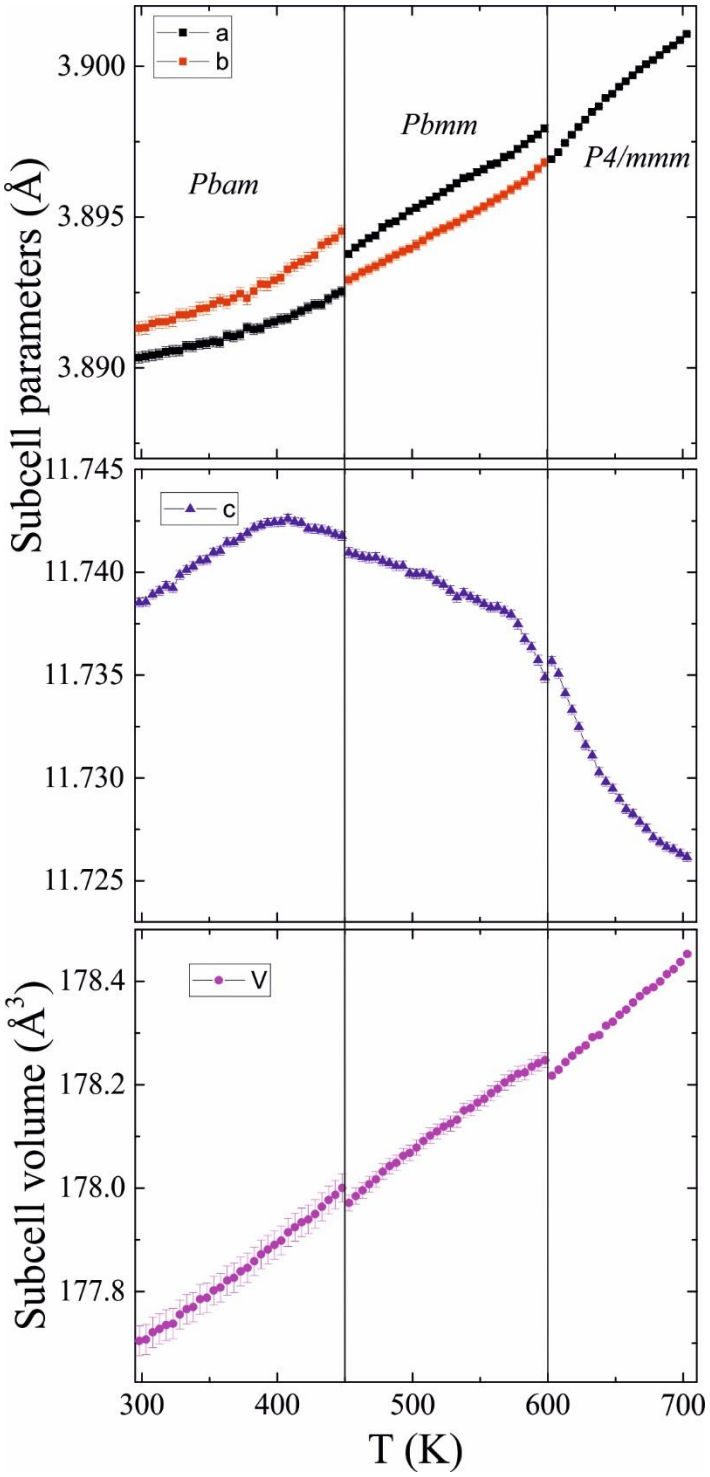

Fig. 3.10 The subcell lattice parameters and the corresponding cell volume of the $(CuCl)La_{1-x}Sr_xNb_2O_{7-1/2x}$ with x = 0.1, as a function of temperature.

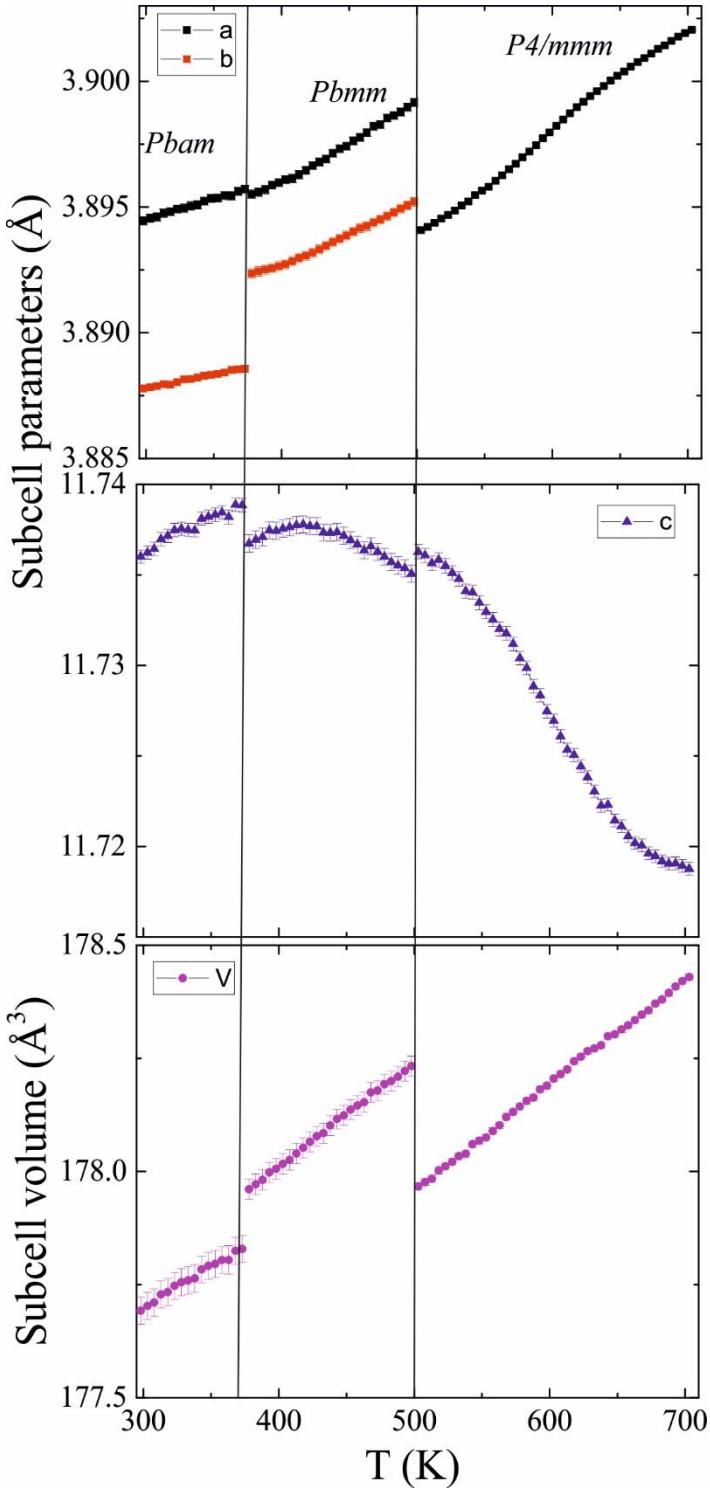

Fig. 3.11 The subcell lattice parameters and the corresponding cell volume of the $(CuCl)La_{1-x}Sr_xNb_2O_{7-1/2x}$ with x = 0.2 as a function of temperature.

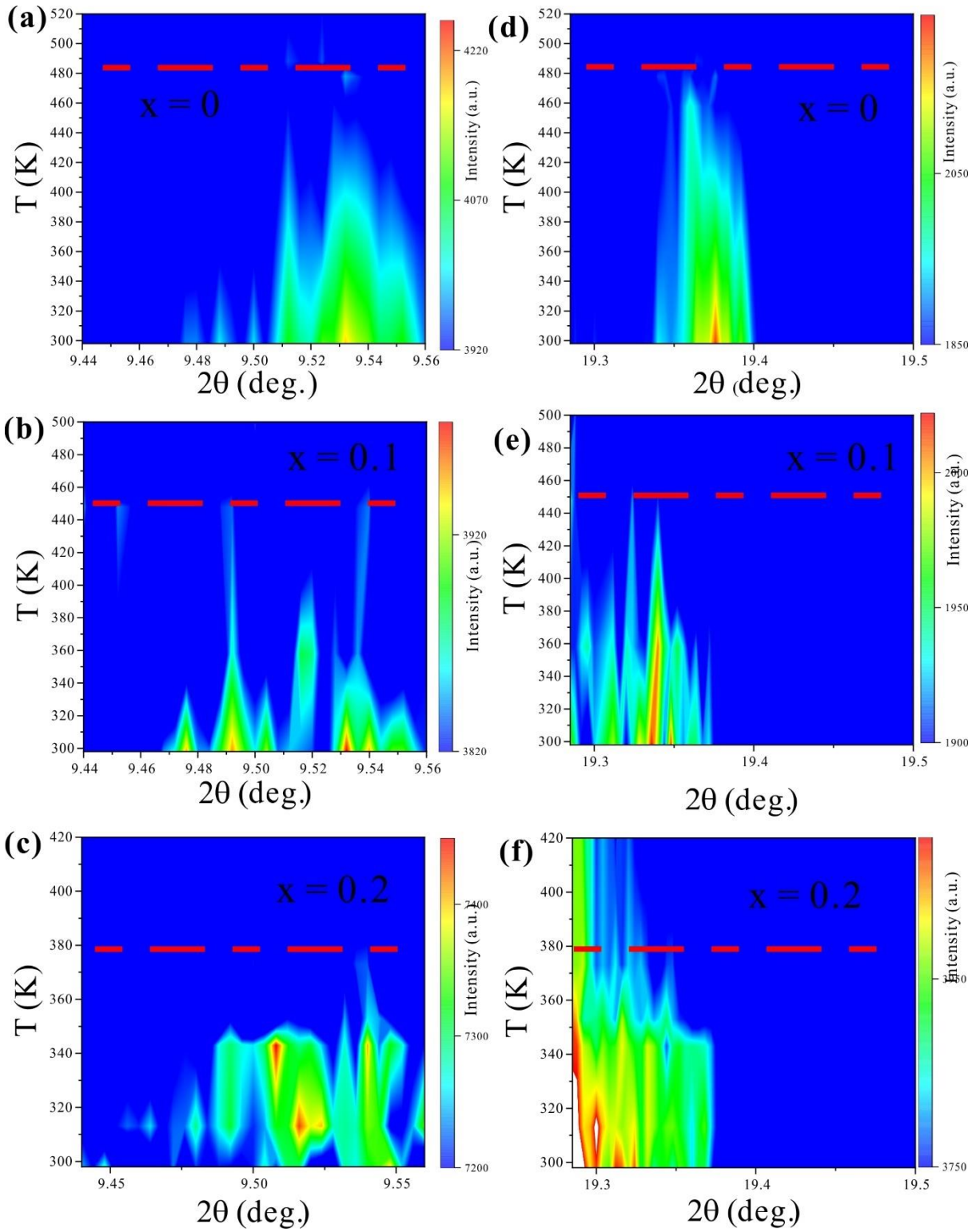

Fig. 3.12 *Pbam* → *Pbmm* heat map of (CuCl)$La_{1-x}Sr_xNb_2O_7$ showing the selected **(a)**, **(b)**, **(c)** *Pbam* superstructure reflection (1 1 1) and **(d)**, **(e)**, **(f)** *Pbam* superstructure reflection (1 3 0) vanished at 488 K, 448 K, 373 K for x = 0, 0.1, 0.2, respectively.

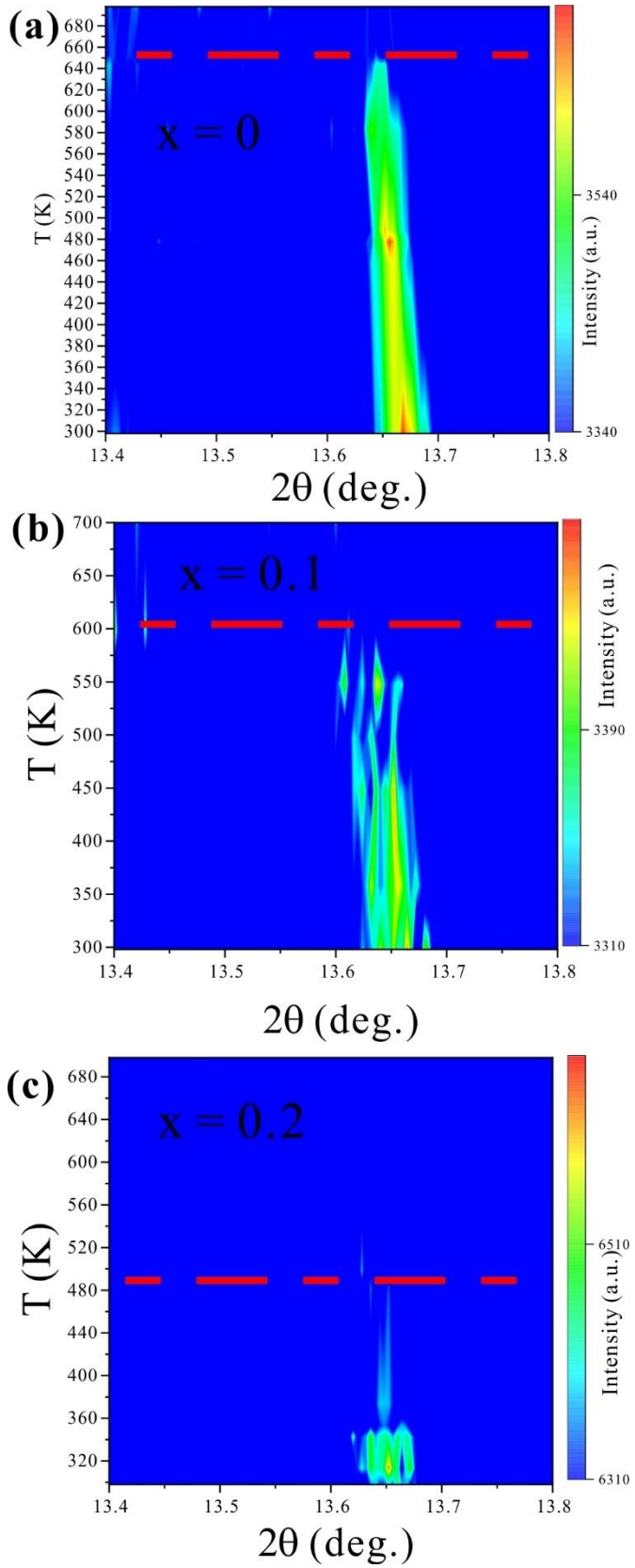

Fig. 3.13 *Pbmm* → *P4/mmm* heat map of (CuCl)$La_{1-x}Sr_xNb_2O_7$ showing the selected **(a)**, **(b)**, **(c)** *Pbmm* superstructure reflection (2 1 0) vanished at 648 K, 598 K, 498 K for x = 0, 0.1, 0.2, respectively.

Compared with the parent compound (CuCl)$LaNb_2O_7$, where the transition temperatures of the *Pbam* → *Pbmm* and *Pbmm* → *P4/mmm* phase transitions are 488 K and 648 K respectively, the structural transition temperatures of the Sr^{2+} substituted compounds are reduced to 448 K and 598 K for x = 0.1 and 373 K and 498 K for x = 0.2. According to the (CuCl)$La_{1-x}Sr_xNb_2O_7$ heat maps, the superstructure reflections (1 1 1), (1 3 0) and (2 1 0) gradually decrease in intensity with increasing temperature. However, the superstructure reflections for x = 0.2 are quite weak, so the transitions are not very clear. Presumably, this is because the intensities of the *Pbam* superstructure reflections in x = 0.2 are still gradually increasing from 373 K to room temperature (298 K) and even lower temperatures (< 298 K). Stronger *Pbam* superstructure reflections may be observed below room temperature. Moreover, because of the large substituted Sr^{2+} ions, the reflection (1 3 0) in x = 0.2 is moved to lower 2θ and is close to the tail of the high intensity reflection (2 2 2), which makes the (1 3 0) reflection hard to observe. The lattice parameter *a* is smaller than b in the *Pbam* phase and then becomes larger than *b* at the *Pbam*→*Pbmm* boundary (x = 0.1). However for x = 0.2, the lattice parameter *a* is larger than *b* in both *Pbam* and *Pbmm* phases. This may due to the unclear phase boundary in x = 0.2 as the typical reflections of *Pbam* symmetry from x = 0.2 compound are already very weak at room temperature. *C* parameters firstly increase and then decrease at the first boundary in all compounds whereas the unit cell volume continuously increases with the increasing temperature, indicating both transitions are of the second order.

Low temperature neutron diffraction studies on (CuCl)$La_{1-x}Sr_xNb_2O_7$ were carried out at the WISH diffractometer. The refined NPD patterns are shown in Fig. 3.14. The corresponding refinement and crystallographic data are shown in Table 3.8 and Table 3.9 while the representative interatomic distances, selected bond angles and BVS calculations are listed in Table 3.10. All the solid solutions adopt *Pbam* orthorhombic structure at 100 K and the *Pbam* structure is retained to the base temperature. Refined data indicate small oxygen deficiencies in both Sr-substitution compounds which confirms a successfully small substitution of La^{3+} with Sr^{2+}. No additional magnetic reflections were observed indicating an absence of long-range magnetic ordering across the solid solution.

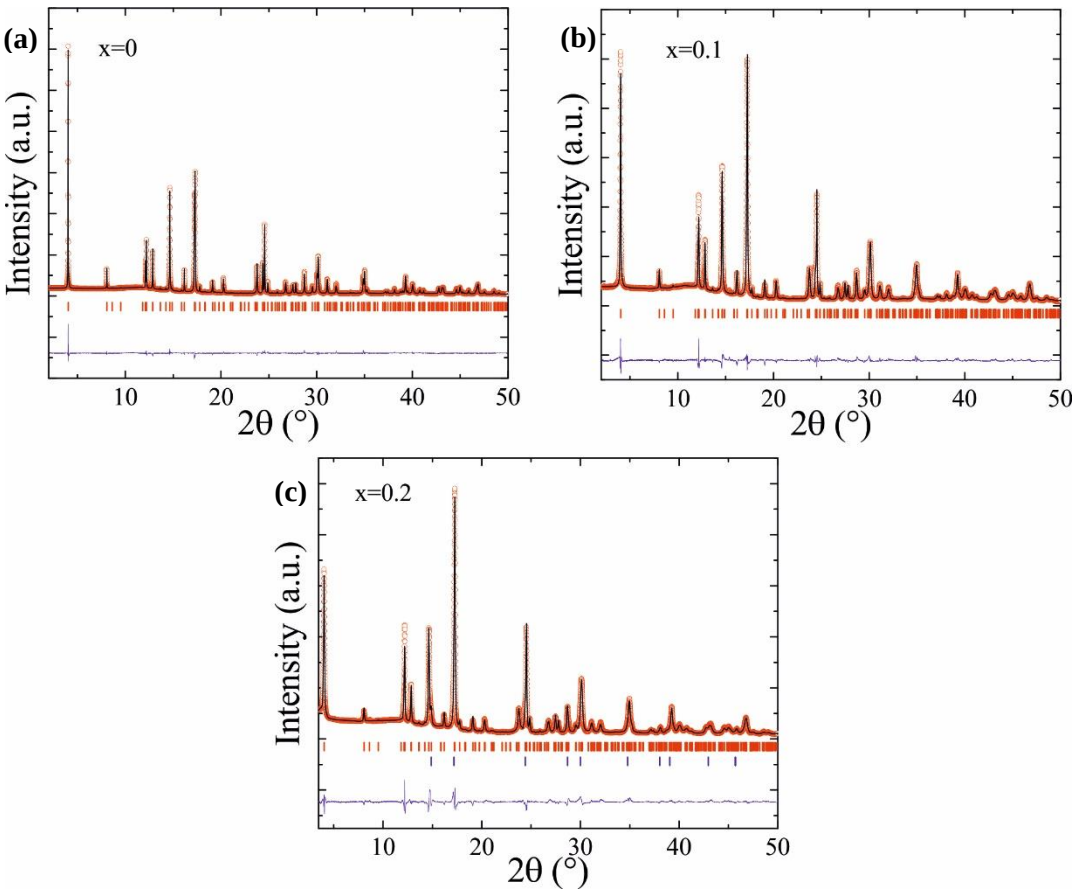

Fig. 3.14 Rietveld fit to the 1.5 K NPD data of (CuCl)$La_{1-x}Sr_xNb_2O_7$. Additional Bragg marks (blue) in x= 0.2 pattern identify the secondary $CuCl_2$ phase.

Table 3.8 Refinement data for (CuCl)$La_{1-x}Sr_xNb_2O_7$ (x = 0, 0.15, 0.2) from the Rietveld fit of NPD at 1.7 K. All compounds adopt in orthorhombic *Pbam* space group.

x	Lattice parameters (Å)	Cell volume (Å^3)	N. of formula unit	Density (g / mol)	*R*-factors (%)	χ^2
0	*a* = 7.7608(3) *b* = 7.7632(3) *c* = 11.7243(2)	706.37 (4)	4	5.038(1)	R_p=3.76 R_{wp}=4.95 R_B=2.57 R_F=2.69	6.13
0.15	*a* = 7.7671(4) *b* = 7.7679(5) *c* = 11.6931(3)	705.49(6)	4	4.971(1)	R_p=4.83 R_{wp}=6.42 R_B=4.39 R_F=5.24	10.9
0.2	*a* = 7.7639(3) *b* = 7.7632(2) *c* = 11.6728(1)	703.55(3)	4	4.961(1)	R_p=4.76 R_{wp}=5.84 R_B=6.41 R_F=7.26	13.7

Table 3.9 Crystallographic details of (CuCl)$La_{1-x}Sr_xNb_2O_7$ (x = 0, 0.15, 0.2) from the NPD Rietveld fits at 1.7 K.

	Atom	Wyckoff	x	y	z	Occupy	B_{iso}/Å^2
x = 0	Cu	4*h*	0.769(2)	0.5020(5)	0.5	1.0	0.65(6)
	Cl	4*h*	0.564(1)	0.2719(5)	0.5	1.0	2.9(2)
	La	4*g*	0.0007(8)	0.2385(5)	0	1.0	0.75(8)
	Nb	8*i*	0.7485(8)	0.5	0.8088(2)	1.0	0.28(6)
	O1	4*f*	0	0.5	0.862(1)	1.0	1.19(5)
	O2	8*i*	0.7484(6)	0.248(2)	0.844(1)	1.0	1.19(5)
	O3	8*i*	0.7336(1)	0.0051(1)	0.6583(2)	1.0	1.19(5)
	O4	4*g*	0.7261(1)	0.5024(1)	0	1.0	1.19(5)
	O5	4*e*	0	0	0.827(1)	1.0	1.19(5)
x = 0.15	Cu	4*h*	0.7731(5)	0.504(2)	0.5	1.0	0.9(1)
	Cl	4*h*	0.5651(7)	0.276(1)	0.5	1.0	5.1(3)
	La/Sr	4*g*	0.0002(7)	0.231(1)	0	0.839(1)/0/161(1)	1.3(1)
	Nb	8*i*	0.751(1)	0.5	0.8103(3)	1.0	1.3(1)
	O1	4*f*	0	0.5	0.859(1)	1.0	1.8(7)
	O2	8*i*	0.743(1)	0.236(2)	0.838(1)	1.0	1.8(7)
	O3	8*i*	0.7400(5)	0.0009(1)	0.6594(2)	1.0	1.8(7)
	O4	4*g*	0.7196(3)	0.5067(1)	0	1.0	1.8(7)
	O5	4*e*	0	0	0.836(1)	0.946(5)	1.8(7)
x = 0.2	Cu	4*h*	0.7734(8)	0.503(3)	0.5	1.0	1.2(2)
	Cl	4*h*	0.558(1)	0.290(2)	0.5	1.0	5.6(3)
	La/Sr	4*g*	0.0010(3)	0.227(1)	0	0.779(1)/0.221(1)	1.0(2)
	Nb	8*i*	0.748(1)	0.5	0.8125(4)	1.0	0.2(1)
	O1	4*f*	0	0.5	0.853(1)	1.0	1.5(1)
	O2	8*i*	0.737(2)	0.236(3)	0.844(1)	1.0	1.5(1)
	O3	8*i*	0.746(1)	0.0015(1)	0.6579(5)	1.0	1.5(1)
	O4	4*g*	0.7236(2)	0.506(1)	0	1.0	1.5(1)
	O5	4*e*	0	0	0.833(1)	0.95 (1)	1.5(1)

Table 3.10 The Metal-anion bond distances, nearest metal-metal distance, selected bond angles and BVS calculation. Cu^{2+} ions bond with two O^{2-} and two Cl^{-} ions forming $[CuCl_2O_2]$ plaquettes.

Pbam 300K	x =0	x = 0.15	x = 0.2
Cu-O3 x2 (Å)	1.855(3)	1.867(1)	1.837(1)
Cu-Cl (Å)	2.46(1)	2.46(2)	2.58(1)
Cu-Cl (Å)	2.41(1)	2.39(1)	2.26(1)
Cu-BVS	1.86(1)	1.86 (2)	2.01(1)
La-O1 x2 (Å)	2.60(1)	2.66(1)	2.72(1)
La-O2 x2 (Å)	2.65(1)	2.68(1)	2.60(1)
La-O2 x2 (Å)	2.68(1)	2.75(1)	2.73(1)
La-O4 x1 (Å)	2.52(1)	2.53(1)	2.54(1)
La-O2 x1 (Å)	2.53(1)	2.51(1)	2.51(1)
La-O5 x2 (Å)	2.75(1)	2.63(1)	2.63(1)
La-BVS	2.97(1)	2.93(1)	2.91(1)
Nb-O1 x1 (Å)	2.04(1)	2.01(1)	2.01(1)
Nb-O2 x1 (Å)	1.97(1)	1.86(2)	1.87(3)
Nb-O2 x1 (Å)	2.00(1)	2.08 (1)	2.08(3)
Nb-O3 x1 (Å)	1.772(4)	1.756(4)	1.81(1)
Nb-O4 x1 (Å)	2.252(3)	2.232(4)	2.198(5)
Nb-O5 x1 (Å)	1.94(1)	1.97(1)	1.94(1)
Nb-BVS	5.12(1)	5.31(2)	5.21(3)
Cu-Cu (Å)	3.892(1)	3.901(1)	3.898(1)
Nb-Nb (Å)	3.881(1)	3.87 (1)	3.881(1)
La-La (Å)	3.71(1)	3.59(2)	3.53(3)
Cu-Cl-Cu (˚)	106.6(2)	106.9(3)	104.2(5)
O3-Cu-O3 (˚)	178.1(9)	173.6(4)	170.6(5)
Nb-O3-Cu (˚)	175.6(6)	179.0(4)	176.7(4)

Thermal analysis using differential scanning calorimetry (DSC) was attempted for $(CuCl)La_{1-x}Sr_xNb_2O_7$. DSC and (thermogravimetry) TG data were collected between 25 ˚C and 550 ˚C on warming and cooling. However, no obvious signs of structural transitions were observed in the DSC data. Presumably this is due to the low entropy change associated with these transitions. A. A. Tsirlin did not report the observation of a phase transition in $(CuCl)LaNb_2O_7$ through DSC either.[3] The original DSC data for $(CuCl)La_{1-x}Sr_xNb_2O_7$ can be found in Appendix A. Higher quality TGA or DSC data will be needed in the future to confirm the phase transitions.

3.4.3 Magnetisation measurements

Variable temperature DC magnetic susceptibility data under ZFC/FC of $(CuCl)La_{1-x}Sr_xNb_2O_7$ (x = 0, 0.1 and 0.2) were collected on warming. As shown in Fig. 3.15, the susceptibility data of the reference sample $(CuCl)LaNb_2O_7$ shows a broad peak at around 15 K characterising a

low-dimensional antiferromagnetic system, followed by a rapid decrease. This drop of the susceptibility elucidates an energy gap separating the spin singlet ground state and the excited state. In the high temperature region, the magnetic measurement reveals a Curie-Weiss behaviour with the Weiss temperature θ_{CW} = 6.8 K and the Curie constant C = 0.385 emu·K/mol, resulting in an experimental effective magnetic moment μ_{eff} = 1.80 μ_B. These results were close to the published data reporting a maximum susceptibility of T_{max}^{χ} = 16 K, θ_{CW} = -5.06 K and C = 0.404 emu·K/mol.[2] The reciprocal susceptibility χ^{-1} data for the Curie-Weiss fit using Eq. 2.30 was only selected between 100 K and 215 K due to an uncertain susceptibility drop at 215 K, which makes the noisy signal above 215 K hard to fit. There is no bifurcation of ZFC-FC, however the unusual outcome of the FC curve being lower than ZFC may be explained by the partial loss of the powder sample from the capsule during the vibration process, as the PPMS utilises a Vibrating-sample magnetometer (VSM) to carry out the magnetisation measurements. ZFC-FC susceptibility with data above 300 K are shown in Appendix A.

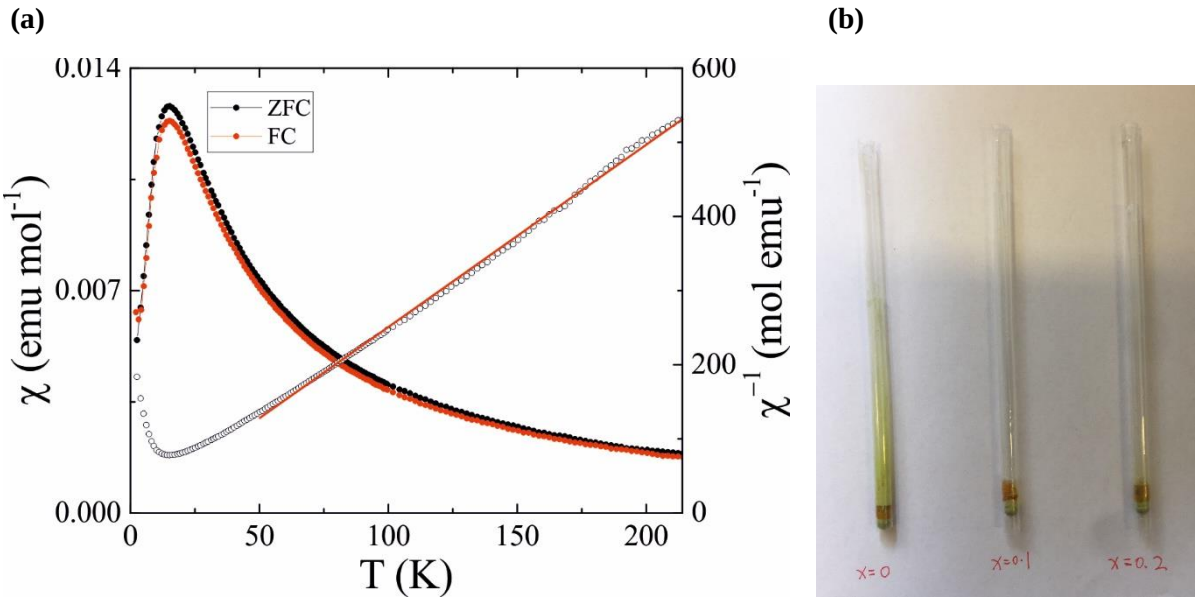

Fig. 3.15 (a) Temperature dependence of the magnetic susceptibility of (CuCl)$LaNb_2O_7$ at a constant field of 0.3 T. Inverse susceptibility is exhibited on the right-Y axis accompanied by the Curie-Weiss fit. **(b)** The straws with green powder samples of (CuCl)$La_{1-x}Sr_xNb_2O_7$ after remove from the PPMS chamber. Only the x = 0 straw shows a sample shaking out from the capsule.

In contrast to the susceptibility data of the reference (CuCl)$LaNb_2O_7$, the two Sr substituted compounds exhibit no sign of an antiferromagnetic-like transition. Only the knee points of 10 K / 7 K for x = 0.1 and 0.2 respectively can be observed which may arise from the residual impurities or Cu^{2+} defects forming a Curie tail. Both sets of susceptibility data of (CuCl)La_{1-}

$_xSr_xNb_2O_7$ (x = 0.1 and 0.2) were fitted using the Cure-Weiss law (Fig. 3.16) and the corresponding fitted results, including the experimental effective moments, can be found in Table 3.11. The theoretical effective moment of Cu^{2+} can be calculated using Eq. 2.27. The copper cation's effective moment for x = 1 and x = 2 are a bit higher than theoretical value, though this may be an effect of the susceptibility data becoming noisy at temperatures higher than 140 K.

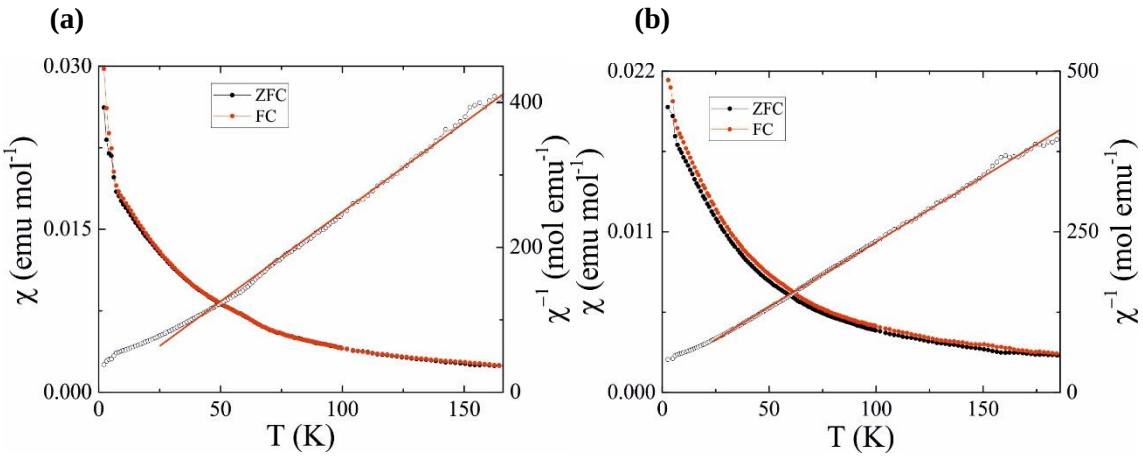

Fig. 3.16 ZFC-FC susceptibility data of (CuCl)$La_{1-x}Sr_xNb_2O_7$ of **(a)** x = 0.1 and **(b)** x = 0.2 showing paramagnetic behaviour in all temperature regions. The Curie-Weiss fit is shown by the red line.

Table 3.11 The magnetic susceptibility results including the Curie constants and the Weiss temperature. The μ_{eff} was calculated using Eq. 2.27 and Eq. 3.1. The high spin $3d^7$ model was used for the theoretical μ_{eff} calculation.

$\chi^{-1} = \frac{(T-\theta)}{C}$	C (emu·K/mol)	θ_{cw} (K)	μ_{eff} (μ_B)	Theo – μ_{eff} (μ_B)
x = 0	0.385	6.8	1.755	1.732
x = 0.1	0.406	-0.9	1.802	1.732
x = 0.2	0.493	-15.5	1.986	1.732

3.5 Discussion

(CuCl)$La_{1-x}Sr_xNb_2O_7$ (x = 0.1 and 0.2) solid solutions was successfully synthesised through a two-step reaction including low temperature ion-exchange reaction. According to thermal analysis, (CuCl)$La_{1-x}Sr_xNb_2O_7$ decomposes above 723 K, so ion-exchange reaction is necessary since the Rb-based precursor can only formed at temperatures well above 1000 K. As introduced in Fig. 1.5 in Chapter 1, both the $RbLa_{1-x}Sr_xNb_2O_7$ precursor and synthesised

$(CuCl)La_{1-x}Sr_xNb_2O_7$ are Dion-Jacobson layered perovskites where layers of Rb^+ or $(CuCl)^+$ are blocked by the nonmagnetic unit $[LaNb_2O_7]^-$. Their structures are compared on page 11, and structural information is provided on page 68. The Rb^+-to-$(CuCl)^+$ exchange within the layers transforms the DJ perovskite $RbLa_{1-x}Sr_xNb_2O_7$ to the metastable DJ perovskite $(CuCl)La_{1-x}Sr_xNb_2O_7$. The exchange ratio of Rb^+ and $(CuCl)^+$ is 1:1 to maintain the charge balance. Therefore, a different precursor such as Ruddlesden−Popper perovskite $Na_2La_2Ti_3O_{10}$ needs to exchange two $(CuCl)^+$, for which there may not be enough room in the interlayer region.[16]

Synchrotron and neutron diffraction both confirmed that $(CuCl)La_{1-x}Sr_xNb_2O_7$ adopts the *Pbam* orthorhombic structure at room temperature and retains its symmetry down to the base temperature. The secondary phase found in $(CuCl)La_{0.8}Sr_{0.2}Nb_2O_7$ is the residual reactant $CuCl_2$, as a 3-fold molar excess of $CuCl_2$ was added to ensure the completion of the reaction and the appearance of the $CuCl_2$ is probably due to an incomplete washing process. Similar to what is seen in the reference compound $(CuCl)LaNb_2O_7$, Cu^{2+} cations in the $(CuCl)La_{1-x}Sr_xNb_2O_7$ are found to bridge between the $[NbO_6]$ perovskite slabs along the *c*-axis and to form a Cu-Cl zig-zag array within the interlayer, resulting in the formation of corner-sharing $[CuCl_2O_2]$ plaquettes. $[NbO_6]$ octahedra were refined to be tilted along the *b*-axis and according to report from A. A. Tsirlin,[3] the *Pbam* superstructure is induced by a combination of $[NbO_6]$ octahedral tilts and the Cu^{2+} cations' and Cl^- anions' displacements in the (CuCl) interlayer. At a higher temperature (T > 448 K for x = 0.1), the *Pbam* structure transforms into another orthorhombic polymorph, *Pbmm*, with no tilt of the $[NbO_6]$ octahedra. Therefore, the superstructure arises only from the atomic displacement existing in the interlayer. At even higher temperatures (T > 598 K for x =0.1), both octahedral tilting distortions and atomic displacements are fully suppressed and the diffraction patterns can be simply refined as a tetragonal square lattice with the space group *P4/mmm*. Hence Cu^{2+} cations here, bridging the apical O^{2-} ions and connecting with 4 Cl^- ions within the (CuCl) layer, are octahedrally coordinated. These formed $[CuCl_4O_2]$ octahedra share edges with each other in the interlayer while also sharing corners with the $[NbO_6]$ octahedra along the *c*-axis. BVS calculations of Cu^{2+} cations from the room temperature *Pbam* phase shows that the actual valence state of Cu become larger with increasing Sr^{2+} substitution, indicating the successful Sr^{2+} substitution at the La^{3+} site according to the theory of charge conservation. It is interesting to note that the *Pbam* $\rightarrow$ *Pbmm* $\rightarrow$ *P4/mmm* structural phase transition temperatures decrease with increasing Sr^{2+} substitution. This could be explained by the replacement of the smaller La^{3+} with the larger

Sr^{2+} cations. The refined data of the unit cell contents of $(CuCl)La_{1-x}Sr_xNb_2O_7$ reveal a layer contraction relative to the reference $(CuCl)LaNb_2O_7$ compound. In addition, increasing the ionic size at the La^{3+} site results in less deviation of the ideal Goldschmidt tolerance factor and is therefore more likely to obtain regular $[NbO_6]$ octahedra and tend to form $[CuCl_4O_2]$ octahedra in the *P4/mmm* symmetry. The distortions within the Cu-Cl interlayers becomes smaller with the increasing Sr^{2+} substitution. BVS calculations from SXRD and NPD confirm that Cu ions in $(CuCl)La_{1-x}Sr_xNb_2O_7$ are all close to two valence state. The analyses of the NPD data reveal a small oxygen deficiency, $(CuClLa_{1-x}Sr_xN_{b2}O_{7-\delta})$, which could be for the result of balancing the charge difference upon Sr^{2+} substitution. Therefore, according to the 1:1 stoichiometric relationship between Rb^+ and $(CuCl)^+$, the chemical formula of the synthesised Rb-based mother compound would be $RbLaNb_2O_{7-\delta}$.

Magnetic susceptibility data collected for the substitution compounds exhibit a distinct contrast in magnetic behaviour to that of the reference compound $(CuCl)LaNb_2O_7$. The broad peak at around 15 K is totally suppressed with Sr^{2+} substitution. The absence of this antiferromagnetic-like transition in the Sr substituted compounds most likely results from the elongation of the Cu-Cu metal distance. However, the possible effect from the unidentified impurity cannot be excluded as well. Cure-Weiss fits at the high temperature region gives the experimental effective moments for x = 0.1 and 0.2, of which the values are higher to the theoretical moments. The very small value of Weiss constants of $(CuCl)La_{1-x}Sr_xNb_2O_7$ indicates weak Cu-Cu couplings. Unfortunately, NPD data confirms no sign of long-range magnetic ordering in all $(CuCl)La_{1-x}Sr_xNb_2O_7$ compounds down to base temperature. No magnetic data were collected for $RbLaNb_2O_7$ as it is a nonmagnetic perovskite without magnetic ions.

In conclusion, a series of Sr^{2+} substituted DJ layered perovskites $(CuCl)La_{1-x}Sr_xNb_2O_7$ have been successfully synthesised via a two-step solid-state reaction. The low temperature ion-exchange reaction is necessary for synthesising layered perovskites with low formation temperatures. Synchrotron and neutron powder diffraction have been employed to examine the crystal structure and have confirmed a reliable substitution though small impurities persist. Crystal structures of the $(CuCl)La_{1-x}Sr_xNb_2O_7$ compounds all adopt the *Pbam* space group at room temperature and retain this symmetry down to the base temperature. The *Pbam*→*Pbmm*→*P4/mmm* structural phase transitions move to the lower temperature region with the increasing amount of the Sr^{2+} substitution. Larger Sr^{2+} cation substitution reduces the structural distortion and hence reduces the transition temperature. The T_1 / T_2 transition temperatures for x = 0.1 and 0.2 are 448 K / 598 K and 373 K / 498 K respectively.

Magnetic susceptibility data reveals that the broad peak in the reference $(CuCl)LaNb_2O_7$ compound is completely suppressed and only knee points of 10 K / 7K for x = 0.1 and 0.2 respectively can be observed. Experimental effective moments of copper cations obtained from the Curie-Weiss fit are closer to the calculated values. NPD data indicates no long-range magnetic ordering for all compounds

Based on the susceptibility result, an interesting thought is whether this kind of suppressing scenario would involve an inhomogeneous cross-over from one kind of behaviour to another on Sr^{2+} substitution. Therefore, the follow-up work will focus on synthesising intermediate Sr^{2+} substituted compounds such as x = 0.01, 0.02, 0.05 to find out the possible boundary. Meanwhile, considering that there still exist small unidentified impurity peaks which may affect structural refinement and magnetic properties, an improved synthetic approach, such as adding an extra step to wash the intermediate Rb-based compounds using distilled water, is imperative.

Another thought of study the reference $(CuCl)LaNb_2O_7$ compound is to synthesise $(CuCl)LaNb_2O_{7-x}$ via hydrogen reduction. This approach could create a different mixed valanced state of Cu^{2+}/Cu^{1+} of which the structural and magnetic properties could be compared with $(CuCl)La_{1-x}Sr_xNb_2O_7$.

References

1. J. B. Goodenough, *Rep. Prog. Phys.*,2005, **67**, 1915.

2. T. A. Kodenkandath, J. N. Lalena, W. L. Zhou, E. E. Carpenter, C. Sangregorio, A. U. Falster, W. B. Simmons, Jr., C. J. O'Connor and J. B. Wiley, *J. Am. Chem. Soc*., 1999, **121**, 10743.

3. A. A. Tsirlin, A. Abakumov, G. Van Teendeloo and H. Rosner, *Phys. Rev. B*, 2010, **82**, 054107.

4. M. B. Stone, I. A. Zaliznyak, T. Hong, C. L. Broholm, and D. H. Reich, *Nature*, 2006, **440**, 187.

5. K. Momma and F. Izumi, *J. Appl. Crystallogr.*, 2011, **44**, 1272.

6. H. Kageyama, T. Kitano, N. Oba, M. Nishi, S. Nagai, K. Hirota, L. Viciu, J. B. Wiley, J. Yasuda, Y. Baba, Y. Ajiro and K. Yoshimura, *J. Phys. Soc. Jpn*., 2005, **74**, 1702.

7. A. A. Tsirlin and H. Rosner, *Phys. Rev. B.*, 2010, **82**, 060409.

8. S. Gražulis, D. Chateigner, R. T. Downs, A. F. T. Yokochi, M. Quirós, L. Lutterotti, E. Manakova, J. Butkus, P. Moeck, and A. Le Bail, J. Appl. Crystallogr., 2009, **42**, 726.

9. *icsd.cds.rsc.org/icsd/*.

10. A. C. Larson and R. B. Von Dreele, *General Structure Analysis System (GSAS)*, Los Alamos National Laboratory Report LAUR, 1994, 86.

11. B. H. Toby, *J. Appl. Crystallogr*., 2001, **34**, 210.

12. J. Rodriguez-Carvajal, *Physica B*, 1993, **192**, 55.

13. J. G. Moberly, M. T. Bernards and K. V. Waynant, *J. Cheminform*., 2018, **10**, 5.

14. H. M. Rietveld, J. *Appl. Crystallogr*., 1969, **2**, 65.

15. J. Rodriguez-Carvajal, *Physica B*, 1993, **192**, 55.

16. K. A. Hyeon and S. H. Byeon, *Chem. Mater*., 1999, **11**, 352

Chapter 4. New NTO-type double corundum Co_2ScSbO_6 and its $Ni_{2-x}Co_xScSbO_6$ solid solutions

4.1 Introduction

One of the challenges currently pursued by solid-state scientists is the development of materials with coupled physical properties. Multiferroics[1], where two ferroic orders coexist, have been intensively investigated throughout recent decades, with special focus on those combining magnetic and electric properties as they present a wide range of potential applications.[2-3] A large proportion of the multiferroic materials studied so far are based on transition metal oxides with a perovskite-related structure. It is also worth noting that materials showing magnetically induced ferroelectricity usually have strong magnetoelectric couplings at low temperature, while the coupling effect is often weak for those having high transition temperatures.[4-5] Geometrically frustrated spin networks[6] favour large magnetoelectric effects, as the development of non-collinear spiral magnetic structures can break the inversion symmetry and consequently allow a net polarisation.[7-8]

Corundum (Al_2O_3), which was first reported by L. Pauling and S. B. Hendricks in 1925, crystallises in the space group $R\bar{3}c$ with a distorted hexagonal closed packing. Three different corundum derivatives $FeTiO_3$, $LiNbO_3$ and Ni_3TeO_6 were found by replacing the Al-position with several different metal ions. Recently, examples of double corundum related oxides with different cations occupying the B (for example Nb site in $LiNbO_3$) sites were reported, for example A_2BSbO_6 where A = Mg, Cd, Ni and B = Sc or In. In the search for multiferroic materials, polar crystal structures are highly sought after. The double corundum derivatives with $LiNbO_3$-type[9] (LN, space group $R3c$), Ni_3TeO_6-type[10] (NTO, $R3$) and ordered ilmenite[11] (OIL, $R3$) structures have been widely studied during the last 20 years. The lack of an inversion centre allows the spontaneous polarisation of the material and the geometrically frustrated honeycomb basal layers may result in helical spin structures, which could give rise to magnetically induced ferroelectricity. A notable example is the high pressure $Mn_2BB'O_6$

family, which has several members such as Mn_2FeSbO_6[12] with different cation orders and complex magnetic behaviours including incommensurate helical magnetic structures.

In this chapter, a new NTO-type Co_2ScSbO_6 was synthesised and the ceramic samples of the solid solutions of $Ni_{2-x}Co_xScSbO_6$ (x = 0, 0.5, 1 and 1.5) were prepared through conventional solid-state synthetic routes at ambient pressure and high pressure-high temperature (HPHT) methods. The results of X-ray and neutron diffraction studies along with the physical property measurements of these materials will be presented. The common (ferromagnetic or antiferromagnetic) and exotic (helical spin structures and spin lock-in from incommensurate to commensurate magnetic structure) magnetic behaviours are investigated in this chapter through chemical substitution of Ni^{2+} ions with Co^{2+} ions. In addition, the complete structural and functional characterisation to determine the structure-property relationship will be discussed.

4.2 Background

4.2.1 Previous studies of Ni_2ScSbO_6

Ni_2ScSbO_6, which was recently published by Ivanov et al. in 2013, adopts a trigonal NTO-type structure with the space group *R*3 at room temperature, and it retains this symmetry down to 1.7 K.[13] 2/3 of the available octahedral cavities are occupied by the cations arranged in special ordered layers of Ni(1)-Sc / Ni(2)-Sb packed along the *z*-axis. Compared to the parent compound Ni_3TeO_6, which is ordered in a collinear antiferromagnetic structure parallel to the *z*-axis (Fig. 4.1(a)),[6] the magnetic structure of Ni_2ScSbO_6 can be described as a spiral structure with an incommensurate propagation vector k = [0 0.036 0]. The half periodic magnetic structure, with ferromagnetic layers coupled antiferromagnetically, is shown in Fig 4.1(b). However, whether the magnetic structure is a helix with spins confined in the *a*-*c* plane or cycloidal with spins in the *b*-*c* plane cannot be distinguished as the powder neutron diffraction cannot confirm the direction of the magnetic component within the hexagonal basal plane. Hence, Ni_2ScSbO_6 is a potential type-II multiferroic with a possible cycloidal magnetic structure although the critical temperatures of the ferroelectric (approximately 1050 K) and antiferromagnetic (60 K) transitions were reported to have a great difference.

Co^{2+} ions have a similar ionic radius to Ni^{2+}, which allows the chemical substitution of Ni^{2+} by Co^{2+} to be carried out. Nevertheless, the presence of spin-orbit coupling and the electronic

anisotropy of Co^{2+} could generate interest and probably alter the magnetic properties of Ni_2ScSbO_6.

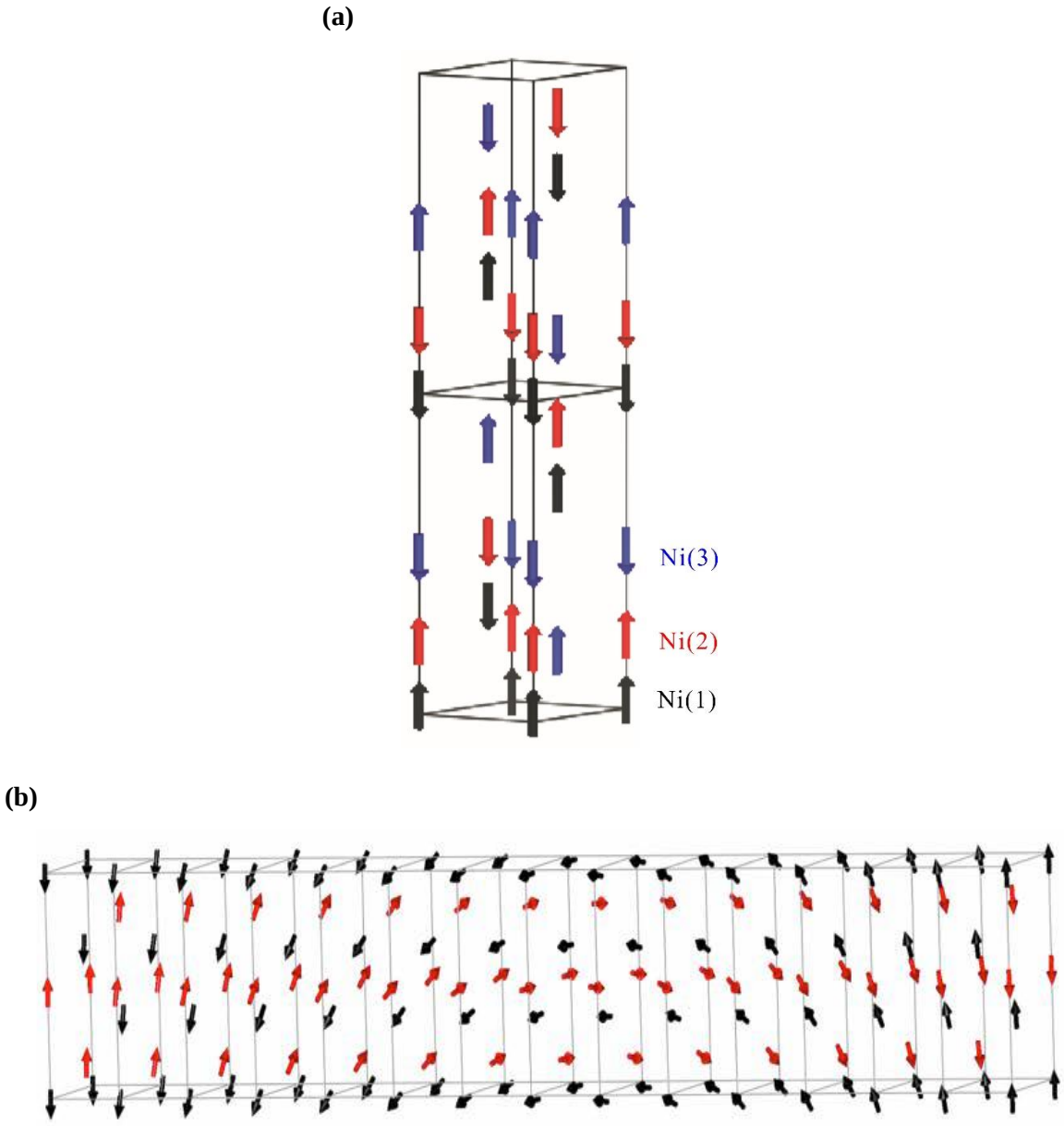

Fig 4.1 (a) Collinear antiferromagnetic structure of Ni_3TeO_6. **(b)** Incommensurate spiral magnetic structure (helix here as an example) of Ni_2ScSbO_6 refined from neutron diffraction at 1.7 K. [13] Arrows represent magnetic spins on different Ni sites. Atoms are not displayed for simplicity.

4.3 Experimental

4.3.1 Ambient-pressure synthesis of $Ni_{2-x}Co_xScSbO_6$

High quality polycrystalline specimens of $Ni_{2-x}Co_xScSbO_6$ (x = 0, 0.5, 1, 1.5) were synthesised via high temperature solid-state reactions. Stoichiometric proportions of high purity NiO (Alfa Aesar, 99.99%), CoO (Alfa Aesar, 99.99%), Sc_2O_3 (Alfa Aesar, 99.99%) and Sb_2O_5 (Sigma-Aldrich, 99.99%) oxides were ground together under acetone to prepare the mixture. A high precision electronic balance was used to weigh the correct proportions of the binary oxides in order to obtain the requested chemical composition. The precursor was then heated between 973 K and 1373 K with intermediate regrinding and pelletizing and with temperature intervals of 100 K in order to supress the formation of undesirable secondary phases, so as to obtain a high purity sample. At each intermediate temperature, the pellets were sintered for 15 hours. CoO oxide needed to be heated at 1373 K under N_2 / Ar gas flow in advance to remove the contained spinel Co_3O_4.

4.3.2 High-pressure synthesis of Co_2ScSbO_6

The synthesis of Co_2ScSbO_6 was carried out under HPHT conditions outlined in detail in the section '2.1.2 High pressure high temperature solid state synthesis'. The mixed precursor was prepared by combining the stoichiometric ratio of binary CoO, Sc_2O_3 and Sb_2O_5 oxides as list above and ground together in an agate mortar under acetone several times to generate a homogeneous mixture. The resulting thoroughly mixed precursor was then loaded into a platinum capsule and placed in a Walker-type multi-anvil apparatus. The experimental pressure and temperature conditions for synthesising Co_2ScSbO_6 were optimised at 6 GPa and 1273 K with a heating time of 1 hour, followed by a 1 hour slow cooling process. Once the reaction was complete, the pressure was slowly released and the pelleted product was taken out from the capsule and ground into powder, followed by phase identification and phase purity inspections through laboratory X-ray diffraction.

4.3.3 Structural characterisation of $Ni_{2-x}Co_xScSbO_6$

The initial phase identification and purity investigation through X-ray diffraction (XRD) was performed on a laboratory D2 Bruker Phaser diffractometer using a Cu $K\alpha/K\beta$ radiation source

with a constant wavelength λ_{K_α} = 1.54050 Å. The pellets of $Ni_{2-x}Co_xScSbO_6$ were ground into a powder in an agate mortar and were then transferred to a glass substrate. Several drops of ethanol were used in order to ensure the powder was evenly distributed on the surface of the glass substrate. The X-ray powder diffraction data was collected at room temperature in the angle range of $5^\circ \leq 2\theta \leq 70^\circ$ with a step size of 0.1˚ and a counting time of 2 s per step.

Since the neutron scattering lengths (b) of Co, Ni, Sc and Sb atoms are quite different (b_{Co} = 2.49 fm, b_{Ni} = 10.30 fm, b_{Sc} = 12.29 fm, b_{Sb} = 5.57 fm), the distribution of cations over the four available crystallographic sites can be determined by neutron powder diffraction (NPD) with good precision. Neutron diffraction analysis will also give accurate information on oxygen ion (b_O = 5.803 fm) positions and their stoichiometry. Several sets of neutron powder diffraction patterns of $Ni_{2-x}Co_xScSbO_6$ (x = 0, 0.5, 1 and 1.5) compounds were collected at the high-resolution SPODI neutron powder diffractometer (FRMII, Munich) at 4, 50, 70 and 100 K. Each pattern was scanned for 5 hours at each temperature step. 1.7 g of each compound was placed in a sealed cylindrical vanadium can then transferred into a helium cryostat. The diffraction patterns were collected over the angle range of $0^\circ \leq 2\theta \leq 150^\circ$ with a constant neutron wavelength λ = 1.538 Å for x = 0 and λ = 2.536 Å for x = 0.5, 1, 1.5 and a step-width of 0.05˚. These data sets were used for the main structural characterisations.

Further NPD experiments of $Ni_{2-x}Co_xScSbO_6$ (x = 1.5) were carried out on the neutron diffractometer D20 (ILL, Grenoble) at 1.5 and 70 K using a (002) face of a highly oriented pyrolytic graphite (HOPG) monochromator with a similar wavelength λ = 2.41 Å (with a take-off angle of 42˚). The sample was also measured at 25, 50 and 70 K using a longer wavelength, λ = 3.594 Å, and a take-off angle of 65˚. A new monochromator, recently custom built for D20 to select this long wavelength, was used for the first time to measure this sample using the high take off angle mode.

Several samples of Co_2ScSbO_6 from different high-pressure experimental cycles were combined and well ground to provide a homogeneous sample of approximately 50 mg in order to meet the minimum weight requirement for a neutron diffraction experiment. NPD data of the combined HPHT Co_2ScSbO_6 samples were collected at the high-resolution T.O.F. WISH neutron diffractometer (ISIS, UK) at 1.7 K (4 hours), 10 K (30 mins), 20 K (30 mins), 30 K (3 hours), 40K (30 mins), 50 K (30 mins), 55 K (30 mins), 60 K (30 mins), 70 K (1 hour) and 100 K (4 hours).

Rietveld analysis against X-ray data was carried out using the GSAS software package,[14-15] while FullProf Suite[16] was used for analysing neutron diffraction data. The magnetic structure was solved as follows: The 'K-search' software installed in FullProf was used to determine the magnetic propagation vector according to the positions of the magnetic reflections in the neutron diffraction pattern. Once the corrected magnetic propagation vector was found, the magnetic symmetry analysis would be carried out using the Baslreps program[17]. All of the possible symmetry model results generated from Baslreps were tested one by one and the one that converged with the best goodness of fit was selected.

4.3.4 Physical property measurements

The magnetisation measurements were performed on a Quantum Design MPMS XL Superconducting Quantum Interference Device (SQUID) magnetometer and a Quantum Design Physical Property Measurement System (PPMS). The DC magnetic susceptibility of $Ni_{2-x}Co_xScSbO_6$ was recorded as a function of temperature using zero field cooling (ZFC) and field cooling (FC) protocols in a temperature range of 2 K < T < 300 K and under a magnetic field of 1 Tesla. Magnetisation measurements as a function of the applied magnetic field were also recorded at 2 K, 40 K and 100 K with magnetic fields up to $\pm$5 T.

4.4 Experimental results

4.4.1 Phase analysis & X-ray crystal structure: $Ni_{2-x}Co_xScSbO_6$

The initial crystallographic characterisation of $Ni_{2-x}Co_xScSbO_6$ compounds was performed by analysing laboratory X-ray powder diffraction data collected at room temperature. Sample colours gradually change from green to purple with increasing cobalt content. X-ray results shown in Fig. 4.2 reveal the targeted phases of $Ni_{2-x}Co_xScSbO_6$ were formed (> 90%) along with minor secondary phases ($Sc_{5.5}Sb_{1.5}O_{12}$ and (Ni,Co)O). Another by-product $Co_{2.33}Sb_{0.67}O_4$, a spinel, was observed in Co-rich compounds with x = 1 and 1.5. Co_2ScSbO_6 (x = 2) was at first synthesised through conventional solid-state routes at ambient pressure, but it formed a large amount of the $Co_{2.33}Sb_{0.67}O_4$ spinel phase and many other impurities that cannot be identified from the Inorganic Crystal Structure Database (ICSD)[18]. Therefore, the HPHT

technique was used in the Co_2ScSbO_6 synthesis and yielded almost pure target phase with only minor secondary phases $Sc_{5.5}Sb_{1.5}O_{12}$, $CoSb_2O_6$ and reactant CoO. The five purest Co_2ScSbO_6 compounds labelled with the corresponding experimental code in Fig. 4.3 from different HPHT cycles were selected for neutron diffraction experiments, as each HPHT cycle can only yield a product of ~15 mg. These Co_2ScSbO_6 compounds, which were well-mixed and prepared for NPD measurement at WISH, will be discussed in a later section.

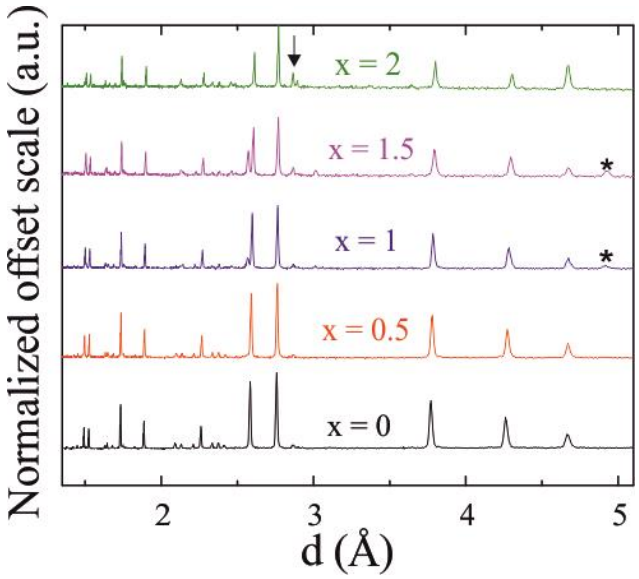

Fig. 4.2 A stacked plot of the raw powder X-ray data collected from ambient pressure samples $Ni_{2-x}Co_xScSbO_6$ (x = 0, 0.5, 1, 1.5) and high-pressure sample #2 Co_2ScSbO_6 (x = 2). The arrow refers to the main peak position of the impurity $Sc_{5.5}Sb_{1.5}O_{12}$ and the asterisks in x = 1 and 1.5 patterns mark the location of main the $Co_{2.33}Sb_{0.67}O_4$ spinel reflection.

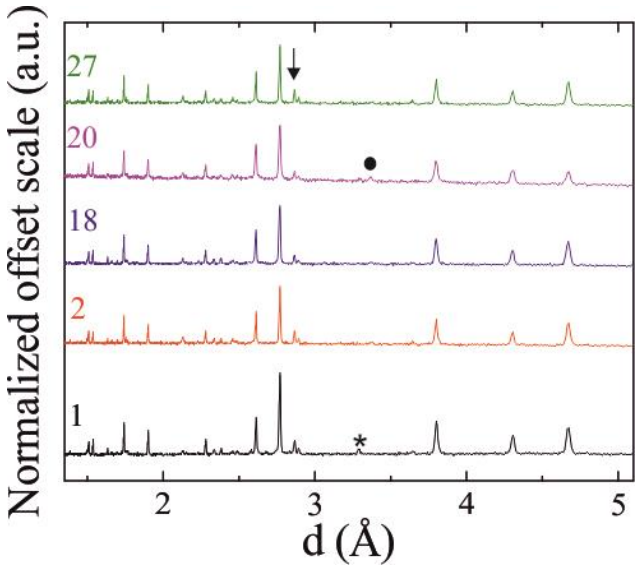

Fig. 4.3 A stacked plot of the raw powder X-ray data sets of Co_2ScSbO_6 labelled with the experimental code. The arrow, black spot and asterisk represent the locations of $Sc_{5.5}Sb_{1.5}O_{12}$, BN and $CoSb_2O_6$ impurities' main reflections, respectively.

These compounds were mixed and measured at the WISH neutron diffractometer. The preliminary structural characterisation of $Ni_{2-x}Co_xScSbO_6$ XRD at 300 K were performed using the GSAS software. The earlier published data of Ni_2ScSbO_6 was used as a starting model for structural refinement. The Rietveld method could be successfully carried out using the lab XRD patterns shown in Fig. 4.4, with space group *R*3 and lattice parameters a = 5.2207(1) Å and c = 14.0086(2) Å (using x = 2 as an example). The crystal structure is related to the corundum (Al_2O_3) type structure with Ni(Co)1, Ni(Co)2, Sc and Sb replacing Al in an ordered path. Lattice parameters coherently evolve with increasing proportions of Co^{2+}, according to its larger ionic radius with respect to that of Ni^{2+} ($r_{Co^{2+}}$ = 0.745 Å and $r_{Ni^{2+}}$ = 0.69 Å)[19]. The crystallographic structure of $Ni_{2-x}Co_xScSbO_6$, depicted in Fig. 4.4 insert, reveals Ni(Co)1/Sc, Ni(Co)2/Sb edge sharing octahedra forming layers along the *z*-axis. As there are four crystallographically distinct cation sites in this type of structure, the investigation of whether Co substitution has a site preference or whether there exists site-selective antisite exchange has been attempted. Accurate cation and oxygen positions are also necessary for further BVS and net polarisation calculations. However, the similar atomic number of Ni (28), Co (27) and Sc (21) do not allow for a proper structural determination of these compounds based on an XRD pattern, which means further characterisation through neutron diffraction is needed, as NPD allows precise locations of cations and O^{2-} anions to be determined, as well as the magnetic structures. The results from Rietveld refinements of this material, including lattice parameters and the weight percentage of impurities, are listed in Table 4.1.

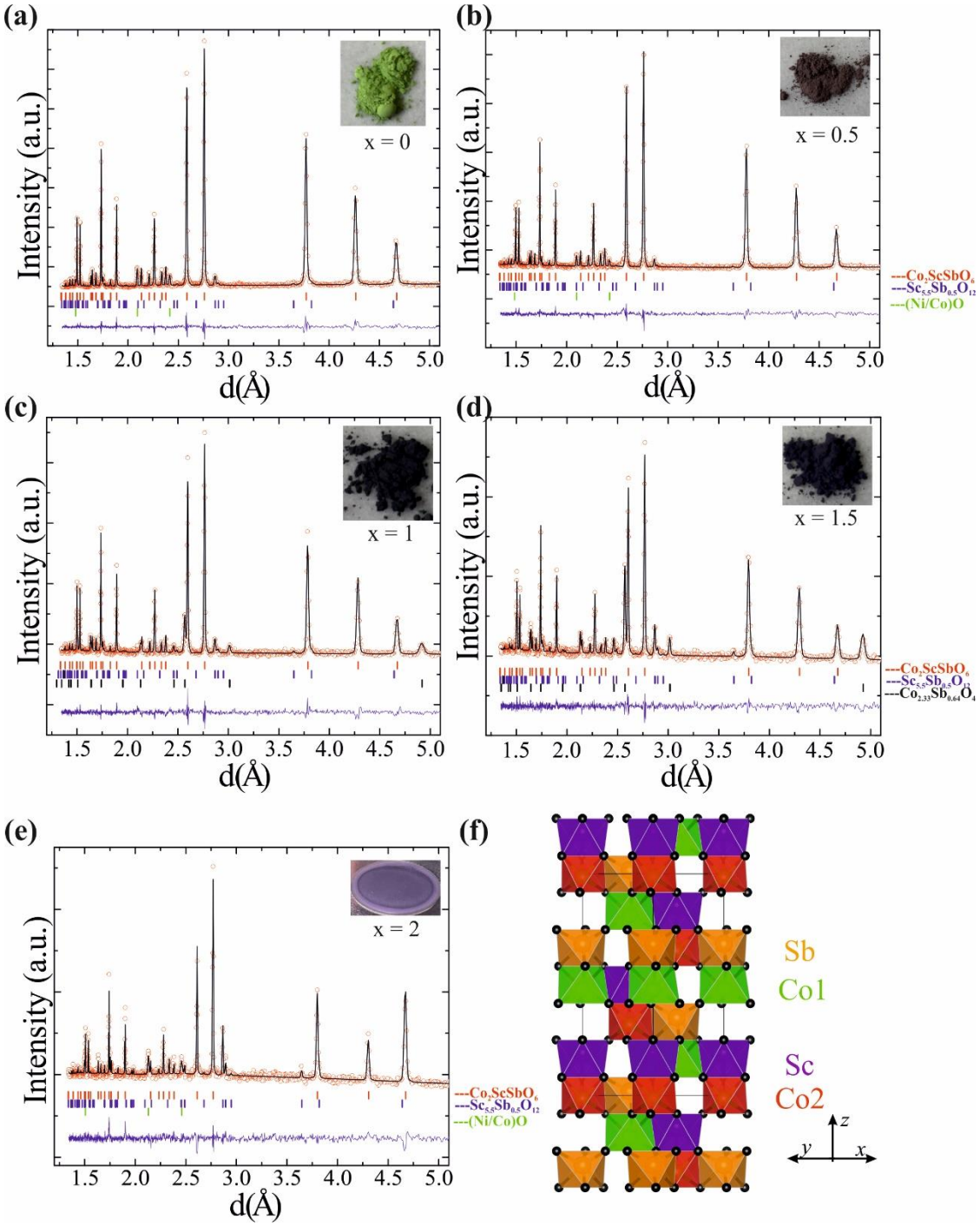

Fig. 4.4. **(a)**, **(b)**, **(c)**, **(d)** and **(e)** The Rietveld fits of the room temperature XRD data for $Ni_{2-x}Co_xScSbO_6$ (x = 0, 0.5 ,1, 1.5 and 2 respectively). The secondary $Sc_{5.5}Sb_{1.5}O_{12}$ (blue) and (Ni/Co)O phases (green) are included in all the refinement patterns and the additional $Co_{2.33}Sb_{0.64}O_4$ spinel phase (black) is also included for x = 1, 1.5. **(f)**The structural model of x = 2 as an example (Co1, Co2, Sc and Sb depicted in green, red, blue and orange respectively) and the powder sample colours. Structural image generated using VESTA[20].

Table 4.1 Results from Rietveld refinements of the structures of $Ni_{2-x}Co_xScSbO_6$ measured at 300 K including lattice parameters and impurity weight percentage. (AP for ambient pressure)

x	*a* (Å)	*c* (Å)	$Sc_{5.5}Sb_{0.5}O_{12}$ (wt %)	$Co_{2.33}Sb_{0.64}O_4$ (wt %)	(Ni/Co)O (wt %)	χ^2	R_{wp} (%)
0	5.1700(1)	14.014(1)	2.9	--	6.3	2.86	4.91
0.5	5.1847(1)	14.021(1)	2.7	--	5.0	1.70	3.35
1	5.1965(1)	14.023(1)	10.2	3.7	--	1.47	2.68
1.5	5.2123(1)	14.026(1)	16.2	6.4	--	1.40	2.49
2 (AP)	5.2258(4)	14.011(2)	17.3	19.5	--	1.93	2.93
2 (6 GPa)	5.2207(1)	14.009(1)	8.1	1.9	--	1.80	1.31

4.4.2 Neutron powder diffraction: nuclear & magnetic structures of $Ni_{2-x}Co_xScSbO_6$

Using neutron powder diffraction data for $Ni_{2-x}Co_xScSbO_6$ samples collected from the SPODI (FRMII, Munich), D20 (ILL, Grenoble) and WISH (ISIS, Oxford) diffractometers, the crystal and magnetic structures were studied at several temperatures ranging from 1.7 K to 100 K. Rietveld analyses of all sample profiles were carried out to refine the structural models using the FullProf software package.**Error! Bookmark not defined.** The pseudo-Voigt profile function was introduced to describe the shape of the diffraction peaks. The background was fitted using equidistant experimental points and modelled using an interpolation method. The patterns could be fitted using the NTO type structure (space group *R*3) determined from the initial analysis of the laboratory XRD data.

The Rietveld fit to the 100 K NPD data (a mixture of sample #1, 2, 18, 20 and 27, a total sample weight of 48 mg, collected from WISH@ISIS) of Co_2ScSbO_6 (x = 2) confirms that it adopts the NTO-type structure with polar space group *R*3. The Rietveld fits of NPD patterns and the crystal structure are shown in Fig. 4.5 and Fig. 4.6, respectively. The NPD data can be indexed on the basis of a trigonal unit cell with $a = b = 5.2264(1)$ Å and $c = 14.0148(4)$ Å. All the cations on the Wyckoff 3*a* (1/3, 2/3, *z*) or (2/3, 1/3, *z*) positions are 6-coordinated forming slightly distorted octahedra with 3 long M-O bonds and 3 short M-O bonds and oxygen anions occupy the general Wyckoff 9*b* site. (00l) layers are constituted by ordered Co1-Sc (green-purple) and Co2-Sb (red-orange) edge-sharing octahedra, while face-sharing Co1-Sb and Co2-Sc ordered twin-octahedra are constructed along the *z*-axis. 2/3 of the octahedral cavities are occupied in this framework. All the cations in Co_2ScSbO_6 are shifted from the centre of their octahedra, as is usually observed in the corundum derivatives. This shift can be determined by

calculating the difference between the ideal and experimental *z* coordinates of each atom. The resulting cation shifts of Co1 and Co2 are 0.154 Å and 0.387 Å respectively. The cation displacements, resulting in puckered (00z) layers, are also related to the octahedral distortion. The experimental octahedral distortions listed are calculated from Eq. 4.1 as shown:

$$\Delta = \frac{1}{n}\sum_{1}^{n}\left(\frac{d_i - \bar{d}}{d}\right)^2 \qquad (4.1)$$

Where d_i and $\bar{d}$ refer to the individual and average M-O bond distances respectively in each octahedron.

It is important to note that in contrast with the parent Ni_3TeO_6 (NTO) compound, which has a collinear antiferromagnetic structure, introducing nonmagnetic Sc^{3+} and Sb^{5+} ions into the framework creates holes between the Ni(Co)1 and Ni(Co)2 magnetic sublattices which possibly increases spin frustrations so as to change the magnetic structure. This will be discussed later in detail. Rietveld analyses of NPD data confirm the secondary phases are $Sc_{5.5}Sb_{1.5}O_{12}$ (9.4%), CoO (7.8%) and $CoSb_2O_6$ (3%) with low intensity BN and V signals. BN and V impurities come from the BN capsule container used during HPHT experiments and the vanadium sample containers used in neutron experiments respectively. However, by refining the Co/Sc cation occupancies, it revealed a 21% substitution of Sc by Co, resulting in a Sc-deficient overall composition $Co_{2.16}Sc_{0.84}SbO_6$. The resulting crystallographic parameters from the 100 K NPD data of Co_2ScSbO_6 are summarised in Table 4.2.

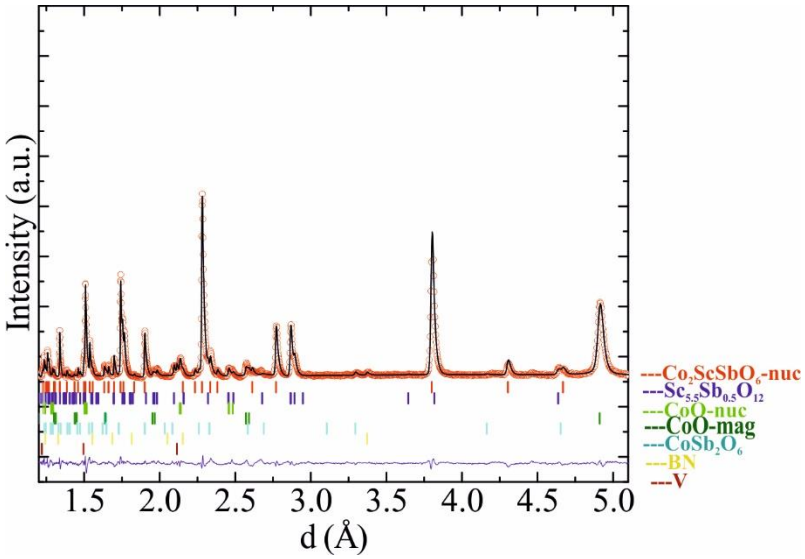

Fig. 4.5 Rietveld fit to the 100 K NPD data of Co_2ScSbO_6. Additional blue, green, olive Bragg marks identify secondary $Sc_{5.5}Sb_{1.5}O_{12}$ (9.4%), CoO (7.8%) and the magnetic reflections of CoO, respectively. The cyan, yellow and dark red tick marks refer to impurities of $CoSb_2O_6$, BN and V respectively.

Table 4.2 Crystallographic data for the NTO-type structure of Co_2ScSbO_6 from the Rietveld fit of the 100 K NPD pattern. BVS and cationic displacements (*d*) in the puckered (00l) layers, calculated from these results, are included in the two last columns.

Wyckoff	Atom	x	y	z	Occ	B_{iso}(Å^2)	BVS	*d*(Å)
3a	Co1	1/3	2/3	0.150(2)	1.0	0.6(1)	1.64 (2)	0.234 (2)
3a	Co2/Sc	2/3	1/3	0.300(2)	0.951/0.048(3)	0.6(1)	2.12 (2)	0.467 (2)
3a	Sc/Co2	2/3	1/3	0.515(1)	0.792/0.207(3)	0.6(1)	2.93 (3)	-0.210 (2)
3a	Sb	1/3	2/3	0.350(1)	1.0	0.6(1)	5.66 (2)	-0.234 (2)
9b	O1	0.323(1)	0.035(2)	0.072(1)	1.0	0.88(1)	_	_
9b	O2	0.323(1)	0.360(1)	1/4	1.0	0.88 (1)	_	_

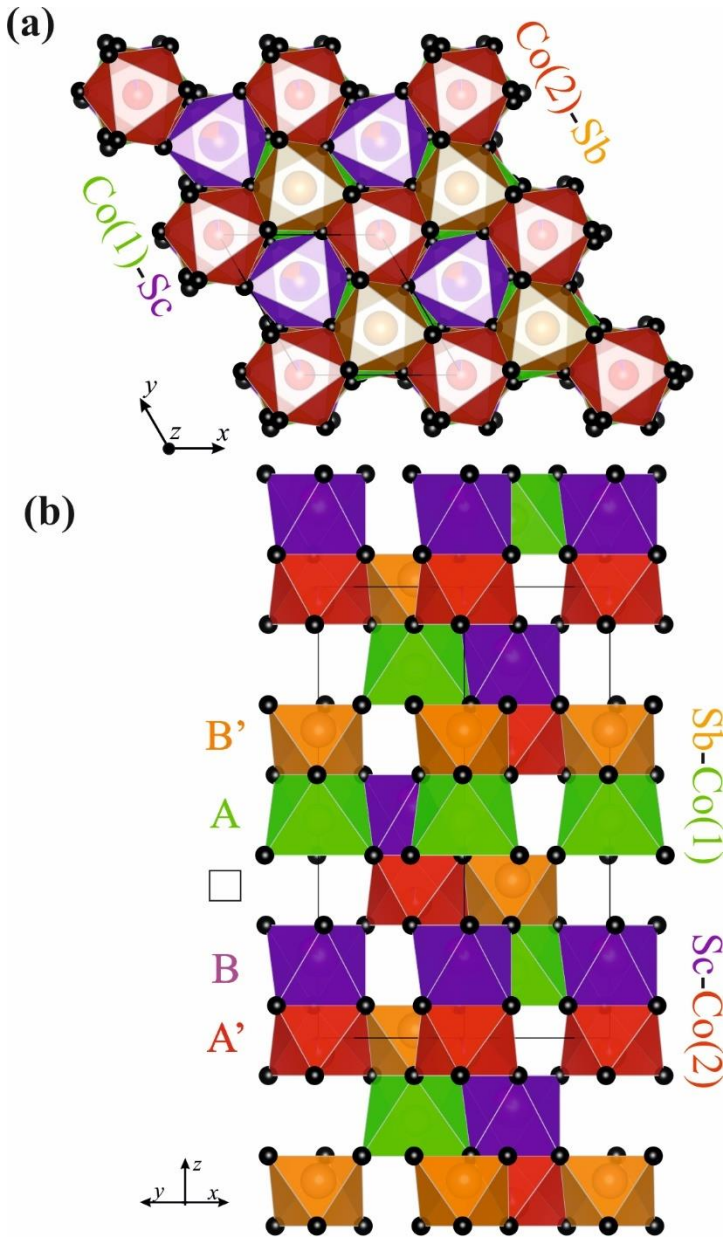

Fig. 4.6 Polyhedral representations of the Co_2ScSbO_6 crystal structure. **(a)** honeycomb-like *ab* planes of edge sharing octahedra (Co(1)-Sc, Co(2)-Sb) and **(b)** layers of edge-sharing cation octahedra (Co(1)-Sb, Co(2)-Sc) stacked by face-sharing along the *z*-axis. The group of letters included on the left-hand side shows the stacking sequence. Co(1), Co(2), Sc and Sb are shown in green, red, purple and orange octahedra respectively. Oxygen atoms are depicted as black spheres. Images generated using VESTA[20].

Rietveld fits to 100 K NPD data (Fig. 4.7) of x = 0, 0.5, 1 and 1.5 (collected from SPODI@FRMII) $Ni_{2-x}Co_xScSbO_6$ samples confirm that a continuous NTO-type solid solution is formed. Combined with the NPD data of Co_2ScSbO_6, the evolution of the lattice parameters depicted in Fig. 4.8 (a) reveal that lattice parameters *a* and *c* of Ni_{2-}

$_x$Co$_x$ScSbO$_6$ generally increase with increasing proportions of Co^{2+}. The asymmetric increase of the lattice parameters *a* and *c* reveal a linear evolution of the hexagonal distortion (*c*/*a*) in the $Ni_{2-x}Co_xScSbO_6$ system. In addition, the reduction of the *c*/*a* ratio against x shown in Fig. 4.8 (b) reveals structural anisotropy arising from the electronic degeneracy of the Co^{2+} ions. In agreement with the details reported by Ivanov et. al,[13] no antisite exchange between Ni/Sc sites was observed in the pure Ni material (x = 0). However, the presence of Co content has been observed to induce site-selective antisite disorder between Co^{2+} and Sc^{3+} cations located in face-sharing octahedra and the amount of substitution of Sc^{3+} by Co^{2+} ions that increases with increasing Co content x is observed across the whole series as shown in Fig. 4.9. The main interatomic distances, M-O-M bond angles and octahedral distortions (*⊿*) arising from these refinements are summarised in Table 4.3. The Ni(Co)-O bond lengths also increase progressively with increasing x, while Sc-O and Sb-O distances almost remain constant throughout the system. All the cation-oxygen bond lengths calculated from the atomic coordinates in Rietveld analysis are in reasonable agreement with the literature data collected from the ICSD.[18] Bond valence sum (BVS) calculations, determined using a standard interpolation method[21] from the obtained experimental bond distances, are consistent with the expected Ni^{2+}, Co^{2+}, Sc^{3+} and Sb^{5+} oxidation states for all the compounds. The net ferroelectric polarisation of Co_2ScSbO_6 (P_S = 19.91 μC/cm^2), which was calculated according to the cationic displacements (Eq. 4.2) using a point charge model[22], is comparable to the value for Ni_2ScSbO_6 of P_S = 13.27 μC/cm^2.

$$P = \frac{e}{V}\sum_i q_i \overrightarrow{r_i} \qquad (4.2)$$

In the Eq. 4.2 listed above, *e* refers to the electron charge (C) while *V* is the unit cell volume (m^3). The q_i stands for the electronic charge of each cation and $\overrightarrow{r_i}$ (m) represents the cationic displacement along the *z*-axis. The resulting crystallographic parameters from the 100 K NPD data (x = 0, 0.5, 1, 1.5), including accurate atomic positions, relative occupancies, thermal factors, BVS calculations and cation displacements are summarised in Table 4.4 – 4.7. The refinement data are listed in Table 4.8.

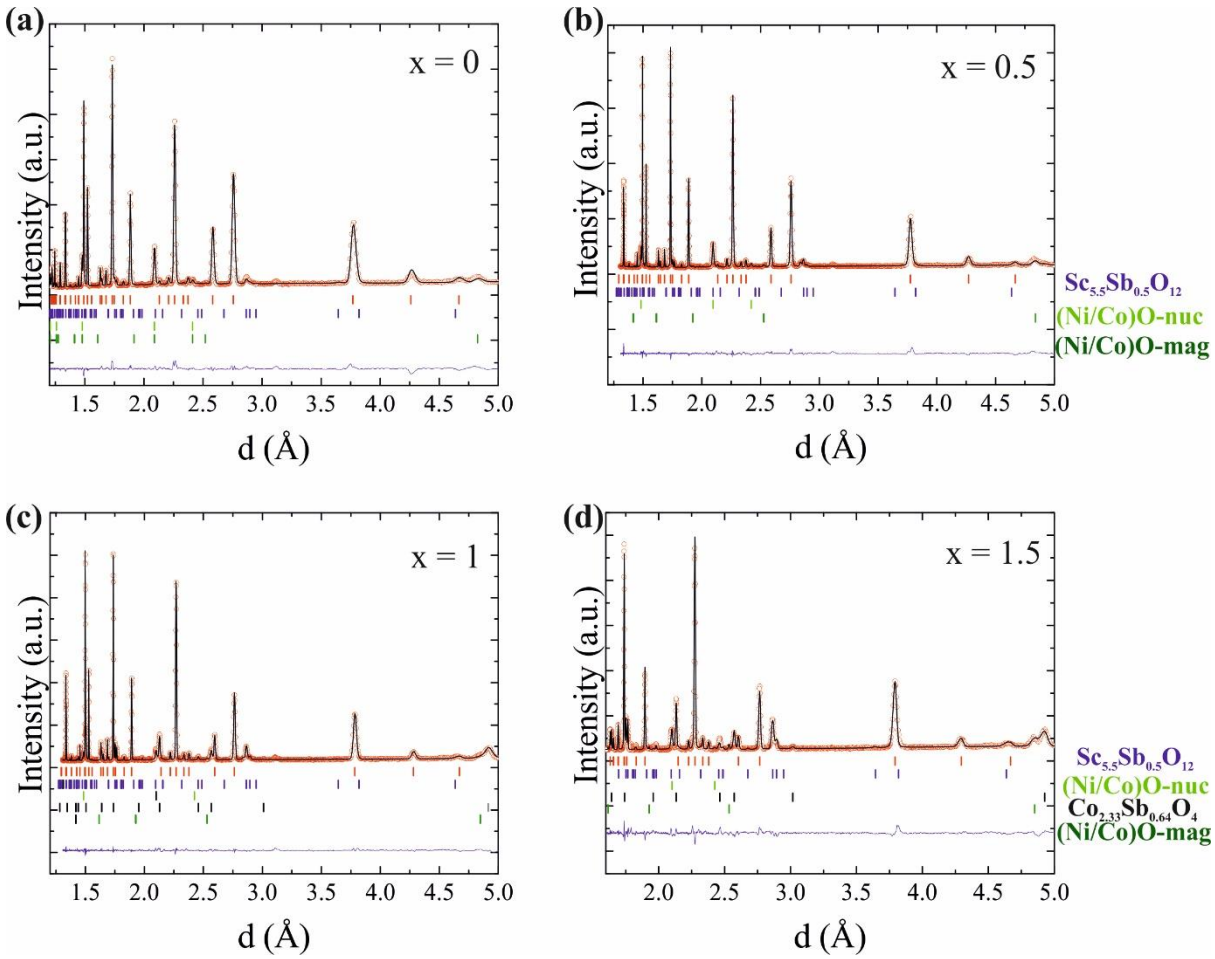

Fig. 4.7. **(a)**, **(b)**, **(c)** and **(d)** The Rietveld fits of the NPD patterns of the NTO solid solutions $Ni_{2-x}Co_xScSbO_6$ (x = 0, 0.5, 1, 1.5, respectively) compounds collected at 100 K. The secondary $Sc_{5.5}Sb_{1.5}O_{12}$ (blue) phase is included in all refinements. Nuclear (green) and magnetic phases (dark green) of the (Ni/Co)O are also included in all refinements. The additional $Co_{2.33}Sb_{0.64}O_4$ spinel (black) is included for x = 1, 1.5. All the secondary phases are listed.

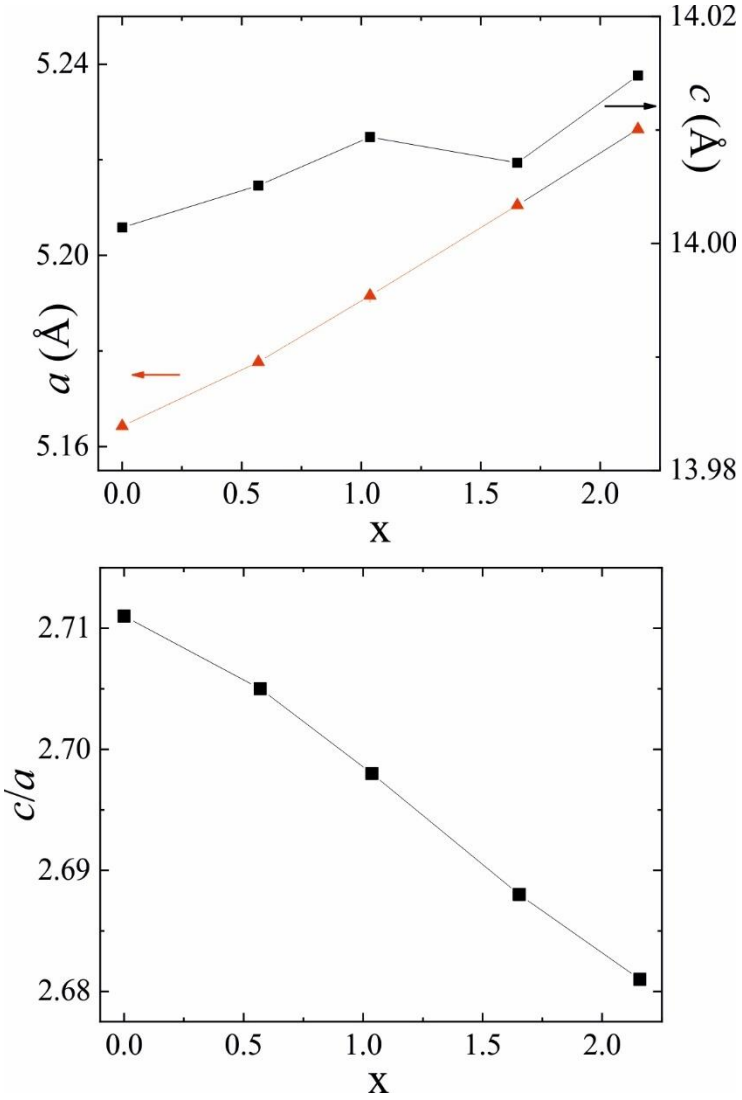

Fig. 4.8 Evolution of the lattice parameters **(a)** and the *c/a* ratio **(b)** of $Ni_{2-x}Co_xScSbO_6$ as a function of the chemical composition, showing that the solid solutions have been successfully formed and the structural anisotropy is confirmed from the trend of *c/a* ratio against x. The error bars are smaller than the marker size.

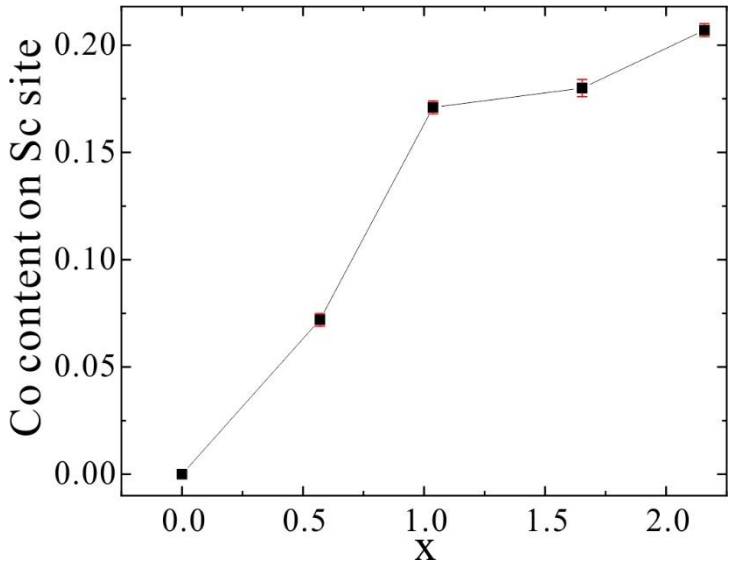

Fig. 4.9 The evolution of the proportion of Co at the Sc site with the amount of Co content exhibiting an approximately positive relationship.

Table 4.3. Bond lengths ($d_{M\text{-}O}$), average M-O distances ($\bar{d}$), angles and octahedral distortions (Δ) of $Ni_{2-x}Co_xScSbO_6$ compounds.

x	$d_{M1\text{-}O}$ (Å)	$d_{M2\text{-}O}$ (Å)	$d_{Sc\text{-}O}$ (Å)	$d_{Sb\text{-}O}$ (Å)	<M1-O1-M2>°	<M1-O2-M2>°
0	3 x 2.06(1) 3 x 2.15(1) $\bar{d}$ = 2.105 (1) Δ = 4.57E-4	3 x 2.11(1) 3 x 2.04(1) $\bar{d}$ = 2.075(1) Δ = 2.85E-4	3 x 2.16(1) 3 x 2.03(1) $\bar{d}$ = 2.095(1) Δ = 9.63E-4	3 x 1.96 (1) 3 x 2.07 (1) $\bar{d}$ = 2.015(1) Δ = 7.45E-4	128.6(2)	131.7(2)
0.5	3 x 2.10(1) 3 x 2.08(1) $\bar{d}$ = 2.09(1) Δ = 2.29E-5	3 x 2.08(1) 3 x 2.10(1) $\bar{d}$ = 2.09(1) Δ = 2.29E-5	3 x 2.25(1) 3 x 1.97(1) $\bar{d}$ = 2.11(1) Δ = 4.40E-3	3 x 1.91(1) 3 x 2.08(1) $\bar{d}$ = 1.995(1) Δ = 1.82E-3	127.7(2)	131.9(3)
1.0	3 x 2.04(1) 3 x 2.17(1) $\bar{d}$ = 2.105(1) Δ = 9.54E-4	3 x 2.14(1) 3 x 2.06(1) $\bar{d}$ = 2.10(1) Δ = 3.63E-4	3 x 2.14(1) 3 x 2.05(1) $\bar{d}$ = 2.095(1) Δ = 4.61E-4	3 x 1.97(1) 3 x 2.07(1) $\bar{d}$ = 2.02(1) Δ = 6.13E-4	125.3(3)	133.7(3)
1.5	3 x 2.10(1) 3 x 2.16(2) $\bar{d}$ = 2.13(2) Δ = 1.98E-4	3 x 2.23(2) 3 x 1.99(1) $\bar{d}$ = 2.11(2) Δ = 3.23E-3	3 x 2.10(1) 3x 2.08(1) $\bar{d}$ = 2.09(1) Δ = 2.29E-5	3 x 1.95(1) 3 x 2.07(2) $\bar{d}$ = 2.01(2) Δ = 8.91E-4	124.7(3)	130.9(3)
2.0	3 x 2.24(2) 3 x 2.1(1) $\bar{d}$ = 2.17(2) Δ = 1.04E-3	3 x 2.18(3) 3 x 1.99(1) $\bar{d}$ = 2.085(3) Δ = 2.08E-3	3 x 2.22(1) 3 x 2.03(1) $\bar{d}$ = 2.125(1) Δ = 1.99E-3	3 x 1.86(1) 3 x 2.11(1) $\bar{d}$ = 1.985(1) Δ = 4.07E-3	127.6(3)	127.1(4)

Table 4.4. Crystallographic data for the NTO-type structure of Ni_2ScSbO_6 from the Rietveld fit of the 100 K NPD pattern. BVS and cationic displacements (*d*) in the puckered (00l) layers, calculated from these results, are included in the two last columns.

Wyckoff	Atom	x	y	z	Occ	B_{iso}(Å^2)	BVS	*d*(Å)
3a	Ni1	1/3	2/3	0.1437(4)	1.0	0.78(1)	1.80(1)	0.322(1)
3a	Ni2	2/3	1/3	0.3145(4)	1.0	0.78(1)	1.94(1)	0.264(1)
3a	Sc	2/3	1/3	0.5168(6)	1.0	0.78(1)	3.17(1)	-0.235(1)
3a	Sb	1/3	2/3	0.348(1)	1.0	0.78(1)	5.01(2)	-0.205(2)
9b	O1	0.316(1)	0.016(1)	0.0796(4)	1.0	0.85(1)	_	_
9b	O2	0.329(2)	0.364(1)	1/4	1.0	0.85(1)	_	_

Table 4.5. Crystallographic data for the NTO-type structure of $Ni_{1.5}Co_{0.5}ScSbO_6$ from the Rietveld fit of the 100 K NPD pattern. BVS and cationic displacements (*d*) in the puckered (00l) layers, calculated from these results, are included in the two last columns.

Wyckoff	Atom	x	y	z	Occ	B_{iso} (Å^2)	BVS	*d*(Å)
3a	M1 (Ni/Co)	1/3	2/3	0.1494(3)	0.712/0.288(3)	0.3(1)	1.82 (1)	0.241 (1)
3a	M2 (Ni/Co)	2/3	1/3	0.3196(4)	0.79/0.21(1)	0.3(1)	1.82 (2)	0.192 (1)
3a	Sc/Co2	2/3	1/3	0.5246(3)	0.928/0.072(3)	0.3(1)	3.15 (2)	-0.344 (2)
3a	Sb	1/3	2/3	0.3506(4)	1.0	0.3(1)	5.31 (2)	-0.242 (2)
9b	O1	0.323(1)	0.023(1)	0.079(1)	1.0	0.4(1)	_	_
9b	O2	0.325(1)	0.366(1)	1/4	1.0	0.4(1)	_	_

Table 4.6. Crystallographic data for the NTO-type structure of $NiCoScSbO_6$ from the Rietveld fit of the 100 K NPD pattern. BVS and cationic displacements (*d*) in the puckered (00l) layers, calculated from these results, are included in the two last columns.

Wyckoff	Atom	x	y	z	Occ	B_{iso} (Å^2)	BVS	*d*(Å)
3a	M1 (Ni/Co)	1/3	2/3	0.1409(4)	0.482/0.518(3)	0.6(1)	1.79 (1)	0.361 (1)
3a	M2 (Ni/Co)	2/3	1/3	0.3174(3)	0.652/0.348(5)	0.6(1)	1.81 (1)	0.223 (1)
3a	Sc/Co2	2/3	1/3	0.5193(3)	0.829/0.171(3)	0.6(1)	3.12 (1)	-0.270 (2)
3a	Sb	1/3	2/3	0.3485(4)	1.0	0.6(1)	4.91 (3)	-0.212 (2)
9b	O1	0.321(1)	0.024(1)	0.085(1)	1.0	0.4(1)	_	_
9b	O2	0.335(1)	0.371(1)	1/4	1.0	0.4(1)	_	_

Table 4.7. Crystallographic data for the NTO-type structure of $Ni_{0.5}Co_{1.5}ScSbO_6$ from the Rietveld fit of the 100 K NPD pattern BVS and cationic displacements (*d*) in the puckered (00l) layers, calculated from these results, are included in the two last columns.

Wyckoff	Atom	x	y	z	Occ	B_{iso}(Å^2)	BVS	d(Å)
3a	M1 (Ni/Co)	1/3	2/3	0.142(2)	0.184/0.816(5)	0.4(1)	1.65(2)	0.345(2)
3a	M2 (Ni/Co)	2/3	1/3	0.306(1)	0.343/0.657(6)	0.4(1)	1.84(2)	0.383(2)
3a	Sc/Co2	2/3	1/3	0.514(1)	0.820/0.180(4)	0.4(1)	3.10(3)	-0.196 (1)
3a	Sb	1/3	2/3	0.348(2)	1.0	0.4(1)	5.06(3)	-0.205 (1)
9b	O1	0.321(1)	0.031(2)	0.083(1)	1.0	0.5(1)	_	_
9b	O2	0.335(2)	0.370(1)	1/4	1.0	0.5(1)	_	_

Table 4.8 Refinement data for $Ni_{2-x}Co_xScSbO_6$. All crystallised in space group *R*3. Phase fractions of the $Ni_{2-x}Co_xScSbO_6$ and secondary phases $Sc_{5.5}Sb_{0.5}O_{12}$ (SSO), (Ni/Co)O (NCO), $Co_{2.33}Sb_{0.64}O_4$ (CSO), $CoSb_2O_6$ (CS2O), BN, V are listed.

x	Lattice parameters (Å)	Cell volume (Å^3)	N. of formula unit	Density (g / mol)	N. of the refined parameters	R-factors (%)	χ^2	Phase fraction (wt %)
0	*a* = 5.16427(2) *c* = 14.0014(1)	323.386(3)	3	5.855(1)	19	R_p=3.43 R_{wp}=4.31 R_B=3.34 R_F=1.90	6.01	x = 0: 90.1(4) SSO: 5.8(2) NiO: 4.1(1)
0.5	*a* = 5.17768(3) *c* = 14.0051(1)	325.152(4)	3	5.840(1)	26	R_p=3.80 R_{wp}=5.05 R_B=3.00 R_F=2.20	5.25	x = 0.5: 87.1 (1) SSO: 6.9(2) NCO: 6.0(1)
1	*a* = 5.19158(1) *c* = 14.0094(1)	327.000(1)	3	5.830(1)	26	R_p=3.26 R_{wp}=4.48 R_B=1.08 R_F=1.10	3.99	x = 1: 70.0(1) SSO:10.1(1) NCO: 2.5(1) CSO:17.4(1)
1.5	*a* = 5.21051(2) *c* = 14.0071(1)	329.335(3)	3	5.793(1)	26	R_p=5.90 R_{wp}=7.69 R_B=3.62 R_F=2.05	11.0	x = 1.5: 65.3(1) SSO:16.7(1) NCO: 3.1(1) CSO:14.9(1)
2	*a* = 5.2264(1) *c* = 14.0148(4)	331.53(1)	3	5.747(2)	30	R_p=2.49 R_{wp}=3.06 R_B=3.71 R_F=5.50	7.45	x = 2: 80.0(1) SSO: 9.5(1) CoO: 7.8(1) CS2O:1.8(1) BN: 0.5(1) V: 0.4(1)

As discussed earlier the neutron diffraction patterns of $Ni_{2-x}Co_xScSbO_6$ show the purely nuclear structure at 100 K and adopt the *R*3 space group, revealing that it is paramagnetic at this temperature. Low temperature neutron diffraction patterns exhibited additional magnetic reflections which confirmed the existence of long-range magnetic ordering below 60 K, as suggested by magnetisation data. Fig. 4.10 shows the evolution of the principal magnetic diffraction contributions in the $Ni_{2-x}Co_xScSbO_6$ series, obtained by

subtracting the 100 K from the 4K NPD profiles (collected from WISH@ISIS for x = 2; SPODI@FRMII for x = 0, 0.5, 1, 1.5). This difference plot of pure magnetic scattering in the region of 3.6 Å < *d* < 5.1 Å reveals that magnetic reflections not only overlap with the nuclear peaks but appear at positions that were not present in the nuclear pattern, as expected for an antiferromagnetic ordering. It is necessary to note that (101) peak position shifting to the high *d*-spacing region shown here also illustrates the successful chemical substitution of smaller Ni^{2+} ions by Co^{2+} ions.

The indexing program 'K-search' installed in the FullProf Suite**Error! Bookmark not defined.** was used to determine the propagation vector of the magnetic structure. As the magnetic satellites cannot be indexed by any propagation vectors directly proportional to the nuclear unit cell, we can only index them with an incommensurate propagation vector. Ni_2ScSbO_6 (x = 0) has prominent magnetic satellite reflections around the (101) peak and a magnetic contribution on top of the nuclear (003) peak, which arises from an incommensurate [0 0.036(1) 0] magnetic propagation vector. The spins were constrained within the *xz* plane and propagated along the *y*-axis as shown in Fig. 4.16a. This is in good agreement with the results in the previous report of Ni_2ScSbO_6.[13] Introduction of Co^{2+} ions to the Ni sites in Ni_2ScSbO_6, giving the x = 0.5 sample, leads to a dramatic change in the magnetic scattering as the splitting between the (101) satellites decreases greatly, and a new pair of satellites appears around (003) while the fundamental peak disappears. These magnetic reflections were indexed by a different [0 0 k_z] propagation vector. The magnetic symmetry analysis of the low temperature NPD data was performed by means of BasIreps[17] software to determine the allowed irreducible representations (Ireps) and basis vectors (BV) for the propagation vector performed in the *R*3 space group. The Ireps and BV describing the magnetic structures of $Ni_{2-x}Co_xScSbO_6$ resulting from the incommensurate propagation vector [0 0 k_z] is summarised in Table 4.9. Their BVs describe the alignment of the spins either parallel to the *z* axis (Ψ_1) or in planes of clockwise (CW, Ψ_2) or counter-clockwise (CCW, Ψ_3) spirals. Since the main magnetic reflections are observed near the (003) and (101) peaks and the propagation vector is the incommensurate [0 0 k_z], Ψ_1 can therefore be excluded. All the Rietveld fits of the low temperature NPD data (Fig. 4.11) have been performed well using Irep Γ_2 for the incommensurate magnetic structures although powder diffraction does not distinguish between CW and CCW helices, so Γ_3 would be equally applicable as well. Spins at the Ni(Co)1 site are coupled ferromagnetically within the (00z) layers while coupled antiferromagnetically with the spins at Ni(Co)2 site of the

adjacent layers and the spin-spin interactions are frustrated along the *z*-direction, as expected from the helical magnetic structure (Fig. 4.16b) with an incommensurate propagation vector. The [0 0 k_z] phase persists across all the Co-substituted compounds with a decrease in k_z, as evidenced by the decreasing splitting between satellite pairs around (101) and (003) in Fig. 4.10. It is notable that all four measured k_z values are within an error of 1/3*n* periodicities for integers *n* = 5, 6, 8 and 10. This demonstrates that the [0 0 k_z] magnetic structures are actually not incommensurate, but are instead locked into a series of very long periodic commensurate spirals (up to 420 Å for *n* = 10 Co_2ScSbO_6), as will be discussed later.

An additional contribution on top of the nuclear Bragg (003) peak appears in x = 1.5 and x = 2 compounds which cannot be indexed with [0 0 k_z], revealing an additional commensurate magnetic phase with the propagation vector *k* = [0 0 0]. The commensurate [0 0 0] component has another three possible Ireps as shown in the bottom row of Table 4.9, which allows the orientation of the spins along the *z* axis (Ψ_1) or confines them to the *xy* plane with independent FM (Ψ_2) or AFM (Ψ_3) components. The intensities were fitted as shown in Fig. 4.12 using Irep Γ_2 with spins confined along the *x*-axis as shown in Fig. 4.16c. This corresponds to the n → ∞ limit of the above [0 0 k_z] series. An important difference is that the [0 0 0] commensurate magnetic phase has antiparallel layers of inequivalent Co(Ni)1 and Co(Ni)2 site spins and so is ferrimagnetic, whereas these spin layers are successively rotated in the [0 0 k_z] spirals with finite *n* which are thus antiferromagnetic. The Rietveld fits, to low temperature NPD data of each $Ni_{2-x}Co_xScSbO_6$ compound in the *d*-spacing range of 3.6 Å < *d* < 5.0 Å, showing the clear refinement of the magnetic peaks are depicted in Fig. 4.12. Results of magnetic analyses of the 4 K NPD data, including the values of propagation vector *k* and the refined magnetic moments, are summarised in Table 4.10.

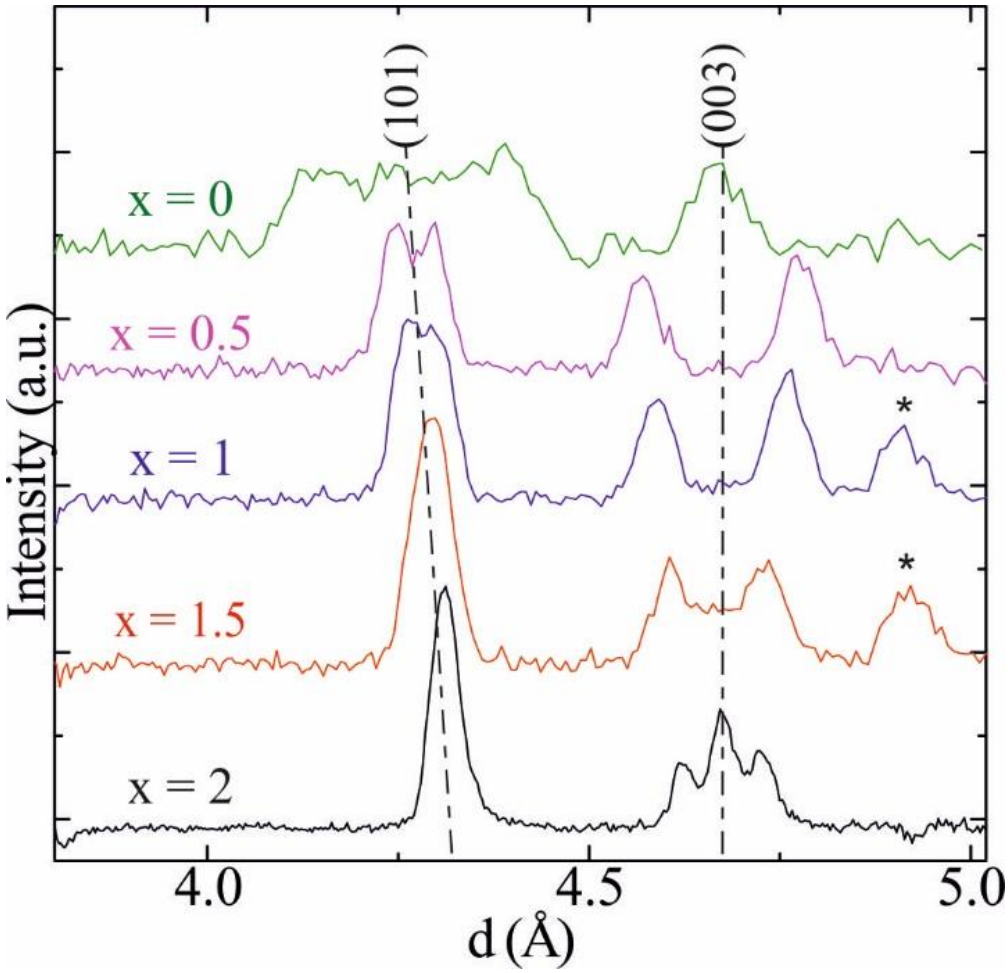

Fig. 4.10 Difference (4 K - 100 K) NPD patterns of $Ni_{2-x}Co_xScSbO_6$ showing only the magnetic reflections. The (003) and (101) peak positions are marked with dashed lines. Magnetic signals from the impurity $Co_{2.33}Sb_{0.64}O_4$ are identified with an asterisk.

Table 4.9. Irreducible representations (Ireps) and basis vectors (BV) for the magnetic symmetry analysis of $Ni_{2-x}Co_xScSbO_6$ with propagation vectors [0 0 k_z] and [0 0 0]. The [0 k_y 0] structure has been refined using the Irep reported by S. A. Ivanov.[13]

Irep (BV)	$\Gamma_1(\Psi_1)$			$\Gamma_2(\Psi_2)$			$\Gamma_3(\Psi_3)$		
	m_x	m_y	m_z	m_x	m_y	m_z	m_x	m_y	m_z
[0 0 k_z]	0	0	1	3/2 – $i\sqrt{}$ 3/2	– $i\sqrt{}3$	0	3/2 + $i\sqrt{}$ 3/2	$i\sqrt{}3$	0
[0 0 0]	0	0	1	1	1	0	1	-1	0

Note: Both independent magnetic cation sites M1 and M2 follow the same Ireps. Irep Γ_2 was used to refine the magnetic structures for both propagation vectors. Γ_2 and Γ_3 Ireps of the first structure describe clockwise and counter-clockwise helices which cannot be distinguished from powder diffraction data.

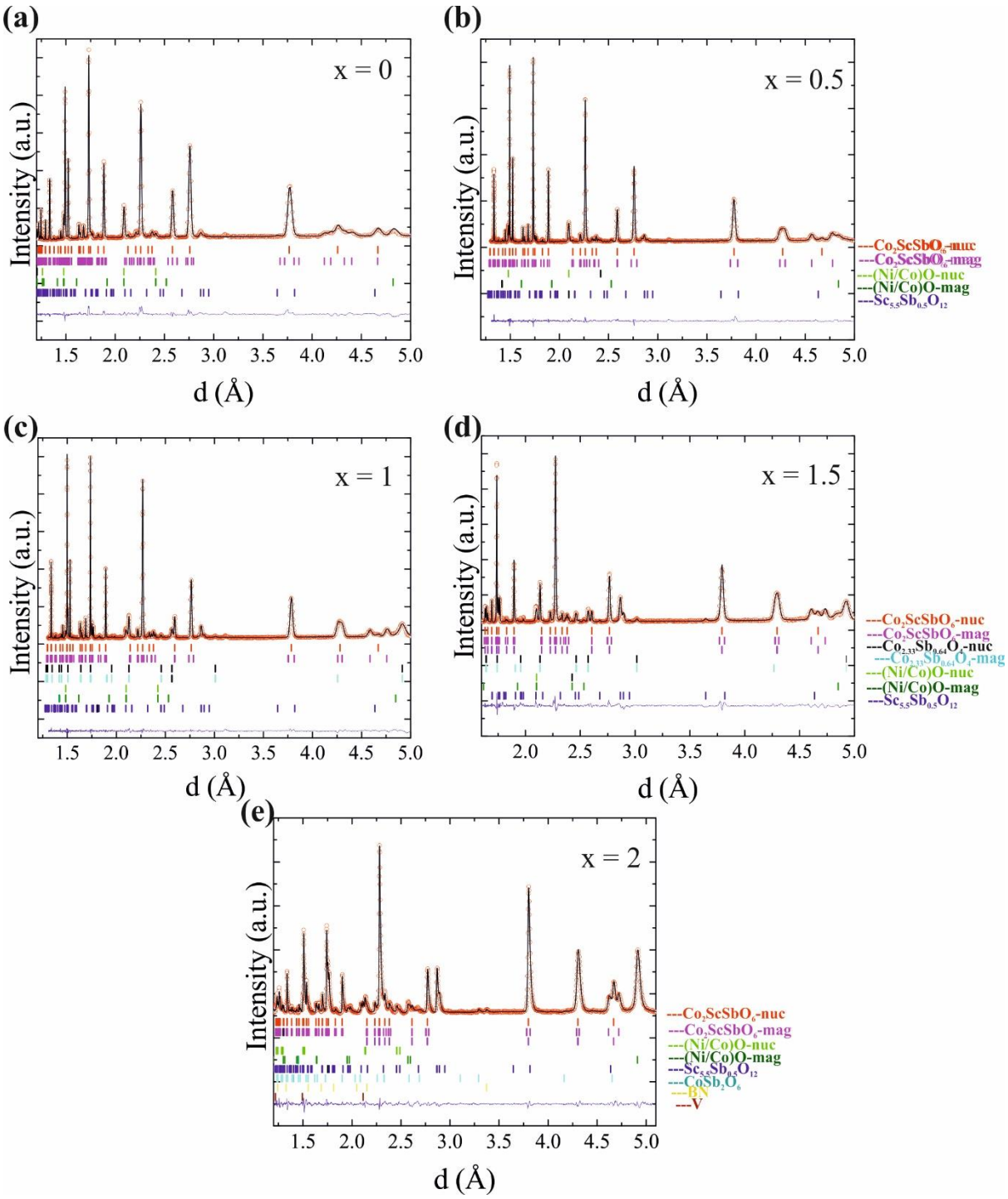

Fig. 4.11 (a), **(b)**, **(c)**, **(d)** and **(e)** The Rietveld fits of the NPD patterns of the NTO type $Ni_{2-x}Co_xScSbO_6$ compounds (x = 0, 0.5, 1, 1.5) collected at 4 K and Co_2ScSbO_6 (x = 2) NPD data collected at 1.7 K. The secondary $Sc_{5.5}Sb_{1.5}O_{12}$ (blue) and nuclear (green) and magnetic reflections (dark green) of the (Ni/Co)O phases are included in all refinements. The nuclear (black) and magnetic signal (light blue) of the $Co_{2.33}Sb_{0.64}O_4$ spinel phases are included for x = 1, 1.5. The cyan, yellow and dark red tick marks refer to impurities of $CoSb_2O_6$, BN and V respectively in the high-pressure phase x = 2. All the secondary phases are listed.

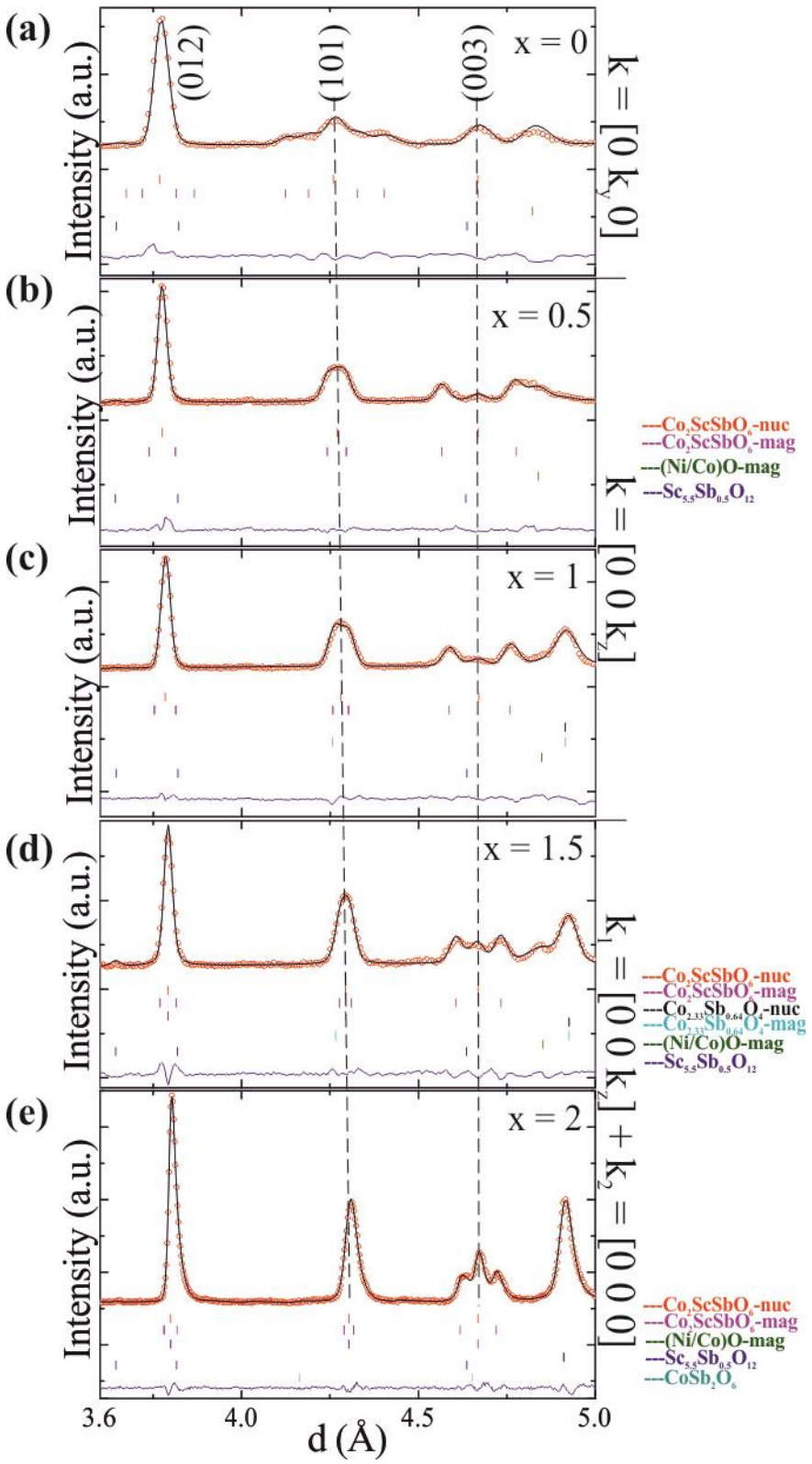

Fig. 4.12 (a), **(b)**, **(c)**, **(d)** and **(e)** refer to the Rietveld fits of 4 K neutron diffraction patterns of $Ni_{2-x}Co_xScSbO_6$ (x = 0, 0.5, 1, 1.5 and 2 respectively) in the range of 3.6 Å < *d* < 5.0 Å showing clearly the incommensurate and commensurate magnetic phases.

The commensurate magnetic contribution is clearly observed over the complete temperature range below T_C for x = 2 data collected at WISH. However, it is not clearly resolved for the x = 1.5 compound from the 50 K SPODI data as shown on the right panel of Fig. 4.13, which shows the 50 K – 70 K and 4 K – 70 K difference patterns. Therefore, the thermal evolution of the spin order for the x = 1.5 compound was also studied using D20 at ILL with wavelength λ = 3.6 Å and a take-off angle of 65°, providing the necessary high resolution to resolve the satellite peaks from the fundamental magnetic reflections. The left panel of the Fig. 4.13 shows similar difference patterns collected at D20 with the longer wavelength. The longer wavelength yields a better resolution of the satellite peaks, which allows the observation of the tiny commensurate magnetic contribution just below T_C. This confirms that the incommensurate and commensurate magnetic phases of $Ni_{2-x}Co_xScSbO_6$ (x = 1.5) emerge at the same time, when the temperature is below the transition temperature (58 K). Assuming the magnetic moments to have the same value in both the [0 0 k_z] and [0 0 0] phases, this gives a saturation value of 2.94(1) μ_B for Co_2ScSbO_6 at 1.7 K, close to the ideal spin-only value of μ_{th} = 3.00 μ_B. The phase proportions of [0 0 k_z]:[0 0 0] magnetic phases are calculated to be 63 % : 37 % from the Rietveld refinement. No changes to the magnetic order are found up to T_C for any of the $Ni_{2-x}Co_xScSbO_6$ materials. Furthermore, proportions of coexisting [0 0 k_z] and [0 0 0] phases for the x = 1.5 and 2 compositions also do not change. The thermal evolution diffraction data of Co_2ScSbO_6 shown in Fig. 4.14 clearly indicates magnetic satellites near (003), (101), (015) and (021) nuclear peaks (d~4.70, 4.30, 2.38 and 2.24 Å respectively) along with the magnetic contribution on the nuclear peak (003) below 60 K and the incommensurate and commensurate phases appear to share a common T_C as shown for Co_2ScSbO_6. The thermal evolution of the magnetic moments of Co_2ScSbO_6 from the Rietveld fits of the NPD data at different temperatures are summarised in Fig. 4.15. This clearly shows the magnetic moment rapidly increases when starting to cool the sample below T_C (59 K) and then increases slowly until almost reaching the spin only saturated moment at the base temperature (1.7 K).

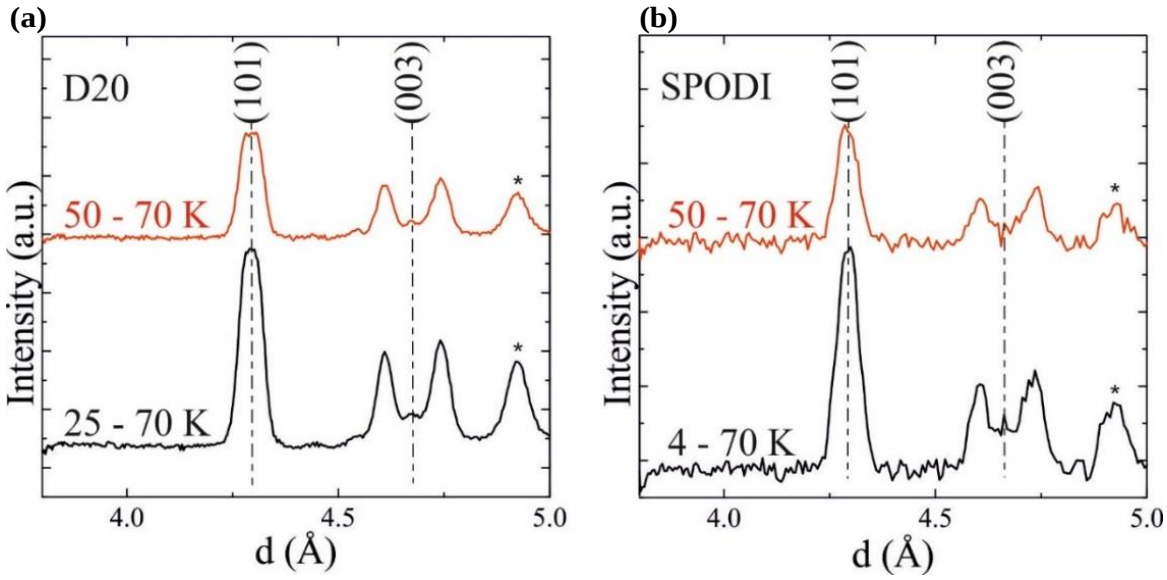

Fig. 4.13 50 K – 70 K (red), 25 K – 70 K (black) and 4 K – 70 K (black) NPD difference patterns of $Ni_{0.5}Co_{1.5}ScSbO_6$ collected at **(a)** D20 and **(b)** SPODI. (003) and (101) main magnetic peaks are labelled and identified with dashed lines. The magnetic signal of the secondary $Co_{2.33}Sb_{0.64}O_4$ spinel phase is identified with an asterisk.

Table 4.10 Magnetic parameters for $Ni_{2-x}Co_xScSbO_6$ materials; ordered moment (μ), theoretical ordered moment (μ_{th}), refined propagation vector component ($k_i = k_y$ for x = 0, $k_i = k_z$ for x ≠ 0), 1/3*n* periodicity for integer *n*, and % of the [0 0 k_z] magnetic phase coexisting with [0 0 0] for x = 1.5 and 2.

x	0	0.5	1	1.5	2
μ (μ_B)	1.72(3)	2.18(2)	2.40(1)	2.63(3)	2.94(1)
μ_{th} (μ_B)	2.00	2.25	2.50	2.75	3.00
k_i	0.036(1)	0.066(1)	0.056(1)	0.041(1)	0.032(1)
1/3*n*	-	0.067	0.056	0.042	0.033
n	-	5	6	8	10
%[0 0 k_z]		100	100	84.8(1)	63.4(1)

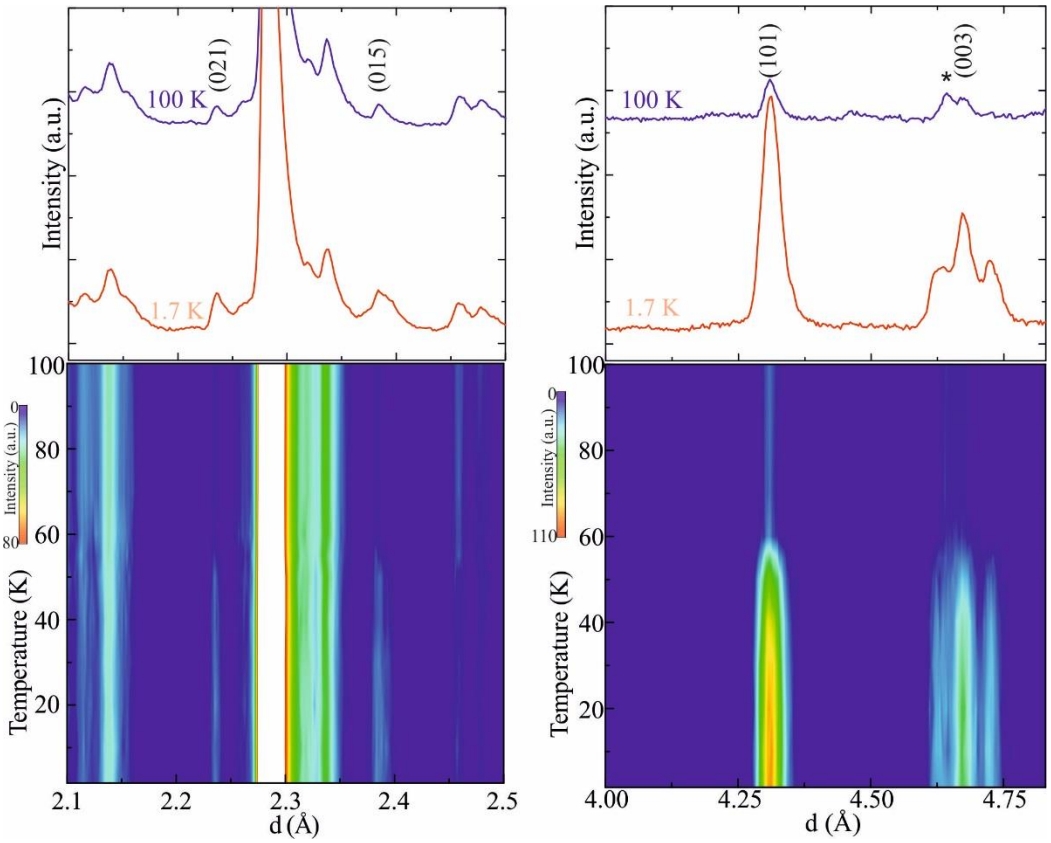

Fig. 4.14 Thermodiffraction neutron data for Co_2ScSbO_6 showing that [0 0 0] and [0 0 k_z] magnetic phases (evidenced by peaks at **(a)** 2.38 Å and 2.24 Å; **(b)** 4.70 Å and 4.30 Å respectively) coexist at all temperatures below T_C = 59 K. The impurity $Sc_{5.5}Sb_{0.5}O_{12}$ reflection are shown by the asterisk.

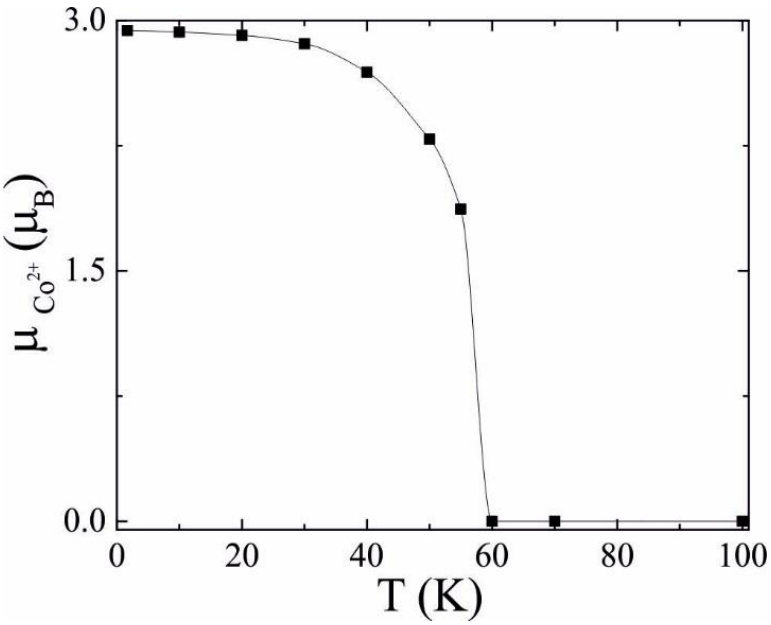

Fig. 4.15 Thermal evolution of the magnetic moments of Co_2ScSbO_6 from the Rietveld fits of the NPD data collected at WISH at different temperatures. The error bars are smaller than the marker size.

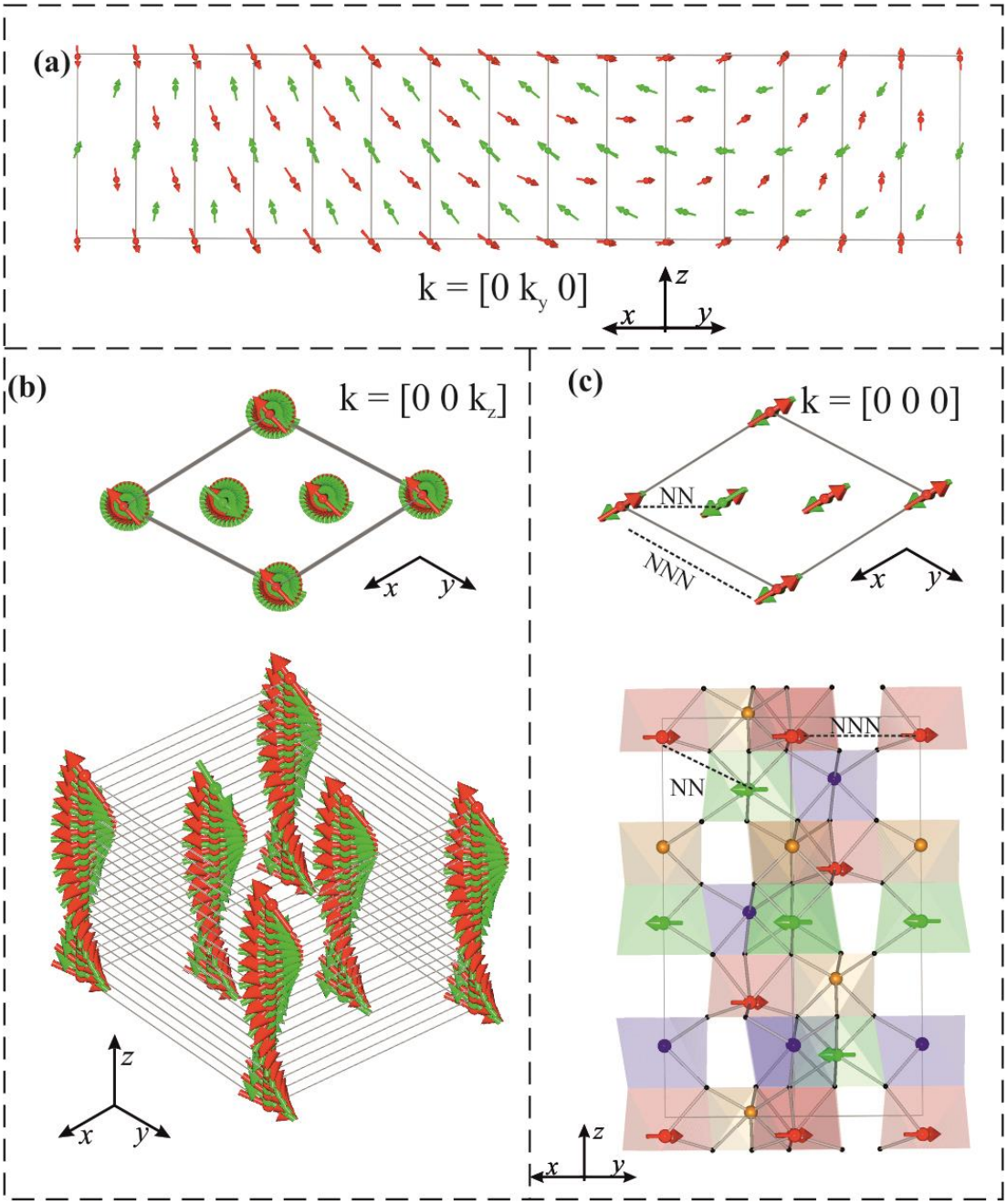

Fig. 4.16 Magnetic structures of $Ni_{2-x}Co_xScSbO_6$ for **(a)** x = 0 with propagation vector k = [0 k_y 0], **(b)** x = 0.5 to 2 with k = [0 0 k_z] and **(c)** the competing commensurate k = [0 0 0] phase for x = 1.5 and 2. Green and red arrows represent the spins at (Ni/Co)1 and (Ni/Co)2 sites respectively. The nearest neighbour couplings (NN) and next nearest neighbour couplings (NNN) are listed.

4.4.3 Magnetisation behaviour of $Ni_{2-x}Co_xScSbO_6$

Magnetometry data collected on $Ni_{2-x}Co_xScSbO_6$ show magnetic behaviour that is consistent with the magnetic structure solved from low temperature neutron diffraction patterns. ZFC/FC magnetic susceptibility curves and the Curie-Weiss (*CW*) fit of ZFC reciprocal susceptibility data of $Ni_{2-x}Co_xScSbO_6$ are shown in Fig. 4.17. The ZFC and FC susceptibilities of Ni_2ScSbO_6 (x = 0) do not diverge and the negative Weiss constant (θ = –44 K), calculated from fitting the reciprocal susceptibility with a *CW* law in the temperature range of 100 K < *T* < 300 K, suggests an existence of antiferromagnetic correlations which is in a good agreement with the earlier published data by Ivanov et al. Through mathematically calculating the maximum slope of the χ vs *T* plot, the Neel temperature T_N of Ni_2ScSbO_6 was estimated to be 65 K. However, a ferromagnetic contribution starts to emerge with the initial Co substitution and increases with the increasing cobalt content x. The magnetic interactions transformed from the pure antiferromagnetic (x = 0) to a competition of antiferromagnetic and ferromagnetic (x ≠ 0). Co_2ScSbO_6, as an example, is ferrimagnetic below T_C = 59 K and the $1/\chi$ high temperature ($T \geq 100$ K) data increases linearly with the temperature revealing a Curie-Weiss behaviour and the Curie-Weiss fit to the reciprocal susceptibility gives a Weiss constant of θ = –142 K suggesting the interactions between spins are still dominated by antiferromagnetic interactions. The experimental effective paramagnetic moment obtained in the Curie-Weiss analysis is μ_{eff} = 7.61 μ_B/f.u. which is equivalent to 5.38 μ_B per Co^{2+} in a high spin $3d^7$ configuration. Similar values, ≈ 5.20 μ_B, have been reported previously for other Co^{2+} containing oxides with a strong $^4T_{1g}$ excited state orbital contribution to the moment.[23-24] The other $Ni_{2-x}Co_xScSbO_6$ compositions also have magnetic transitions near 60 K. Curie-Weiss fitting results, summarised in Table 4.11, show that all of the effective magnetic moments are close to calculated values for the corresponding proportions of spin only Ni^{2+} (considering *S* = 1, *L* = 0, μ_{eff} = 2.83 μ_B) and Co^{2+} (μ_{eff} = 5.20 μ_B is assumed).

The hysteresis loops of magnetisation (M) against magnetic field (H) show an interesting change in the bulk magnetic properties as soon as the Co^{2+} ion is introduced. As seen in the Fig. 4.18, the magnetisation of x = 0 Ni_2ScSbO_6 is essentially linear with the applied magnetic field, as expected for an antiferromagnetic compound. However x = 1 and 1.5 samples have a similar *S*-shape ferrimagnetic behaviour with Co_2ScSbO_6 below T_N, with the spontaneous magnetisations extrapolated to zero field of M_0 ≈ 0.14

μ_B/f.u. at 2 K. The coercive field (H_{co}) at 2 K for x = 0.5 is negligible while the H_{co} are 0.11 T, 0.12 T and 0.24 T for x = 1, 1.5 and 2 respectively. Interestingly, the x = 0.5 compound shows metamagnetism with a critical field of H = 1.5 T at 2 K, and metamagnetic transitions are also observed for x = 0.5 and 1 samples at 40 K (Fig. 4.19). The small ferromagnetic component in these series of $Ni_{2-x}Co_xScSbO_6$ materials shown from the magnetisation measurements reflect complex magnetic structures derived from the existence of competing magnetic correlations observed in NPD data as discussed above. The observation of spontaneous magnetisations for the Co-rich materials in this polar NTO-type family demonstrates the potential for multiferroism.

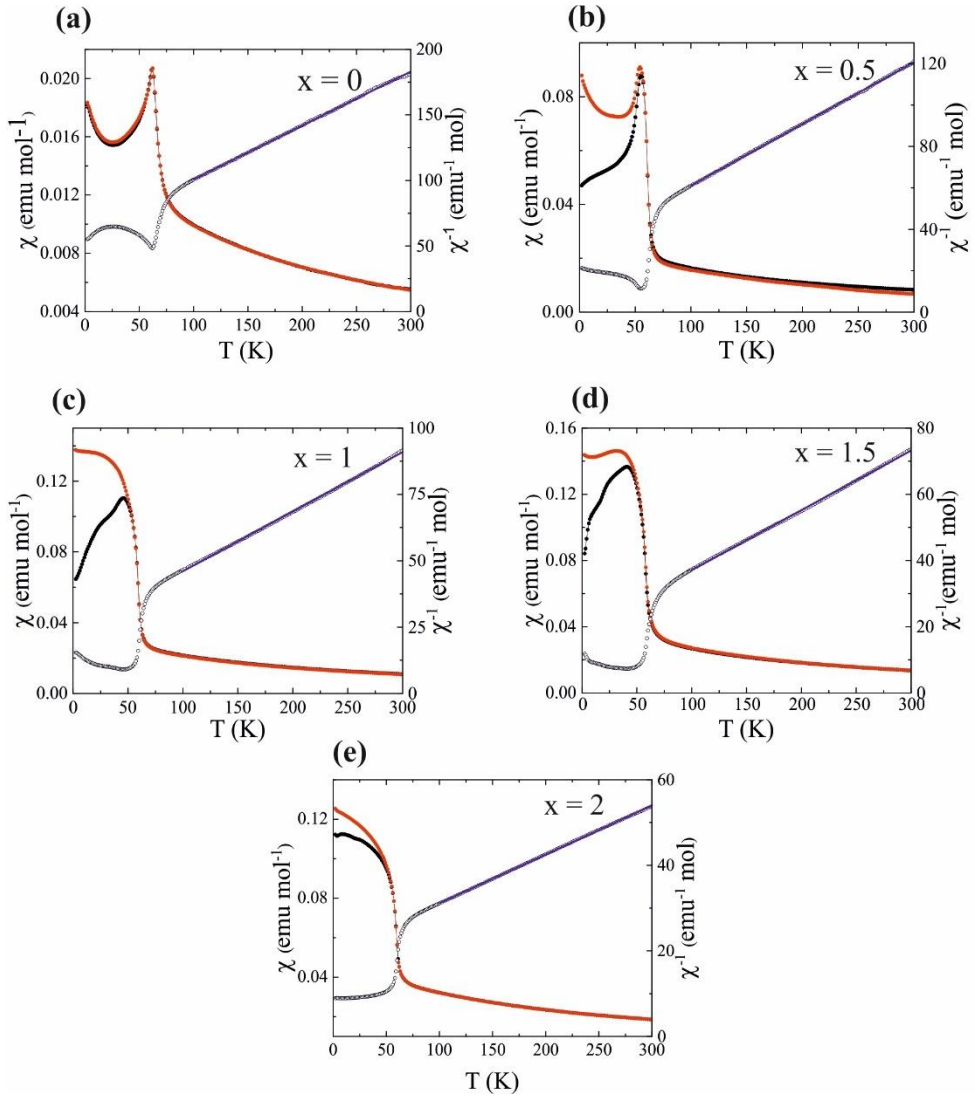

Fig. 4.17 (a), **(b)**, **(c)**, **(d)**, **(e)** ZFC-FC magnetic susceptibility of $Ni_{2-x}Co_xScSbO_6$ as a function of temperature under an applied magnetic field of 1 T (black and red circles). Reciprocal susceptibility (open circles) is on the right axis and is fitted (blue line) to the Curie–Weiss law.

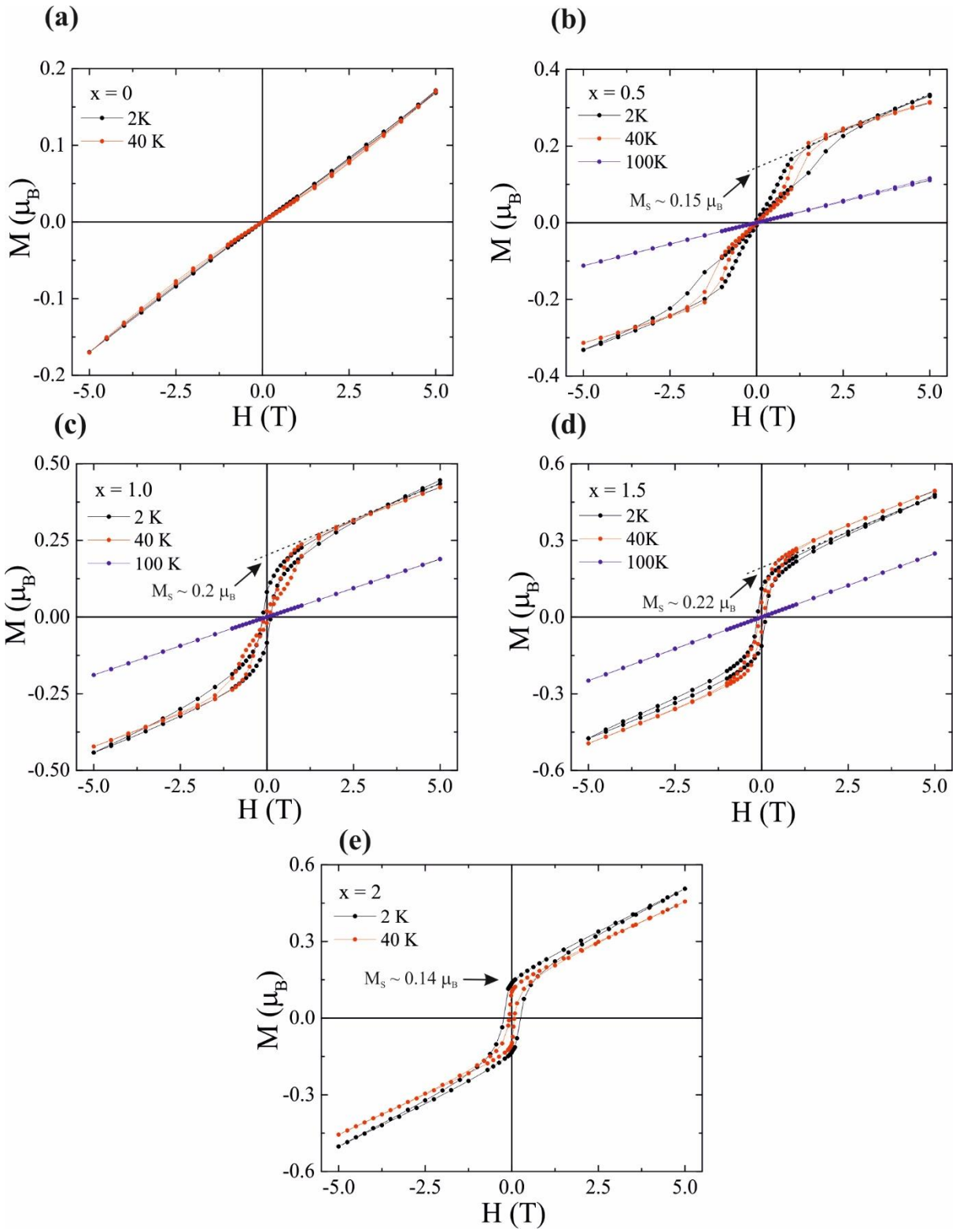

Fig. 4.18 (a), **(b)**, **(c)**, **(d)**, **(e)** Field dependent magnetisation loops of $Ni_{2-x}Co_xScSbO_6$ (x = 0, 0.5, 1, 1.5, 2) at different temperatures. Spontaneous magnetisations (M_S) are labelled.

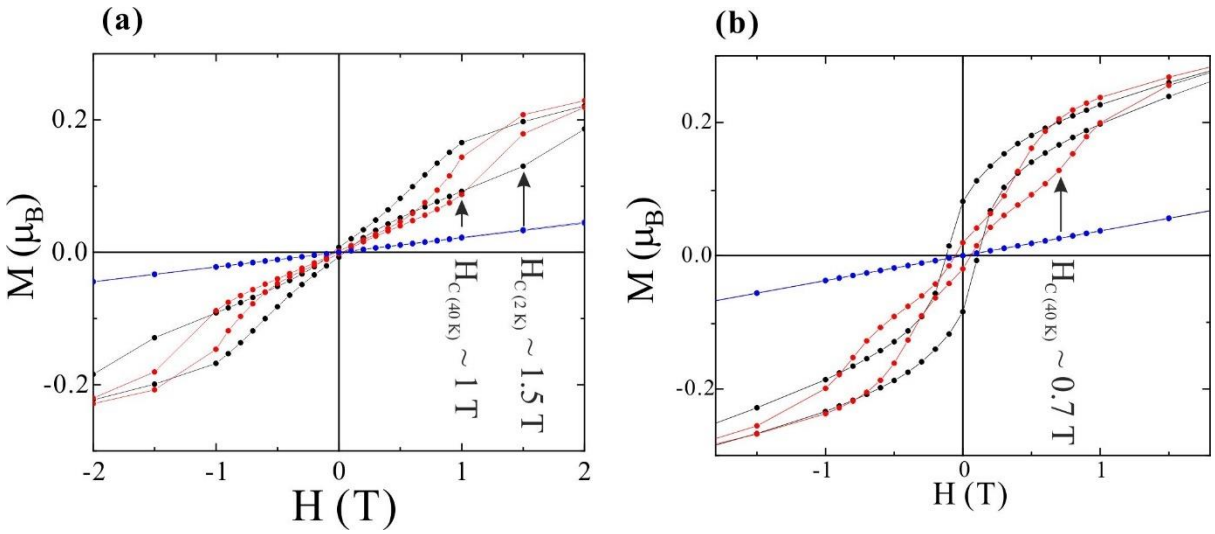

Fig. 4.19 An enlargement of the magnetisation loops of $Ni_{2-x}Co_xScSbO_6$ showing the metamagnetic transitions for **(a)** x = 0.5 and **(b)** x = 1. Critical fields (H_C) are labelled.

Table 4.11 Magnetic parameters for $Ni_{2-x}Co_xScSbO_6$ materials; T_C, Weiss constant (θ), effective moments (μ_{eff}), theoretical effective moments (μ_{th}) calculated by equation 2.27, critical field (H_C) and spontaneous magnetisation at 2 K (M_S) determined from magnetic measurements. (μ_{eff} = 5.20 μ_B is assumed)[23-24]

x	0	0.5	1	1.5	2
T_C (K)	65	61	59	58	59
θ (K)	-144	-104	-105	-106	-142
μ_{eff} (μ_B / atom)	2.83	3.57	4.19	4.72	5.20
μ_{eff} (μ_B / f.u.)	4.41	5.18	5.97	6.66	7.61
$\mu_{th.}$ (μ_B / f.u.)	4.00	5.05	5.92	6.68	7.35
H_C (T)	-	1.5	0.7	-	-
M_S (μ_B)	-	0.15	0.2	0.22	0.14

4.5 Discussion and conclusion

It is found that the crystal structure of $Ni_{2-x}Co_xScSbO_6$ retains *R*3 symmetry down to 4 K. The presence of four independent crystallographic sites for cations in the NTO-type structure provides several degrees of freedom to manipulate its properties. The magnetic cations Ni(Co)1 and Ni(Co)2 are shifted away from the centroid of their polyhedron which induced a net polarisation. It was also found that the lattice parameters change asymmetrically with an increasing amount of Co content x, as the *a*-parameter increases more significantly than the lattice parameter *c*. The hexagonal distortion explained by the *c*/*a* ratio in all the $Ni_{2-x}Co_xScSbO_6$ compounds is smaller than that of the ideal corundum structure (2.833) and almost linearly decreases with x. This trend exhibits the structural anisotropy of $Ni_{2-x}Co_xScSbO_6$ resulting from the electronic degeneracy of the Co^{2+} ions.

The low temperature neutron diffraction data along with the magnetisation measurements demonstrate a very rich magnetic behaviour in the $Ni_{2-x}Co_xScSbO_6$ system as shown by the magnetic phase diagram in Fig. 4.20. Compared to the pure Ni containing Ni_2ScSbO_6 (x = 0) compound where spins are constrained in the *xz* plane, the strong magnetic anisotropy associated with orbitally-degenerate Co^{2+} ions confines spins to the *xy* plane for all Co-containing materials. This switches magnetic order from the incommensurate [0 k_y 0] type previously reported for Ni_2ScSbO_6 to a new [0 0 k_z] helical antiferromagnetic arrangement for x = 0.5 to 2 samples. The nature of the helical magnetic structure suggests that the spin interactions are frustrated along the *z*-axis and this complex magnetic structure results from competition of antiferromagnetic couplings between nearest neighbour (NN) spin layers and next nearest neighbour (NNN) layers. NN couplings through Co/Ni–O–Co/Ni bonds are strongly antiferromagnetic while NNN couplings through Co/Ni–O–Sc/Sb–O–Co/Ni bridges are weaker and diminish relative to NN as x increases resulting in a decrease in the value of the propagation vector k_z.

Although the balance of NN and NNN couplings in $Ni_{2-x}Co_xScSbO_6$ compounds may favour the incommensurate periodicities, the strong anisotropy of Co^{2+} ions causes the helical magnetic structures to lock into nearby commensurate values so that more spins can lie parallel to easy-axes which have a 3-fold symmetry in the *xy* plane of the *R*3 crystal structure. Hence, the value of propagation vector k_z can be expressed with the

formula $k_z = 1/3n$.Values of n = 5, 6, 8 and 10 are observed at the x = 0.5, 1, 1.5 and 2 compositions respectively, and we speculate that other periodicities such as n = 7 and 9 may lie at the intermediate compositions, as shown on the magnetic phase diagram. $3n$ also represents the number of unit cells forming a complete periodic spiral structure and hence the angle separating the of spins between two neighbouring unit cells can be calculated as $\alpha = 360^\circ / 3n$. The extra collinear magnetic structure phase with propagation vector k = [0 0 0] presented in x = 1.5 and 2 compositions increase with increasing cobalt content x and the $k_z = 1/3n = 0$ can be expressed as $n \rightarrow \infty$. Studies of further $Ni_{2-x}Co_xScSbO_6$ compositions will be required to explore the full variety of spin structures and to clearly understand the competitive relationship between [0 0 k_z] and [0 0 0] magnetic phases in Co-rich materials. Lock-in spin orders are previously reported in other Co^{2+} containing oxides such as the multiferroic spinel $CoCr_2O_4$[25] and the kagomé staircase compound $Co_3V_2O_8$[26], but the $Ni_{2-x}Co_xScSbO_6$ series represents an unusually rich series of lock-in magnetic phases accessible through chemical tuning at zero field strength.

It is also worth mentioning that the polar *R*3 symmetry of the NTO-type structure allows the existence of net polarisation. The electric polarisations of all $Ni_{2-x}Co_xScSbO_6$ compounds, calculated from the cation displacement from the ideal centre of its coordinated octahedron refined from the NPD data, are in the range of E_0 = 13 - 20 μC cm^{-2} and the polarisation direction is parallel to the *z*-axis. These polarisation results are rather small when compared to other reported corundum derivatives, such as the NTO-type Mn_2FeWO_6[27] and Mn_2FeMoO_6[28] of which have polarisations of 59.5 μC cm^{-2} and 68 μC cm^{-2} respectively. The net magnetisations (M_0) of the Co-rich samples observed from the magnetisation measurements probably arise from a combination of the presence of the ferrimagnetic [0 0 0] phase and spin canting within the [0 0 k_z] helical magnetic phases, although the slight canting is undetectable from neutron diffraction. The [0 0 0] ferrimagnetic phase has net magnetisation in the *xy* plane and so a potential perpendicular coupling mechanism between M_0 and E_0 that is usually observed in multiferroic compounds may exist, as discussed in the previous report of polar $MnTiO_3$.[29] Canting of the spins in the [0 0 0] or [0 0 k_z] magnetic phases to give a small magnetisation parallel to E_0 may also arise from antisymmetric Dzyaloshinskii-Moriya coupling. Overall, the *R3* lattice symmetry of the $Ni_{2-x}Co_xScSbO_6$ materials allows

potential linear or bilinear magnetoelectric effects as discussed above, making these materials potential multiferroics.

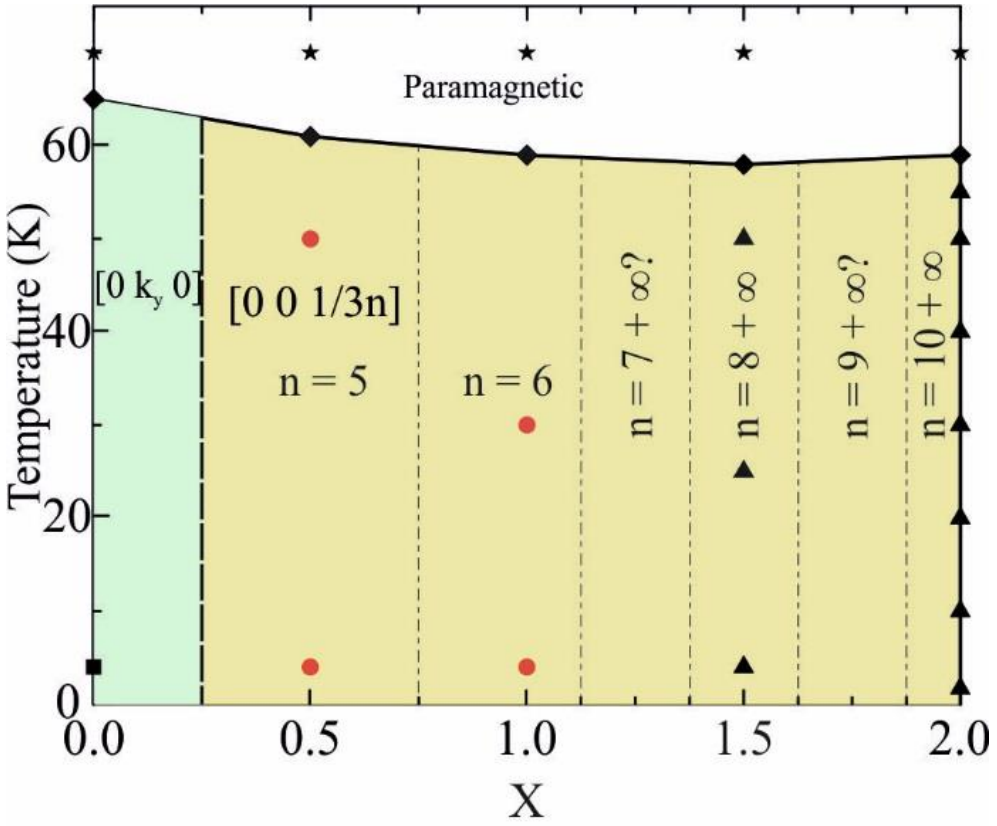

Fig. 4.20 Magnetic phase diagram of $Ni_{2-x}Co_xScSbO_6$ system. The *n* values include those observed and those postulated (marked '?') [0 0 1/3*n*] lock-in phases. Star/rhombus/square/circle/triangle symbols refer to paramagnetic phase/T_C/[0 k_y 0]/[0 0 k_z]/[0 0 k_z]+[0 0 0] observations.

In conclusion, a new oxide Co_2ScSbO_6 has been synthesised using high-pressure techniques at 6 GPa, 1273 K, and solid solutions $Ni_{2-x}Co_xScSbO_6$ (x = 0, 0.5, 1 and 1.5) were prepared at ambient pressure, 1373 K. Polycrystalline compounds of $Ni_{2-x}Co_xScSbO_6$ have been characterised using X-ray and neutron diffraction, magnetometry. All compositions adopt the Ni_3TeO_6-type structure with polar space group *R*3 at room temperature, and retain this symmetry down to 4 K. These compounds are all magnetically ordered below $T_C \approx 60$ K. The crystallographic cation arrangement for $Ni_{2-x}Co_xScSbO_6$ follows Ni/Co(1)-Sc, Ni/Co(2)-Sb ordering in the *xy* plane stacked along the *z*-axis and 2/3 of the available octahedral holes were filled, as high resolution neutron diffraction allows accurate determination of cation positions and occupancy. The anti-site disorder between (Ni/Co) site and Sc site was also observed in all $x \neq 0$

compositions. The $Ni_{2-x}Co_xScSbO_6$ series all possess a similar T_C of around 60 K with effective paramagnetic moments in the range of μ_{eff} = 4.41 ~ 7.61 μ_B/f.u. Ferromagnetic contributions become larger with increasing Co content, as observed in the magnetisation measurements. Magnetisation against applied magnetic fields indicate metamagnetic transitions in both x = 0.5 and 1 compounds and net magnetisation in Co-rich materials (x = 1.5 and 2). A very rich magnetic phase diagram is discovered from neutron diffraction data with magnetic order switching from an incommensurate [0 k_y 0] phase for pure Ni_2ScSbO_6 to a series of long-period lock-in [0 0 k_z] spin structures with $k_z = 1/3n$ for Co-containing x = 0.5 - 2 samples. The [0 0 1/3*n*] propagation vector leads to a helical magnetic structure with a length of up to 30 unit cells (approximately 420 Å) and a turning angle of 12˚ between spins in neighbouring unit cells. These spin structures coexist with a commensurate ferrimagnetic [0 0 0] phase in the x = 1.5 and 2 compounds which contributes to a net magnetisation in the *xy* plane. The spins in both magnetic phases are ferromagnetically coupled in the *xy* plane antiparallel along the *z*-axis. Resistivity measurements were attempted using the PPMS. However, the resistances of the $Ni_{2-x}Co_xScSbO_6$ samples were found to be outside the measurement range of the instrument. This implies that the $Ni_{2-x}Co_xScSbO_6$ materials are all insulators at room temperature.

Generally speaking, high pressure can be a useful technique to synthesise metastable materials and separate target phases from its by-products when they have very similar synthesis temperature. The presence of electrical polarisations and spontaneous magnetisations for Co-rich materials opens up possibilities for magnetoelectric coupling leading to the multiferroic properties. Further exploration of other intermediate compositions in between x = 0 and x = 0.5 will help understand the spin reorientation transforming from the *xz* plane to the *xy* plane while the intermediate compositions between x = 1.1 and 1.5 will help confirm the transition point when the second magnetic phase [0 0 0] emerges. All of the possible *n* values of the [0 0 1/3*n*] magnetic phases (*n* = 7 or 9) need to be tested as well to further complete the magnetic phase diagram.

References

1. N. A. Hill, *J. Phys. Chem.* 2000, **B104**, 6694.

2. M. Fiebig, *J. Phys. D: Appl. Phys.*, 2005, **38**, R123.

3. J. F. Scott, *Nature Mater*., 2007, **6**, 256

4. W. Eerenstein, N. D. Mathur and J. F. Scott, *Nature*, 2006, **442**, 759.

5. S. W. Cheong and M. Mostovoy, *Nature Mater.*, 2007, **6**, 13.

6. Y. S. Oh, S. Artyukhin, J. J. Yang, V. Zapf, J. W. Kim, D. Vanderbilt, and S. W. Cheong., *Nature Comm*., 2014, **5**, 3201

7. N. A. Hill, A. Filippetti, *J. Magn. Magn. Mater.* 2002, **242**, 976.

8. D. I. Khomskii, *Physics* 2009, **2**, 20.

9. Y. Shiozaki, T. Mitsui, *J. Phys. Chem. Solids*, 1963, **24**, 1057

10. R.E. Newnham, E.P. Meagher, *Mater. Res. Bull.*, 1967, **2**, 549.

11. R. J. Harrison, U. Becker and S. A. T. Redfern, *Am. Mineral.*, 2000, **85**, 1694.

12. A. J. Dos Santos-García, C. Ritter, E. Solana-Madruga and R. Sáez-Puche, *J. Phys.: Condens Matter.*, 2013, **25**, 206004.

13. S.A. Ivanov, R. Mathieu, P. Nordblad, R. Tellgren, C. Ritter, E. Politova, G. Kaleva, A. Mosunov, S. Stefanovich and M. Weil, *Chem. Mater*., 2013, **25**, 935.

14. A.C. Larson and R.B. Von Dreele, Los Alamos National Laboratory Report LAUR, 2000, 86

15. B. H. Toby, *EXPGUI*, a graphical user interface for *GSAS*, *J. Appl. Cryst.*, 2000, **34**, 210

16. J. Rodriguez-Carvajal, *Physica B*, 1993, **192**, 55.

17. J. Rodriguez-Carvajal, BASIREPS: *a program for calculating irreducible representations of space groups and basis functions for axial and polar vector properties. Part of the FullProf Suite of programs*, accessed on May 15th, 2019, http://www.ill.eu/suites/fullprof/.

18. Inorganic Crystal Structure Database, accessed on May 15th, 2019, *icsd.cds.rsc.org/icsd/*.

19. R. D. Shannon, *Acta Cryst. A*, 1976, **32**, 751.

20. K. Momma and F. Izumi, *J. Appl. Crystallogr.*, 2011, **44**, 1272.

21. J.P. Attfield, *Solid State Sci*., 2006, **8**, 861.

22. H. J. C. Berendsen, J. R. Grigera and T. P. Straatsma, *J. Phys. Chem*., 1987, **91**, 6269.

23. V. Primo-Martín and M. Jansen, *J. Solid State Chem.*, 2001, **157**, 76.

24. M. C. Viola, M. J. Martínez-Lope, J. A. Alonso, J. L. Martínez, J. M. De Paoli, S. Pagola, J. C. Pedregosa, M. T. Fernández-Díaz and R. E. Carbonio, *Chem. Mater.*, 2003, **15**, 1655.

25. Y. Yamasaki, S. Yamasaki, Y. Kaneko, J. P. He, T. Arima and Y. Tokura, *Phys. Rev. Lett*., 2006, **96**, 207204.

26. Y. Chen, J. W. Lynn, Q. Huang, F. M. Woodward, T. Yildirim, G. Lawes, A. P. Ramirez, N. Rogado, R. J. Cava, A. Aharony, O. Entin-Wohlman and A. B. Harris, *Phys. Rev. B*, 2006, **74**, 014430.

27. M. R. Li, M. Croft, P. W. Stephens, M. Ye, D. Vanderbilt , M. Retuerto, Z. Deng, C. P. Grams, J. Hemberger, J. Hadermann, W.M. Li, C. Q. Jin, F. O. Saouma, J. I. Jang, H. Akamatsu, V. Gopalan, D. Walker and M. Greenblatt, *Adv Mater*., 2015, **27**, 2177.

28. M. R. Li, M. Retuerto, D. Walker, T. Sarkar, P. W. Stephens, S. Mukherjee, T. S. Dasgupta, J. P. Hodges, M. Croft, C. P. Grams, J. Hemberger, J. Sanchez-Benitez, A. Huq, F. O. Saouma, J. I. Jang, and M. Greenblatt, *Angew. Chem. Int. Ed*., 2014, **53**, 10774.

29. A. M. Arévalo-López and J. P. Attfield, *Phys. Rev. B*, 2013, **88**, 104416.

Chapter 5. Synthesis and characterisation of $YRuO_3$

5.1 Introduction

Ruthenate perovskites and related materials have a diverse range of unusual electronic and magnetic properties from electron-electron correlations within broad 4*d* bands. Ruthenium, like many other transition metals, has a wide range of oxidation states from 0 to VIII. Ruthenium usually adopts a tetravalent state in pseudo-cubic simple perovskites, where the A site could be occupied with Ca^{2+}, Sr^{2+} Ba^{2+} and Pb^{2+} ions, such as in the metallic ferromagnetic perovskites $SrRuO_3$ [1] and $BaRuO_3$ [2]. These materials along with the spin-triplet superconductivity compound Sr_2RuO_4,[3] and magnetic-field-induced quantum criticality compound $Sr_3Ru_2O_7$[4] are based on Ru(IV) which is very common. Numerous double perovskites A_2BRuO_6 with Ru(V) have been published recently as well.[5-6]However, ruthenium in the trivalent state, adopting a $4d^5$ electronic configuration, is rarely reported for crystal and magnetic information in oxide materials.

The first report of pseudo cubic $LnRuO_3$ (Ln = La and Pr) perovskites with the low spin $4d^5$ electronic configuration of Ru(III) was published in the 1970's.[7] Recently Sinclair et al.[8] from our group reported the first crystal characterisations and magnetic properties of an extensive series of new $LnRuO_3$ perovskites (Ln = La, Pr, Nd, Sm, Eu, Gd, Tb, Dy, Ho and Y). This work describes an extended project of synthesising and characterising pure $YRuO_3$ perovskite as Sinclair could only achieve 15 % purity of $YRuO_3$ at that time. Measurement of the low temperature magnetic properties of the synthesised $YRuO_3$ has been carried out using a Quantum Design MPMS XL Superconducting Quantum Interference Device (SQUID) and a Quantum Design Physical Property Measurement System (PPMS) between 2 - 300 K. Synchrotron X-ray and neutron diffraction techniques were used to characterise nuclear structure and magnetic structures.

5.2 Background

5.2.1 Previous high-pressure studies of $LnRuO_3$

High-pressure conditions are well known for favouring denser perovskite phases rather than the corresponding pyrochlores. Isolating ruthenate perovskites with small rare-earth cations at the A-site requires high pressure to stabilise the crystal structures with a low tolerance factor *t*. In addition, $LaRuO_3$ can be synthesised via several different chemical routes under ambient pressure due to the relatively large size of La^{3+} ($r_{La^{3+}}$ = 1.216 Å[9])[10]. The theoretical calculation of the tolerance factor *t* of $LnRuO_3$ compounds based on their ionic radii are all less than the ideal value of 1 as the Ln^{3+} is too small for the A-site to form the ideal cubic ABO_3 perovskite structure. Hence, the BO_6 octahedra are cooperatively rotated along the [001] and [110] cubic directions to reduce the size of the interstice of the A-site and stabilise the structure. As a result, the space group symmetry is reduced from the ideal cubic to the orthorhombic *Pnma* in $LnRuO_3$.

$LaRuO_3$ was earlier reported as an environmental catalyst and adopted an orthorhombic *Pnma* superstructure at room temperature.**Error! Bookmark not defined.** Later Sinclair et al.[8] reported the low temperature crystal structure and magnetic properties of the extended $LnRuO_3$ family by introducing high-pressure techniques. The experimental conditions were optimised at 1200 ˚C and 12 GPa. The lattice parameters (*a*, *b* and *c*) and unit cell volume *V* as a function of the Ln^{3+} ionic radii of the $LnRuO_3$ perovskites are depicted in Fig. 5.1. At room temperature, orthorhombic distortions gradually decrease from $HoRuO_3$ to $PrRuO_3$ with the increasing size of the A-site cations. A remarkable reduction of orthorhombic distortion was observed for $LaRuO_3$, assuming that $LaRuO_3$ undergoes a structural phase transition to adopt a higher symmetry perovskite structure in the high temperature region. It was also reported that all the $LnRuO_3$ compounds exhibit an average of 9 % cationic vacancies at the Ru site, resulting in the refined compositions for the perovskite phases being $LnRu_{0.91}O_3$. No significant deficiency was found from the refinement of the Ln site occupancies except for $LaRuO_3$, which was synthesised at ambient pressure, and has a 9% vacancy at the La^{3+} site. Therefore, these materials have mixed Ru^{3+}/ Ru^{4+} states which are in an agreement with bond valence sum (BVS) calculations. The resistivity data from the literature indicates that all the $LnRuO_3$ (Ln ≠ La) are semiconducting with a relatively small bandgap whereas $LaRuO_3$ is metallic. Magnetisation data show no indication of magnetic ordering down to 2 K for $LnRuO_3$, however the small

anomalies in magnetic data that appear for Ln = Pr, Nd, Sm and Eu are attributed to the corresponding pyrochlores $Ln_2Ru_2O_7$.

Therefore, introducing the diamagnetic Y^{3+} cations to the A-site is vital as it is difficult to study the weak magnetic behaviour of Ru^{3+} S = ½ against the rare-earth Ln^{3+} magnetic cations with larger moments.

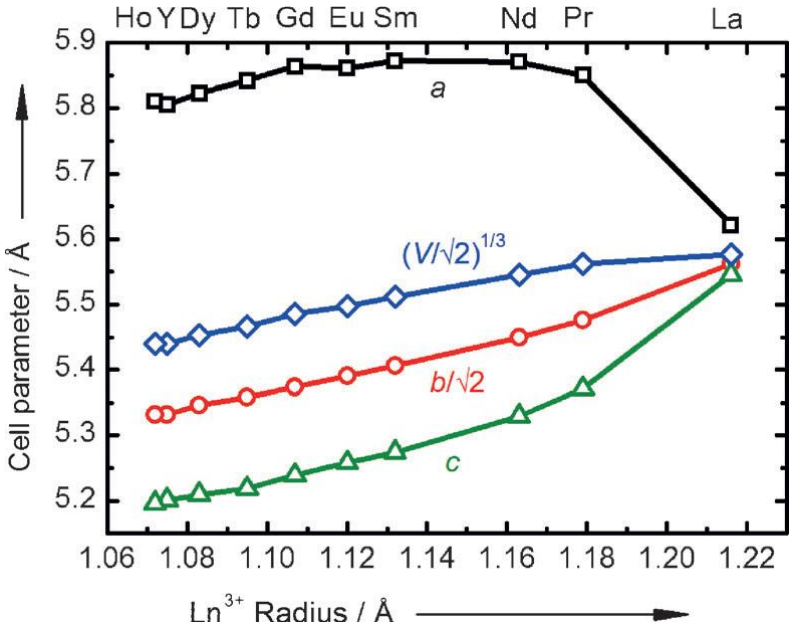

Fig. 5.1 Lattice parameters *a*, *b*, *c* and the unit cell volume *V* of $LnRuO_3$ perovskites plotted against the Ln^{3+} ionic radius. Figure was taken from A. Sinclair et al.[8]

5.3 Experimental

5.3.1 High-pressure synthesis of $YRuO_3$

The precursor for the high-pressure reaction of $YRuO_3$ was prepared as follows: the stoichiometric proportions of Y_2O_3 and RuO_2 oxides with Ru metal powder were intimately ground under acetone with a mortar and a pestle to prepare the powder precursor (100 mg). Y_2O_3 was dried at 800 ˚C for 8 hours before use. Approximately one third of the well-mixed precursor was then loaded into a platinum capsule and heated under pressure in a multianvil–type press using a Walker module. The pressure and temperature synthesis conditions were explored using tungsten carbide (WC) cubic anvils with truncation edge lengths of 14 mm up to 15 GPa and of 7 mm for pressures above 15 GPa. Temperatures up to the maximum 1200 ˚C were applied and the heating duration was 20 minutes at 12, 13, 14 and 15 GPa respectively using graphite sleeve heaters within the first set up, while the use of a Re resistive heater in the

small set up allowed temperatures to reach up to 1600 ˚C. This was used for samples synthesised at 14 and 20 GPa with the same heating duration of 20 minutes. The reaction is depicted below:

$$0.5\ Y_2O_3 + 0.75\ RuO_2 + 0.25\ Ru \longrightarrow YRuO_3 \qquad (5.1)$$

5.3.2 X-ray powder diffraction of $YRuO_3$

X-ray powder diffraction was carried out for a series of $YRuO_3$ samples with a D2 Bruker laboratory X-ray diffractometer in flat-plate mode using Cu *K*α radiation ($\lambda_{K\alpha1}$ = 1.54056 Å and $\lambda_{K\alpha2}$ = 1.54439 Å) at room temperature. The scan was run for 15 minutes over the angular range of $0^\circ < 2\theta < 70^\circ$ with a 0.03˚ step size and a counting time of 0.45 s per step.

High-resolution X-ray data were collected for the purest $YRuO_3$ sample (HP11) at 300 K using λ = 0.82660 Å (E = 15 KeV) synchrotron radiation at the I11 diffractometer at the Diamond Light Source (Oxfordshire, UK). The sample was loaded in a quartz capillary with a diameter of 0.1 mm and measured using 5 arms of multi-analysing crystal-detectors (MACs) over a range of angle $3^\circ < 2\theta < 150^\circ$. The data profile fits were carried out within the FullProf Suite[11] and refined by the Rietveld method.[12]

5.3.3 Neutron powder diffraction

Neutron powder diffraction (NPD) profiles were collected for $YRuO_3$ at 1.7 K and 120 K using the high-resolution time-of-flight (T.O.F) WISH diffractometer (ISIS facility, Oxfordshire, UK). 38 mg of high-pressure $YRuO_3$ sample was placed in a sealed vanadium can within a He cryostat and data were collected by 10-banks covering a wide range of *d*-spacings from 0.7 to 50 Å. Rietveld analysis of the $YRuO_3$ NPD data was carried out with the FullProf software package.[11] The magnetic symmetry analysis of the low temperature neutron data was performed with the BasIreps program.[13]

5.3.4 Magnetic measurements of $YRuO_3$

Magnetic direct current (DC) susceptibility measurements were performed with the SQUID magnetometer under zero-field cooled (ZFC) and field cooled conditions (FC) over the

temperature range 2 K < *T* < 300 K under a magnetic field strength of 0.1 T. Magnetisation (*M*) as a function of the applied field (*H*) was carried out on the Quantum Design PPMS. Hysteresis data were collected between 2 K and 150 K with an interval of 10 K under magnetic fields up to 9 T. Alternating current (AC) susceptibility measurements with frequencies of 100, 355, 885, 1128, 1438, 2976, 6158, 7847 and 10000 Hz were made using the PPMS device. The measured sample size was 6.1 mg.

5.3.5 Resistivity measurements

A four-probe resistivity measurement was made on a Quantum Design PPMS using a polycrystalline pellet of $YRuO_3$ a few mm in dimensions. Resistivity against temperature was measured on both cooling and warming between temperatures of 20 K and 300 K under magnetic fields of 0 and 7 T.

5.4 Results

5.4.1 In-house X-ray diffraction study of $YRuO_3$

The $YRuO_3$ powder compounds synthesised under different temperature/pressure conditions were first measured using the D2 X-ray diffractometer at room temperature. The collected data were initially analysed using a combination of the EVA database and the Inorganic Crystal Structure Database (ICSD) in order to identify the main perovskite phase and by-products.[14-15] The collected XRD patterns of $YRuO_3$ under different reaction conditions are shown in Fig. 5.2. The patterns show that $YRuO_3$ contains the $LnRuO_3$ perovskite as the main phase for syntheses above 13 GPa, although the $Y_2Ru_2O_7$ pyrochlore and residual Ru are present as secondary phases. Altering the pressure from 12 to 15 GPa increases the perovskite $YRuO_3$ phase fraction and minimises the secondary pyrochlore phase. Although increasing temperature avoids the presence of the pyrochlore phase, several other unidentified by-products are formed in detriment of $YRuO_3$.

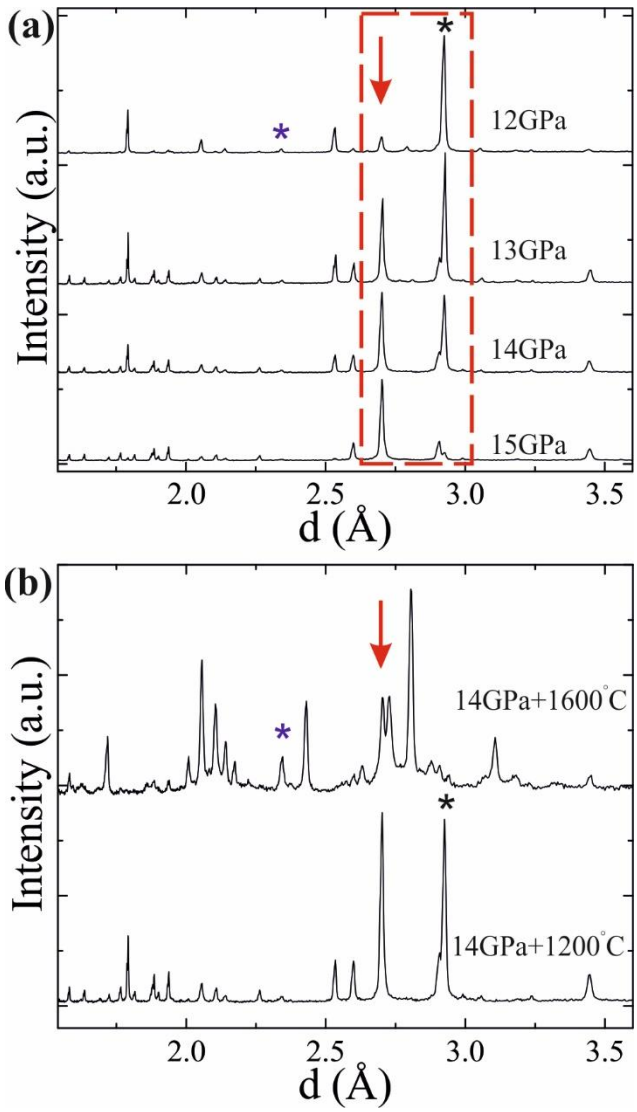

Fig. 5.2 (a) Powder X-ray diffraction patterns of $YRuO_3$ under different pressure conditions at 1200 ˚C using Cu K_α as the radiation source. The most intense peak of the perovskite $YRuO_3$ is at d = 2.7 Å shown by the red arrow. The peak at d = 2.92 Å is attributed to the $Y_2Ru_2O_7$ pyrochlore (black asterisk). The peak at d = 2.34 Å is attributed to the Ru (blue asterisk). The d-spacing region in the red box clearly indicates the relative proportions of $YRuO_3$ perovskite and secondary phase $Y_2Ru_2O_7$ under different reaction conditions. **(b)** The XRD patterns under different temperature conditions at 14 GPa. Several unidentified impurity phases were observed at 1600 ˚C although the pyrochlore phase has been successfully eliminated.

The crystal structure of $YRuO_3$ was refined using GSAS software by the Rietveld method. The background was modelled with a polynomial function (Shifted Chebyshev) and the peak shape was fitted using a pseudo-Voigt function. The zero shift, scale factor, lattice parameters and atomic coordinates were also refined. The refined patterns are depicted in Fig. 5.3 and corresponding crystal information is listed in Tables 5.1 and 5.2. Accurate structural information for $YRuO_3$ such as oxygen positions and atom-site occupancies could not be

obtained due to the presence of many secondary phases and the low data quality from the laboratory X-ray diffractometer.

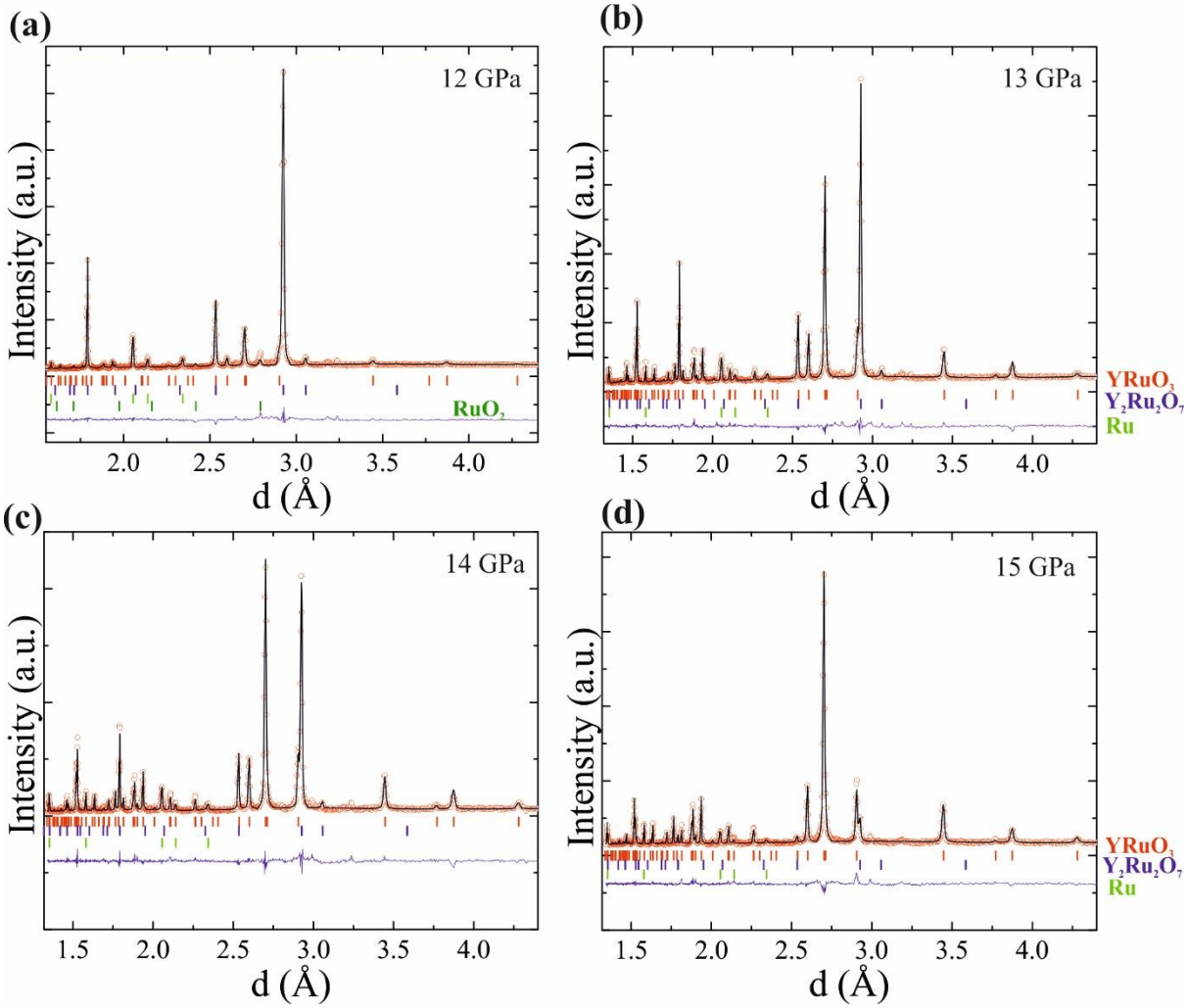

Fig. 5.3 (a), **(b)**, **(c)**, **(d)** Rietveld fits of the room temperature XRD patterns of $YRuO_3$ compounds synthesised at 1200 ˚C under different pressure conditions (12 GPa, 13GPa, 14 GPa, 15 GPa). The secondary $Y_2Ru_2O_7$ (blue) and Ru metal phases (green) are included in all the refinements and the additional RuO_2 (olive) is included for $YRuO_3$ synthesised under 12 GPa.

Table 5.1 The refined weight fractions of $YRuO_3$ and secondary phases synthesised under different pressure conditions.

	Pressure (GPa)	R_{wp} (%)	$YRuO_3$ (%)	$Y_2Ru_2O_7$ (%)	Ru (%)	RuO_2 (%)
$YRuO_3$-HP8	12	6.47	14.3	76.3	7.5	1.9
$YRuO_3$-HP9	13	6.02	49.2	46.2	4.6	--
$YRuO_3$-HP10	14	10.51	60.5	34.7	4.8	--
$YRuO_3$-HP11	15	5.91	92.3	4.8	2.9	--

Table 5.2 The atom positions, thermal parameters Biso and occupancy of the purest $YRuO_3$ (HP11) synthesised under 15 GPa. The lattice parameters a = 5.8131(2) Å, b = 4.5416(3) Å, c = 5.1999(2) Å and the space group is *Pnma*.

Atom	x	y	z	B_{iso} (Å^2)	Occ.
Y	0.079(1)	0.25	-0.031(1)	0.24(1)	1
Ru	0	0	0.5	0.24(1)	0.93(1)
O(1)	0.264	0.056	0.683	0.24(1)	1
O(2)	0.442	0.25	0.118	0.24(1)	1

5.4.2 Synchrotron powder X-ray diffraction

The 300 K data of $YRuO_3$ (15 GPa) collected at the I11 synchrotron X-ray diffractometer was used for the crystallographic characterisation. Rietveld structural fitting analysis was refined over a *d*-spacing range between 1 Å and 6 Å using the FullProf software package[16] The Rietveld refinement (Fig. 5.4) confirmed that the $YRuO_3$ perovskite adopted the orthorhombic *Pnma* superstructure owing to the ordered tilts of RuO_6 octahedra at ambient conditions. Secondary phases $Y_2Ru_2O_7$(15.1%) and Ru (5.0%) were observed as in the laboratory XRD patterns. The following parameters were refined and converged: lattice parameters for each phase, background fitted using equidistant experimental points and modelled by interpolation, scale factors, phase fractions and peak shape parameters *U, V, W* using pseudo-Voigt function (Npr 5). The thermal parameters B of the perovskite $YRuO_3$ were refined with each of the cations and anions constrained to identical values. The Ru-site occupancy was refined to 0.95(1) which improved the goodness-of- fit, while the Y-site and O-site occupancies were fixed to 1 as no significant vacancy concentration was obtained. The refined structural parameters of $YRuO_3$ are listed in Table 5.3. The Ru-O bond lengths and Ru-O-Ru angles are listed in Table 5.7. The Y-O bond lengths and Ru-Ru distances are shown in Appendix B. BVS calculations using a standard interpolation method[17] determined from the experimental M-O bond distances are consistent with the expected bond length of Ru^{3+} and Y^{3+}.

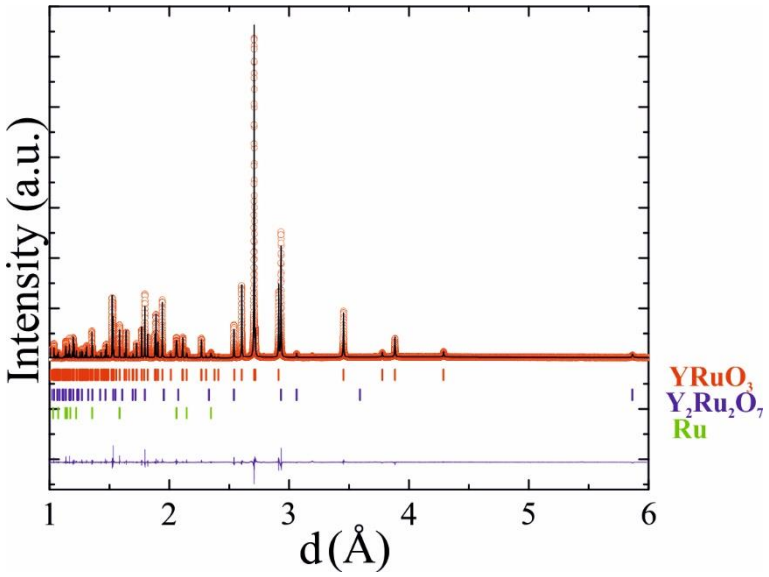

Fig. 5.4 Rietveld fitting to synchrotron X-ray powder data of $YRuO_3$. Additional Bragg marks identify secondary $Y_2Ru_2O_7$ (blue) and Ru (green).

Table 5.3. Crystallographic details of $YRuO_3$ from the Rietveld fit to the 300 K SXRD pattern, using space group *Pnma* and cell parameters a = 5.82480(1) Å, b = 7.55415(1) Å and c = 5.20894(1) Å. BVS calculated from the M-O bond lengths results are included in the last column.

Wyckoff	Atom	x	y	z	Occ	B_{iso}(Å^2)	BVS
4c	Y	0.0815(1)	0.25	-0.0289(1)	1.0	0.04(1)	2.99(1)
4b	Ru	0	0	0.5	0.944(1)	0.04(1)	2.81(2)
8d	O1	0.3096(4)	0.0603(3)	0.6824(4)	1.0	0.47(4)	_
4c	O2	0.4496(5)	0.25	0.1290(5)	1.0	0.47(4)	_

5.4.3 Neutron powder diffraction & magnetic structure of $YRuO_3$

Neutrons are essential to analyse the structures of metal oxides as they give accurate information on cation and oxygen atom positions and their stoichiometry. Previous reports illustrated that all $LnRuO_3$ perovskites exhibited approximately 10 % Ru-site vacancies and found no long-range magnetic ordering at any temperatures. Neutron diffraction was carried out on $YRuO_3$ to investigate the cation-site occupancy and magnetic properties. The Y^{3+} cation is diamagnetic which minimises the magnetic effect from the A-site in comparison to $LnRuO_3$ where a strong paramagnetic contribution arises from Ln^{3+}. $YRuO_3$ was synthesised using a HP-HT route; however, it could only yield a limit of ~12 mg product for each HP-HT experiment cycle. Consequently, several samples of $YRuO_3$ from several press cycles were well mixed to reach the neutron diffraction requirement of the sample volume. The high-flux

high-resolution WISH diffractometer (ISIS) could be used to measure a high-pressure sample volume with a minimum weight of 30 mg and provide the possibility of observing magnetic reflections at very long *d*-spacing.

Crystallographic analysis was carried out using the Rietveld method against diffraction data of $YRuO_3$ collected from multibanks of the WISH diffractometer. The refined *Pnma* structure of $YRuO_3$ from the synchrotron X-ray diffraction was used as the starting model to fit the 120 K neutron pattern.

For the 120 K data, most peaks could be identified using the *Pnma* perovskite structure, Ru and RuO_2. Tiny Bragg reflections of BN and the V-can were observed as well. The BN came from the capsule holder used in the HP-HT synthesis which broke when opening the sample capsule.

Profiles from banks 2-9 of the WISH diffractometer were fitted by refining 30 variables. The profile background was fitted using equidistant experimental points and modelled using an interpolation. Scale factors, lattice parameters, absorption correction parameters and the parameters Sig-2 and Gam-1 for the peak function (Npr = 13) were refined for all phases. For the $YRuO_3$ model, atomic coordinates, thermal parameters B_{iso} and the Ru-site occupancy were refined as well. The Rietveld fit of the NPD pattern collected at 120 K (Fig. 5.5) confirmed that $YRuO_3$ could be indexed with an orthorhombic unit cell (space group *Pnma*) with lattice parameters a = 5.835(1) Å, b = 7.528(1) Å and c = 5.193(1) Å. The structure consists of corner-sharing RuO_6 octahedra with Y^{3+} cations occupying the large coordination site. No significant vacancy concentrations were found for the Y, O1 and O2 sites, therefore the occupancies of these sites were fixed at 1 during the refinement. The refined Ru-site occupancy is 99%, in contrast with other $LnRuO_3$ (Ln = La, Pr and Nd)[8] compounds where Ru sites have 7-11% vacancies. 4 short Ru-O bonds (2.026 Å, 2.043 Å) and 2 longer Ru-O bonds (2.089 Å) are observed from NPD data revealing an octahedra elongation in the $YRuO_3$ crystal structure. The refined crystal information from the NPD data is summarised in Table 5.4. The ruthenium oxidation state in $YRuO_3$, estimated from BVS calculations from the experimental Ru-O bond lengths as +2.73, agrees with that estimated from SXRD refinements.

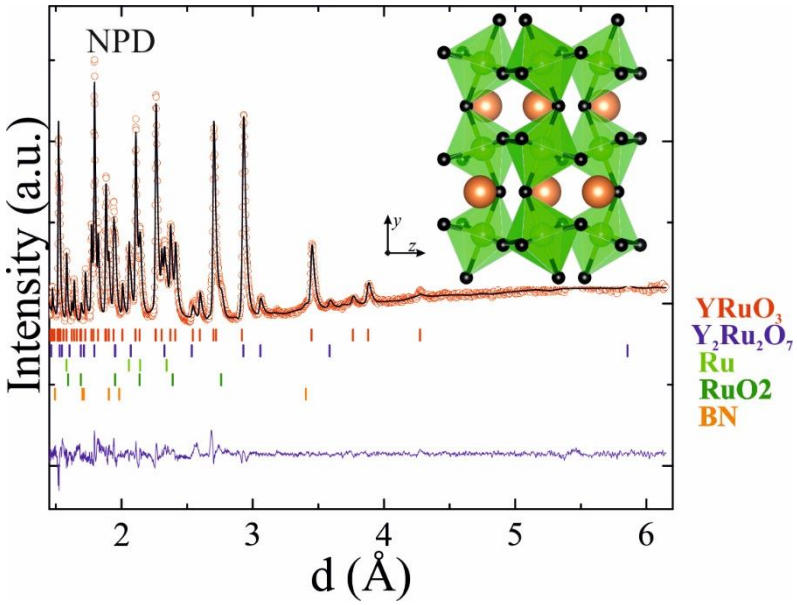

Fig. 5.5 Rietveld fit to the 120 K NPD data of $YRuO_3$. Bragg tick marks correspond, from top to bottom, to $YRuO_3$, $Y_2Ru_2O_7$ (16 %), Ru (8 %), RuO_2 (6 %) and BN from the sample assembly. The inset shows the crystal structure of $YRuO_3$ where Y, Ru and O are depicted in orange, green and black, respectively.

Table 5.4. Crystallographic details of $YRuO_3$ from the Rietveld fit to the 120 K NPD pattern, using space group *Pnma* and cell parameters a = 5.835(1) Å, b = 7.528(1) Å and c = 5.193(1) Å. BVS calculated from these results, are included in the last column.

Wyckoff	Atom	x	y	z	Occ	B_{iso}(Å^2)	BVS
4c	Y	0.082(6)	0.25	-0.024(1)	1.0	0.8(1)	3.10(2)
4b	Ru	0	0	0.5	0.992(2)	0.8(1)	2.73(3)
8d	O1	0.307(1)	0.0606(4)	0.671(1)	1.0	0.44(2)	_
4c	O2	0.448(1)	0.25	0.139(1)	1.0	0.44(2)	_

A single weak magnetic peak (red star in Fig. 5.6) was observed in the NPD data collected at 1.7 K. This magnetic reflection could be indexed with a propagation vector k = [0 0 0] in the *Pnma* space group. The magnetic symmetry analysis was carried out using the program BasIreps to determine the allowed irreducible representations (Irreps) and basis vectors (BV)13 which are summarised in Table 5.8. Fig. 5.8 depict the resulting magnetic unit cell, which can be describe as a G-type antiferromagnetic structure with the spins aligned along the z direction. Small spin cantings usually exist in *Pnma* perovskite structures however it cannot be observed from this neutron diffraction due to the resolution limit. The Ru^{3+} ordered magnetic moment obtained from the Rietveld fit of the low temperature NPD pattern (Fig.5.7) is 0.33 μ_B, close to the reported value for α-$RuCl_3$.[18] The crystallographic information is summarised in Table 5.5 and the refinement data is listed in Table 5.6. The structure is almost unchanged upon

cooling, with Ru-O bond lengths and Ru-O-Ru angles slightly changed (Table 5.7). The Y-O bond lengths and Ru-Ru distances are shown in Appendix B.

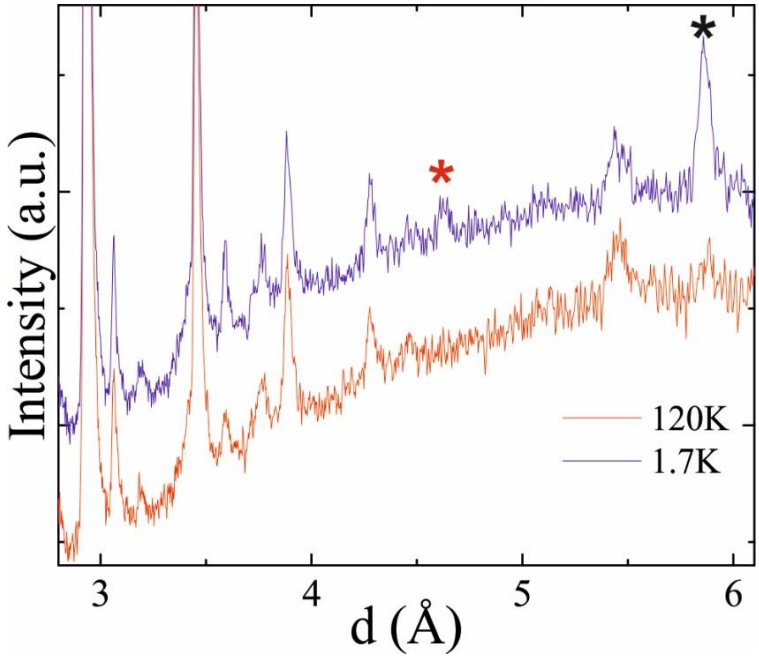

Fig. 5.6 $YRuO_3$ NPD patterns collected at 100 K and 1.7 K respectively. The red star identifies the magnetic signal from $YRuO_3$ while the black star represents the magnetic impurity of $Y_2Ru_2O_7$.

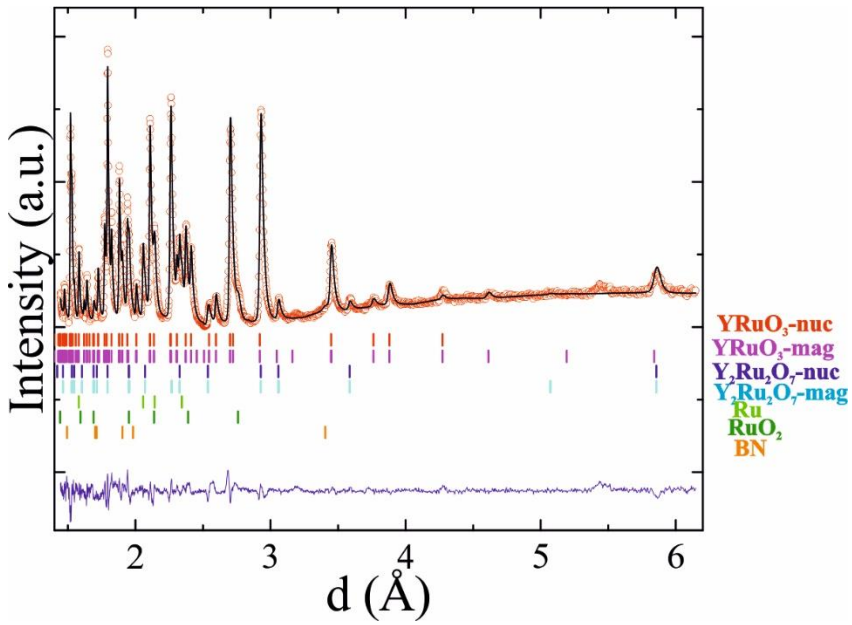

Fig. 5.7 Observed and calculated neutron powder diffraction pattern of $YRuO_3$ at 1.7 K. Tick marks corresponding to the positions of the structural and magnetic Bragg reflections of $YRuO_3$ are red and purple. The secondary $Y_2Ru_2O_7$ (nuclear/blue, magnetic /cyan), with Ru (green), RuO_2 (olive) and BN (orange) are depicted as well.

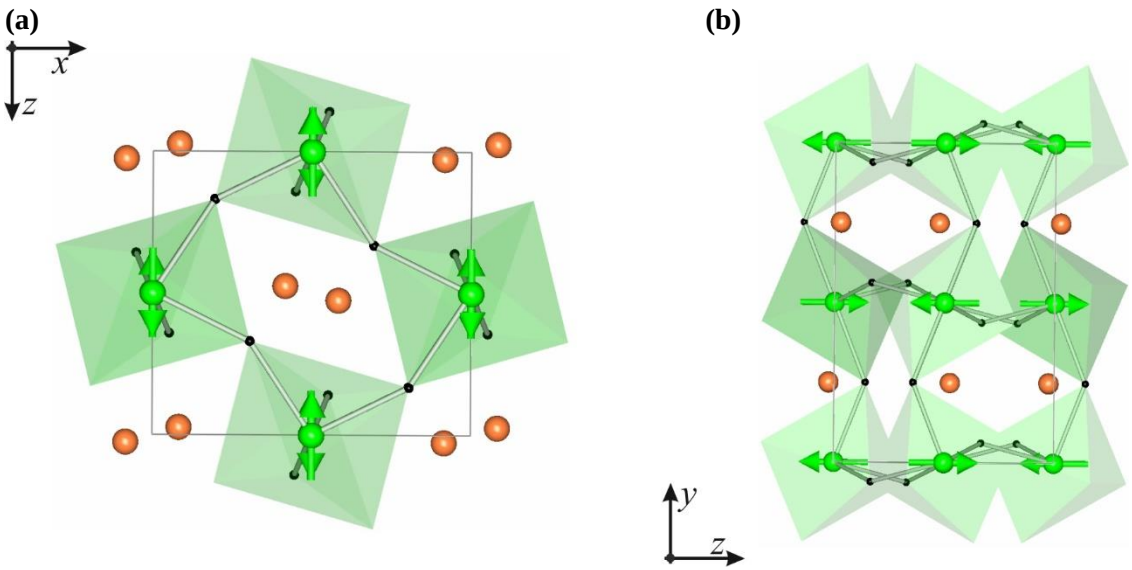

Fig. 5.8 The $YRuO_3$ magnetic structure viewed along **(a)** *z*-axis and **(b)** *x*-axis. The spins are ordered along the *z* direction.

Table 5.5 Crystallographic details for $YRuO_3$ from the Rietveld fit to the 1.7 K NPD pattern, using space group *Pnma* and cell parameters a = 5.839(1) Å, b = 7.523(1) Å and c = 5.192(1) Å. The magnetic structure with k = [0 0 0] results in μ = 0.33(3) μ_B. BVS calculated from these results, are included in the last column.

Wyckoff	Atom	x	y	z	Occ	B_{iso}(Å^2)	BVS
4c	Y	0.084(1)	0.25	-0.026(1)	1.0	0.5(1)	3.10(2)
4b	Ru	0	0	0.5	0.992(2)	0.5(1)	2.71(4)
8d	O1	0.305(1)	0.0617(4)	0.669(1)	1.0	0.4(1)	_
4c	O2	0.448(1)	0.25	0.141(1)	1.0	0.4(1)	_

Table 5.6 Refined data for $YRuO_3$ from the Rietveld fit to the NPD and SXRD pattern.

	N. of formula unit	Density (g / mol)	N. of the refined parameters	R-factors (%)	χ^2	Phase fraction (wt %)
NPD 300K	4	6.904(3)	30	R_p=1.63 R_{wp}=1.9 R_B=7.20 R_F=4.39	3.63	$YRuO_3$: 68.2(1) $Y_2Ru_2O_7$: 16.9(1) Ru: 8.2(1) RuO_2: 6.2(1) BN: 0.5(1)
NPD 1.7K	4	6.906(3)	23	R_p=1.56 R_{wp}=1.83 R_B=5.88 R_F=4.29 R_{mag}=3.78	3.48	$YRuO_3$: 68.2(1) $Y_2Ru_2O_7$: 17.0(1) Ru: 8.1(1) RuO_2: 6.3(1) BN: 0.4(1)
SXRD 300 K	4	6.731(2)	26	R_p=8.99 R_{wp}=11.9 R_B=5.32 R_F=7.52	6.13	$YRuO_3$: 78.0(1) $Y_2Ru_2O_7$:16.8(1) Ru: 5.2(1)

Table 5.7 Refined Ru-O bond lengths and Ru-O-Ru angles.

$YRuO_3$	d_{Ru-O} (Å)		<Ru-O1-Ru>°	<Ru-O2-Ru>°
NPD: 120 K	2 x 2.039(2) 2 x 2.048(4) 2 x 2.098(4) d_{Av} = 2.062(4)	Along b-axis In the *a*-*c* plane	140.8(2)	134.7(2)
NPD: 1.7 K	2 x 2.041(2) 2 x 2.040(3) 2 x 2.113(3) d_{Av} = 2.065(3)	Along b-axis In the *a*-*c* plane	140.4(2)	134.2(2)
SXRD: 300 K	2 x 2.026(1) 2 x 2.043(3) 2 x 2.089(3) d_{Av} = 2.053(3)	Along b-axis In the *a*-*c* plane	142.1(1)	137.6(1)

Table 5.8 Irreducible representations (IrReps) and basis vectors (BV) for the Ru spin order in $YRuO_3$ at 1.7 K, with propagation vector [0 0 0]. The magnetic atom is Ru at (0, 0, 0.5). The symmetry related positions are generated by the operator 1: (x, y, z), 2: (x+½, -y+½, -z+½), 3: (-x, y+½, -z+1), 4: (-x+½, -y, z-½). The structure was solved using $\Gamma_4\Psi_{10}$, $\Gamma_4\Psi_{11}$ and $\Gamma_4\Psi_{12}$ for the Ru site, with R_{mag} = 3.78%.

IrReps	Γ_1			Γ_2			Γ_3			Γ_4		
BV	Ψ_1	Ψ_2	Ψ_3	Ψ_4	Ψ_5	Ψ_6	Ψ_7	Ψ_8	Ψ_9	Ψ_{10}	Ψ_{11}	Ψ_{12}
Atoms	m_x	m_y	m_z	m_x	m_y	m_z	m_x	m_y	m_z	m_x	m_y	m_z
Ru_1	+	+	+	+	+	+	+	+	+	+	+	+
Ru_2	+	-	-	-	+	+	+	-	-	-	+	+
Ru_3	-	+	-	+	-	+	+	-	+	-	+	-
Ru_4	-	-	+	-	-	+	+	+	-	+	+	-

5.4.4 Magnetometry measurements of $YRuO_3$

Zero-field cooled / field cooled (ZFC/FC) magnetic susceptibility measurements collected in a 0.1 T magnetic field are shown in Fig. 5.9. Unlike the previously investigated $LnRuO_3$ perovskites which are paramagnetic down to 2 K,[8] $YRuO_3$ shows a weak ferromagnetic transition near 97 K. The inverse susceptibility in the high temperature range (150 - 300 K) cannot be fitted with a linear Curie Weiss expression (Fig. B.2) due to the existence of an unidentified ferromagnetic impurity which was confirmed as well in the hysteresis data shown in Appendix B. Magnetisation-field hysteresis loops in Fig. 5.10 show that $YRuO_3$ has a weak ferromagnetic moment of $M_w \approx 0.025\ \mu_B$ per ion at low temperatures. The *M*-*H* loops have a conventional shape from T_C = 97 K to 70 K, below which a positive magnetisation step at ¾M_w emerges as the field decreases (hence denote as +¾M_w(-)), persisting to $\mu_0 H$ = -0.35 T at 50 K (Fig. 5.10(d)). At temperatures below 10 K a prominent positive ¾M_w plateau appears with increasing field [+¾M_w(+); Fig. 5.10(a)]. This is retained up to 6.2 T at 2 K, and although this switches to the towards the M_w state at higher fields, it is notable that the maximum field of 9 T is not enough to fully saturate the weak ferromagnetism at 2 K, resulting in the apparent small decrease in measured M_w shown in Fig. 5.10(e).

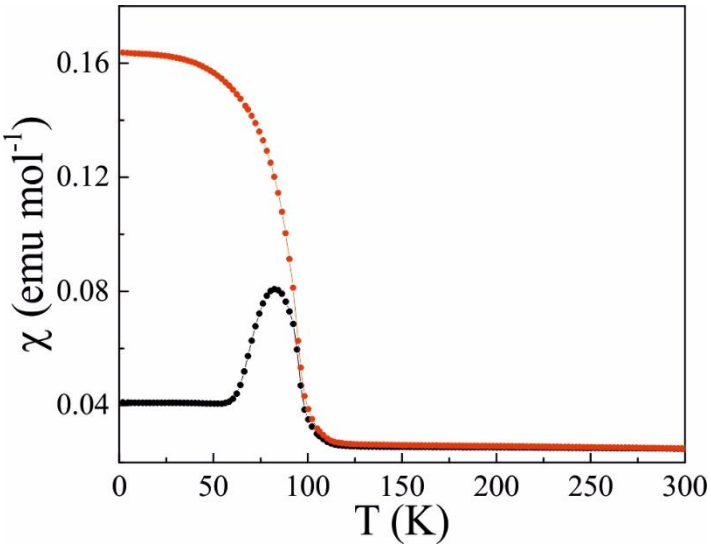

Fig. 5.9 ZFC/FC magnetic susceptibilities of $YRuO_3$ under a magnetic field of 0.1 T showing a magnetic transition at T_C = 97 K. The error bars are smaller than the marker size.

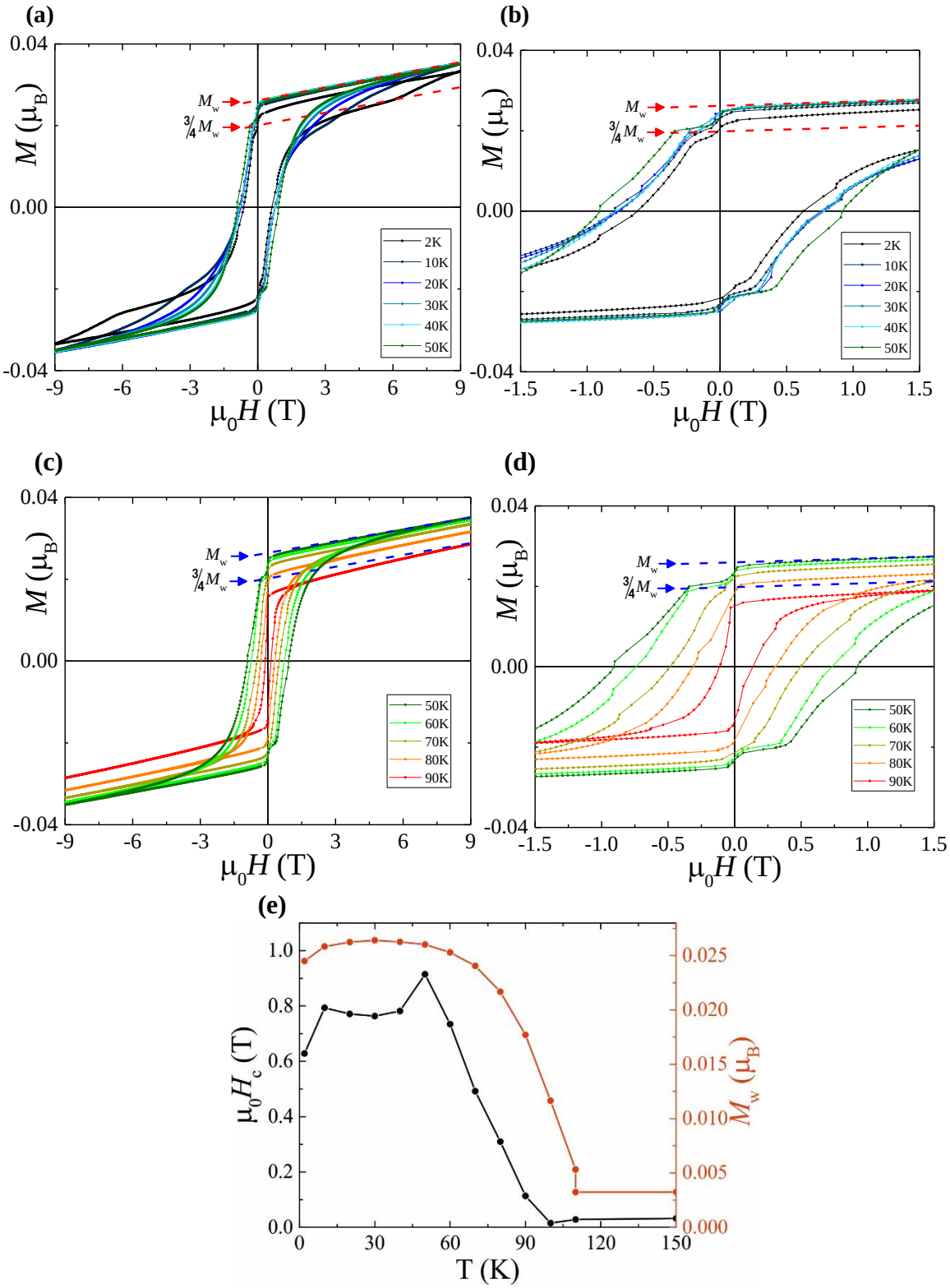

Fig. 5.10 Magnetisation-field loops for $YRuO_3$ **(a)** between 2 and 50 K, with **(b)** showing an expansion of the low-field region, and **(c)** between 50 and 90 K, with low-field expansion in (**d**). The saturated weak magnetisation M_w and the ¾M_w fractional weak ferromagnetic features are labelled. **(e)** Temperature dependences of M_w and coercive field H_c derived from the hysteresis loops. Error bars are smaller than the marker size.

As the observed magnetic transition temperature of $YRuO_3$ is close to that reported for the impurity phase $Y_2Ru_2O_7$ (antiferromagnetic below 80 K),[19-20] additional AC susceptibility measurements were carried out using a range of frequencies to identify their independent features (Fig. 5.11). As expected, two clear transitions are observed at 97 and 80 K, assigned to the perovskite $YRuO_3$ and the pyrochlore $Y_2Ru_2O_7$ respectively. The other impurities, Ru and RuO_2, are paramagnetic over the measured temperature range. A broad frequency-dependent feature is also observed in the real and imaginary susceptibilities. This emerges below 70 K and increases rapidly below 47 K with a sharp drop at 27 K and finally disappears below 10 K. The emergences of the +¾M_w(-) and +¾M_w(+) steps from the hysteresis loops respectively correspond to the appearance and disappearance of the frequency dependent signal in the AC susceptibility (Fig. 5.11), with the sharp changes at 27 and 47 K coinciding with a local minimum and the overall maximum in coercive field (Fig. 5.10(e)). These features are assigned to $YRuO_3$ as no magnetic hysteresis or other unusual low temperature features were observed in a study of the impurity phase $Y_2Ru_2O_7$.[20] Magnetisation loops at 100-300 K in Appendix show that a trace of ferromagnetic impurity is present but with a saturated magnetisation far below the weak ferromagnetism of $YRuO_3$.

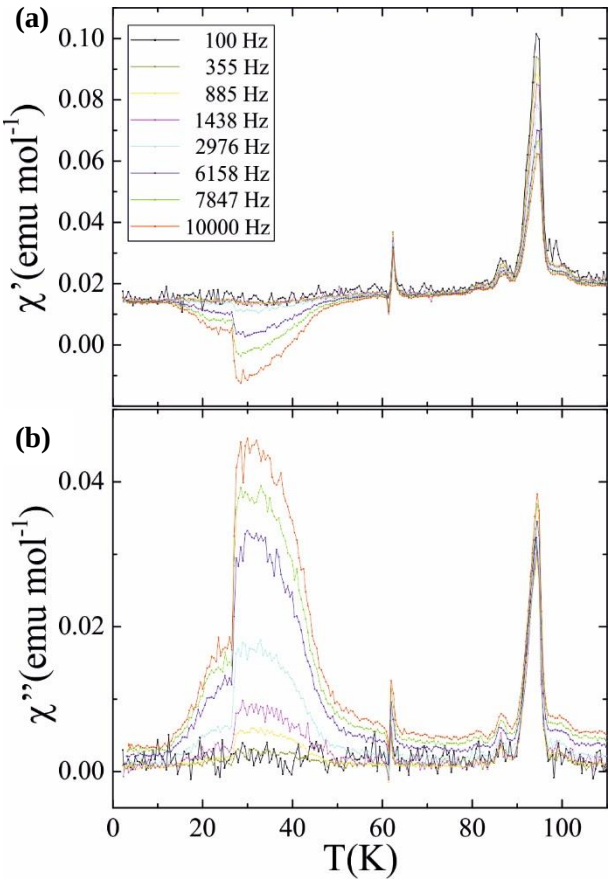

Fig. 5.11 (a) Real and **(b)** imaginary contributions to the AC susceptibility at various frequencies from 100 Hz to 10 kHz.

5.4.5 Electrical resistivity measurements

The temperature dependent electrical resistivity measurement (Fig. 5.12) was carried out with a four-probe configuration on an $YRuO_3$ ceramic pellet using the Quantum Design PPMS. $YRuO_3$ exhibits semiconducting behaviour between 30 - 400 K, with the resistance increasing as the temperature is decreased. The result, depicted in Fig. 5.12b showing the logarithmic resistivity against inverse temperature, follow the Arrhenius law (Equation 5.1 & 5.2) over the temperature range 80 K < T < 400 K.

$$\rho\,(T) = Ae^{\frac{-E_a}{k_B T}} \tag{5.1}$$

$$\log(\rho) = \log(A) + \frac{-E_a}{k_B}\left(\frac{1}{T}\right) \tag{5.2}$$

A is the pre-exponential factor and k_B is the Boltzmann constant (8.617 x 10^{-5} eV·K^{-1}). E_a refers to the activation energy which correlates with the semiconductor bandgap. The experimental activation energy of $YRuO_3$ is 70 meV.

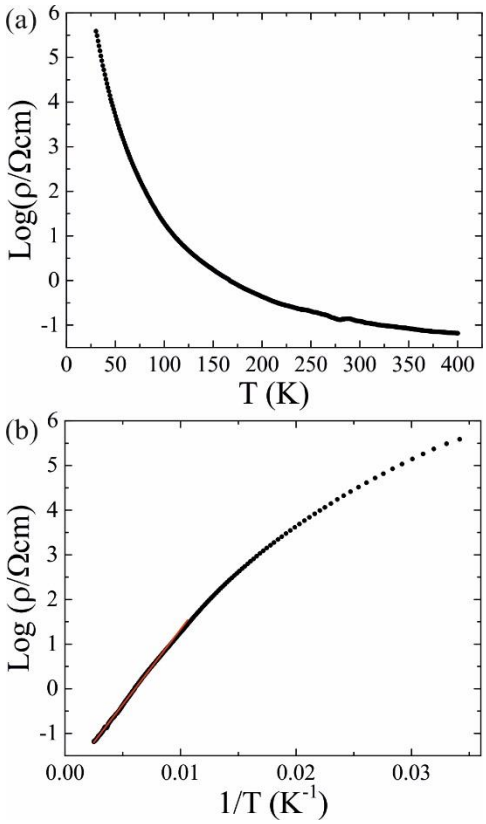

Fig. 5.12 (a) Thermal dependence of the logarithmic (log_{10}) resistivity of $YRuO_3$. **(b)** The logarithmic resistivity as a function of inverse temperature fitted to the Arrhenius law over the temperature range of 30 K ≤ T ≤ 400 K. Error bars are smaller than the marker size.

5.5 Discussion and conclusion

In contrast to $LaRuO_3$ which can be synthesised at ambient pressure, high pressure-high temperature conditions are essential to synthesise $YRuO_3$ with the smaller A-site cation Y^{3+}. According to synthesis conditions (10 GPa, 1200˚C) of $NdRuO_3$ ($r_{Nd^{3+}}$ = 1.16 Å) in the literature,[8] a higher pressure is required to stabilise the even smaller Y^{3+} cation ($r_{y^{3+}}$ = 1.02 Å). By increasing the pressure from 12 to 15 GPa and maintaining the temperature at 1200 ˚C, the relative proportion of the $YRuO_3$ phase increases from 15% to 90% indicating that applying further high pressure (>15 GPa) may favour the $LnRuO_3$ perovskite over the $Ln_2Ru_2O_7$ pyrochlores when the A site is occupied with even smaller cations such as Ln^{3+} = Yb^{3+} (r = 0.98 Å) or Lu^{3+} (r = 0.97 Å).

All powder diffraction techniques including laboratory X-ray, synchrotron X-ray and neutron powder diffraction confirm that $YRuO_3$ adopts the orthorhombic space group *Pnma* at 300 K and it maintains the *Pnma* symmetry down to 1.7 K. Neutron diffraction is particularly sensitive to oxygen positions which allows further investigation of the M-O bond lengths and RuO_6 octahedral geometry. The A-site coordination decreases from 12 in a cubic perovskite structure to 8 in orthorhombic $YRuO_3$ due to the large octahedral tilting system that stabilises the small A-site cation. The Ru-O1-Ru and Ru-O2-Ru bond angles of 140.8˚(2) and 134.7˚(2) respectively are considerably smaller than the ideal 180˚ B-O-B bond angles in the cubic perovskite structure. From these values, tilt angles of 19.6˚ and 22.65˚ are calculated from the equation $\varphi = (180-\alpha)/2$.[21-22] These large tilt angles are typical for highly distorted double perovskites,[5, 23] justifying the high-pressure conditions required to stabilise this compound. Compared to the related $LaRuO_3$ and $NdRuO_3$ (see Table 5.9), the Ru-O1-Ru and Ru-O2-Ru bond angles exhibit a decreasing trend inducing the occurrence of large octahedral tilting which contributes to stabilising smaller A-site cations in the perovskite structure, although the increasing distortion requires higher synthesis pressure conditions.

The experimental bond lengths obtained from the Rietveld fit of the NPD pattern collected at 120 K reveals an elongated Jahn-Teller distortion of the RuO_6 octahedra. These Ru-O bond distances from NPD data are consistent with an orbital ordering as 4 short and 2 long bonds are expected for a Jahn-Teller distortion of the low spin $4d^5$ configuration.

Table 5.9 $LnRuO_3$ perovskites crystal information. $LaRuO_3$ and $NdRuO_3$ (150 K) data are collected from A. Sinclair's thesis.[24]

M	d_{Ru-O} (Å)	<Ru-O1-Ru>˚	<Ru-O2-Ru>˚
La (150K)	2 x 2.0197(4) 2 x 2.027(1) 2 x 2.038(1) d_{Av} = 2.028(1)	152.34(6)	153.2(1)
Nd (150K)	2 x 2.007(1) 2 x 2.077(2) 2 x 2.079(2) d_{Av} = 2.054(2)	145.5(1)	146.5(1)
Y (120 K)	2 x 2.039(2) 2 x 2.048(4) 2 x 2.098(4) d_{Av} = 2.062(4)	140.8(2)	134.7(2)

Neutron diffraction analysis of $YRuO_3$ has also been used to compare the atomic vacancies with other $LnRuO_3$ as it is more accurate in determining the cation and oxygen stoichiometry. The neutron diffraction data of $YRuO_3$ reveals only 1% vacancies at the Ru-site in comparison with other $LnRuO_3$ perovskites where the Ru-sites normally have around 10 % vacancies. This has been confirmed by BVS calculations as well which calculate the ruthenium oxidation state to be close to +3. $YRuO_3$ is the first perovskite in the $LnRuO_3$ family which contains only pure Ru^{3+}. This may contribute to the formation of the long-range magnetic ordering as the cation-site vacancies and mixed Ru^{3+}/Ru^{4+} oxidation states in other $LnRuO_3$ could be the reason for their spin disorder and featureless magnetisation measurements.

The information on Ru^{3+} magnetic properties in metal oxides is very rare in the literature. In comparison with $LnRuO_3$ reported in the literature which exhibit paramagnetic behaviour at all temperatures, data from DC and AC susceptibilities confirm that $YRuO_3$ with diamagnetic Y^{3+} and spin ½ Ru^{3+} shows a weak ferromagnetic ordering at around 97 K. The diamagnetic Y^{3+} minimises the magnetic effect from the A-site and the fully occupied Ru^{3+} at the B-site is conducive to the formation of long-range magnetic ordering. The observation of a fractional weak magnetisation plateau that persists to high field (6.2 T at 2 K) results from the very high magnetic anisotropy that arises from strong spin orbital coupling (SOC) in Ru^{3+}. Very large coercive fields of 52 and 55 T were reported for the switching of ferromagnetic order in Sr_3CoIrO_6 and Sr_3NiIrO_6 reflecting the SOC of Ir^{4+}.[25] However to fully understand the

unprecedented fractional weak ferromagnetic state at ¾, more magnetisation hysteresis data need to be collected at different temperatures and at higher field. Sample purification is important as well to remove any magnetic contribution from the impurities. The magnetic structure of $YRuO_3$ has been solved from neutron data and can be described as a G-type antiferromagnetic spin ordering along the *z*-axis. Magnetic symmetry analysis reveals that the observed antiferromagnetic order can coexist with a ferromagnetic component parallel to the *y*-axis suggesting that $YRuO_3$ is a weak ferromagnet. Similar orders have been reported in other G-type *Pnma* perovskites such as $GdFeO_3$.[26,27,28] The small ordered magnetic moment of 0.33(3) μ_B is possibly due to the magnetic spin canting observed in many *Pnma* perovskites.

$LaRuO_3$ was reported to be metallic at room temperature. $NdRuO_3$ and $GdRuO_3$ however exhibit semiconducting behaviour with narrow bang gaps of 22 meV and 41 meV respectively.[8] $YRuO_3$ is a semiconductor as well with a band gap of 70 emV. Grain-grain boundary resistances in polycrystalline samples may be masking the intrinsic metallic behaviour of the bulk materials although the band gap of $LnRuO_3$ perovskites becomes larger as the radius of the A-site cation decreases.

References

1. J. M. Longo, *J. Appl. Phys.*, 1968, **39**, 1327

2. C.-Q. Jin, J.-S. Zhou, J. B. Goodenough, Q. Q. Liu, J. G. Zhao, L. X. Yang, Y. Yu, R. C. Yu, T. Katsura, A. Shatskiy, and E. Ito., *PNAS*., 2008, **105**, 7115

3. K. Ishida, H. Mukuda, Y.Kitaok, K. Asayama, Z. Q. Mao, Y. Mori, and Y. Maeno, *Nature*, 1998, **396**, 658.

4. S. A. Grigera, R. S. Perry, A. J. Schofield, M. Chiao, S. R. Julian, G. G. Lonzarich, S. I. Ikeda, Y. Maeno, A. J. Millis, A. P. Mackenzie, *Science*, 2001, **294**,329.

5. P. Kayser, S. Injac, B. Ranjbar, B. J. Kenedy, M. Avdeev and K. Yamaura, *Inorg. Chem*., 2017, **56**, 9009.

6. E. Granado, J. W. Lynn, R.F. Jardim and M. S. Torikachvili, *Phys. Rev. Lett*., 2013, **110**, 017202.

7. R. J. Bouchard, J. F. Weiher, *J. Solid State Chem*. 1972, **4**, 80.

8. A. Sinclair, J. A. Rodgers, C. V. Topping, M. Misek, R. D. Stewart, W. Kockelmann, J. G. Bos and J. P. Attfield, *Angew. Chem. Int. Ed*. 2014, **53**, 8343.

9. R. D. Shannon, *Acta Cryst. A*, 1976, **32**, 751

10. N. K. Labhsetwar, A. Watanabe, and T. Mitsuhashi, *Appl. Catal. B-Environ*., 2003, **40**, 21.

11. J. Rodriguez-Carvajal, *Physica B*, 1993, **192**, 55.

12. H. M. Rietveld, *J. Appl. Cryst*., 1969, **2**, 65.

13. J. Rodriguez-Carvajal 2007 BASIREPS: a program for calculating irreducible representations of space groups and basis functions for axial and polar vector properties; C. Ritter, *Solid State Phenom*. 2011, **170**, 263.

14. S. Gražulis, D. Chateigner, R. T. Downs, A. F. T. Yokochi, M. Quirós, L. Lutterotti, E. Manakova, J. Butkus, P. Moeck, and A. Le Bail, *J. Appl. Crystallogr*., 2009, **42**, 726.

15. *icsd.cds.rsc.org/icsd*

16. J. Rodriguez-Carvajal, *Physica B*, 1993, **192**, 55.

17. J.P. Attfield, *Solid State Sci*., 2006, **8**, 861.

18. A. Banerjee, C. A. Bridges, J. Yan, A. A. Aczel, L. Li, M. B. Stone, G. E. Granroth, M. D. Lumsden, Y. Yiu, J. Knolle, S. Bhattacharjee, D. L. Kovrizhin, R. Moessner, D. A. Tennant, D. G. Mandrus and S. E. Nagler, *Nat. Mater*., 2016, **15**, 733.

19. M. Ito, Y. Yasui, M. Kanada, H. Harashina, S. Yoshii, K. Murata, M. Sato, H. Okumura and K. Kakurai, J. *Phys. Soc. Jpn*, 2000, **69**,888.

20. N. Taira, M. Wakeshima and Y. Hinatsu, *J. Solid State Chem*. 2000, **152**, 441.

21. R. H. Mitchell, Perovskite: modern and ancient. 2002, Thunder Bay; Almaz Press

22. P. M. Woodward, *Acta Cryst*., 1997, **53**, 32.

23. P. D. Battle, C. W. Jones and F. Studer, *J. Solid State Chem*., 1991, **90**, 302.

24. A. L. Sinclair, High pressure synthesis and study of ternary ruthenates, Thesis, University of Edinburgh, 2013.

25. J. Singleton et al. *Phys. Rev. B*, 2016, **94**, 224408.

26. Y. Tokunaga, N. Rurukawa, H. Sakai, Y. Taguchi, T. Arima and Y. Tokura, *Nat. Mater*., 2009, **8**, 558.

27. Z. Y. Zhao, X. M. Wang, C. Fan, W. Tao, X. G. Liu, W. P. Ke, F. B. Zhang, X. Zhao and X. F. Sun, *Phys. Rev. B: Condens. Matter Mater. Phys*., 2011, **83**, 014414.

28. X. H. Zhu, X. B. Xiao, X. R. Chen and B. G. Liu, *RSC Adv*., 2017,**7**, 4054.

Chapter 6. Conclusion & future work

The study described in this thesis introduces the structural and physical properties of some 3*d* / 4*d* transition metal oxides that crystallise in the perovskite-type or corundum type structures. High-pressure techniques which helps the complex crystal structure ordered or stabilises unusual oxidation states was utilised in this work for synthesising new magnetic materials.

Chapter 3 describes the ambient pressure synthesis of a solid solution of Dion-Jacobson layered perovskites (CuCl)$La_{1-x}Sr_xNb_2O_7$ (x = 0, 0.1 and 0.2) via a two-step procedure including a low temperature ion-exchange route. The synchrotron X-ray diffraction data reveal that the room temperature crystal structures of all the solid solution members adopt the orthorhombic *Pbam* space group. The two high temperature structural order-disorder phase transitions of *Pbam* → *Pbmm* and *Pbmm* → *P*4/*mmm* (T_1 = 500 K, T_2 = 640 K) [1] reported in the reference (CuCl)$LaNb_2O_7$ have been observed in the Sr substituted compounds as well, however the transition temperatures decrease to $T_{1'}$ = 448 K, 373 K, and $T_{2'}$ = 598 K, 498 K for x = 0.1 and 0.2, respectively. The 3 different crystal structures of (CuCl)$La_{1-x}Sr_xNb_2O_7$ result from the order-disorder displacements of the Cu and Cl atoms within the (CuCl) interlayers. Four fold square-like coordination of Cu atoms constructing the core-sharing $[CuO_2Cl_2]$ plaquettes (two in-plane Cl atoms and two out-of-plane apical O atoms from the $[NbO_6]$ octahedra) result in zig-zag Cu-Cl---Cu-Cl chains along the *a* axis. The antiferromagnetic-like transition of T_N = 15 K in (CuCl)$LaNb_2O_7$ is suppressed with Sr substitution with effective moments of μ_{eff} = 1.802 μ_B and μ_{eff} = 1.986 μ_B for x = 0.1 and 0.2 respectively. Low temperature neutron powder diffraction data confirms the crystal structures of (CuCl)$La_{1-x}Sr_xNb_2O_7$ retain *Pbam* symmetry to 2 K and no long-range magnetic ordering was observed.

Future work on this series of layered copper oxyhalides could initially focus on using an ion-exchange reaction to synthesise new solid solutions such as (CuBr)$La_{1-x}Sr_xNb_2O_7$ or the triple layered compound (CuBr)$Sr_{2-x}La_xNb_3O_{10}$ for which the reference (CuBr)$Sr_2Nb_3O_{10}$ compound exhibits a complex helical AFM spin structure.[2] The advantage of using the ion-exchange route is that any spin lattices can be designed in principle as long as an appropriate precursor can be found. The phase purity of the existing samples needs to be enhanced to effectively prevent the magnetic contributions from the secondary phases so that a better Curie-Weiss fit can be carried out. This could be potentially implemented by using a higher annealing temperature under the

premise that no sample decomposition will occur. The same synthetic route may also be applied to looking for new layered perovskites, for example using other magnetic 3*d* transition metal cations other than Cu^{2+} or using two different cations to make intermediate solid solutions and to study their potential interesting magnetic properties as this system possesses low dimensional physical properties.

Chapter 4 describes a new double corundum polycrystalline material Co_2ScSbO_6 and its solid solutions $Ni_{2-x}Co_xScSbO_6$ (x = 0, 0.5, 1 and 1.5). The high-pressure method was required for the Co_2ScSbO_6 sample preparation (6 GPa, 1273 K) while other intermediate compounds are synthesised using a conventional solid-state route (1373 K) under ambient pressure. All compounds crystallised in the NTO-type structure with the polar space group *R*3. A B-antisite disorder was observed by neutron powder diffraction and was found to have a nearly linear relationship with the Co content x. Long range magnetic ordering was observed in all compounds below $T_N \approx 60$ K. The nominal magnetic phase boundaries were observed to occur near x = 0.5 and 1.5. An incommensurate [0 k_y 0] magnetic structure with spins confined in the *xz*/*yz* plane was found for x = 0 while for compounds with x = 0.5 - 2 a series of long period lock-in [0 0 k_z] spin structures with $k_z = 1/3n$ was observed. The strong anisotropy of the Co^{2+} cation caused the [0 0 k_z] spirals to lock into the nearby commensurate values so that more spins can lie parallel to the easy-axes which have a 3-fold symmetry in the *xy* plane of the *R*3 crystal structure, and therefore lead to the 1/3*n* formula. A competing [0 0 0] ferrimagnetic phase, which appears simultaneously with the lock-in phase at around 60 K, only arises with a Co content $x \geq 1.5$. A linear relationship between magnetisation and applied magnetic field with no loop has been observed in Ni-only Ni_2ScSbO_6 (x = 0) while a hysteresis loop revealing ferrimagnetic interactions has been found in Co-only Co_2ScSbO_6 (x = 2). Meta-magnetic transitions were observed in the intermediate compounds x = 0.5 and x = 1.0 indicating that these spin structures may be tuneable under a certain magnetic field. The net ferroelectric polarisation of Co_2ScSbO_6 is $P_S = 19.91$ μC cm^{-2} which is calculated from a point charge model.[3] In combination with its spiral spin structures and its rich magnetic information, the crystal *R*3 symmetry of the $Ni_{2-x}Co_xScSbO_6$ series allows possible linear or bilinear magnetoelectric effects, making these compounds possible multiferroic candidates.

According to the present magnetic phase diagram (Fig. 4.20), future work of this series could be concentred on synthesising and characterising further $Ni_{2-x}Co_xScSbO_6$ compositions to explore the full variety of spin structures and to find out the corresponding compositions for the predicted *n* values. The lower x-region ($x < 0.5$) needs to be particularly studied to

understand the spin structure transition between [0 k_y 0] and [0 0 k_z]; whether there is a structural boundary or whether it is a soft transition where two different spin structures may coexist. As some of the intermediate compounds exhibit a metamagnetic phenomenon, a high field neutron diffraction study is required to discover how the spin order changes near the metamagnetic transition and to determine the temperature-field-Co content, x (T-H-X) phase diagram. Electric measurements such as ferroelectric *P-E* loops and polarisation as a function of magnetic field need to be carried out for these compounds as well to investigate whether the potential magnetoelectric couplings exist. Single crystal or thin film studies of $Ni_{2-x}Co_xScSbO_6$ would also be promising and could further reveal the accurate crystal/magnetic structure along with ferroelectric and magnetoelectric couplings.

A simple ruthenate perovskite $YRuO_3$ with uncommon oxidation state Ru^{3+} detailed in Chapter 5 has been synthesised using high-pressure technique at 1473 K under 15 GPa. The pressure conditions are essential to prevent the formation of the competing pyrochlore phase $Y_2Ru_2O_7$ and to stabilise the very small A-site Y^{3+} cation in the crystal structure along with the very distorted RuO_6 octahedral frameworks. Synchrotron and neutron powder diffraction both confirmed that $YRuO_3$ adopts an orthorhombic crystal structure in space group *Pnma* at room temperature and retains this symmetry down to 2 K. Rietveld refinement using NPD data reveals an almost fully occupied B-site with formula $LaRu_{0.99}O_3$ for the first time and BVS calculations also confirmed that both Y and Ru ions exist in the trivalent state. In contrast to other $LnRuO_3$ perovskites, which are all paramagnetic down to 2 K, both DC and AC susceptibility measurements confirm that $YRuO_3$ exhibits a weak ferromagnetic ordering at 97 K. Magnetisation hysteresis loops at variable temperatures reveal an unprecedented fractional weak ferromagnetic state at 3/4 which reflects extreme single-ion anisotropy resulting from the strong spin-orbit coupling of the d^5 Ru^{3+} ion. The magnetic structure was solved as a G-type antiferromagnetic coupling with each Ru spin coupled antiferromagnetically to its six neighbours. The ordered spins are parallel to the *z*-axis and the ordered magnetic moment of $4d^5$ S = ½ Ru^{3+} cation is 0.33(3) μ_B. Further, electric resistivity measurements reveal that $YRuO_3$ exhibits semiconducting behaviour with a narrow band gap of 70 meV.

To fully explore the $LnRuO_3$ family, even smaller Ln^{3+} ions such as Ho^{3+} or Lu^{3+} need to be synthesised and therefore higher pressure and higher temperature conditions are required for this. Meanwhile, improving the synthetic methods to minimise the pyrochlore phase contribution is needed as well. This can be possibly done by adding an excess of Ru metal as the reducing reagent. Since the example of Ru (III) in metal oxides is rarely reported, searching

for suitable A-site cations with a trivalent state is essential to fully understand the electronic and magnetic properties of the very uncommon Ru^{3+} cations. New synthetic approaches or advanced techniques are desired to remove the laboratory pressure limitation and to enable the stabilisation of the crystal structure with a lower tolerance factor.

In summary, synthesising and characterising the first and second row transition metal oxides with interesting chemical and physical properties is essential in solid-state chemistry. Advanced technologies such as high-pressure techniques offer great help for achieving new magnetic oxides which have smaller magnetic cations or are metastable. Searching for new Dion-Jacobson layered perovskites with low dimensional physical properties, designing new polar magnets in the $AA'BB'O_6$ double corundum family with potential multiferroicity or synthesising new metal oxides with uncommon Ru (III) will be the next steps after this thesis.

References

1. A. A. Tsirlin, A. M. Abakumov, G. Van Tendeloo, and H. Rosner, *Phys. Rev. B*, 2010, **82**, 054107.

2. Y. Tsujimoto and H. Kageyama, Ion-Exchange Reactions for Two-Dimensional Quantum Antiferromagnetism, INTECH Open Access Publisher, 2012.

3. H. J. C. Berendsen, J. R. Grigera and T. P. Straatsma, J. *Phys. Chem*., 1987, **91**, 6269.

Appendix A: Structural models and susceptibility data for (CuCl)$La_{1-x}Sr_xNb_2O_7$

As described in Chapter 3, Rietveld analysis of synchrotron XRD has been used to understand the crystal structures of (CuCl)$La_{1-x}Sr_xNb_2O_7$. The following Figures and Tables provide the refined crystal details for (CuCl)$La_{1-x}Sr_xNb_2O_7$ with *Pbmm* and *P4/mmm* symmetry. Differential Scanning Calorimetry (DSC) and thermogravimetry (TG) data of (CuCl)$La_{1-x}Sr_xNb_2O_7$ is present as well.

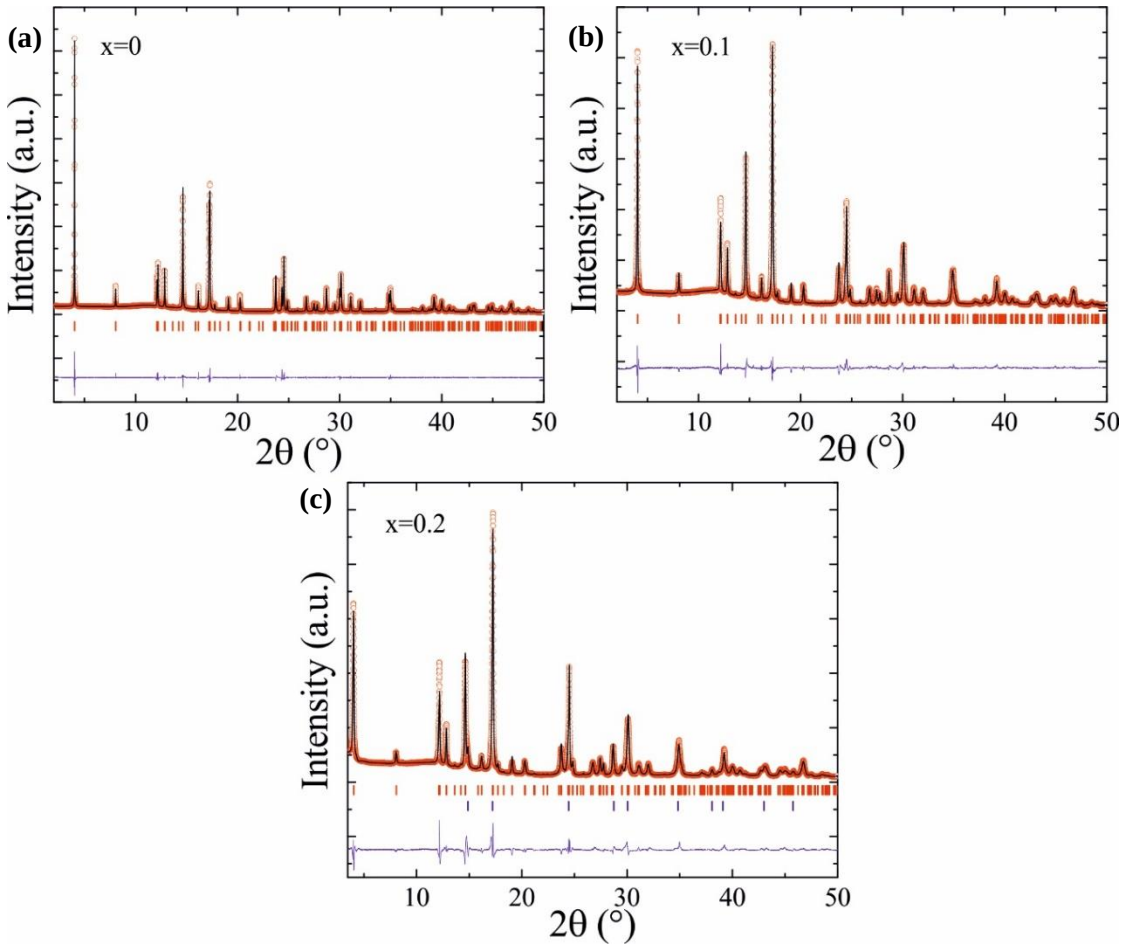

Fig. A.1 (a), **(b)**, **(c)** SXRD patterns for (CuCl)$La_{1-x}Sr_xNb_2O_7$ (x = 0, 0.1 and 0.2) that adopt the *Pbmm* orthorhombic structure. The blue tick marks in the x = 0.2 pattern refer to the secondary phase $CuCl_2$.

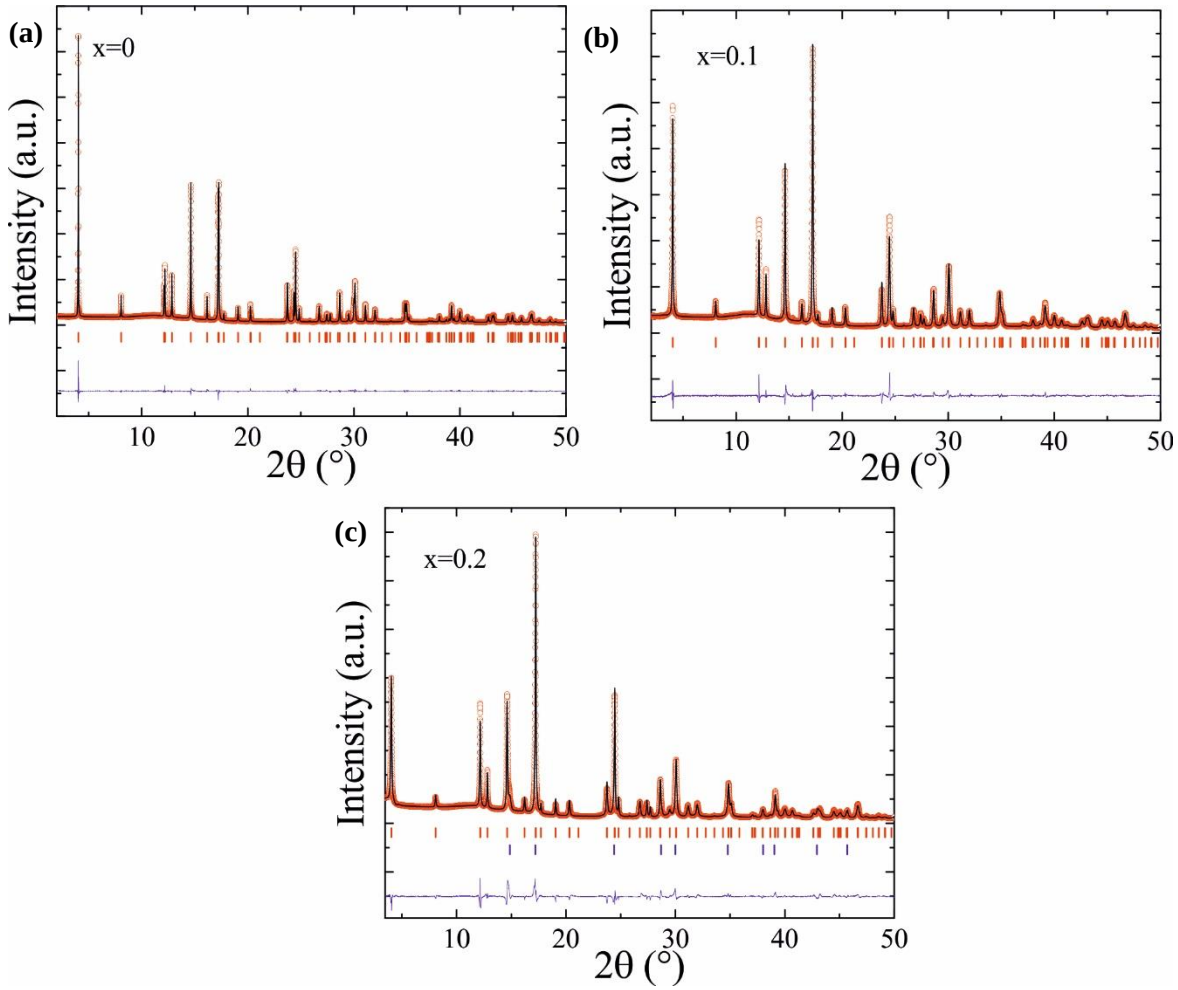

Fig. A.2 (a), **(b)**, **(c)** High temperature SXRD patterns for (CuCl)$La_{1-x}Sr_xNb_2O_7$ (x = 0, 0.1 and 0.2). All of them adopt the *P4/mmm* tetragonal structure. The blue tick marks in the x = 0.2 pattern refer to the secondary phase $CuCl_2$.

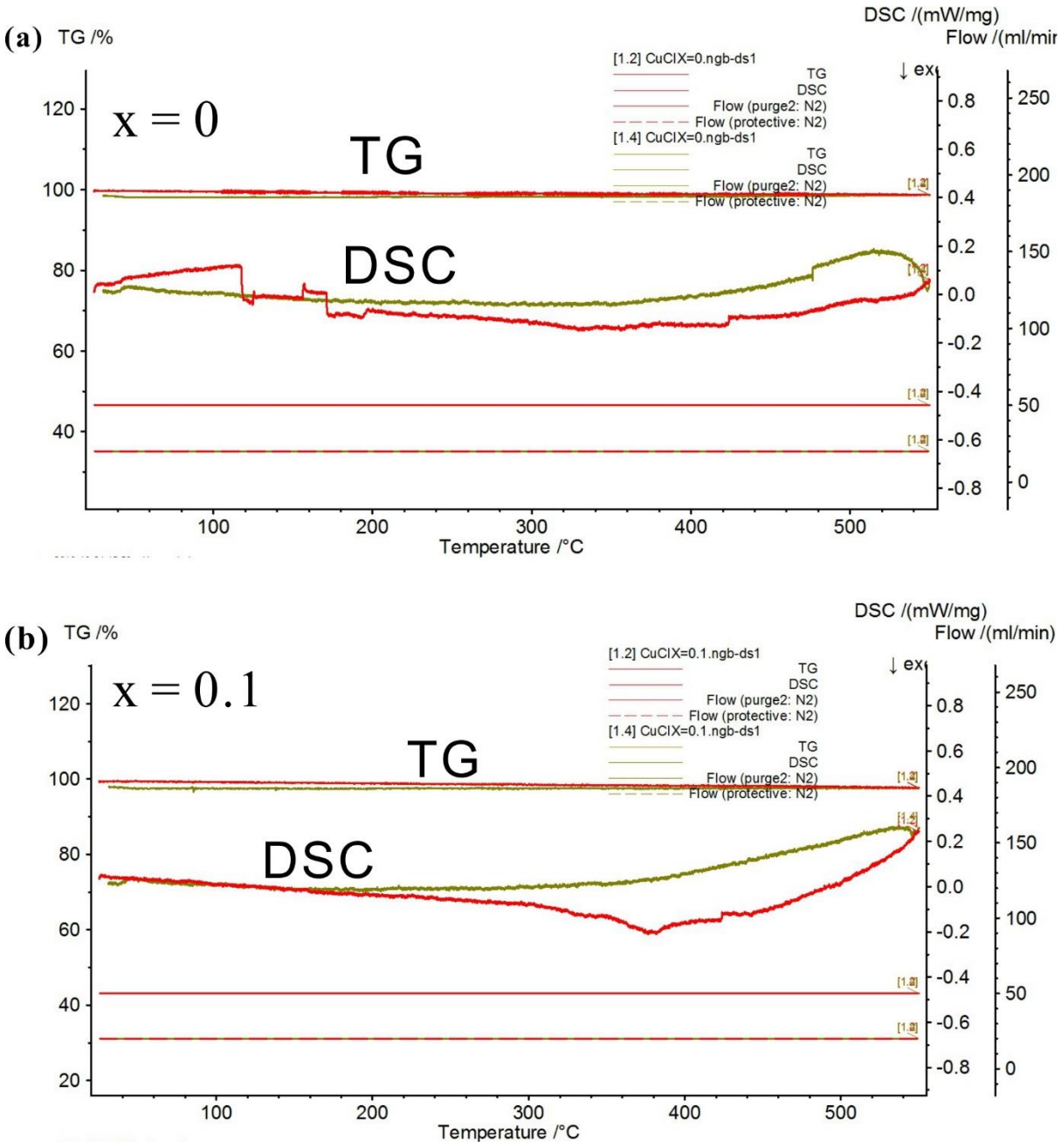

Fig. A.3 Differential Scanning Calorimetry (DSC) and thermogravimetry (TG) data of $(CuCl)La_{1-x}Sr_xNb_2O_7$, for **(a)**, x = 0 and **(b)**, x = 0.1. Red solid line represents data collected at warming, while black solid line represents the cooling data. No clear transition was observed

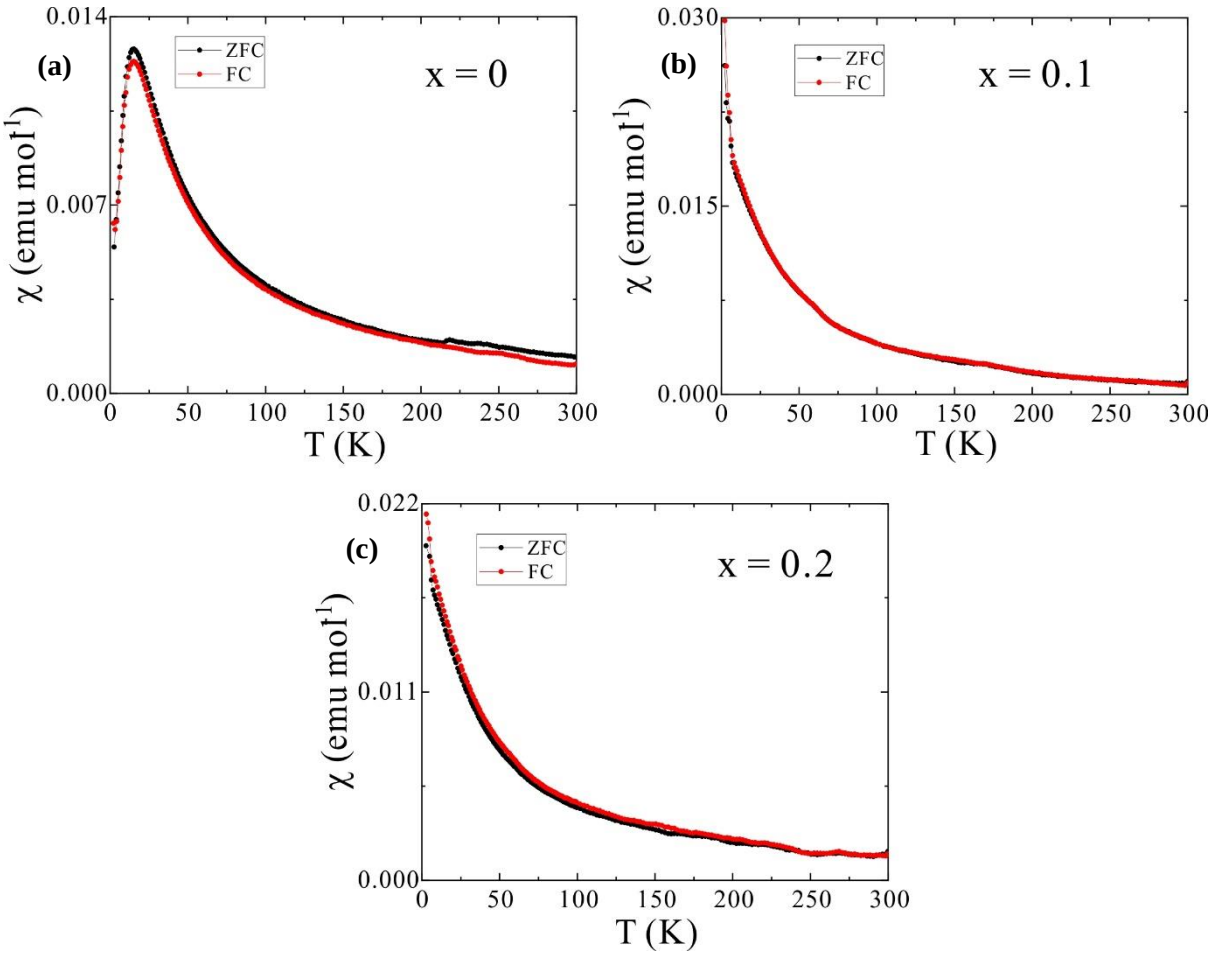

Fig. A.4 ZFC (black) and FC (red) susceptibility data for **(a)** x = 0, **(b)** x = 0.1 and **(c)** x = 0.2. The anomaly above 225 K in x = 0 may be a result from the partial loss of the powder sample from the capsule during the vibration process.

Table A.1 Crystallographic details of $RbLa_{1-x}Sr_xNb_2O_7$ (x = 0, 0.1, 0.2) from the lab X-ray Rietveld fits at room temperature.

	Atom	Wyckoff	x	y	z	Occupy	B_{iso}/Å^2
x = 0	Rb	4*a*	0	0	0	1.0	0.4(1)
	La	4*e*	0.5	0.25	0.489(5)	1.0	0.4(1)
	Nb	8*h*	0	0.349(1)	0.494(4)	1.0	0.4(1)
	O1	4*e*	0	0.25	0.45(1)	1.0	0.4(1)
	O2	8*h*	0	0.44(1)	0.57(1)	1.0	0.4(1)
	O3	8*g*	0.25	0.34(1)	0.25(2)	1.0	0.4(1)
	O4	8*g*	0.75	0.33(1)	0.75	1.0	0.4(1)
x = 0.1	Rb	4*a*	0	0	0	1.0	0.2(1)
	La/Sr	4*e*	0.5	0.25)	0.513(4)	0.94(1)/0.06(1)	0.2(1)
	Nb	8*h*	0	0.352(1)	0.507(4)	1.0	0.2(1)
	O1	4*e*	0	0.25	0.44(1)	1.0	0.2(1)
	O2	8*h*	0	0.44(1)	0.52(1)	1.0	0.2(1)
	O3	8*g*	0.25	0.34(1)	0.25	1.0	0.2(1)
	O4	8*g*	0.75	0.34(1)	0.75	1.0	0.2(1)
x = 0.2	Rb	4*a*	0	0	0	1.0	0.3(1)
	La/Sr	4*e*	0.5	0.25	0.509(7)	0.83(1)/0.17(1)	0.3(1)
	Nb	8*h*	0	0.354(1)	0.506(7)	1.0	0.3(1)
	O1	4*e*	0	0.25	0.44(1)	1.0	0.3(1)
	O2	8*h*	0	0.44(1)	0.52(1)	1.0	0.3(1)
	O3	8*g*	0.25	0.34(1)	0.25	1.0	0.3(1)
	O4	8*g*	0.75	0.33(1)	0.75	1.0	0.3(1)

Table A.2 Crystallographic details for the (CuCl)$La_{1-x}Sr_xNb_2O_7$ from the SXRD Rietveld fits.

	Atom	x	y	z	Occupy	B_{iso}/Å^2
x = 0	Cu	0.5622(5)	0	0.5	1.0	0.32(1)
493 K	Cl	0.1296(9)	0.75	0.5	1.0	0.46(5)
Pbmm	La	0.0001(5)	0.75	0	1.0	0.32(1)
a = 3.89135(3)	Nb	0.5	0	0.80799(5)	1.0	0.32(1)
b = 7.77401(5)	O1	0	0	0.8300(6)	1.0	0.46(5)
c = 11.76129(7)	O2	0.511(3)	0.25	0.8559(3)	1.0	0.46(5)
R_p = 4.40%	O3	0.5	0.5	0.6571(3)	1.0	0.46(5)
R_{wp} = 5.43%	O4	0.5	0	0	1.0	0.46(5)
x = 0.1	Cu	0.5671(6)	0	0.5	1.0	0.11(1)
483 K	Cl	0.115(1)	0.75	0.5	1.0	0.55(7)
Pbmm	La/Sr	0.0016(8)	0.75	0	0.864(2)/0.136(2)	0.11(1)
a = 3.8947(1)	Nb	0.5	0	0.80926(6)	1.0	0.11(1)
b = 7.7872(2)	O1	0	0	0.8614(8)	1.0	0.55(7)
c = 11.7404(2)	O2	0.527(4)	0.25	0.8244(8)	1.0	0.55(7)
R_p = 4.10%	O3	0.5	0.5	0.6563(4)	1.0	0.55(7)
R_{wp} = 5.64%	O4	0.5	0	0	1.0	0.55(7)
x = 0.2	Cu	0.557(1)	0	0.5	1.0	0.07(1)
423 K	Cl	0.143(2)	0.75	0.5	1.0	0.07(1)
Pbmm	La/Sr	-0.0001(9)	0.75	0	0.730(2)/0.270(2)	0.07(1)
a = 3.8967(1)	Nb	0.5	0	0.8108(1)	1.0	0.07(1)
b = 7.7864(2)	O1	0	0	0.8668(8)	1.0	0.07(1)
c = 11.7377(5)	O2	0.531(4)	0.25	0.8074(7)	1.0	0.07(1)
R_p = 5.16%	O3	0.5	0.5	0.6516(5)	1.0	0.07(1)
R_{wp} = 7.30%	O4	0.5	0	0	1.0	0.07(1)

Table A.3 Crystallographic details for the (CuCl)$La_{1-x}Sr_xNb_2O_7$ from the SXRD Rietveld fits at 703 K.

	Atom	x	y	z	Occupy	B_{iso}/Å^2
x = 0	Cu	0.570(1)	0.5	0.5	1.0	0.9(6)
703 K	Cl	0.107(1)	0	0.5	1.0	3.4(2)
P4/mmm	La	0	0	0	1.0	0.41(1)
a = 3.89368(1)	Nb	0.5	0.5	0.19226(4)	1.0	0.41(1)
c = 11.75650(5)	O1	0	0.5	0.1552(2)	1.0	0.71(4)
R_p = 2.70%	O2	0.5	0.5	0.3384(3)	1.0	0.71(4)
R_{wp} = 3.91%	O3	0.5	0.5	0	1.0	0.71(4)
x = 0.1	Cu	0.578(2)	0.5	0.5	1.0	1.1(1)
703 K	Cl	0.073(4)	0	0.5	1.0	5.5(4)
P4/mmm	La/Sr	0	0	0	0.904(1)/0.096(1)	0.05(1)
a = 3.90107(4)	Nb	0.5	0.5	0.19155(6)	1.0	0.05(1)
c = 11.7262(2)	O1	0	0.5	0.1571(3)	1.0	0.87(6)
R_p = 3.74%	O2	0.5	0.5	0.3402(5)	1.0	0.87(6)
R_{wp} = 5.39%	O3	0.5	0.5	0	1.0	0.87(6)
x = 0.2	Cu	0.5898(7)	0.5	0.5	1.0	0.02(1)
703 K	Cl	0.138(1)	0	0.5	1.0	0.02(1)
P4/mmm	La/Sr	0	0	0	0.774(1)/0.227(1)	0.02(1)
a = 3.90205(5)	Nb	0.5	0.5	0.1903(1)	1.0	0.02(1)
c = 11.7188(4)	O1	0	0.5	0.1588(3)	1.0	0.02(1)
R_p = 4.83%	O2	0.5	0.5	0.3511(5)	1.0	0.02(1)
R_{wp} = 7.26%	O3	0.5	0.5	0	1.0	0.02(1)

Appendix B: Magnetisation data for $YRuO_3$.

As introduced in Chapter 5, $YRuO_3$ has a ferromagnetic transition at 97 K. Extra magnetisation hysteresis data were collected near and above the transition temperature up to 300 K. A weak ferromagnetic signal was observed even at 300 K indicating a small amount of magnetic impurity exists. The Curie-Weiss fit cannot be reasonably fitted due to this impurity as well. This impurity cannot be identified and may come from the high-pressure sample preparation process or from the MPMS chamber.

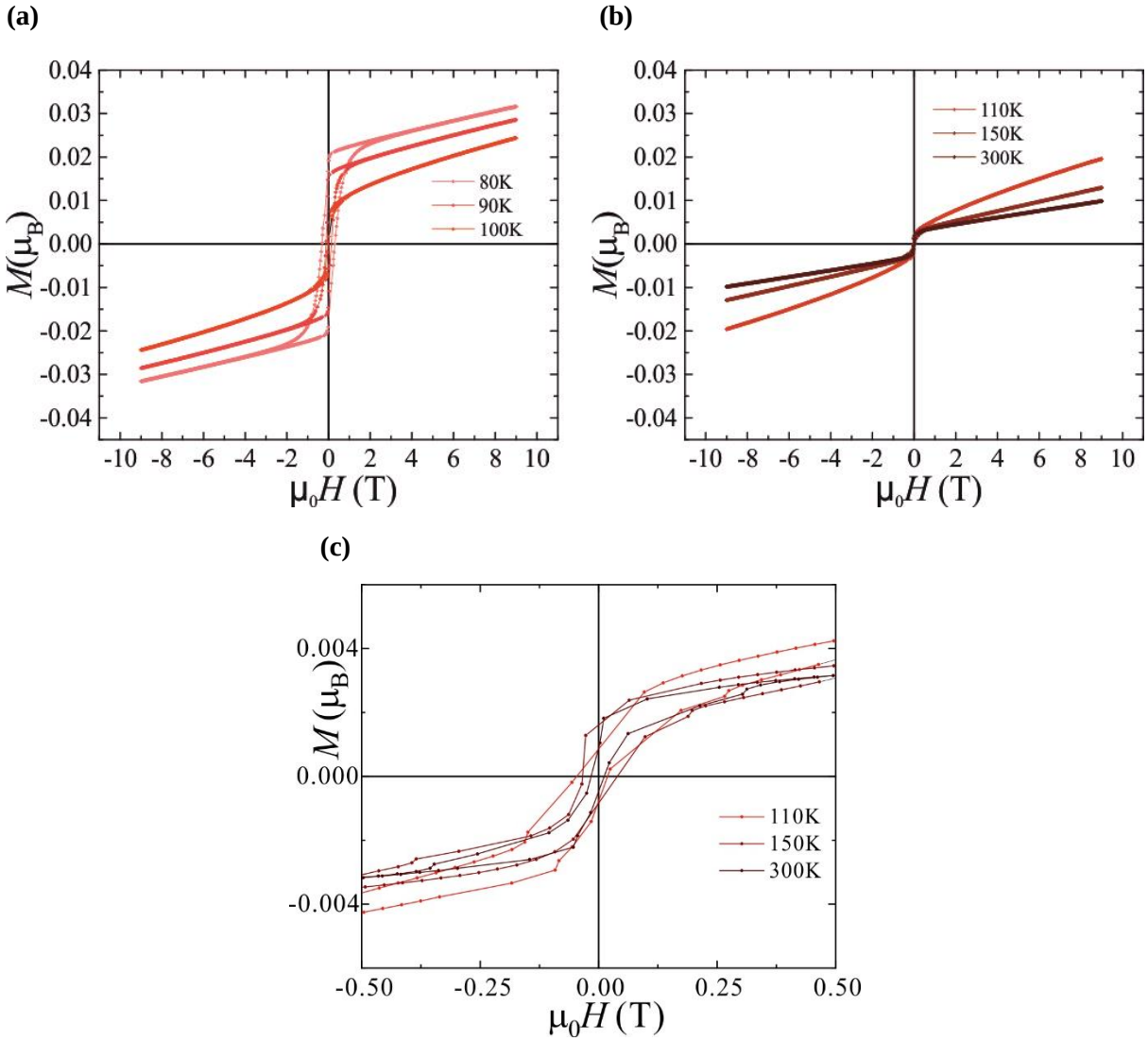

Fig. B.1 Magnetisation-field loops for $YRuO_3$, **(a)** between 80 K and 100 K, **(b)** between 110 K and 300 K. **(c)** The MH loop between -0.5 T and 0.5 T indicating the M_R, M_S H_C values at 300 K are 0.001 μ_B, 0.003 μ_B and 0.013 T respectively.

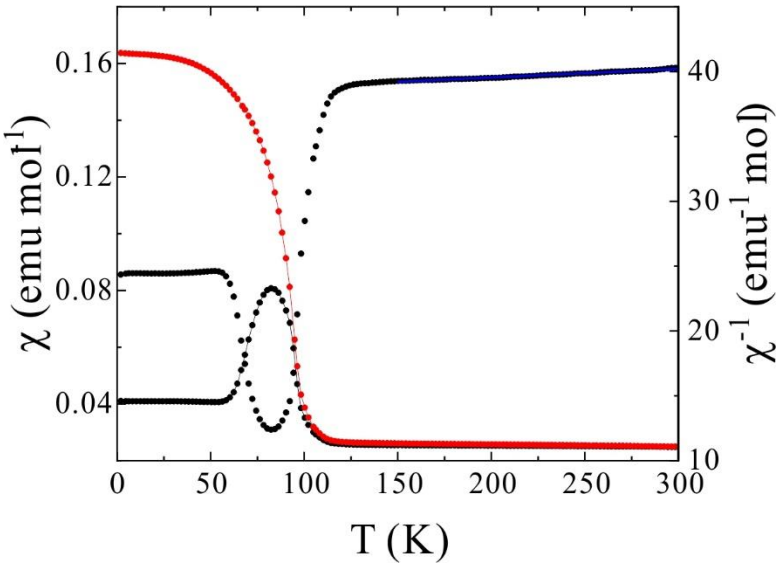

Fig. B.2 The attempted Curie-Weiss fit for $YRuO_3$ reciprocal susceptibility. The almost flat *CW* fit indicates a magnetic impurity present at 300 K. The error bars are smaller than the marker size.

Table B.1 Lab XRD refinement data from $YRuO_3$.

	N. of formula unit	Density (g/mol)	N. of refined parameters	*R*-factors (%)	χ^2
$YRuO_3$-HP8	4	6.931	28	R_P= 4.56	3.51
$YRuO_3$-HP9	4	6.933	28	R_P= 5.12	3.13
$YRuO_3$-HP10	4	6.935	28	R_P= 8.14	2.17
$YRuO_3$-HP11	4	6.707	28	R_P= 4.56	2.28

Table B.2 Refined Y-O bond lengths and nearest- nearest (n-n) and next n-n Ru-Ru distance.

$YRuO_3$	$D_{Y\text{-}O}$ (Å)	$D_{Ru\text{-}Ru}$ (Å)
NPD: 120 K	2 x 2.279(5)	
	2 x 2.629(4)	
	2 x 2.504(5)	3.9057(4)
	1 x 2.302(7)	3.7634(5)
	1 x 2.140(7)	
	d_{Av} = 2.408(3)	
NPD: 1.7 K	2 x 2.635(4)	
	2 x 2.487(4)	
	2 x 2.282(4)	3.9068(3)
	1 x 2.296(6)	3.7614(4)
	1 x 2.149(6)	
	d_{Av} = 2.407(4)	
SXRD: 300 K	2 x 2.667(3)	
	2 x 2.466(3)	
	2 x 2.280(3)	3.9079(3)
	1 x 2.297(3)	3.7708(4)
	1 x 2.220(4)	
	d_{Av} = 2.418(3)	

Publications

The following publications have resulted from work presented in this Thesis:

- Lock-in spin structures and ferrimagnetism in polar $Ni_{2-x}Co_xScSbO_6$ oxides
  K. Ji, E. Solana-Madruga, A. M. Arevalo-Lopez, P. Manuel, C. Ritter, A. Senyshyne and J. Paul Attfield, Chem. Commun., 2018, **54**, 12523

- Fractional weak ferromagnetism in $YRuO_3$
  K. Ji, A. Paul, E. Solana-Madruga, A. M. Arevalo-Lopez, U. V. Waghmare and J. Paul Attfield, in preparation.